UNIVERSITÉ PARIS-EST

THÉSE DE DOCTORAT
DE L'UNIVERSITÉ PARIS EST

École Doctorale : **SIE - Sciences, Ingénierie et Environnement**

Spécialité : **Géotechnique**

Présentée par

Ali Gandomzadeh

pour obtenir le titre de Docteur
de l'Université Paris Est

Titre

Interaction Dynamique Sol-Structure : Influence des Nonlinéarités de Comportement du Sol

Soutenue le 8 février 2011, devant le jury composé de :

Présidente	**Mme. Arezou MODARESSI**
Rapporteurs	**M. Roberto PAOLUCCI** **M. Philippe GUEGUEN**
Examinateurs	**M. Fabrice COTTON** **M. Jean-Mathieu RAMBACH**
Directeurs de thèse	**M. Jean-François SEMBLAT** **M. Fabian BONILLA**

To my lovely parents

Habib and Mahvash

In memory of my family members

who lost their lives in the Tabas earthquake (1978)

Avant-propos

Cette thèse a été réalisée au Laboratoire Central des Ponts et Chaussées (LCPC)[1] au sein du département GER (Géotechnique, Eau et Risque). La thèse a été financée par le LCPC et l'IRSN[2] (Institut de Radioprotection et de Sûreté Nucléaire).

Tout d'abord, je tiens à remercier Jean-François SEMBLAT et Fabian BONILLA, mes directeurs de thèse pour avoir accepté de me confier cette thèse et également pour leur soutien, leurs encouragements et leurs conseils précieux dans l'orientation de mon travail. Je tiens aussi à remercier Luca LENTI pour son aide et ses conseils au cours de ces années de thèse. Je remercie également Benoît PEBOSCQ pour ses aides généreuses concernant la programmation au sein du logiciel CESAR-LCPC. À Stéphane RIGOBERT, j'adresse aussi mes remerciements pour son aide au cours de l'implémentation des éléments de contact dans le logiciel CESAR-LCPC.

Je voudrais aussi exprimer ma gratitude à Messieurs Roberto PAOLUCCI et Philippe GUEGUEN qui m'on fait l'honneur d'accepter la lourde tâche d'être rapporteurs de ma thèse. Je remercie également Mme. Arezou MODARESSI, M. Fabrice COTTON et M. Jean-Mathieu RAMBACH qui ont accepté d'examiner mon travail.

Enfin, je tiens à associer à ces remerciements les membres du groupe GER (anciennement MSRGI) pour les moments agréables que nous avons passée ensemble au cours des ces années. Je pense particulièrement à Aurélie, Camille, Catherine, Céline, Eva, Irina, Julien, Lamis, MariaPaola, Morgane, Pedram et les autres qui ont contribué à faire de mon passage au LCPC une très bonne expérience personnelle et scientifique.

[1] LCPC-IFSTTAR : 58, boulevard Lefebvre, 75732, Paris Cedex 15

[2] IRSN : 31, avenue de la Division Leclerc, 92260, Fontenay-aux-Roses

Résumé

L'interaction dynamique sol-structure a été largement explorée en supposant le comportement linéaire du sol. Néanmoins, pour des séismes d'intensité modérée à forte, la contrainte de cisaillement maximale peut facilement atteindre la limite élastique du sol. Du point de vue de l'interaction sol-structure, les effets non linéaires peuvent modifier la rigidité du sol à la base de la structure ainsi que la quantité d'énergie dissipée dans le sol. En conséquence, ignorer les caractéristiques non linéaires du sol dans l'interaction dynamique sol-structure (IDSS) peut conduire à des prédictions erronées de la réponse de la structure.

Le but de ce travail est d'implémenter dans un code numérique une loi de comportement non linéaire pour le sol afin d'examiner l'effet de la nonlinéarité du sol sur l'interaction dynamique sol-structure. De plus, différents aspects sont pris en compte tels que l'effet de la contrainte de confinement sur le module de cisaillement du sol, les conditions statiques initiales, les conditions d'interface entre le sol et la structure, etc. Durant ce travail, une méthode simple de couche absorbante basée sur une formulation de Rayleigh/Caughey pour l'amortissement, qui est généralement disponible dans les logiciels existants d'éléments finis, a également été développée. Les conditions de stabilité des problèmes de propagation d'onde sont étudiées et on montre que les comportements linéaire et non linéaire sont très différents en ce qui concerne la dispersion numérique. La règle habituelle de 10 points par longueur d'onde, recommandée dans la littérature pour les milieux élastiques, apparaît pas suffisante dans le cas non linéaire.

Le modèle implémenté est d'abord vérifié numériquement en comparant les résultats avec ceux d'autres codes numériques connus. Après cela, une étude paramétrique est menée pour différents types de structures et des profils de sol variés afin de caractériser les effets non linéaires. Différentes caractéristiques de l'IDSS sont comparées à celles du cas linéaire: modification de l'amplitude et du contenu fréquentiel des ondes se propageant dans le sol, fréquence fondamentale, dissipation de l'énergie dans le sol et réponse du système sol-structure. A travers ces études paramétriques nous montrons qu'en fonction des propriétés du sol, le contenu fréquentiel de la réponse du sol peut changer significativement à cause des nonlinéarités de comportement. Les pics de la fonction de transfert entre le champ libre et le rocher affleurant se décalent vers les basses fréquences et l'amplification se produit dans cette gamme de fréquences. Une réduction de l'amplification pour les hautes fréquences et même une dé-amplification peuvent se produire pour un fort niveau des mouvements d'entrée. Ces changements influencent la réponse de la structure.

Ce travail montre également que la proximité des fréquences fondamentales de la structure et du sol influence fortement l'interaction sol-structure. Enfin, l'effet du poids de la structure et du balancement de la superstructure peut être significatif. Finalement, le bassin de Nice est utilisé comme un exemple de propagation d'onde dans un milieu non linéaire hétérogène et d'interaction dynamique sol-structure. La réponse du bassin dépend fortement de la combinaison de la nonlinéarité du sol, des effets topographiques et du contraste d'impédance entre les couches de sol. Pour les structures et les profils de sol sélectionnés dans ce travail, les simulations numériques réalisées montrent que le décalage de la fréquence fondamentale n'est pas un bon indicateur pour distinguer le comportement linéaire du sol du comportement non linéaire.

Mots-clés: *sol non linéaire, interaction dynamique sol-structure, éléments finis, dissipation d'énérgie, couches absorbantes, dispersion numérique, interface sol-structure*

Abstract

The interaction of the soil with the structure has been largely explored the assumption of material and geometrical linearity of the soil. Nevertheless, for moderate or strong seismic events, the maximum shear strain can easily reach the elastic limit of the soil behavior. Considering soil-structure interaction, the nonlinear effects may change the soil stiffness at the base of the structure and therefore energy dissipation into the soil. Consequently, ignoring the nonlinear characteristics of the dynamic soil-structure interaction (DSSI) this phenomenon could lead to erroneous predictions of structural response.

The goal of this work is to implement a fully nonlinear constitutive model for soils into a numerical code in order to investigate the effect of soil nonlinearity on dynamic soil structure interaction. Moreover, different issues are taken into account such as the effect of confining stress on the shear modulus of the soil, initial static condition, contact elements in the soil-structure interface, etc. During this work, a simple absorbing layer method based on a Rayleigh/Caughey damping formulation, which is often already available in existing Finite Element softwares, is also presented. The stability conditions of the wave propagation problems are studied and it is shown that the linear and nonlinear behavior are very different when dealing with numerical dispersion. It is shown that the 10 points per wavelength rule, recommended in the literature for the elastic media is not sufficient for the nonlinear case.

The implemented model is first numerically verified by comparing the results with other known numerical codes. Afterward, a parametric study is carried out for different types of structures and various soil profiles to characterize nonlinear effects. Different features of the DSSI are compared to the linear case: modification of the amplitude and frequency content of the waves propagated into the soil, fundamental frequency, energy dissipation in the soil and the response of the soil-structure system. Through these parametric studies we show that depending on the soil properties, frequency content of the soil response could change significantly due to the soil nonlinearity. The peaks of the transfer function between free field and outcropping responses shift to lower frequencies and amplification happens at this frequency range. Amplification reduction for the high frequencies and even deamplication may happen for high level input motions. These changes influence the structural response.

We show that depending on the combination of the fundamental frequency of the structure and the the natural frequency of the soil, the effect of soil-structure interaction could be significant or negligible. However, the effect of structure weight and rocking of the superstructure could change the results. Finally, the basin of Nice is used as an example of wave propagation on a heterogeneous nonlinear media and dynamic soil-structure interaction. The basin response is strongly dependent on the combination of soil nonlinearity, topographic effects and impedance contrast between soil layers. For the selected structures and soil profiles of this work, the performed numerical simulations show that the shift of the fundamental frequency is not a good index to discriminate linear from nonlinear soil behavior.

Key words: *nonlinear soil, dynamic soil-structure interaction, finite element, energy dissipation, boundary condition, numerical dispersion, soil-structure interface*

Contents

List of Figures

Introduction

Earthquake engineering research has shown that a structure founded on a deformable soil could respond differently compared to a fixed base situation. Indeed, in a flexible supported case, mutual interaction between structure and the nearby soil takes place inducing modifications in the dynamic response. It has conventionally been considered that soil-structure interaction has beneficial effect on the seismic response of a structure. Many design codes have suggested that the effect of SSI can reasonably be neglected for the seismic analysis of structures. Most of the design codes use oversimplified design spectrum, which attain constant acceleration up to a certain period, and thereafter decreases monotonically with period. Considering soil-structure interaction makes a structure more flexible and thus, increasing the natural period of the structure compared to the corresponding fixed base structure. This conservative simplification is valid for certain classes of structures and soil conditions, such as light structures in relatively stiff soil. Unfortunately, this assumption does not always hold true. In fact, the SSI can have a detrimental effect on the structural response, and neglecting SSI in the analysis may lead to unsafe design for both the superstructure and the foundation.

The interaction of the soil with the structure has been largely explored the assumption of material and geometrical linearity of the soil. Nevertheless, for moderate or strong seismic events, the maximum shear strain can easily reach the elastic limit of the soil behavior. Considering soil-structure interaction, the nonlinear effects may change the soil stiffness at the base of the structure and therefore energy dissipation into the soil. Consequently, ignoring the non-linear characteristics of the dynamic soil-structure interaction (DSSI) this phenomenon could lead to erroneous predictions of structural response.

For years, the fully nonlinear dynamic analyses were not a usual practice, restricted by the computation cost of such operations. Nowadays, nonlinear analyses are more and more frequent in engineering practice. Consequently, it is a challenge for researchers to identify configurations where the structural response is highly affected by the nonlinear soil behavior.

The goal of this work is to implement a fully nonlinear constitutive model for soils into a numerical code in order to investigate the effect of soil nonlinearity on dynamic soil structure interaction. Moreover, different issues should be taken into account such as the effect of confining stress on the shear modulus of the soil, initial static condition, contact elements in the soil-structure interface, etc. During this work, a simple absorbing layer method based on a Rayleigh/Caughey damping formulation, which is often already available in existing Finite Element softwares, is also presented.

The implemented model is first numerically verified by comparing the results with other known numerical codes. Afterward, a parametric study is carried out for different types of structures and various soil profiles to characterize nonlinear effects. Different features of the DSSI are compared to the linear case: modification of the amplitude and frequency content of the waves propagated into the soil, fundamental frequency, energy dissipation in the soil and response of the soil-structure system. Finally, the effect of soil nonlinearity on DSSI is investigated in case of a structure based on a real basin (Nice basin).

Organization and outline

The organization and outline of this thesis are as follows:

Chapter 1 presents the theory behind general dynamic soil-structure interaction problem by defining the related governing equations in the soil-structure domain. The numerical program, CESAR-LCPC, that is used during this work to study the dynamic soil-structure interaction is briefly presented. Furthermore, the new developments (nonlinear constitutive model for soils, effect of confining stress on the shear modulus of the soil, initial static condition, absorbing boundaries, contact elements in the soil-structure interface, etc.) on the CESAR-LCPC code are also mentioned which are necessary to model the nonlinear dynamic soil-structure interaction.

Chapter 2 presents a simple absorbing layer method. It is based on a Rayleigh/Caughey damping formulation which is often already available in existing Finite Element softwares. The efficiency of the method is then shown through 1D and 2D Finite Element simulations considering homogeneous and heterogeneous damping in the absorbing layer. Moreover, a comparison with the PML method is also performed.

Chapter 3 is dedicated to the nonlinear behavior of soils and soil constitutive models. A review of various existing soils constitutive models, particularly the nonlinear model that is selected in this work are presented. The theoretical aspects of this model and its implementation to the CESAR-LCPC numerical program are summarized. Finally, in order to verify the implemented model, the results are compared with other numerical tools in time and frequency domains.

Chapter 4 presents the investigation of the numerical dispersion in the case of waves propagating in nonlinear elastoplastic materials. A 1D parametric analysis is performed to investigate the number of points per wavelength in various nonlinear cases. The more important features of numerical dispersion are discussed and some efforts in quantifying the dispersion considering nonlinear materials are reviewed.

Chapter 5 introduces the effect of soil nonlinearity on dynamic soil-structure interaction through a parametric study. Various combinations of the fundamental frequency of the structure and natural frequency of soil are considered. Different features of nonlinear DSSI are studied and finally, the soil nonlinearity is quantified by energy dissipation into the soil index and its effect on dynamic soil-structure interaction is discussed.

Chapter 6 is dedicated to the study of a case study. The basin of Nice is selected to investigate the effect of soil nonlinearity. The response of this basin is compared between linear and nonlinear soil rheology. First, the effect of soil nonlinearity on site effect is studied and in the second step, dynamic analyses of the soil-structure system composed of Nice basin and a 10-story building are performed considering linear and nonlinear rheology for the soil layers of the basin.

Chapter 1

Seismic wave propagation and dynamic soil-structure interaction

Contents

1.1 Introduction

The assessment of dynamic soil-structure interaction needs several parameters to be identified: site geometry, the non-linear soil behavior under cyclic loading, the soil material properties, the dynamic response of the superstructure, the wave content and amplitude modifications due to stiffness of the structures. Nevertheless, due to the limitation of the state of the art of the today's numerical method, several simplifications must be done in order to formulate a soil-structure interaction problem. In this chapter, a global definition of the dynamic soil-structure interaction problem through the governing equations and different aspects of its numerical modeling are presented.

In §1.2, different examples of site effects are discussed. As the goal of this work is to investigate the effect of soil nonlinearity, the observed nonlinearity in measured accelerograms is also presented in this section. §1.3 deals with the general effects of the dynamic soil-structure interaction (DSSI) through several simple examples.

A brief review of the theoretical and numerical existing methods to solve the DSSI is presented in §1.4. Also, a review of the governing equations of the dynamic soil-structure problem in view of a material nonlinear finite element numerical implementation is presented in §1.5. The numerical tool CESAR-LCPC software used in this thesis for all the developments and simulations is presented in §1.6. Also, a brief review of all the additional necessary developments performed in this work in CESAR-LCPC program are explained in this section.

1.2 Site effects

The seismic ground motion is strongly influenced by the source and path effects, but the propagation and amplification of seismic waves in surficial soil layers are also a key issue. The reflection and refraction of seismic waves at the interface between layers having different velocities may lead to larger amplitudes at the free-surface. Hence, it is necessary to estimate, through experimental as well as numerical approaches, the *amplification factor* at a specific site and the corresponding frequency range. Characterizing the seismic ground motion is mandatory to assess the seismic risk in a particular area.

The amplification factor may be estimated experimentally through various techniques. The analysis may also be performed through different numerical approaches investigating the propagation process in complex geological structures such as alluvial deposits. Various methods such as the Spectral Element Method, the Boundary Element Method and Finite Element Method are very useful techniques for modeling seismic wave propagation and amplification. They allow the analysis of various earthquake scenarios and the assessment of the seismic hazard at a specific site.

Simple and extensive experimental methods, such as the measurement of ambient vibrations, are also available. They give very interesting results allowing a simplified characterization of alluvial deposits. From a theoretical point of view, it is also possible to consider simplified approaches such as the modal method. It leads to a fast and reliable estimation of the fundamental frequency of sedimentary basins. Finally, the characterization of the soil properties directly on site or in the laboratory is also a key issue to quantify seismic ground motion in alluvial deposits. It is especially the case for strong events for which various (inelastic) constitutive parameters are needed.

1.2.1 Main governing phenomena

1.2.1.1 Site effects: some examples

The propagation of seismic waves in surficial geological structures may often lead to strong motion amplifications due to the velocity contrast between alluvial deposits and the bedrock. Such phenomena, named *site effects*, may considerably increase the impact of an earthquake.

One of the first large earthquakes to show the importance of this issue was the Michoacan 1985 earthquake in Mexico (Fig.1.1) (Singh et al., 1988; Fäh et al., 1994).

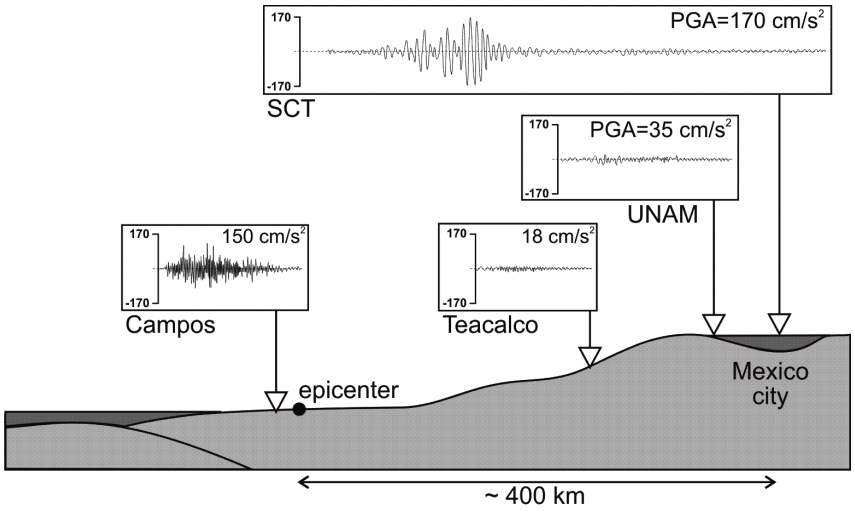

Figure 1.1: Propagation of seismic waves for the Michoacan 1985 earthquake in Mexico, after Semblat and Pecker (2009).

The maximum acceleration at sixty kilometers from the epicenter was around $0.28g$. It reached $0.2g$ in the center of Mexico city located much farther (400 kilometers away). As shown in Fig.1.1 in terms of acceleration, the Peak Ground Acceleration was even larger in the Mexico basin (SCT station) than at the Campos station located nearby the epicenter. The thick clay deposit in the lake-bed area nearby the volcanic belt amplified up to a factor 5 the seismic motions when compared to the bedrock (maximum acceleration in time domain).

In the case of areas with moderate seismicity, the site effect influence is also very important. As depicted in Fig.1.2, for alpine valleys, deep and narrow alluvial deposits may lead to complex propagation patterns. In this figure, the 500m deep Grenoble basin (French alps) is schematized. The reference bedrock site is called OGMU (top left) and other stations are located at the surface of the deposit. These stations are part of the French accelerometric network (RAP). Numerical studies show that the Grenoble basin strongly amplifies the seismic motion due to multiple reflections and diffractions at the basin edges (Chaljub, 2006; Delépine and Semblat, 2006; Chaljub et al., 2010).

From these examples, it is obvious that the assessment of seismic wave amplification is a crucial issue. It is not only useful for the quantification of the seismic hazard but also for seismic risk purposes.

Another historical case is the 1967 Caracas earthquake which was strongly amplified by the alluvial deposit in the center of the city. The fundamental frequency of a basin is linked to the geometrical configuration as well as the velocity contrast in the various soil layers. For Caracas, this frequency was around 0.6Hz for the most damaged blocks (Duval et al., 1998; Semblat et al., 2002). It has been shown that the three buildings that collapsed during the earthquake were structures including more than 14 stores leading to eigen frequencies close to 0.6Hz. In the case where the amplification of the seismic motion may be large, it is then necessary to characterize the local seismic response of the soil to scale the features of the reference earthquake considered for the design of the buildings in this area.

1.2.2 Nonlinearity in observed accelerograms

Among the clearest examples of nonlinear response are the Port Island borehole records of the 1995 Hyogoken Nanbu (Kobe) earthquake (Bonilla, 2000). In the acceleration records, there

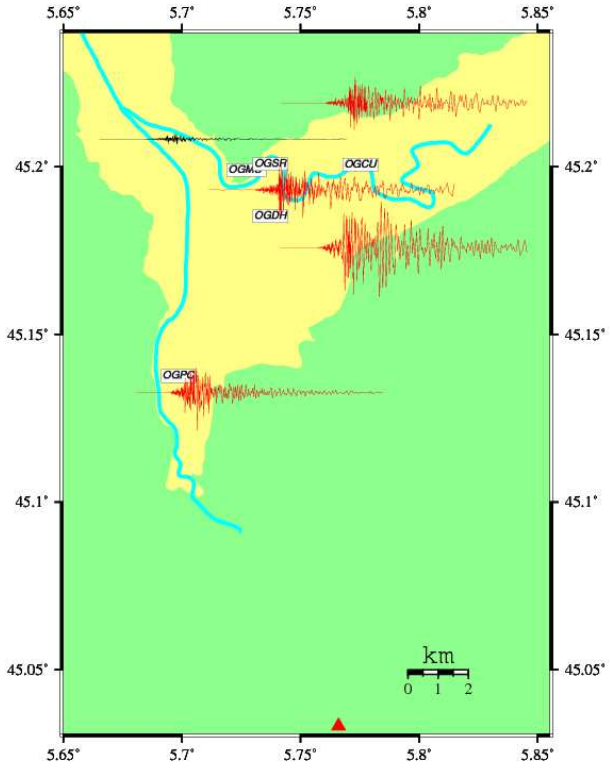

Figure 1.2: Velocities ($N - S$ component) recorded at various locations in the city of Grenoble during the 1999 Laffrey earthquake (data: French accelerometric network, `www-rap.obs.ujf-grenoble.fr`, reference: (Lebrun et al., 2001).

is a clear change in the high-frequency waveforms of acceleration with less obvious changes in the low-frequency velocity and displacement time histories. While not as direct an observation as from borehole recordings, nonlinear response is generally associated with accelerograms that show a pronounced change in frequency content that occurs during or immediately after strong shaking. A classic example of such behavior is the response at Treasure Island (a soft soil site) during the 1989 Loma Prieta earthquake (Bonilla, 2000). Fortunately, there was an accelerogram recorded on rock about two kilometers away at Yerba Buena Island for comparison (Fig.1.3)

Other than borehole observations of strong shaking or in the serendipity situation where accelerograms are recorded at rock and soil sites close to each other, nonlinearity of the soil must be inferred by indirect methods. A basic approach is to compare the transfer function for weak and strong ground motion recorded at the same site (for review of seismological observations see Beresnev and Wen (1996)). The principle observation one expects for nonlinear response is a shift of the fundamental frequency of the transfer function to longer periods. An example is shown in Fig.1.4. It shows the transfer function computed at station TTRH02 using the Tottori M7.2 earthquake and its aftershocks during 2000 in Japan. This station belongs to the Kiknet network, surface and borehole stations up to GL-100 and GL-200 m depth (Aochi et al., 2008). The orange shaded area corresponds to 95% confidence limits of the transfer function computed using small amplitude PGA events (less than 50 cm/s^2). The black solid line is the transfer function obtained from the mainshock data. Note the deamplification above 2 Hz and the amplification below 1 Hz. This change of behavior is not concentrated in a particular frequency range, but over a broadband frequency range.

A major difficulty with this approach is finding a reference site. Using the data from the 1994 Northridge earthquake, Field et al. (1997) compared the average amplification of strong and weak shaking for a class of soil sites with that of a few rock sites and found nonlinear soil response at frequencies between 1.0 and $4.0Hz$.

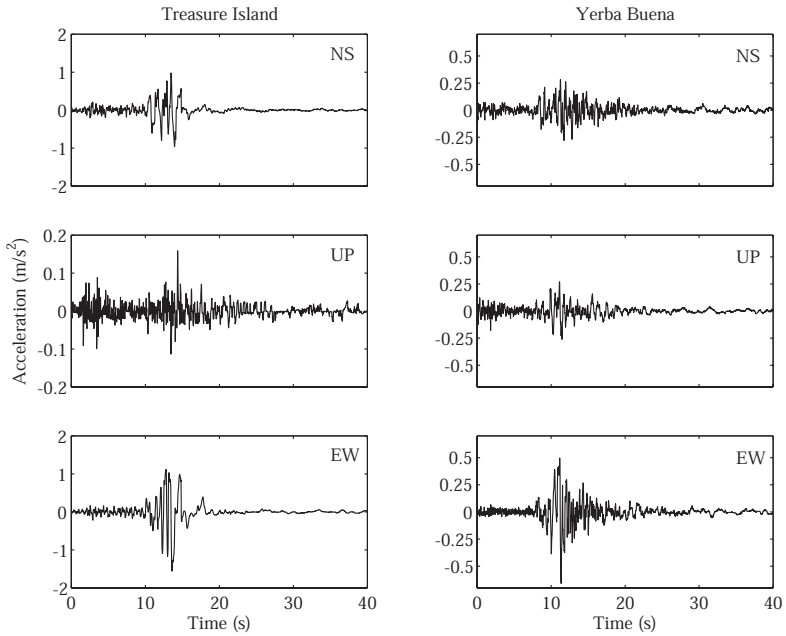

Figure 1.3: Accelerograms from the 1989 Loma Prieta earthquake recorded at two sites that are within 2.5 kilometers of each other.

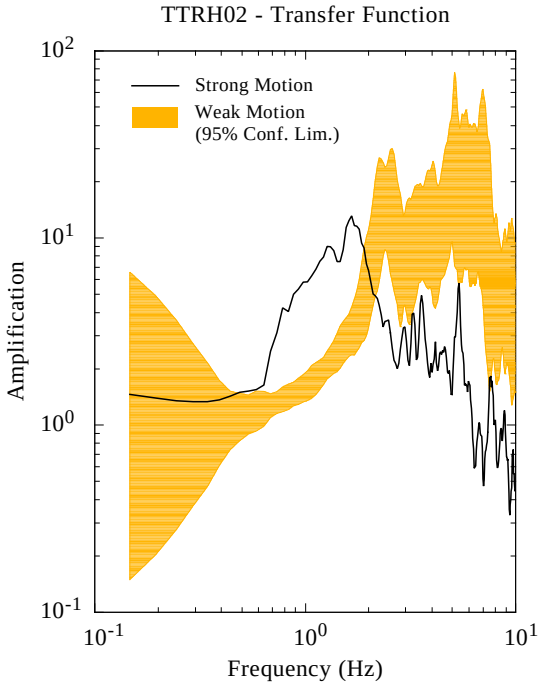

Figure 1.4: Transfer function computed between the surface and the borehole (GL-100 m) at station TTRH02 using the mainshock and aftershocks of the Tottori M7.2 earthquake (Aochi et al., 2008)

In general, borehole data provide an excellent baseline for such studies (Bonilla, 2000). However, a difficulty using borehole data is the downgoing waves effect. The downgoing waves (those reflected from the free surface and other pronounced changes in impedance) can produce suspicious peaks in the transfer function that might be interpreted as a shift in the fundamental frequency (Steidl et al., 1996).

1.3 Dynamic soil-structure interaction

1.3.1 SSI effects

One of the easiest way to represent a structure is through an equivalent single-degree-of-freedom (SDOF) oscillator. In the most general case, the SDOF system consists of a mass-spring-dashpot arrangement, having only one degree of freedom, representing the translation of the mass. In a SSI analysis, this simple model is combined with the degrees of freedom of the foundation and the soil media. A simple representation of the soil-structure system is given in Fig.1.5. The structure is modeled as a SDOF system consisting of a mass m at a height h above the foundation, having a stiffness k. If the structure was supported by a fixed base, the degree of freedom would be the horizontal displacement u of the mass due to the bending of the structure, when subjected to a force F (in this case, the base motion u_g is neglected). In the SSI analysis, the number of degrees of freedom of the total system increases due to the degrees of freedom of the foundation medium. The foundation is represented by two horizontal and rotational springs k_f and k_θ. These characteristics are shown in Fig.1.5. The foundation is allowed to translate by u_f and to rotate by θ_f.

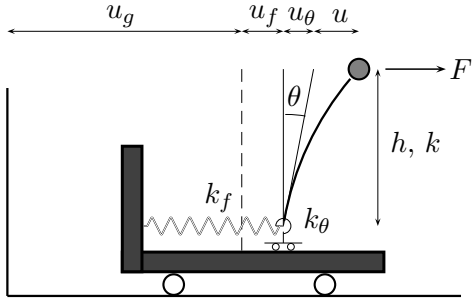

Figure 1.5: A simple soil-structure system representation

The total displacement of the structure u_t can be summarized in three different displacements, u, u_f and $u_\theta = h\theta_f$. Then,

$$u_t = u + u_f + u_\theta \tag{1.1}$$

We also have,

$$\begin{cases} u & = F/k \\ u_f & = F/k_f \\ u_\theta & = h\theta_f \end{cases}$$

The equilibrium equation leads to $Fh = k_\theta\theta$. Consequently, the total displacement can be rewritten as,

$$u_t = u + u_f + u_\theta = F\left(\frac{1}{k_f} + \frac{h^2}{k_\theta} + \frac{1}{k}\right)$$

and,

$$F = \frac{ku_t}{\left[1 + \frac{k}{k_f}\left(1 + \frac{k_f h^2}{k_\theta}\right)\right]} \tag{1.2}$$

Comparing to the fixed base condition (where k_f and k_θ tend to infinity), we see that the stiffness of the system decreases. This reduction influences the fundamental period of the structure that is related to the inverse of the square of the stiffness. Therefore,

$$\frac{T}{T_\infty} = \sqrt{1 + \frac{k}{k_f}\left(1 + \frac{k_f h^2}{k_\theta}\right)} \tag{1.3}$$

where T_∞ is the fixed base fundamental period of the structure. This period lengthening is the first effect of the soil-structure interaction. According to Veletsos and Meek (1974), there are two basic effects of the soil-structure interaction on the structural response:

- The flexibility supported system on a compliant foundation has more degrees of freedom than the fixed base superstructure and thus, different dynamic characteristics. A period lengthening due to the additional foundation compliance is always evidenced.

- A significant part of the vibration energy of the compliant system may be dissipated by radiating waves, emanating from the vibrating foundation-structure system back into the soil, or by hysteretic material damping in the soil.

The second one reduces the response of the structure. In general, the response of the equivalent SDOF oscillator shown in Fig.1.5 differs in amplitude and in frequency content from the response of the fixed base SDOF structure. The fundamental period lengthening is traditionally assumed to be beneficial for the seismic response of the system. This assumption is adopted in many of the design codes as a rather simple and conservative approach. Nevertheless, the effects of the SSI can be also detrimental for the structure in certain seismic and soil environments, depending mostly on the design response spectrum at the site (Mylonakis and Gazetas, 2000).

In general, two mechanisms of interaction take place between the structure, foundation, and soil (Stewart et al., 1999):

- *Inertial interaction*: Inertia developed in the structure due to its own vibrations gives rise to base shear and moment, which in turn cause displacements of the foundation relative to the free field. Frequency dependent foundation impedance functions describe the flexibility of the foundation support as well as the damping associated with the foundation-soil interaction.

- *Kinematic Interaction*: The presence of the stiff foundation elements on or in the soil causes foundation motions to deviate from the free field motions as a result of the ground motion incoherence, wave inclination, or foundation embedment. Kinematic effects are described by a frequency dependent transfer function relating the free field motion to the motion that would occur on the base slab if the slab and structure were massless.

In the case of the shallow foundations, where the foundation is simply laid on the soil surface, there is not any kinematic interaction for the model with vertical propagation (Betbeder-Matibet, 2003). In the next section, the second aforementioned effect of SSI will be studied through a simple model named cone model.

1.3.2 Geometric or radiative damping

1.3.2.1 Basic principles

Cone models were initially proposed by Meek and Wolf (1992) and allow the description of dynamic soil-structure interaction under a simplified form. This method considers a certain soil volume with a conical geometry to account for wave radiation into the soil. The schematic proposed in Fig.1.6 shows the basic principle of the method: a conical soil volume intersecting the base of the foundation is isolated and seismic wave propagation is then studied in this soil volume only (Pecker, 2008). It allows a simplified analysis of dynamic soil-structure interaction.

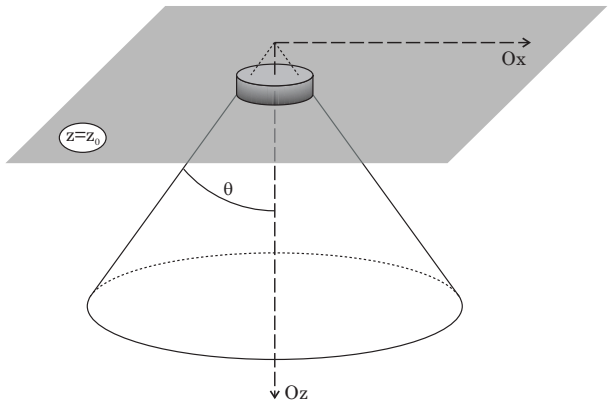

Figure 1.6: Principle of cone models after Semblat and Pecker (2009)

1.3.2.2 Equations of motion for the soil

One thus considers a conical soil column assumed as a one-dimensional bar having a variable cross-section with depth (area $S(z)$). The wavefield in the soil cone may then be derived from the 1D wave equations (details in Semblat and Pecker (2009)). For a purely horizontal motion, the following expression is obtained:

$$\frac{\partial V}{\partial z} = \rho S \frac{\partial^2 u_x}{\partial t^2} \tag{1.4}$$

where: $V = \mu S' \dfrac{\partial u_x}{\partial z}$ is the shear force (bending being neglected). Furthermore:

$$S' = S(z) = \pi (z \tan\theta)^2 \tag{1.5}$$

hence:

$$\frac{\partial}{\partial z}\left(\mu S(z) \frac{\partial u_x}{\partial z}\right) = \rho S(z) \frac{\partial^2 u_x}{\partial t^2} \tag{1.6}$$

Since S depends on z, it leads to the following equation:

$$\frac{\partial S(z)}{\partial z}\frac{\partial u_x}{\partial z} + S(z)\frac{\partial^2 u_x}{\partial z^2} = \frac{\rho}{\mu} S(z) \frac{\partial^2 u_x}{\partial t^2} \tag{1.7}$$

the spatial derivative of the area of the cross-section is: $\frac{\partial S(z)}{\partial z} = 2\pi z \tan^2\theta$, yielding:

$$\frac{2}{z}\frac{\partial u_x}{\partial z} + \frac{\partial^2 u_x}{\partial z^2} = \frac{\rho}{\mu}\frac{\partial^2 u_x}{\partial t^2} \tag{1.8}$$

The solution is then of the form (Pecker, 2008):

$$u_x(z,\omega) = \frac{u_x(z_0,\omega)}{z/z_0} \exp\left[-i\frac{\omega}{V_S}(z - z_0)\right] \exp(i\omega t) \tag{1.9}$$

The previous analysis performed for pure shear may be considered under a similar form for pure compression. The same expression holds for the vertical displacement u_z.

1.3.2.3 Case of a surface excitation

Considering a harmonic force $F(\omega)$ transmitted at the free surface by the foundation, the boundary condition fulfilled by the solution (1.9) reads:

$$F(\omega) = V(z_0) = -\mu S(z_0)\frac{\partial u_x}{\partial z} \tag{1.10}$$

Since:

$$\begin{aligned}\frac{\partial u_x}{\partial z} &= -\frac{u_x(z_0,\omega)}{z^2/z_0}\exp\left[-i\frac{\omega}{V_S}(z-z_0)\right]\exp(i\omega t)\\ &\quad -i\frac{\omega}{V_S}\frac{u_x(z_0,\omega)}{z/z_0}\exp\left[-i\frac{\omega}{V_S}(z-z_0)\right]\exp(i\omega t)\end{aligned}$$

it implies:

$$\frac{\partial u_x(z_0,\omega)}{\partial z} = -u_x(z_0,\omega)\left(\frac{1}{z_0}+i\frac{\omega}{V_S}\right) \tag{1.11}$$

Hence:

$$F(\omega) = \mu\pi z_0\tan^2\theta\left(1+i\frac{\omega z_0}{V_S}\right)u_x(z_0,\omega) \tag{1.12}$$

Considering that $R = z_0\tan\theta$ and denoting $\bar{\omega} = \frac{\omega R}{c}$ and $K = \mu\pi R\tan\theta$, Eq.(1.12) becomes:

$$F(\omega) = K\left(1+i\frac{\bar{\omega}}{\tan\theta}\right)u_x(z_0,\omega) \tag{1.13}$$

Using the static stiffness $K_{stat} = \frac{8\mu R}{2-\nu}$, θ may be identified:

$$K(\bar{\omega}=0) = \mu\pi R\tan\theta = K_{stat}\ , \quad \text{that is:} \quad \tan\theta = \frac{8}{(2-\nu)\pi} \tag{1.14}$$

The impedance of the foundation thus becomes:

$$K(\bar{\omega}) = K_{stat}\left[1+i\frac{(2-\nu)\pi}{8}\bar{\omega}\right] \tag{1.15}$$

To assess the influence of the foundation geometry as well as of the soil properties on the dynamic soil-structure interaction, the K_{dyn}/K_{stat} ratio, defined through equation 1.15, is plotted as a function of the foundation radius R for various values of the shear wave velocity in the soil V_s (Fig.1.7). The K_{dyn}/K_{stat} ratio is larger for lower shear wave velocities and larger foundation. The dynamic soil-structure interaction is thus stronger for large structures and soft soils.

1.4 Modeling soil-structure interaction

1.4.1 Basic methods

According to Wolf (1985), there are two basic methods of approaching the soil-structure interaction, the *direct method* and the *superstructure method*. The superstructure method is based on the decomposition of the complete soil-foundation-structure domain to several subdomains. This method underlain by the assumption of the geometrical and the material linearity, evaluates the response of each subdomain separately and superposes them to obtain the total system response. A commonly used approach is to divide the SSI phenomenon into kinematic and inertial interaction, evaluated through the foundation dynamic impedance functions. This method could be very efficient for the analysis of rather simple systems, because each subdomain is analyzed independently of the others. Various studies on the soil-structure interaction phenomena such as Aubry and Clouteau (1992); Koh et al. (1995); Bode et al. (2002); Clouteau and Aubry (2003);

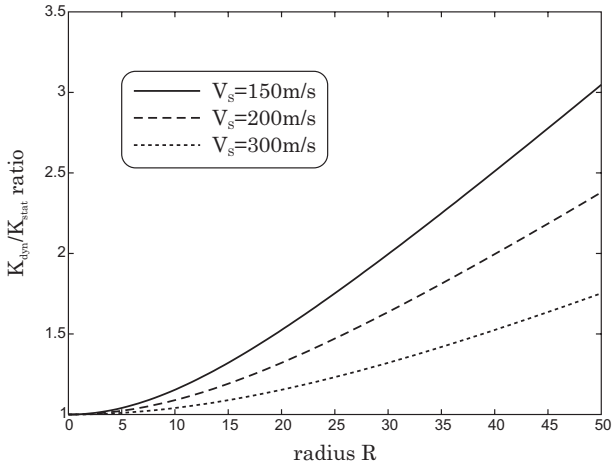

Figure 1.7: K_{dyn}/K_{stat} ratio estimated through cone models as a function of the foundation radius R for various shear wave velocities: V_S = 150m/s, V_S = 200m/s and V_S = 300m/s ($\nu = 0.25$, μ=200 MPa and $f = \frac{\omega}{2\pi}$=2 Hz).

Pitilakis (2006); Gerolymos and Gazetas (2006); Gouasmia and Djeghaba (2007) are based on the superstructure method.

However, these methods, rely on the principle of the superposition and, consequently are limited to the linear elastic or viscoelastic domains. In general, the soil is known to behave nonlinearly under even relatively weak to moderate ground motions. Ignoring the nonlinear characteristics of the soil may lead to an overestimation of the forces induced in the structure, as well as to neglect the permanent displacements that the structure might undergo.

Conceptually, the easiest way to analyze the soil-structure system for a seismic excitation is to model a significant part of the soil around the structure (direct methods). These methods analyze the complete soil-foundation-structure system in its integrity. In the most direct methods, the input motion needs to be defined at the external nodes of the model. Thus, in the most usual case of an earthquake signal recorded at the outcropping bedrock, a *deconvolution* has to be performed to calculate the excitation at the desired external nodes.

However, the number of dynamic degrees of freedom in the soil region is large, resulting in a large computer-storage requirement and in significant running time. Therefore, these restrictions limit their extensive application in the usual engineering practice. However, increasing the capacity of the computers, the direct methods are widely used in research area. Different works on the SSI are based on these methods such as Cai et al. (2000); Casciati and Borja (2004); Lu et al. (2005); Buehler et al. (2006); Jeremic et al. (2009); Saez (2009).

A third class of numerical methods, named as *hybrid methods*, exists for the assessment of the SSI phenomenon. It consists of the combination of the direct and the superstructure methods. These hybrid methods are mostly favored by the advantage of the substructure technique for the separate solution of the bounded structure domain and the unbounded soil domain. Thus, the unbounded soil domain is treated with the boundary element method, while the structure or the structure with a part of the soil is treated with the finite element method. Among the works that are performed with this model we can cite Estorff and Firuziaan (2000); Rizos and Wang (2002); Halabian and Naggar (2002).

1.4.2 Numerical Methods

The complexity of the soil-structure interaction problem rises from the fact that the response of the total soil-foundation-structure system depends on two separate, but strongly coupled, components, the superstructure and the soil. Various analytical and numerical tools exist for the analysis of each of the two components. For simple structural models, the mass-spring-

dashpot configuration is challenging. For more complicated systems, however, the *finite element method (FEM)* (Hughes, 1987; Zienkiewicz and Taylor, 2000) seems to be very convenient to model the soil-structure system.

For the analysis of the unbounded domain the *Boundary Element Method (BEM)* (Bonnet, 1999) and lately the *Fast Multipole Method (FMM)* (Chaillat, 2008) are the efficient methods but their use is restricted to the simple geometric and elastic or viscoelastic domains.

Comparing to the BEM, the FEM is more efficient for dealing with complex geometries and heterogeneous media. This method is also capable of handling inelastic constitutive models. But the numerical dispersion and the spurious reflections at the boundaries are the main disadvantages of this method.

The *Finite Difference Method (FD)* (Moczo and Robertsson, 2007) is also another method to model the wave propagation. One reason of the widespread use is the simplicity and its implementation. Also, the local nature of the finite difference operators makes the method suitable for parallelization.

The *Spectral Element Method (SEM)* (Faccioli et al., 1996; Komatitsch et al., 1999; Chatzigogos, 2007) combines the flexibility of the FEM to handle complex geometries with the accuracy and exponential convergence rate afforded by spectral approximations. This time-domain method is based on the high order approximations of the elastodynamic variational formulations, and hence takes naturally into account the interface conditions and the free surfaces.

In this work, the finite element method is selected due to its capacity to solve the nonlinear media with complex geometry.

1.5 Resolution of the problem by Finite Element method

1.5.1 Weak formulation of the equations of motion of the dynamic system

Figure 1.8 presents the schematic problem of soil-structure interaction. The weak formulation of the equation of equilibrium is the base of the finite element method. First of all, we should determine the unknowns, the boundary conditions, initial conditions, the external forces and the equations of motion of the domain considering the hypothesis of small strains. The main unknowns of the problem are,

$\underline{u}(\underline{X},t)$, $\dot{\underline{u}}(\underline{X},t)$, $\ddot{\underline{u}}(\underline{X},t)$ and $\underline{\underline{\sigma}}(\underline{X},t)$ in Ω

where $\underline{u}(\underline{X},t)$ is the displacement field which depends on the position of the point, the global coordinate $\underline{X}$ and the time t. $\dot{\underline{u}}(\underline{X},t)$ and $\ddot{\underline{u}}(\underline{X},t)$ are the velocity and acceleration fields respectively. Ω includes the structure, the soil and the interface.

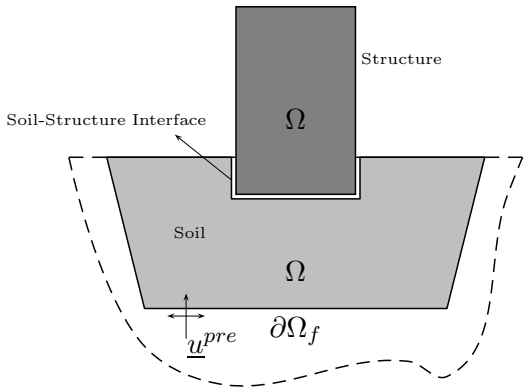

Figure 1.8: Definition of the global system

The equations of the system are (Sercombe, 1997),

- Geometric compatibility (small strain hypothesis) :

$$\underline{\underline{\epsilon}} = \frac{1}{2}\left(\underline{\underline{\text{grad}}}(\underline{u}) + \underline{\underline{\text{grad}}}^T(\underline{u})\right) \tag{1.16}$$

- Equation of motion

$$\underline{\text{div}\underline{\sigma}} + \underline{f} - \rho\underline{\ddot{u}} = \underline{0} \tag{1.17}$$

- Equation of state (Constitutive law)

$$\underline{\underline{\sigma}} = \underline{\underline{\sigma}}(\underline{\underline{\epsilon}}, \underline{\underline{\epsilon}}^p, ...) \tag{1.18}$$

where ρ is the density of the material and $\underline{f}$ is the vector of body forces in Ω. Equation 1.18 defines the constitutive equations of the different materials of the system that would be linear in case of the structure and nonlinear for soil. The boundary conditions of the problem are,

$$\underline{\underline{\sigma}}(\underline{X}, t) \cdot \underline{n} = \underline{t} \qquad and \qquad \underline{u}(\underline{X}, t) = \underline{u}^{pre} \quad at \quad \partial\Omega_f$$

where $\underline{t}$ is the vector of the boundary forces and $\underline{u}^{pre}$ is the vector of applied (prescribed) displacement. The initial conditions at t_0 are,

$\underline{u}(\underline{X}, t_0)$, $\underline{\dot{u}}(\underline{X}, t_0)$, $\underline{\ddot{u}}(\underline{X}, t_0)$ and $\underline{\underline{\sigma}}(\underline{X}, t_0)$ at Ω

Considering an arbitrary displacement vector $\underline{\hat{u}}(\underline{X}, t)$, and multiplying the equation of motion by this vector and integrating this product at all of the system Ω, the weak formulation of the equation of motion (equation 1.17) of the system is obtained.

$$\int_\Omega \underline{\hat{u}} \cdot \left[\underline{\text{div}\underline{\sigma}} + \underline{f} - \rho\underline{\ddot{u}}\right] d\Omega = 0 \tag{1.19}$$

By means of symmetry of the stress tensor and the divergence theorem, we have,

$$\int_\Omega \underline{\underline{\hat{\epsilon}}} : \underline{\underline{\sigma}} d\Omega + \int_\Omega \rho\underline{\hat{u}} \cdot \underline{\ddot{u}} d\Omega - \int_{\partial\Omega_f} \underline{\hat{u}} \cdot [\underline{\underline{\sigma}} \cdot \underline{n}] dS - \int_\Omega \underline{\hat{u}} \cdot \underline{f} d\Omega = 0 \tag{1.20}$$

We also have,

$$\underline{\underline{\hat{\epsilon}}} = \frac{1}{2}\left(\underline{\underline{\text{grad}}}(\underline{\hat{u}}) + \underline{\underline{\text{grad}}}^T(\underline{\hat{u}})\right)$$

Equation 1.20 is the weak formulation of the system at any time t. Consequently, to solve the problem, the displacement vector $\underline{u}(\underline{X}, t)$ should be found to minimize equation 1.20 for any arbitrary virtual admissible displacement field $\underline{\hat{u}}(\underline{X}, t)$. The finite element method is used to find the approximate solution of this equation.

1.5.2 Space and time discretization of the problem

1.5.2.1 Space discretization

Through the finite element method the system is discretized in space to reduce the size of the admissible $\underline{\hat{u}}$ fields. Concerning the discretization in space, the system can be divided into finite elements, corresponding to a certain number of nodes where the displacements are the unknowns of the problem. The relation between the displacement field and the vector of nodal displacements is given in the matrix form as (Sercombe, 1997),

$$\underline{u}(\underline{X}, t) = [N(\underline{X})] \{\underline{U}(t)\} \tag{1.21}$$

where $\{\underline{U}(t)\}$ is the vector of the nodal displacements and $[N(\underline{X})]$ is the matrix of the shape functions of the elements that depends on the type of elements. In the same way, the velocity

$\underline{\dot{u}}(\underline{X},t)$ and acceleration $\underline{\ddot{u}}(\underline{X},t)$ fields can be obtained for each node and at each time by the nodal vectors of velocity $\underline{\dot{U}}(t)$ and $\underline{\ddot{U}}(t)$.

$$\underline{\dot{u}}(\underline{X},t) = [N(\underline{X})]\{\underline{\dot{U}}(t)\} \tag{1.22}$$

$$\underline{\ddot{u}}(\underline{X},t) = [N(\underline{X})]\{\underline{\ddot{U}}(t)\} \tag{1.23}$$

The strain field $\underline{\underline{\epsilon}}(\underline{X},t)$ is obtained using the nodal displacements and the spatial derivative of the shape functions.

$$\underline{\underline{\epsilon}}(\underline{X},t) = [B(\underline{X})]\{\underline{U}(t)\} \tag{1.24}$$

where $[B(\underline{X})]$ contains the spatial derivative of the shape functions.

$$[B(\underline{X})] = \frac{\partial[N]}{\partial \underline{X}}$$

1.5.2.2 Discretization in time

The problem can be discretized in time using interval series of $\Delta_n t$. Therefore, the problem can be reformulated into the increment of time, $\Delta_n t = t_n - t_{n-1}$, considering the unknown values in the time t_n and the known values in previous increment, t_{n-1}. The incremental form of the weak formulation of the equilibrium equation 1.20 becomes,

$$\int_\Omega \hat{\underline{\underline{\epsilon}}} \colon \Delta_n \underline{\underline{\sigma}} d\Omega + \int_\Omega \rho \hat{\underline{u}} \cdot \Delta_n \underline{\ddot{u}} d\Omega - \int_{\partial\Omega_f} \hat{\underline{u}} \cdot \Delta_n \underline{t} dS - \int_\Omega \hat{\underline{u}} \cdot \Delta_n \underline{f} d\Omega = 0 \tag{1.25}$$

with initial conditions at t_{n-1} in Ω : $\underline{u}_{n-1}$, $\underline{\dot{u}}_{n-1}$, $\underline{\ddot{u}}_{n-1}$ and $\underline{\underline{\sigma}}_{n-1}$.

1.5.2.3 Matrix formulation of the problem

By using the spatial discretization of the equations 1.21 to 1.24, the incremental equation 1.25 can be rewritten in matrix form as,

$$\int_\Omega [B]^T \Delta_n \underline{\underline{\sigma}} d\Omega + \int_\Omega \rho [N]^T [N] \Delta_n \underline{\ddot{U}}(t) d\Omega = \int_{\partial\Omega_f} [N] \Delta_n \underline{t} dS + \int_\Omega [N] \Delta_n \underline{f} d\Omega \tag{1.26}$$

or in another form,

$$[\mathrm{M}]\{\Delta_n \underline{\ddot{U}}(t)\} + \{\Delta_n \underline{\mathrm{F}}_{int}\} = \{\Delta_n \mathrm{T}\} + \{\Delta_n \underline{\mathrm{F}}\} = \{\Delta_n \underline{\mathrm{F}}_{ext}\} \tag{1.27}$$

where,

$$\begin{aligned}
[\mathrm{M}] &= \int_\Omega \rho [N]^T [N] d\Omega \\
\{\Delta_n \underline{\mathrm{F}}_{int}\} &= \int_\Omega [B]^T \Delta_n \underline{\underline{\sigma}} d\Omega \\
\{\Delta_n \underline{\mathrm{T}}\} &= \int_{\partial\Omega_f} [N] \Delta_n \underline{t} dS \\
\{\Delta_n \underline{\mathrm{F}}\} &= \int_\Omega [N] \Delta_n \underline{f} d\Omega
\end{aligned}$$

In equation 1.27, $\{\Delta_n \underline{\mathrm{F}}_{int}\}$ is the matrix form of the incremental vector of internal forces of the system. It depends on the incremental stress matrix between t_{n-1} and t that in general,

for a nonlinear constitutive model, can not be expressed directly in terms of incremental strain $\Delta_n\underline{\underline{\epsilon}}$. In general, the system defined in equation 1.27 is nonlinear. Therefore, its resolution must be carried out using an iterative algorithm. The Newton-Raphson method is used here to linearize the incremental vector of the internal forces with respect to the strain. The Newton-Raphson method is the most rapidly convergent process for solutions of problems in which only one evaluation of the equation is made in each iteration (Zienkiewicz and Taylor, 2000). The problem of this method is that at each iteration the stiffness matrix should be recalculated. In this work, the modified Newton-Raphson is used. Obviously, the procedure will converge at a slower rate but the stiffness matrix will be constant during each increment. Briefly, the resolution of the system becomes iterative, also, the system is resolved at increment n and iteration $(i-1)$ and the solution of the system at increment n and iteration (i) is searched until the differences between two successive solutions becomes sufficiently small (convergence criteria). Therefore,

$$\begin{aligned}
\{\Delta_n^{(i)}\underline{\mathrm{F}}_{int}\} &= \{\Delta_n^{(i-1)}\underline{\mathrm{F}}_{int}\} + \frac{\partial\{\Delta_n^{(i-1)}\underline{\mathrm{F}}_{int}\}}{\partial\underline{\underline{\epsilon}}} \\
&= \{\Delta_n^{(i-1)}\underline{\mathrm{F}}_{int}\} + \frac{\partial\{\int_\Omega [B]^T\Delta_n^{(i-1)}\underline{\underline{\sigma}}d\Omega\}}{\partial\underline{\underline{\epsilon}}} \\
&= \{\Delta_n^{(i-1)}\underline{\mathrm{F}}_{int}\} + \int_\Omega [B]^T\frac{\partial\{\Delta_n^{(i-1)}\underline{\underline{\sigma}}\}}{\partial\{\Delta_n^{(i-1)}\underline{\underline{\epsilon}}\}}\{d_n^{(i)}\underline{\underline{\epsilon}}\}d\Omega \\
&= \{\Delta_n^{(i-1)}\underline{\mathrm{F}}_{int}\} + \int_\Omega [B]^T\frac{\partial\{\Delta_n^{(i-1)}\underline{\underline{\sigma}}\}}{\partial\{\Delta_n^{(i-1)}\underline{\underline{\epsilon}}\}}[B]\{d_n^{(i)}(\underline{U}(t))\}d\Omega
\end{aligned} \tag{1.28}$$

where the elastoplastic behavior matrix $\partial\{\Delta_n^{(i-1)}\underline{\underline{\sigma}}\}/\partial\{\Delta_n^{(i-1)}\underline{\underline{\epsilon}}\}$ is known at increment n and iteration $(i-1)$. By means of equation 1.24 into 1.28, the incremental form of the equilibrium equation 1.26 can be obtained at iteration (i) :

$$[\mathrm{M}]\{\Delta_n^{(i)}\ddot{\underline{U}}(t)\} + [\mathrm{K}]_n^{(i-1)}\{d_n^{(i)}(\underline{U}(t))\} = \{\Delta_n\underline{\mathrm{F}}_{ext}\} - \{\Delta_n^{(i-1)}\underline{\mathrm{F}}_{int}\} \tag{1.29}$$

where

$$\begin{aligned}
[\mathrm{K}]_n^{(i-1)} &= \int_\Omega [B]^T\frac{\partial\{\Delta_n^{(i-1)}\boldsymbol{\sigma}\}}{\partial\{\Delta_n^{(i-1)}\boldsymbol{\epsilon}\}}[B]d\Omega \\
\{\Delta_n\underline{\mathrm{F}}_{ext}\} &= \{\Delta_n\mathrm{T}\} + \{\Delta_n\underline{\mathrm{F}}\}
\end{aligned} \tag{1.30}$$

[M] is the mass matrix, $[\mathrm{K}]_n^{(i-1)}$ the stiffness matrix and $\{\Delta_n\underline{\mathrm{F}}_{ext}\}$ is the vector of the incremental external forces applied to the system.

1.5.2.4 Time integration algorithm

To integrate the incremental equation 1.29 in time, there are two different numerical schemes. First, the implicit method, where different unknowns are obtained at time t_n by means of the equilibrium equation 1.29 formulated at time t_n; the second one, the explicit method, where the unknowns are obtained at time t_n by means of the equation 1.29 formulated at time t_{n-1}. Here, we use the second order implicit method, known for its performance and its character being unconditionally stable well-known as Newmark algorithm. The steps of this method are written as follows. Considering,

$$\Delta_n^{(i)}\underline{U} = \underline{U}_n^{(i)} - \underline{U}_{n-1}$$

$$\Delta_n^{(i)}\underline{\dot{U}} = \underline{\dot{U}}_n^{(i)} - \underline{\dot{U}}_{n-1}$$

$$\Delta_n^{(i)}\underline{\ddot{U}} = \underline{\ddot{U}}_n^{(i)} - \underline{\ddot{U}}_{n-1}$$

and,

$$\underline{U}_n^{(i)} - \underline{U}_n^{(i-1)} = \mathrm{d}_n^{(i)}\underline{U} \quad \Rightarrow \quad \Delta_n^{(i)}\underline{U} = \Delta_n^{(i-1)}\underline{U} + d_n^{(i)}\underline{U} \tag{1.31}$$

By definition of the method :

$$\Delta_n^{(i)}\underline{U} = (\Delta_n t)\underline{\dot{U}}_{n-1} + \frac{(\Delta_n t)^2}{2}\left[(1-2\beta)\underline{\ddot{U}}_{n-1} + 2\beta\underline{\ddot{U}}_n^{(i)}\right] \tag{1.32}$$

$$\Delta_n^{(i)}\underline{\dot{U}} = (\Delta_n t)\left[(1-\gamma)\underline{\ddot{U}}_{n-1} + \gamma\underline{\ddot{U}}_n^{(i)}\right] \tag{1.33}$$

Substituting equation 1.31, we can obtain,

$$\Delta_n^{(i)}\underline{U} = (\Delta_n t)\underline{\dot{U}}_{n-1} + (\Delta_n t)^2\left[\frac{1}{2}\underline{\ddot{U}}_{n-1} + \beta\Delta_n^{(i)}\underline{\ddot{U}}\right] \tag{1.34}$$

$$\Delta_n^{(i)}\underline{\dot{U}} = (\Delta_n t)\left[\underline{\ddot{U}}_{n-1} + \gamma\Delta_n^{(i)}\underline{\ddot{U}}\right] \tag{1.35}$$

$\Delta_n^{(i)}\dot{\mathrm{U}}$ and $\Delta_n^{(i)}\ddot{\mathrm{U}}$ can be obtained by equations 1.34 and 1.35.

$$\Delta_n^{(i)}\underline{\ddot{U}} = \frac{1}{\beta(\Delta_n t)^2}\left(\Delta_n^{(i-1)}\underline{U} + d_n^{(i)}\underline{U}\right) - \frac{1}{\beta(\Delta_n t)}\underline{\dot{U}}_{n-1} - \left(\frac{1}{2\beta} - 1 + 1\right)\underline{\ddot{U}}_{n-1} \tag{1.36}$$

$$\Delta_n^{(i)}\underline{\dot{U}} = \frac{\gamma}{\beta(\Delta_n t)}\left(\Delta_n^{(i-1)}\underline{U} + d_n^{(i)}\underline{U}\right) - \left(\frac{\gamma}{\beta} - 1 + 1\right)\underline{\dot{U}}_{n-1} - (\Delta_n t)\left(1 - \frac{\gamma}{2\beta}\right)\underline{\ddot{U}}_{n-1} \tag{1.37}$$

And finally by definition of the a_i,

$$\Delta_n^{(i)}\underline{\ddot{U}} = a_0\left(\Delta_n^{(i-1)}\underline{U} + d_n^{(i)}\underline{U}\right) - a_2\underline{\dot{U}}_{n-1} - (a_3+1)\underline{\ddot{U}}_{n-1} \tag{1.38}$$

$$\Delta_n^{(i)}\underline{\dot{U}} = a_1\left(\Delta_n^{(i-1)}\underline{U} + d_n^{(i)}\underline{U}\right) - (a_4+1)\underline{\dot{U}}_{n-1} - a_5\underline{\ddot{U}}_{n-1} \tag{1.39}$$

where,

$$\begin{cases} a_0 = \frac{1}{\beta(\Delta_n t)^2} & a_3 = \frac{1}{2\beta} - 1 \\ a_1 = \frac{\alpha}{\beta\Delta_n t} & a_4 = \frac{\alpha}{\beta} - 1 \\ a_2 = \frac{1}{\beta\Delta_n t} & a_5 = \Delta_n t(1 - \frac{\alpha}{\beta}) \end{cases}$$

The parameters β and α are the constants of the method. The numerical stability of the integration scheme in time is depended to these parameters. Here, we select $\beta = 0.25$ and $\alpha = 0.5$ for which the scheme is unconditionally stable and does not induce any numerical damping in the system. Therefore, the dissipation in the system will be only due to the elastoplastic behavior of the soil and radiation damping.

By substituting $\{\Delta_n^{(i)}\underline{\ddot{U}}\}$ from equation 1.38 into the equilibrium equation of the system (equation 1.29),

$$[\mathrm{M}]\left[a_0(\Delta_n^{(i-1)}\underline{U}+\mathrm{d}_n^{(i)}\underline{U})-a_2\underline{\dot{U}}_{n-1}-(a_3+1)\underline{\ddot{U}}_{n-1}\right]+[\mathrm{K}]_n^{(i-1)}\{d_n^{(i)}(\underline{U}(t))\} = \{\Delta_n\underline{\mathrm{F}}_{ext}\}-\{\Delta_n^{(i-1)}\underline{\mathrm{F}}_{int}\} \tag{1.40}$$

and finally we obtain a new equation of the system presented as,

$$[\hat{\mathrm{K}}]_n^{(i-1)}\{d_n^{(i)}(\underline{U}(t))\}=\{\mathrm{R}\}_n^{(i-1)} \tag{1.41}$$

where $[\hat{\mathrm{K}}]_n^{(i-1)}$ is the equivalent stiffness matrix such as,

$$[\hat{\mathrm{K}}]_n^{(i-1)}=[\mathrm{K}]_n^{(i-1)}+a_0[\mathrm{M}] \tag{1.42}$$

and $\{\mathrm{R}\}_n^{(i-1)}$ is the equivalent residual vector of the dynamic system,

$$\{\mathrm{R}\}_n^{(i-1)}=\{\Delta_n\underline{\mathrm{F}}_{ext}\}-\{\Delta_n^{(i-1)}\underline{\mathrm{F}}_{int}\}-[\mathrm{M}]\left[a_0\Delta_n^{(i-1)}\underline{U}-a_2\underline{\dot{U}}_{n-1}-(a_3+1)\underline{\ddot{U}}_{n-1}\right] \tag{1.43}$$

In the next section the treatment of the prescribed degree of freedoms will be discussed.

1.5.2.5 Prescribed degrees of freedom

In order to decrease the size of the problem to be solved that could be very important in 2 or 3 dimensions especially in the case of nonlinear problems, it is common to distinguish the prescribed degrees of freedom from the unknown degrees of freedom at each node. Therefore, we divide the displacement vector of the nodes into two sub-vectors :

$$\{\underline{U}\}=\{\underline{U}_{unk}\}+\{\underline{U}_{pre}\}$$

where $\{\underline{U}_{unk}\}$ is the unknown displacements vector and $\{\underline{U}_{pre}\}$ is the prescribed displacements vector. Therefore, the resolution of the system will be performed only on the unknown degrees of freedom $\{\underline{U}_{unk}\}$. In statics, this partitioning adds at each increment one additional force term in the second part of the equilibrium equation of the system as

$$[\mathrm{K}]_n^{(i-1)}\{d_n^{(i)}\underline{U}_{unk}\}=\{\Delta_n\underline{\mathrm{F}}_{ext}\}-\{\Delta_n^{(i-1)}\underline{\mathrm{F}}_{int}\}-[K_{elas}]\{\Delta_n\underline{U}_{pre}\} \tag{1.44}$$

where $[\mathrm{K}_{elas}]$ is the elastic stiffness matrix of the system defined by means of the elastic behavior matrix [C] of the system,

$$[\mathrm{K}_{elas}]=\int_\Omega[\mathrm{B}]^T[\mathrm{C}][\mathrm{B}]d\Omega \tag{1.45}$$

In dynamic problems, in order to decrease the size of the system in addition to the nodal displacements, the nodal velocities and accelerations should also be partitioned in the same manner : $\{\underline{\dot{U}}\}=\{\underline{\dot{U}}_{unk}\}+\{\underline{\dot{U}}_{pre}\}$ and $\{\underline{\ddot{U}}\}=\{\underline{\ddot{U}}_{unk}\}+\{\underline{\ddot{U}}_{pre}\}$. Such as global vector of the nodal displacement $\{\underline{U}\}$, $\{\underline{\dot{U}}\}$ and $\{\underline{\ddot{U}}\}$, the prescribed degrees of freedom could be formulated in an incremental way by use of the Newmark algorithm,

$$\Delta_n\underline{\ddot{U}}_{pre}=a_0\Delta_n\underline{U}_{pre}-a_2(\underline{\dot{U}}_{pre})_{n-1}-(a_3+1)(\underline{\ddot{U}}_{pre})_{n-1} \tag{1.46}$$

$$\Delta_n\underline{\dot{U}}_{pre}=a_1\Delta_n\underline{U}_{pre}-(a_4+1)(\underline{\dot{U}}_{pre})_{n-1}-a_5(\underline{\ddot{U}}_{pre})_{n-1} \tag{1.47}$$

By substituting these equations into the equation of motion 1.29, we obtained a new system that can be defined in the same manner as equation 1.41 :

$$[\hat{\mathrm{K}}]_n^{(i-1)}\{d_n^{(i)}\underline{U}_{unk}\} = \{\mathrm{R}\}_n^{(i-1)} \tag{1.48}$$

with $[\hat{\mathrm{K}}_n^{(i-1)}]$ previously defined and the only modification is the residual vector $\{\mathrm{R}_n^{(i-1)}\}$ as follows,

$$\begin{aligned}\{\mathrm{R}\}_n^{(i-1)} =&\{\Delta_n\underline{\mathrm{F}}_{ext}\} - \{\Delta_n^{(i-1)}\underline{\mathrm{F}}_{int}\}\\ &- [\mathrm{M}]\left[a_0\Delta_n^{(i-1)}\underline{U}_{unk} - a_2\{\dot{\underline{U}}_{unk}\}_{n-1} - (a_3+1)\{\ddot{\underline{U}}_{unk}\}_{n-1}\right]\\ &- [K_{elas}]\{\Delta_n\underline{U}_{pre}\} - [\mathrm{M}]\left[a_0\{\Delta_n\underline{U}_{pre}\} - a_2\{\dot{\underline{U}}_{pre}\}_{n-1} - (a_3+1)\{\ddot{\underline{U}}_{pre}\}_{n-1}\right]\end{aligned} \tag{1.49}$$

The third line of this equation takes into account an additional dynamic loading associated to the prescribed degrees of freedom. This general formulation permits, besides decreasing the size of the system, directly introducing the loads in the form of initial velocity $\{\dot{\underline{U}}_{pre}\}_0$ or initial acceleration $\{\ddot{\underline{U}}_{pre}\}_0$ prescribed at certain nodes.

1.5.2.6 Stress calculation at integration points

At each iteration (i), by means of equation 1.48, the new incremental nodal displacements $d_n^{(i)}\underline{U}$ permit after integration of the constitutive laws, to determine in each integration point, the new stress state $\underline{\underline{\sigma}}_n^{(i)}$. There are two different methods to determine this new stress state; whether by considering the stress state at the previous increment $\underline{\underline{\sigma}}_{n-1}$ (where it is statically and kinematically admissible and satisfies the constitutive equations), and the displacement increment (or strain by equation 1.24) $\Delta_n^{(i)}\underline{U} = \Delta_n^{(i-1)}\underline{U} + d_n^{(i)}\underline{U}$; or by considering the state of the stress at the previous iteration $\underline{\underline{\sigma}}_{n-1}^{(i-1)}$ (that satisfies only the constitutive equations), and the incremental displacement $d_n^{(i)}\underline{U}$ only. In the first case, the stress update in each increment is performed by an implicit integration scheme; whereas in the second case, it is performed by an explicit one. The new stress state $\underline{\underline{\sigma}}_n^{(i)}$ permits to obtain the new residual vector and particularly the vector of internal forces :

$$\{\Delta_n^{(i)}\underline{\mathrm{F}}_{int}\} = \int_\Omega [B]^T\Delta_n^{(i)}\underline{\underline{\sigma}}d\Omega = \int_\Omega [B]^T\{\underline{\underline{\sigma}}_n^{(i)} - \underline{\underline{\sigma}}_{n-1}\}d\Omega \tag{1.50}$$

The convergence rate of the Newton-Raphson algorithm, integrated in the Newmark scheme in time, depends, first on the exact calculation of stresses $\underline{\underline{\sigma}}_n^{(i)}$ satisfying the constitutive laws and secondly, the calculation of the tangent stiffness matrix $[\mathrm{K}]_n^{(i-1)}$. To obtain the tangent stiffness matrix, the calculation of $\partial\{\Delta_n^{(i-1)}\underline{\underline{\sigma}}\}/\partial\{\Delta_n^{(i-1)}\underline{\underline{\epsilon}}\}$ is necessary, but since, the modified Newton-Raphson algorithm is used in this work, we do not need to calculate this term in each iteration and the elastic behavior of the material will be sufficient to obtain $[\mathrm{K}]_n^{(i-1)}$ at the beginning of each increment. Despite this, the constitutive laws for the nonlinear soil are required to obtain the stresses at each iteration.

1.6 Numerical implementation into the CESAR-LCPC finite element program

Modeling civil engineering problems provides valuable assistance in understanding complex phenomena, in designing structures by predictive models, and in providing assistance to make the decision. It relies on the analysis of phenomena and their physical-mathematical representation, the numerical solution of corresponding equations and comparison with experiment; The LCPC (Laboratoire Central des Ponts et Chaussées) is committed in this area in the late 1960s, and during the last twenty years, it has gathered its modeling efforts through the development of the CESAR-LCPC program.

1.6.1 Presentation of the CESAR-LCPC program

CESAR-LCPC is a general computation software, mainly based on the finite element method, having its own pre-processing and post-processing (Humbert and Dubouchet, 2001). The modular architecture of its solver also enables to have the models based on the boundary element method. This software is particularly adapted to solve problems in civil engineering and environment such as structural analysis, soil and rock mechanics, thermal problems, hydrogeology, etc. (Humbert, 1989). Research and Development CESAR-LCPC software is also an industrial package and a stable and validated version is regularly available to outside users. CESAR-LCPC, originally a research software, continuously develops new possibilities. Meanwhile, a major change in its functionality and interfaces pre- and post-processing is recently strengthen its industrial aspect.

If one looks back in search of the predecessors of CESAR-LCPC, a prominent place should be assigned to the ROSALIE (Guellec et al., 1976) system, first computing system of LCPC based on the finite element method, developed in the early seventies (Table 1.1).

1970 to 1983	**ROSALIE** system of calculation : - originally for modeling of underground structures
1980	First restructuring : development of **CESAR** solver
from 1985	CESAR-LCPC software - CESAR solver, pre- and post-processors **MAX** and **PEGGY**
1992	CESAR-LCPC version **3.0**
1994	Distribution by Itech company
1995 to 1997	**CESAR** project
1998 to 2002	**CLEO** project : -modernization works
2003	CESAR-LCPC version **4.0**

Table 1.1: History of CESAR-LCPC software (Humbert et al., 2005)

CESAR's development began in the early eighties by the critical analysis of the ROSALIE system, considering the state of the art, especially in the field of architecture of computer codes. The development of CESAR's solver then began, first by writing new software components, and secondly by restructuring reusable software components of ROSALIE. At the same time, developments in hardware and the introduction of design standards has allowed the development of interactive tools for data generation (MAX software) and the interpretation of results (PEGGY software), first in 2D and after that in 3D thanks to the advent of workstations. This software package (MAX+CESAR+PEGGY) accompanied by the user documentation and test data sets was the first version of CESAR-LCPC. It has definitely followed ROSALIE system after the outside broadcast LCPC version 2.0 in 1986. Later, versions 3.0 and the other versions have been developed during the years. The purpose of the latest evolution (version 4.0) of CESAR was to make a perfectly developed industrial software, and with strengthened capabilities in pre- and post-processing (Humbert et al., 2005). All the developments made in this thesis have been undertaken within the program of FEM CESAR.

CESAR-LCPC is the combination of the pre-processor MAX, the finite element calculation code, CESAR, by the post-processor PEGGY and utility programs. These programs communicate with each other through a database (Fig.1.9).

Therefore, to model a problem with CESAR-LCPC, requires the next three steps.

- Use of pre-processor MAX to generate the data required for CESAR (such as the mesh and material properties, forces, etc.)
- Use of calculation code, CESAR, to obtain the numerical resolution of the studied problem

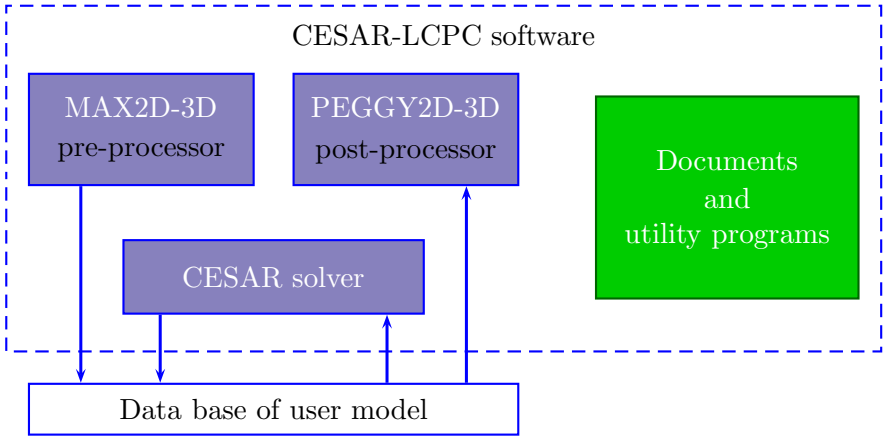

Figure 1.9: Components of the CESAR-LCPC software

- Use of post-processor PEGGY to graphically interpret the results

CESAR-LCPC software is divided into different parts named as "modules" for each specific computational problem to be solved: linear elasticity, elasto-plasticity, contact, dynamics, thermal, diffusion, etc. These modules include adaptable algorithms to solve the problem. During my thesis work, I modified an existing calculation module named MCCI (Mécanique de Comportement aux Chocs et Impacts) to introduce the nonlinear cyclic behavior of soils. This calculation module was developed by Sercombe (1997) to perform the nonlinear dynamic analyses by the implementation of Newton-Raphson algorithm integrated within Newmark time scheme presented in §1.5.2. In the next section a brief introduction of this module will be presented.

1.6.2 Presentation of the MCCI module

The general nonlinear dynamic computational algorithm presented in §1.5.2 has been programmed by Sercombe (1997) into the computer code CESAR-LCPC and led to the creation of a specific calculation module dedicated to model the concrete behavior at high strain rates and its application to the finite element calculation of concrete, reinforced concrete and fiber-reinforced concrete structures. The structure of the module was chosen to solve the dynamic problem but also static and quasi-static problems with nonlinear constitutive laws. The name of this calculation module is MCCI (Mécanique de Comportement aux Chocs et Impacts, Lussou (2006)).

The general work of the Sercombe (1997) consisted, on one hand, in the development of a suitable constitutive law for concrete in dynamics and, on the other hand, in the development of algorithms for its integration in a finite element code. His work led to a visco-elasto-plastic constitutive law in which a new concept of viscous hardening was introduced to account, at the macroscopic level, for the strength enhancement of concrete observed in dynamics. This constitutive law was then implemented in finite element CESAR-LCPC program by Sercombe (1997).

1.6.3 Convergence criteria

The global convergence criteria of the iterative Newton-Raphson scheme used here are the usual criteria for nonlinear problems. They consist of the norms of displacement vector, second member (residual vector) and the work done during each iteration (Mestat, 1993) :

$$\begin{cases} ||\{d_n^{(i)}\underline{U}\}|| < \epsilon_d ||\{\underline{U}_n^{(i)}\}|| \\ ||\{\mathrm{R}_n^{(i)}\}|| < \epsilon_r ||\{\mathrm{R}_n^{(0)}\}|| \\ |\{\mathrm{R}_n^{(i)}\}\{d_n^{(i)}\underline{U}\}| < \epsilon_t |\{\mathrm{R}_n^{(0)}\}\{\underline{U}_n^{(i)}\}| \end{cases}$$

where the global tolerances ϵ_d, ϵ_r and ϵ_t are the parameters that defined by user and generally are equal to 10^{-3} or 10^{-4}.

In general, the convergence rate of the algorithm is quantified in two manners, first, by the number of iterations in each increment and second, by the calculation time of each increment. In the MCCI module, two calculation approaches of initial stress and tangent matrix can be used (Sercombe, 1997). In the initial stress approach (modified Newton-Raphson), the tangent matrix is only determined at the beginning of each increment and remains constant during the iterations. Therefore, the tangent matrix remains elastic and can be obtained by equation 1.45. In the tangent method, at each iteration a new stiffness matrix is obtained through updated stresses. The choice of the method depends on the number of degrees of freedom. When we have a few degrees of freedom, the tangent method gives a faster convergence and fewer number of iterations for each increment, but when this number is large, it is preferable to use the initial stress method, because the calculation of the stiffness matrix at each iteration is very expensive.

1.6.4 A review of the performed developments necessary to model the nonlinear SSI

The MCCI module is basically created to model the concrete structures with an elastoplastic behavior excited by dynamic loadings. Initially, this module was conceived to model the fixed base structures, and the input motion could be applied as prescribed displacement or force. Therefore, different issues should be added into this module in order to deal with the nonlinear dynamic soil-structure interaction problem. First of all, a constitutive law is required to model the nonlinear cyclic behavior of the soil. Also, to have a more realistic soil-structure model, the interface of the soil and the structure should be modeled by appropriate elements.

In wave propagation problems, the spurious waves due to the fictitious truncation of the soil media should be treated. In the following, a brief review of all the numerical implementation performed at the CESAR-LCPC program during this thesis is presented.

1.6.4.1 Nonlinear constitutive law for soil

A nonlinear elastoplastic cyclic constitutive initially proposed by Iwan (1967) is implemented and numerically validated in the CESAR-LCPC program. The details of the constitutive model, its implementation and verification are presented at §3.2.5, §3.3 and §3.3.3. The advantage of this model is that it uses only the shear modulus reduction curve as the input nonlinear properties.

- **Effect of the confinement stress on the shear moduli of the soil**

The soil stiffness increases for larger confining stresses. This effect is taken into account by a nonlinear elastic approach considered as,

$$G = G_{ref} \left(\frac{P}{P_{ref}} \right)^n \tag{1.51}$$

where the elastic shear moduli, G, is a function of the mean compressive stress P. The G_{ref} is the elastic shear moduli measured at the mean pressure P_{ref} and n depends on the soil type. It is usually 0.5 for granular soils and close to 1 for clays. Therefore, the low-strain shear moduli increases with depth. This effect is added to the MCCI module as an option.

- **Effect of the superstructure weight on the shear moduli of the soil**

The weight of the superstructure influences the confining stress in the soil and modifies its low-strain shear moduli. This issue is added to the MCCI module as an option using the Boussinesq formulations. Consequently, if this option is activated by the user, the program computes the confinement stress due to the weight of the superstructure and adds it to the total confining stress at each point of the soil media. Then the confining stress serves to compute the modification of the soil shear modulus at low strains.

1.6.4.2 Energy dissipation and maximum strain in the soil

The goal of this work is to study the effect of the soil nonlinearity on DSSI. Therefore, most of the efforts during this work was performed for the soil media. The formulation of the computation of the energy dissipation in the soil is implemented into the CESAR-LCPC program. Consequently, the program is capable to obtain the cumulative dissipated energy in the soil during the propagation at each node of the finite element model. The results can be seen at any given time as isovalues and can be used to verify which part of the soil dissipates more energy during the propagation process.

The maximum strain reaches during the propagation can also be useful to control the strain levels at each point. This issue is also added to the MCCI model and the results will be shown especially at §5 and §6.

1.6.4.3 Soil-structure interface

To have a realistic model, the soil-structure interface should be modeled by the appropriate elements. In order to avoid traction between the foundation and the surrounding soil, the contact elements presented in Appendix §A are used to model the soil-structure interface. These contact elements existed in another calculation module of the CESAR-LCPC program. During this work, they are implemented and adapted to the dynamic case (MCCI module). These elements are able to simulate the friction phenomena using Coulomb's friction law. They are also capable of taking into account the foundation uplift but this issue is out of the scope of this work.

1.6.4.4 Boundary condition

When the dynamic SSI problem is treated by the finite element method, some special considerations must be included in order to ensure that the truncated domain model being compatible with the unbounded nature of the real problem. We divide the boundaries of the model into two parts, the base boundary and the lateral boundary. For the base boundary, a simple multi-directional absorbing method presented in §2 is used in this work to avoid the reflection of the downgoing waves to the media. This method was already implemented into another calculation module and is adapted to the MCCI model during this work.

For the lateral boundaries, a tied lateral boundary approach or repeatable approach (with a periodic nature) is retained as modeling strategy (for more details refer to Saez (2009)). In this method, the values of displacements, stresses, etc. are identical on both vertical lateral sections. Correct results are obtained if a sufficiently large domain is used.

1.6.4.5 Initial static condition

The initial static condition of the soil-structure system such as the initial displacements and stresses due to the weight of the superstructure and the soil should be considered before applying the seismic excitation. This issue is less critical in our case because the soil is considered in dry condition. Hence, the necessary modification is performed during this work to divide the problem into two parts. In the first part, the system is analyzed considering the static condition and in the second one, the dynamic loading is applied to the system. In general, this option is not used in this work except when clearly mentioned in the text.

1.6.4.6 Divergence problem

In addition to the convergence criteria presented in §1.6.3, another internal criteria is considered for the nonlinear constitutive soil model. It is related to the transfer of the yielding surfaces of the model and helps us to have a more precise solution.

In general, the nonlinear dynamic analyses are very expensive in time. In particular, the nonlinear constitutive model used in this work contains more than one yield surface, the more the number of yield surfaces, the more the computation time. A strategy is examined during this work to decrease the total time for the analysis. It is based on an automatic approach to change the time step, dt, during the analysis, when the convergence is not obtained. This approach allows us to have a greater time step, dt, and decreases the total computation time. We can summarize this approach as follows:

At the beginning a time step, dt, is selected. The program uses this time step for all the increments except if the convergence in an increment is not obtained. Therefore, the program divides the time step by two, $dt/2$, (it divides the incremental displacement by two as the solution is based on displacement). Then it solves again the equations for the first part of the divided time step ($dt/2$). The convergence criteria are then controlled. If the convergence is obtained, the program continues with the second part of the time step (second $dt/2$), if not, it divides again the first time step ($dt/4$) and it continues the resolution. This procedure is repeated until the convergence is obtained. Then the program passes to another increment and so on.

This procedure produces an irregular time discretization. This method works very well when the general time step, dt, is not too large. When the general time increment is large, this internal automatic time discretization will be performed for lots of increments and a high level of irregularity of the time discretization may be produced. Therefore, based on the author's experience, the loading path of the dynamic response (i.e. in the stress-strain curve) will be changed. Consequently, the precision of the results decreases or the convergence will be never obtained during the calculation. A great deal of tests were performed during this work in the goal of decreasing the total time duration of the solution. But especially for high level of nonlinearity this method did not work, for the reason mentioned above. Conversely, for smaller time steps, this method works very well.

1.7 Concluding remarks

The general dynamic soil-structure interaction problem was presented theoretically by defining the related governing equations in the soil-structure domain.

The numerical program, CESAR-LCPC, that is used during this work to study the dynamic soil-structure interaction was briefly presented. Also, the new developments (nonlinear constitutive model for soils, effect of confining stress on the shear modulus of the soil, initial static condition, absorbing boundaries, contact elements in the soil-structure interface, etc.) on the CESAR-LCPC code are mentioned which are necessary to model the nonlinear dynamic soil-structure interaction.

Chapter 2

Simple absorbing layer method for seismic waves [1]

Contents

[1] Extracted from :J.F. Semblat, A. Gandomzadeh, L. Lenti, (2010). A simple numerical absorbing layer method in elastodynamics. *Comptes Rendus Mécanique*. 338(1):24-32
Semblat, J.-F., Lenti, L., and Gandomzadeh, A. (2011). A simple and efficient multi-directional absorbing layer method to simulate elastic wave propagation in unbounded domains. *International Journal for Numerical Methods in Engineering*. 85(12):1543-1563

2.1 Introduction

The numerical analysis of elastic wave propagation in unbounded media may be difficult due to spurious waves reflected at the model artificial boundaries. This point is critical for the analysis of wave propagation in heterogeneous or layered solids. Various techniques such as Absorbing Boundary Conditions, infinite elements or Absorbing Boundary Layers (e.g. Perfectly Matched Layers) lead to an important reduction of such spurious reflections (§2.2). In this chapter, a simple absorbing layer method is proposed: it is based on a Rayleigh/Caughey damping formulation which is often already available in existing Finite Element softwares. The principle of the *Caughey Absorbing Layer Method* including a rheological interpretation is first presented in §2.3. The efficiency of the method is then shown through 1D Finite Element simulations considering homogeneous and heterogeneous damping in the absorbing layer (§2.4). 2D models are considered afterwards to assess the efficiency of the absorbing layer method for various wave types and incidences. A comparison with the PML method is first performed for pure P-waves (§2.5) and the method is shown to be reliable in a more complex 2D case involving various wave types and incidences (§2.6). It may thus be used for various types of problems involving elastic waves (e.g. machine vibrations, seismic waves, etc.).

2.2 Modeling wave propagation in unbounded domains

Various numerical methods are available to simulate elastic wave propagation in solids: finite differences (Virieux, 1986; Moczo et al., 2002), finite elements (Hughes, 1987; Semblat and Pecker, 2009), boundary elements (Beskos, 1997; Bonnet, 1999), spectral elements (Faccioli et al., 1997; Komatitsch et al., 1999), mesh-free methods (Li and Liu, 2007), etc. Such methods as finite or spectral elements have strong advantages (for complex geometries, non-linear media, etc) but also important drawbacks such as numerical dispersion (Ihlenburg and Babuška, 1995a; Semblat and Brioist, 2000; Hughes et al., 2008) for low-order finite elements or spurious reflections at the mesh boundaries (Semblat and Pecker, 2009; Modaressi and Benzenati, 1992). Other methods such as the Boundary Element Method (BEM) are generally limited to weakly heterogeneous linear media but allow an accurate description of the radiated waves at infinity (Bonnet, 1999; Gaul and Schanz, 1999; Semblat et al., 2000). Another limitation of the classical BEM is that it leads to unsymmetric fully populated matrices. New efficient Fast BEM formulations have been recently proposed to model 3D elastic wave propagation (Fujiwara, 1998; Chaillat et al., 2009).

All these methods, however, need to deal with spurious reflections. For that, (Dangla, 1988) proposed to use the BEM or coupling it with another numerical method. At very large scales, domain Reduction Methods are also available in the framework of Finite Element approaches (Bielak et al., 2003).

Another alternative is to directly attenuate the spurious reflections at the mesh boundaries considering Non Reflecting Boundary Conditions (NRBCs). A detailed review of such techniques was proposed by Givoli (1991) and Harari and Schohet (1998) and a recent paper by Festa and Vilotte (2005) gives additional references. The various NRBCs approaches may be characterized in the following manner:

- *Absorbing boundary conditions ('ABCs')*: They involve specific conditions at the model boundaries to approximate the radiation condition for the elastic waves (Modaressi and Benzenati, 1992). Engquist and Majda (1979) proposed a technique based on local approximate boundary conditions of increasing order (also see the work of Bayliss and Turkel (1980)). As these techniques involve 'one-way' boundary operators (i.e. along one direction only), it is difficult to avoid spurious reflections due to various wave types involving different polarizations. Furthermore, the extension of such techniques to elastic waves leads to complex systems of equations difficult to analyse in terms of stability (Festa and Vilotte, 2005). Givoli (1991) also proposed NRBCs (Dirichlet-to-Neumann, 'DtN', operator) that

are nonlocal in space or in time (or both) and may be considered as more effective than local boundary conditions (independent of the angle of incidence).

- *Infinite elements*: They allow the approximation of the decaying laws governing the waves radiation process at infinity (Chadwick et al., 1999). The principle is to use finite elements with their end nodes moved at infinity. Their drawbacks are similar to that of the absorbing boundaries.

- *Absorbing boundary layers ('ABLs')*: Such methods (e.g. Perfectly Matched Layers or PMLs) have been widely studied in the recent years (Basu and Chopra, 2003; Festa and Nielsen, 2003; Festa et al., 2005; Komatitsch and Martin, 2007; Meza-Fajardo and Papageorgiou, 2008). The PML technique, introduced by Bérenger (1994) in the field of electromagnetic, is based on the description of attenuating properties along a specific direction in an absorbing layer of finite thickness located at the medium boundaries. Inside the PML, a field described by the plane wave $exp[-i(\underline{\mathrm{k}}.\underline{\mathrm{x}} - \omega t)]$ decreases, in the x_i direction, by a factor generally independent of frequency (Festa and Vilotte, 2005):

$$exp\left(-\frac{k_i}{\omega}\int \alpha_i(\zeta)d\zeta\right) \tag{2.1}$$

  where α_i is an analytical function.

- The extension of PML techniques to acoustic and elastic wave propagation was proposed by various authors (Festa and Nielsen, 2003; Chew and Liu, 1996; Collino and Tsogka, 2001; Marcinkovich and Olsen, 2003). Classical PMLs are more efficient than 'ABCs' but several cases lead to some instabilities: grazing incidence, shallow models involving surface waves, anisotropic media. Several improved PML formulations were recently proposed to overcome such difficulties. The filtering or convolutional PML allows the treatment of surface waves in shallow media (Festa and Nielsen, 2003). In this formulation, the field decay in the x_i direction is governed by a factor depending on frequency (Festa and Vilotte, 2005):

$$exp\left(-\frac{k_i}{\omega}\frac{\omega^2 - i\omega\omega_c}{\omega^2 + \omega_c^2}\int \alpha_i(\zeta)d\zeta\right) \tag{2.2}$$

  where ω_c is a cut-off frequency.

  The multi-directional PML formulation was recently proposed to deal with grazing incidences and strong anisotropies (Meza-Fajardo and Papageorgiou, 2008). It allows various choices for the attenuation vector $\underline{\alpha}$ in the absorbing layer:

$$\underline{\mathrm{u}} = \underline{\mathrm{A}}exp(-\underline{\alpha}.\underline{\mathrm{x}})exp[-i(\underline{\mathrm{k}}.\underline{\mathrm{x}} - \omega t)] \tag{2.3}$$

  where $\underline{u}$ is the displacement vector, $\underline{A}$ the polarization vector, $\underline{x}$ the position vector, $\underline{k}$ the wave vector, ω the frequency and t the time.

  It is thus possible to deal with various wave types (i.e. polarizations) and incidences. The multi-directional PML formulation leads to better efficiency and numerical stability.

In this chapter, we propose a simple and reliable absorbing layer method to reduce the spurious reflections at the model boundaries. The aim of the method is to be simple since the damping model is already available in most general purpose finite element softwares.

2.3 A simple multi-directional absorbing layer method

2.3.1 Basic idea

In order to deal with spurious reflections we consider absorbing layers and multi-directional attenuating properties; thus we follow the PML technique but with a simple description of the attenuation process. Physical models are generally very efficient to describe the attenuation process (frequency dependence, causality, etc.), but they are not very easy to implement or are cost-effective due to the use of memory variables (J.M.Carcione et al., 2002; S.M.Day and Minster, 1984; Delépine et al., 2009; Emmerich and Korn, 1987; Kausel and Assimaki, 2002; Kjartansson, 1979; Moczo and Kristek, 2005). As Caughey damping is already available in most finite element softwares, we propose to use this formulation to describe the attenuation of the waves in an absorbing layer of finite thickness. The method is thus called the *Caughey Absorbing Layer Method* or 'CALM'. This damping formulation is purely numerical but, as recalled hereafter, a rheological interpretation is possible in some cases (i.e. second-order Caughey formulation).

2.3.2 Rayleigh and Caughey damping

Rayleigh damping is a classical method to easily build the damping matrix [C] for a Finite Element model (Hughes, 1987) under the following form:

$$[\mathrm{C}] = a_0[\mathrm{M}] + a_1[\mathrm{K}] \tag{2.4}$$

where [M] and [K] are the mass and stiffness matrices of the whole model respectively. It is then called *Rayleigh damping matrix* and a_0, a_1 are the Rayleigh coefficients.

A more general damping formulation was proposed by Caughey (Caughey, 1960; Munjiza et al., 1998) and is expressed as follows:

$$[\mathrm{C}] = [\mathrm{M}] \sum_{j=0}^{m-1} a_j \left([\mathrm{M}]^{-1}[\mathrm{K}]\right)^j \tag{2.5}$$

As evidenced by Equation 2.5, the Rayleigh formulation (Equation 2.4) corresponds to a second-order Caughey damping ($m = 2$) involving a linear combination of the mass and stiffness matrices.

This way of building the damping matrix is very convenient since it can be easily computed and is often available in general purpose FEM softwares. Furthermore, for modal approaches, the *Rayleigh* (or *Caughey*) *damping matrix* is diagonal in the real modes base (Chopra, 2001). Damping is therefore called proportional or classical. In case of non-proportional damping, the complex modes have to be computed (in order to uncouple the modal equations).

Rayleigh (or Caughey) damping formulation may also be used to analyze the propagation of damped elastic wave (Semblat, 1997). For such problems, it may be useful to have a rheological interpretation of these purely numerical formulations. In the field of mechanical wave propagation, the equivalence between the Rayleigh formulation and a Generalized Maxwell model was already proposed (Semblat, 1997) and is briefly recalled hereafter.

2.3.3 Rheological interpretation of Rayleigh damping

Considering Rayleigh damping (Chopra, 2001) (i.e. second-order Caughey damping), the loss factor η can be written as follows:

$$\eta = 2\zeta = \frac{a_0}{\omega} + a_1\omega \tag{2.6}$$

where ω is the circular frequency and ζ is the damping ratio.

Considering the relationship between internal friction and frequency for Rayleigh damping, it is possible to build a rheological model involving the same attenuation-frequency dependence. For a linear viscoelastic rheological model of complex modulus $M = M_R + iM_I$ (Bourbié et al., 1987), the expression of the quality factor Q is given in the fields of geophysics and acoustics as follows:

$$Q = \frac{M_R}{M_I} \tag{2.7}$$

For weak to moderate Rayleigh damping, there is a simple relation between the inverse of the quality factor Q^{-1} and the damping ratio ζ (Chopra, 2001):

$$Q^{-1} \approx 2\zeta \tag{2.8}$$

For Rayleigh damping, the loss factor is infinite for zero and infinite frequencies. It clearly gives the behavior of the model through instantaneous and long term responses. As shown in (Semblat, 1997), the rheological model perfectly meeting these requirements (attenuation-frequency dependence, instantaneous and long-term effects) is a particular type of generalized Maxwell model.

Figure 2.1 gives a schematic of the proposed rheological interpretation: it connects, in parallel, a classical Maxwell cell to a single dashpot. The generalized Maxwell model may be characterized by its complex modulus (Semblat and Pecker, 2009; Bourbié et al., 1987) from which we easily derive the inverse of the quality factor Q^{-1} (generally frequency independent) which takes the same form as the loss factor of Rayleigh damping (expression 2.6): it is the sum of two terms, one proportional to frequency and one inversely proportional to frequency.

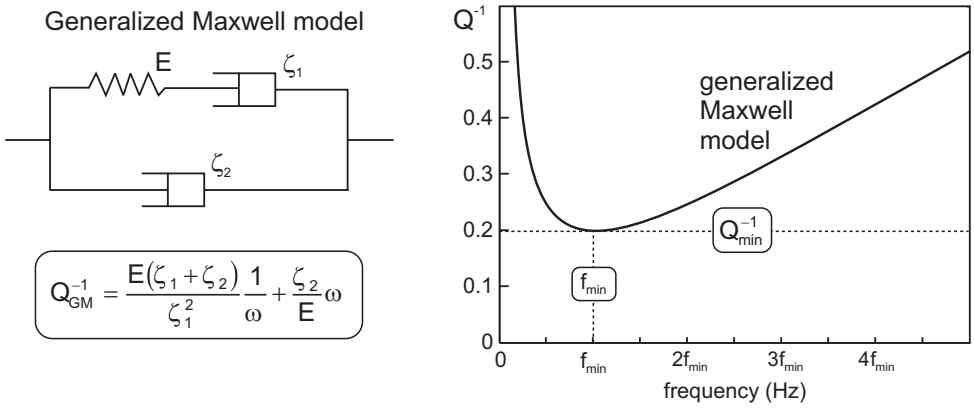

Figure 2.1: Schematic of the proposed rheological interpretation

Considering Equation 2.6 and Fig.2.1, the Rayleigh coefficients can be easily related to the rheological parameters of the Generalized Maxwell model:

$$\begin{cases} a_0 = \frac{E(\zeta_1+\zeta_2)}{\zeta_1^2} \\ \\ a_1 = \frac{\zeta_2}{E} \end{cases}$$

This equivalence between Rayleigh damping and the Generalized Maxwell model is evidenced for wave propagation problems in (Semblat, 1997). If one needs to characterize a real material, the Rayleigh coefficients may thus be identified from experimental results. In this work, a target theoretical damping will be chosen for a fictitious absorbing material (no experiments are needed).

2.3.4 Caughey absorbing layer method

In the framework of the Finite Element Method, an elastic medium is considered and an absorbing layer system will be designed at its boundaries. The absorbing layer is thus modelled with appropriate damping properties (i.e. Rayleigh/Caughey damping coefficients) in order to attenuate the spurious reflections at the mesh boundaries. This *Caughey Absorbing Layer Method* (*'CALM'*) may thus reduce the amplitude of the elastic wave coming from the elastic medium and reflecting at the artificial boundaries of the medium. In the following, the proposed technique is described for different damping variations in the absorbing layer thickness. The spatial variations of damping are controlled by variable damping coefficients in the Finite Elements. Such techniques were already used to model wave propagation in media with stress state dependent damping (Idriss et al., 1974; Semblat and Brioist, 1998). Considering Rayleigh damping, the element damping matrix for finite element, e, is thus written as:

$$[\mathrm{C}]^{(e)} = a_0^{(e)}[\mathrm{M}]^{(e)} + a_1^{(e)}[\mathrm{K}]^{(e)} \tag{2.9}$$

where $[\mathrm{M}]^{(e)}$ and $[\mathrm{K}]^{(e)}$ are the mass and stiffness matrices for finite element, e, respectively.

The Rayleigh damping coefficients $a_0^{(e)}$ and $a_1^{(e)}$ may be different in each finite element or chosen piecewise constant in the absorbing layer. In the following, the efficiency of the *CALM* is assessed for 1D and 2D elastic wave propagation.

2.4 Efficiency of the 1D Caughey Absorbing Layer

2.4.1 Definition of the propagating wave

For the 1D case, a second-order Ricker wavelet is considered. As depicted in Fig.2.2, this type of wavelet is derived from a Gaussian and is rather well localized in both time and frequency domain (Semblat and Pecker, 2009). It is thus ideal to perform a detailed analysis on wave propagation in a narrow frequency band investigating the reflection of short duration waves (to easily distinguish incident and reflected waves).We shall consider longitudinal elastic waves first and the predominant frequency of the Ricker wavelet $f_R = 1/t_p$ will be chosen in order to have an integer number of wavelengths along the medium. For the finite element computations, a Newmark non-dissipative time integration scheme is chosen to avoid algorithmic damping (Hughes et al., 2008) due to the time integration process.

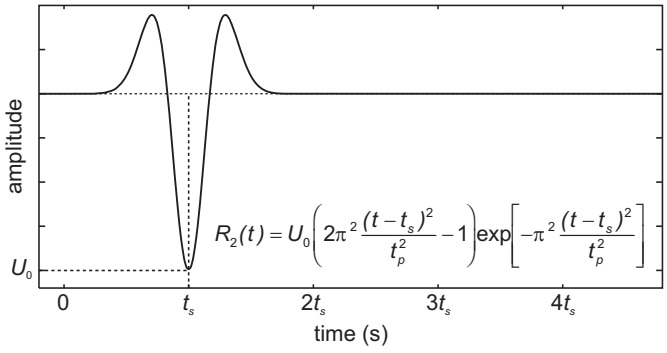

Figure 2.2: Second-order Ricker wavelet $R_2(t)$: maximum amplitude U_0, time shift t_s and fundamental period t_p

2.4.2 Rayleigh damping in the absorbing layer

In the following, the absorbing layer involves Rayleigh damping (second-order Caughey damping) which is frequency dependent (Fig.2.1) and is rheologically equivalent to a Generalized Maxwell

model for wave propagation problems (Semblat, 1997). To define a reference attenuation value (inverse of the quality factor Q^{-1}) in the absorbing layer, the minimum attenuation value will be chosen at the predominant frequency of the Ricker wavelet f_R. As the Generalized Maxwell model has a band-pass behavior (Fig.2.1, right), it is thus probably the worst case in terms of efficiency of the absorbing layer. From the expression of the damping ratio, Equation 2.6, it is possible to determine the frequency of minimum damping ω_{min} from the Rayleigh coefficients as follows:

$$\omega_{min} = \sqrt{\frac{a_0}{a_1}} \tag{2.10}$$

Choosing the minimum damping ζ_{min} (or attenuation Q^{-1}_{min}) at the predominant frequency of the Ricker wavelet f_R, it is then possible to derive the following relation:

$$\omega_R = 2\pi f_R = \sqrt{\frac{a_0}{a_1}} \tag{2.11}$$

and thus, using the definition of Rayleigh damping, derive the following system:

$$\begin{cases} Q^{-1}_{min} = 2\zeta_{min} = \frac{a_0}{\omega_R} + a_1\omega_R \\ \\ \omega_R = 2\pi f_R = \sqrt{\frac{a_0}{a_1}} \end{cases}$$

From the choice of the predominant frequency of the Ricker wavelet f_R and the minimum attenuation Q^{-1}_{min}, the Rayleigh damping coefficients in the absorbing layer may then be estimated. In the following, we shall choose several typical values for Q^{-1}_{min} ranging from 0.5 (i.e. $\zeta_{min} = 0.25$ or 25%) to 2.0 (i.e. $\zeta_{min} = 1.0$ or 100%).

2.4.3 Homogeneous absorbing case

As depicted in Fig.2.3, the first numerical case corresponds to a 1D elastic medium (left) and a homogeneously absorbing layer (right). The length of the elastic layer (left) is 4λ and that of the homogeneously damped layer (right) is λ (λ: wavelength of the longitudinal wave). Linear quadrilateral finite elements are considered and a $\lambda/20$ size is chosen to have low numerical wave dispersion (Semblat and Brioist, 2000; Hughes et al., 2008). In the elastic medium, the element damping matrices $[C]^{(e)}$ are zero, whereas homogeneous Rayleigh damping is considered in the absorbing layer by choosing identical Rayleigh coefficients $a_0^{(e)}$, $a_1^{(e)}$ for each element damping matrix in this area (the elastic properties being identical in both domains). In each case, the attenuation value Q^{-1} is chosen as the minimum attenuation value at the predominant frequency of the propagating wave (Ricker wavelet). As shown in Fig.2.2, because of the damping frequency dependence given by the Rayleigh formulation, all other frequency components are thus more strongly attenuated in the layer. Three attenuation values were chosen for the homogeneously absorbing case: $Q^{-1}_{min} = 0.5$, 1.0 and 2.0 (leading to damping values $\zeta_{min} = 25$, 50 and 100%, respectively).

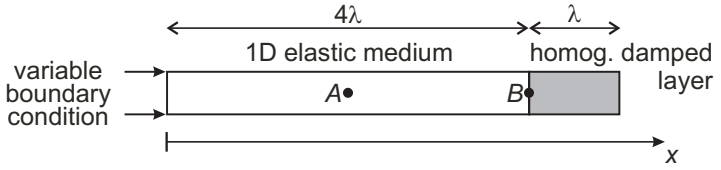

Figure 2.3: Schematic of the first numerical test: undamped elastic layer (left) and homogeneously damped layer (right)

The equation of motion of the whole finite element model is thus:

$$[\mathrm{M}]\underline{\ddot{u}} + [\mathrm{C}]\underline{\dot{u}} + [\mathrm{K}]\underline{u} = \underline{0} \tag{2.12}$$

with the following variable boundary condition at $x = 0$:

$$u(x = 0, t) = R_2(t, t_s, t_p) \tag{2.13}$$

[M], [C], [K] being the mass, damping and stiffness matrices (resp.), u_l the lth component of displacement, $R_2(t, t_s, t_p)$ the Ricker wavelet and, as shown in Fig.2.2, t_s , t_p its parameters (time shift and fundamental period resp.).

For the three different attenuation values in the absorbing layer, the results are displayed in Fig.2.4 for point A (left) at the center of the elastic medium and point B (right) at the interface between the elastic medium and the absorbing layer (see points location in Fig.2.3).

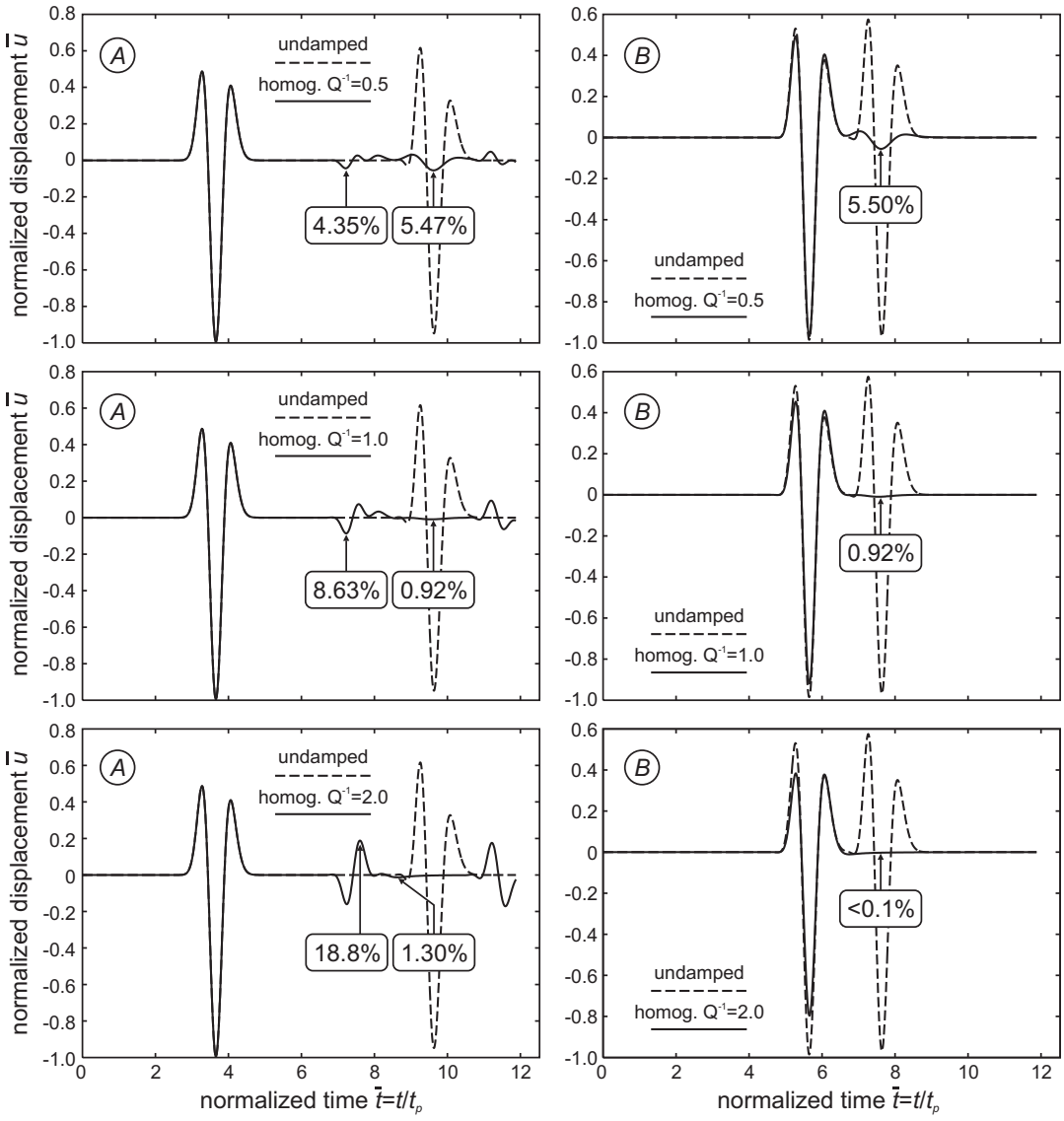

Figure 2.4: Comparison between the homogeneously damped layer (solid) and the undamped case (dashed) at points A (left) and B (right) for different attenuations: $Q_{min}^{-1} = 0.5$ (top), $Q_{min}^{-1} = 1.0$ (middle) and $Q_{min}^{-1} = 2.0$ (bottom).

These curves are plotted in terms of normalized displacement $\overline{u} = u/U_0$ vs normalized time $\overline{t} = t/t_p$ (U_0 and t_p being the Ricker wavelet amplitude and fundamental period resp.) and lead to the following conclusions:

- For $Q_{min}^{-1} = 0.5$ (top, solid), when compared to the undamped case ($Q_{min}^{-1} = 0.0$, dashed), the amplitude of the reflected wave at point A is much smaller (5.47% of U_0) but the incident wave is also reflected at the interface between the elastic medium and the absorbing layer (4.35%). It is due to the velocity contrast between the elastic medium and the viscoelastic layer (in terms of complex wavenumber). For $Q_{min}^{-1} = 0.5$ at point B (top right, solid), the amplitude at the interface between the elastic medium and the absorbing layer is also small (5.50%). The efficiency of the homogeneously absorbing layer thus appears acceptable.

- For $Q_{min}^{-1} = 1.0$ (middle, solid), the amplitude of the reflected wave at the end of the absorbing layer is very small (0.92% of U_0) but the reflected wave at the interface with the elastic medium is larger than for $Q_{min}^{-1} = 0.5$ (8.63% instead of 4.35%). This is due to the fact that the complex velocity contrast with the elastic medium is larger for $Q_{min}^{-1} = 1.0$.

- Finally, for $Q_{min}^{-1} = 2.0$ (bottom, solid), the contrast being larger again, the results are not very good for the wave reflected at the interface (18.8%). However, the reflected wave at the end of the absorbing layer is again very small (1.30%) and the amplitude at the interface (point B) is nearly zero.

The authors obtained similar results for transverse waves (SV waves). From these three different homogeneously damped cases, the *Caughey Absorbing Layer Method* (*'CALM'*) can already be considered as an efficient absorbing layer method but its efficiency may probably be improved and its artefacts reduced.

2.4.4 Heterogeneous absorbing case

In the homogeneous case, the velocity contrast between the elastic layer and the absorbing layer may have a detrimental effect. The idea is now to have an increasing damping value in the absorbing layer system along the direction of the incident wave and a lower damping contrast at the interface with the elastic medium.

As depicted in Fig.2.5, the second numerical case corresponds to a heterogeneously absorbing layer. The absorbing layer is divided into two $\lambda/2$ thick (top) or five $\lambda/5$ thick sub layers (bottom) involving piecewise constant Rayleigh damping coefficients in each sub-layer but increasing from one layer to the other. Two different sets of minimum attenuation values in each absorbing sub-layer are chosen:

- First set: $Q_{min}^{-1} = 1.0$ in the rightmost sub-layer and piecewise constant in each other sub-layers ($Q_{min}^{-1} = 0.5$ in the first layer of the two-layers case and $Q_{min}^{-1} = 0.2$, 0.4, 0.6 and 0.8 for the leftmost layers in the five-layer case).

- Second set: $Q_{min}^{-1} = 2.0$ in the rightmost sub-layer and piecewise constant in each other sub-layers ($Q_{min}^{-1} = 1.0$ in the first layer of the two-layers case and $Q_{min}^{-1} = 0.4$, 0.8, 1.2 and 1.6 for the leftmost layers in the five-layer case).

For the heterogeneous damped case, the results are displayed in Fig.2.6 for point A (i.e. centre of the elastic medium) and compared to the undamped case and the homogeneously damped case (first set of damping values: top, second set: bottom). A closer view on the reflected waves is also proposed (right). As the incident elastic wave is reflected at the interface and at the absorbing layer boundary, two different relative amplitudes are obtained for both reflected waves.

For the first set of damping values (i.e. $Q_{min}^{-1} = 1.0$ in the rightmost sub-layer):

- The first value corresponds to the reflection at the interface and ranges from 8.63% for the homogeneous case down to 1.66% for the five-layer case (4.35% for two layers).

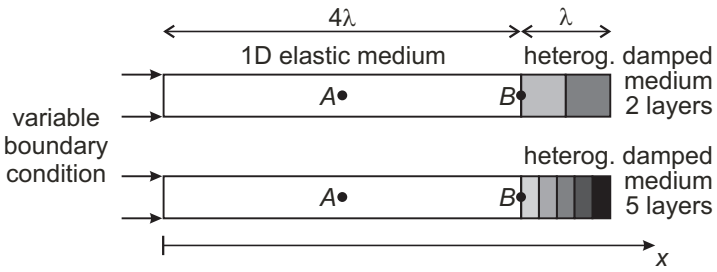

Figure 2.5: Schematic of the second numerical test: undamped elastic layer (left) and heterogeneously damped layer (right) involving two layers (top) or five layers (bottom)

- The second value is related to the reflection at the absorbing layer boundary and ranges from 0.92% for the homogeneous case up to 4.41% for the five-layer case (2.10% for two layers).

For the second set of damping values (i.e. $Q_{min}^{-1} = 2.0$ in the rightmost sub-layer):

- The first value corresponds to the reflection at the interface and ranges from 18.8% for the homogeneous case down to 2.78% for the five-layer case (8.63% for two layers).
- The second value is related to the reflection at the absorbing layer boundary and ranges from 1.30% for the homogeneous case up to 2.86% for the five-layer case (2.83% for two layers).

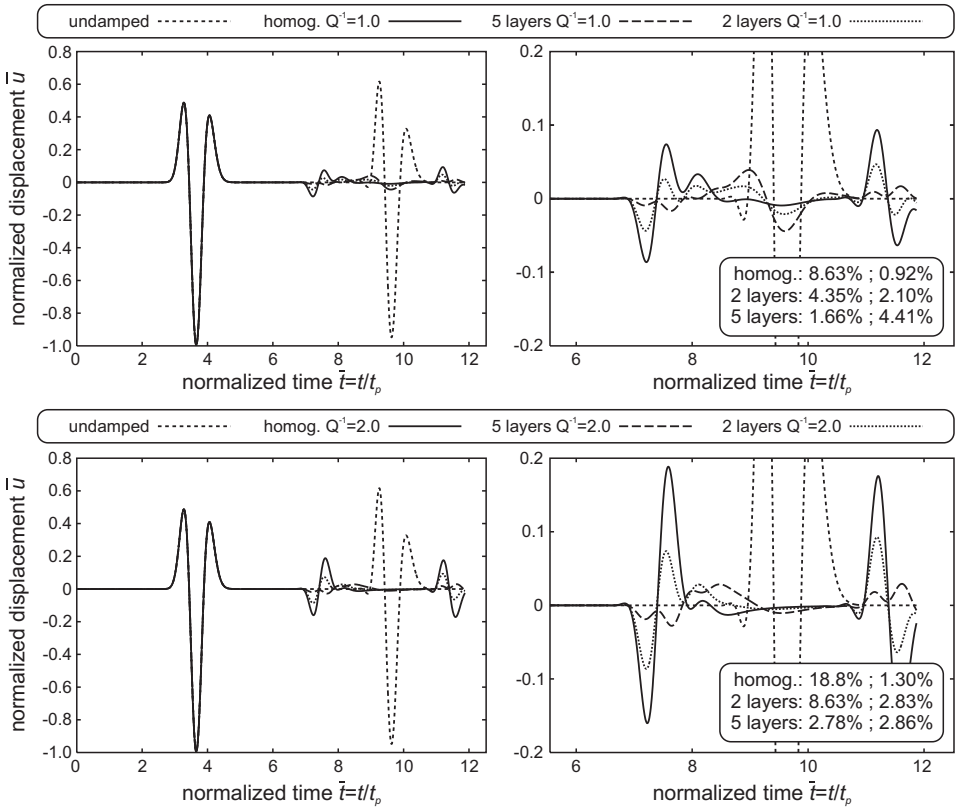

Figure 2.6: Comparison between the heterogeneously damped layer (dashed or dotted) and the homogeneous case (solid) at point A: first set (top) and second set of attenuation values (bottom)

From these results, it appears that it is necessary to balance the advantage of a strong damping in a thick layer (strong amplitude reduction in the layer) and slow variations of the damping

properties (low amplitude for the reflections at the interfaces). As in the PML approach, the parameters governing the amplitude decrease (or the coordinate stretching) are 'perfectly matched' at the interface (Basu and Chopra, 2003; Festa and Nielsen, 2003; Festa and Vilotte, 2005; Komatitsch and Martin, 2007; Meza-Fajardo and Papageorgiou, 2008), the case of a continuous damping variation in the absorbing layer will thus be studied hereafter.

2.4.5 Continuously varying damping

As depicted in Fig.2.7, the third numerical case corresponds to a continuously varying damping in the absorbing layer. The absorbing layer involves variable Rayleigh damping coefficients increasing linearly with the horizontal distance. The idea is to have a continuously increasing damping value in the absorbing layer system. Two cases are considered: attenuation Q_{min}^{-1} increasing linearly from 0 to 1.0 (first case) and from 0 to 2.0 (second case).

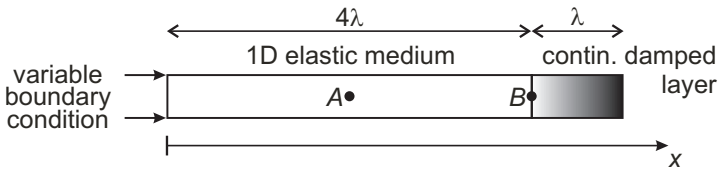

Figure 2.7: Schematic of the third numerical test: undamped elastic layer (left) and continuously absorbing layer system (right)

For the continuously (i.e. linearly) damped case, the results at point A (centre of the elastic medium) are displayed in Fig.2.8 for the two cases (top/bottom) and compared to the undamped case ($Q_{min}^{-1} = 0.0$). Closer views are also displayed in this Figure (right). For both cases, the efficiency of the continuous absorbing layer system is slightly better than that of the 5-layers system for the reflection at the interface: 1.11% instead of 1.66% for $Q_{min}^{-1} = 1.0$ (top), 2.17% instead of 2.78% for =2.0 (bottom). For the reflection at the medium boundary, the efficiency of the continuous system is a bit less for $Q_{min}^{-1} = 1.0$ (5.25% vs 4.41%) whereas it is nearly the same for $Q_{min}^{-1} = 2.0$ (2.80% vs 2.86%). When compared to the homogeneous case, the overall efficiency of the 5-layers and continuous systems are satisfactory.

2.4.6 Influence of the size of the absorbing layer

As the amplitude decay is influenced by the traveling distance, it is necessary to assess the influence of the absorbing layer thickness, another configuration involving a half wavelength thick layer is thus considered (Fig.2.9, bottom). The thickness of this absorbing layer system being smaller than in the previous case (Fig.2.9, top), the efficiency of this configuration should be less due to a shorter traveling distance in the layer (see Equation 2.3), whereas the number of degrees of freedom in the Finite Element model will be less.

The influence of the absorbing layer thickness is shown in Fig.2.10 for the homogeneous case (top) and the continuous case (bottom) and for two different attenuations $Q_{min}^{-1} = 1.0$ (left) and $Q_{min}^{-1} = 2.0$ (right).

For the reflection at the interface, the results are:

- *Homogeneous case (top)*: identical efficiency (8.63% for $Q_{min}^{-1} = 1.0$ and 18.8% $Q_{min}^{-1} = 2.0$) for both thicknesses since the velocity (or complex modulus) contrast is the same.

- *Continuous case (bottom)*: since the linear increase of damping is faster for the thinnest layer, the velocity contrast is a bit larger thus leading to a larger amplitude (2.19% instead of 1.11% for $Q_{min}^{-1} = 1.0$ and 4.21% instead of 2.80% for $Q_{min}^{-1} = 2.0$).

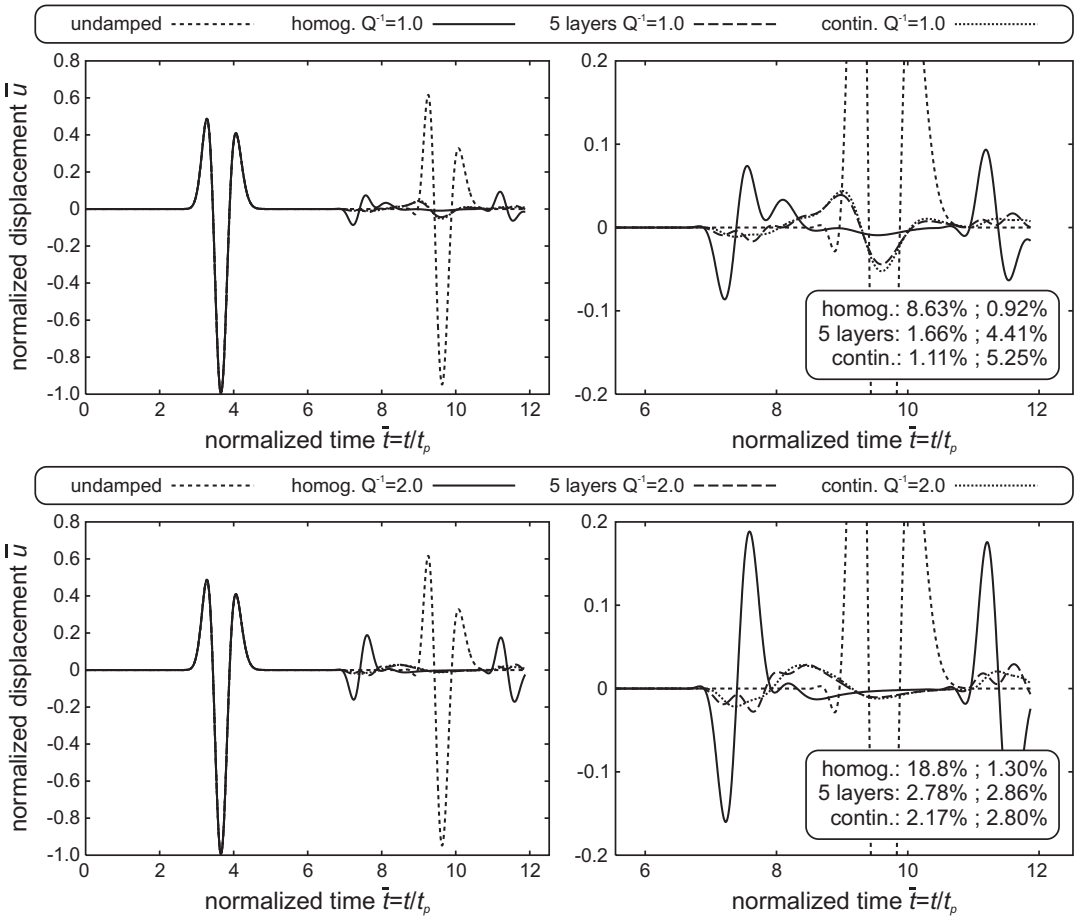

Figure 2.8: Comparison between the continuously damped layer and the homogeneous, heterogeneous and undamped cases at point A: first case (top) and second case (bottom). Closer views at right.

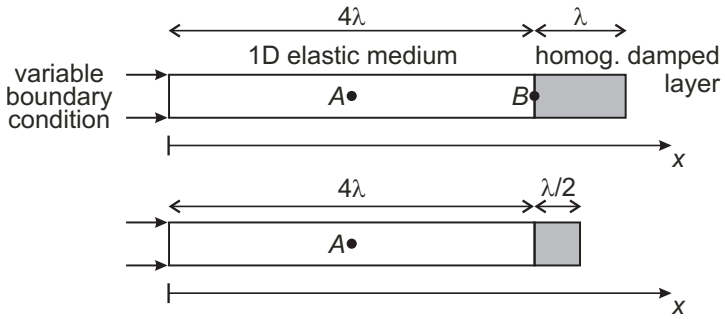

Figure 2.9: Various absorbing layer thicknesses to compare their efficiency: one wavelength thick layer (top) and half wavelength thick layer (bottom).

For the reflection at the model boundary, the efficiency of the half wavelength absorbing layer is significantly less than that of the one wavelength case since the distance along which the waves are attenuated is much less:

- *Homogeneous case (top)*: for $Q_{min}^{-1} = 1.0$ (left), the relative amplitude of the reflected wave is 6.80% for the $\lambda/2$ thick absorbing layer instead of 0.92% for the λ thick layer. For $Q_{min}^{-1} = 2.0$, the relative amplitude is 2.33% for the $\lambda/2$ thick instead of 1.30%.
- *Continuous case (bottom)*: for $Q_{min}^{-1} = 1.0$ (left), the relative amplitude of the reflected wave is 16.9% for the $\lambda/2$ thick absorbing layer instead of 5.25% for the λ thick layer. For

$Q_{min}^{-1} = 2.0$, the relative amplitude is 9.51% for the $\lambda/2$ thick instead of 2.80%.

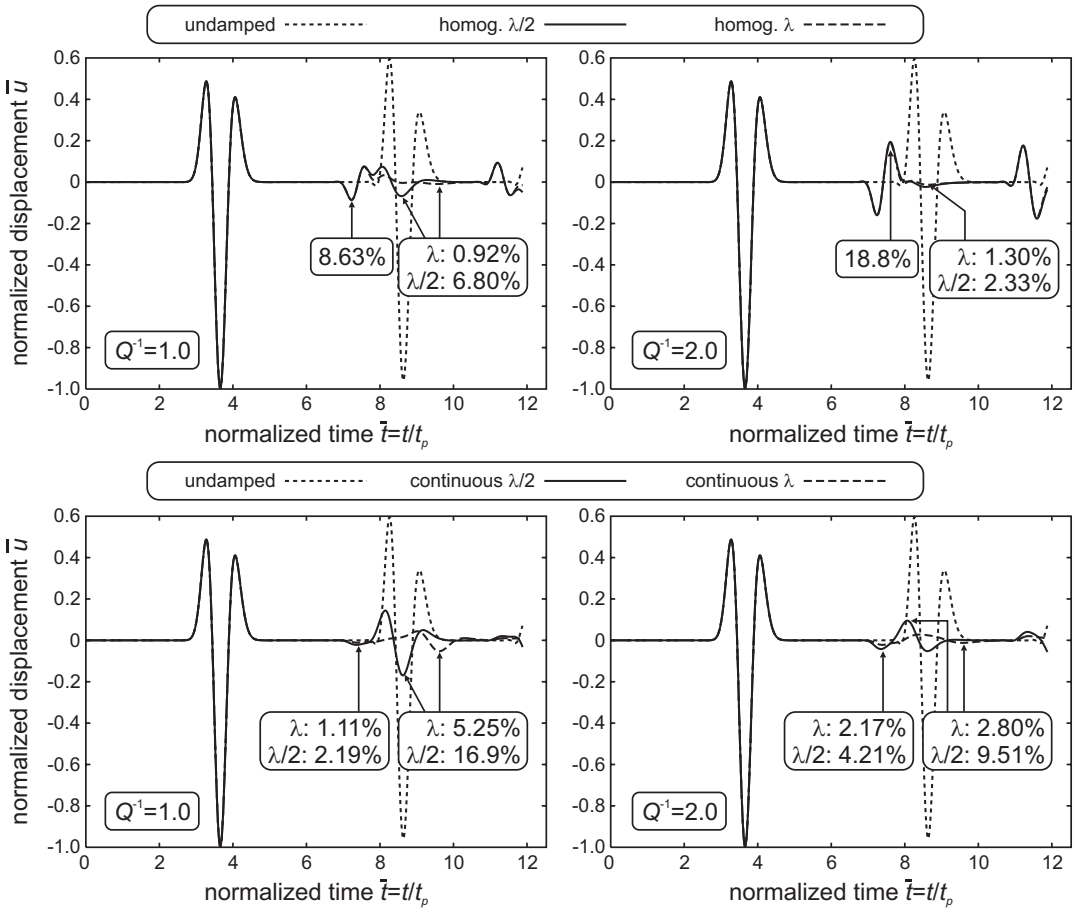

Figure 2.10: Influence of the thickness of the absorbing layer system: homogeneous case (top) and continuous case (bottom).

The influence of the absorbing layer thickness (or length) is thus very large and $\lambda/2$ is obviously not a very efficient choice since the efficiency is much less than for a λ-thick absorbing layer and the relative reduction of the number of degrees of freedom in the finite element model would not be so large for a wide model.

2.5 Efficiency of the 2D Caughey Absorbing Layer for pure P-waves

2.5.1 Simple 2D case from the PML technique: geometry and loading

To analyze the efficiency of the *CALM* in 2D configurations, we shall first study a simple 2D case involving pure P-waves. We shall consider a simple 2D case proposed by Festa and Vilotte (2005) for pure P-waves in the framework of the PML technique. As shown in Fig.2.11, a 2D absorbing layer is designed all around a square elastic domain. The wave velocities are $V_P = 4km/s$ and $V_S = 2.31km/s$ and the mass density is $\lambda = 2.5g/cm^3$ (see (Festa and Vilotte, 2005) for other details on the PML model). The size of the elastic domain ($2L = 1500m$) thus corresponds to $3.75\lambda_P$ and the width of the Caughey absorbing layer is chosen as $\lambda_P/2$. As Festa and Vilotte (2005) chose an explosive source using a Ricker wavelet for the time variations ($t_p = 0.1s$, i.e. $f_p = 10Hz$), we considered a finite element model (Fig.2.11 right) involving a pressure loading with similar time variations.

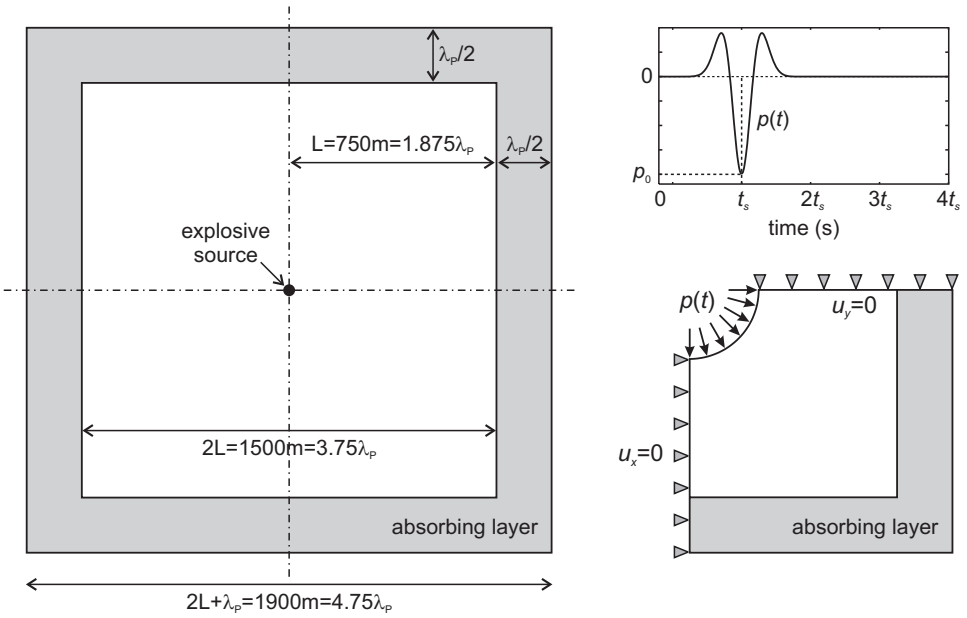

Figure 2.11: 2D plane strain model for pure P-waves proposed by Festa and Vilotte (2005): adapted schematic (left), pressure loading (top right) and finite element model considered for the *CALM* (bottom right).

2.5.2 Comparison between the CALM and PMLs

The wavefield is computed in terms of normalized displacement $\overline{u} = \|u\|/|p_0|$ ($\|u\|/$ being the norm of the displacement vector and $|p_0|$ the maximum loading pressure) for the undamped 2D case and the 5 layers 2D case (Q_{min}^{-1} = 0.4, 0.8, 1.2, 1.6 and 2.0 in each layer resp.). The numerical results are displayed in Fig.2.12 for three different normalized times $\overline{t}_1 = t_1/t_p = 2.49$ (left) ; $\overline{t}_2 = t_2/t_p = 3.32$ (centre) ; $\overline{t}_3 = t_3/t_p = 4.56$ (right). For the undamped case (Fig.2.12 top), the wave reflections at the model boundaries are obvious for times $\overline{t}_2$ and $\overline{t}_3$. For the Caughey absorbing layer (Fig.2.12 bottom), the wavefield is partially absorbed in the first layers at time $\overline{t}_2$ and no reflections from the model boundaries appear at time $\overline{t}_3$. Similar results were obtained by Festa and Vilotte (2005) for the PML technique. The thickness of the absorbing layer is nevertheless larger in *CALM*. The efficiency is also less since, for the same configuration, Festa and Vilotte obtained reflections coefficients ranging from 0.1% to 1% for a cubic decay function and from 0.6% to 2% for a quadratic decay function (Festa and Vilotte, 2005). They also studied 2D cases to describe soft geological deposits such as a thin surface layer or a curved surface layer.

As the previous results correspond to a simple incident wavefield, we shall now study a more complex case in terms of both polarization and incidences.

2.6 Efficiency of the 2D Caughey Absorbing Layer for various wave types

To assess the efficiency of the Caughey Absorbing Layer Method for more complex 2D wavefields, another 2D FEM model is considered (Fig.2.13). A plane strain model is chosen in order to avoid strong geometrical damping. It involves a 4λx4λ square elastic medium and two λ thick absorbing layers (right and bottom). The model is symmetrical along the left boundary and the variable boundary condition (vertical displacement varying as a Ricker wavelet at $f_R = 1/t_p$) is applied at the free surface along a distance of λ/2 (Fig.2.13). The wavefield in the model is thus composed of various wavetypes (longitudinal, transverse and surface waves) and the motion

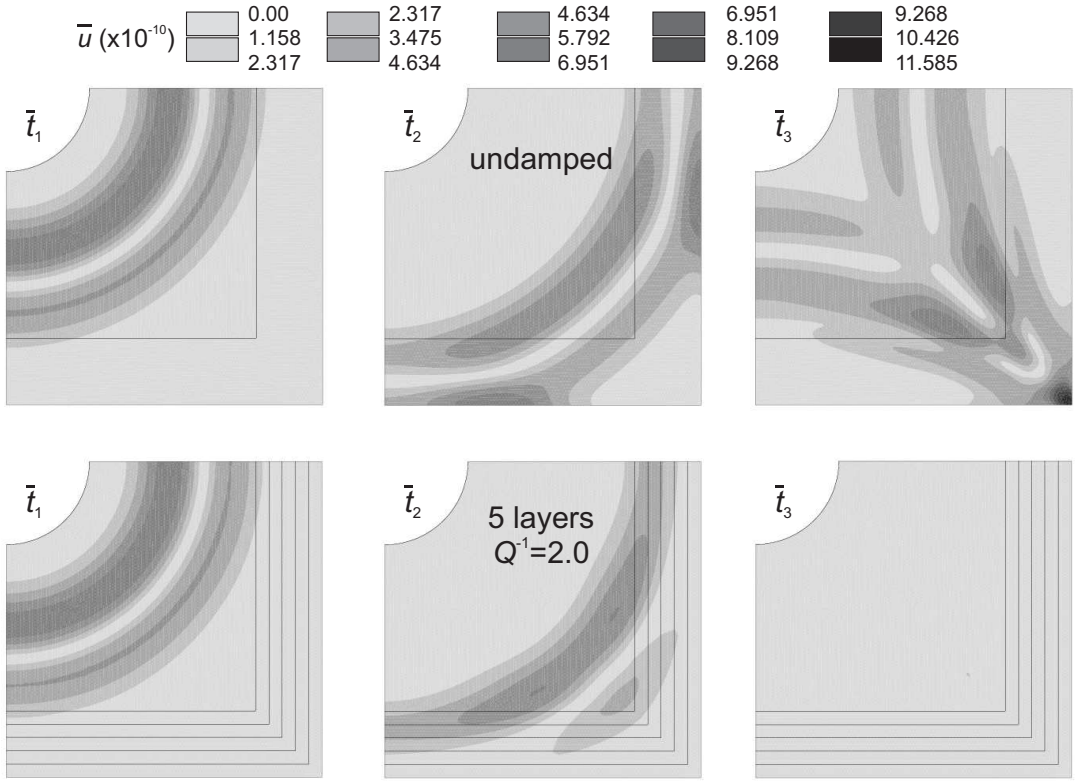

Figure 2.12: Comparison between the undamped 2D case (top) and the five layers 2D case ($Q_{min}^{-1} = 2.0$, bottom) for pure P-waves at three different times: normalized displacement at $\overline{t}_1 = t_1/t_p = 2.49$ (left); $\overline{t}_2 = t_2/t_p = 3.32$ (centre) and $\overline{t}_3 = t_3/t_p = 4.56$ (right).

duration is larger than in the 1D case and the previous 2D case. The element size, $\lambda/20$, is identical to that of the 1D case.

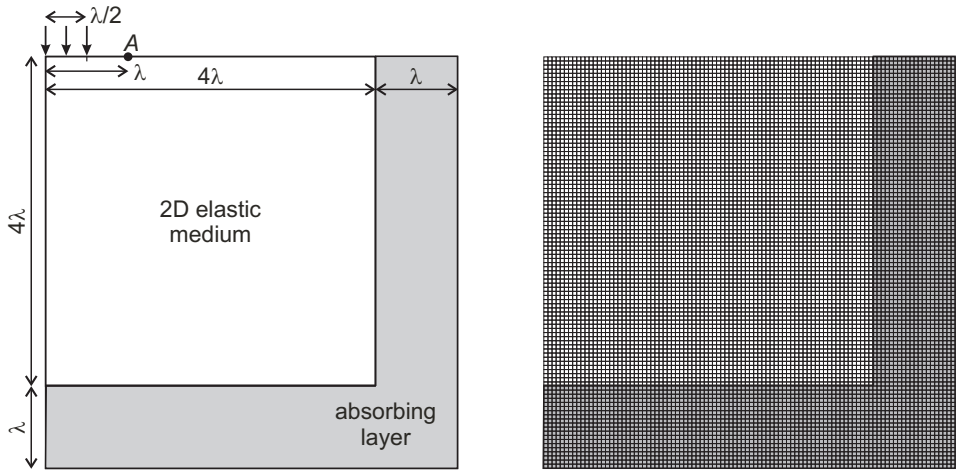

Figure 2.13: Schematic of the 2D plane strain model (left) showing the boundary condition (top) and finite element mesh (right).

It should be noticed that the total storage will be significantly increased but it is nevertheless independent of the model size and the relative storage amount will thus be smaller for a larger model.

The efficiency of the homogeneous, heterogeneous and continuous damped cases will be assessed in the whole model (isovalues plots at some selected times) and at point A along the

free surface (normalized displacement vs normalized time).

2.6.1 Efficiency of the homogeneous absorbing layers

The results obtained in the homogeneous case are displayed in Fig.2.14 in terms of normalized displacement (norm of the displacement vector divided by the maximum amplitude in the undamped case at the same time) at three different normalized times ($\overline{t}_1 = 4.15$, $\overline{t}_2 = 9.135$ and $\overline{t}_3 = 14.1$). For this displacement isovalue scale ($0.0 \leqslant \overline{u} \leqslant 0.6$), the reflected waves are obvious in the undamped case (top). For both homogeneously damped cases (middle and bottom), when compared to the amplitudes of the undamped case, the first reflections are not significant at time $\overline{t}_2$ (only the incident wavefield is present in this plot) and no reflection at all can be identified at time $\overline{t}_3$. The efficiency of the *CALM* thus appears satisfactory in the 2D homogeneous case.

As the displacement isovalues scale is rather large in Fig.2.14, a narrower scale will now be considered to compare the various cases in detail.

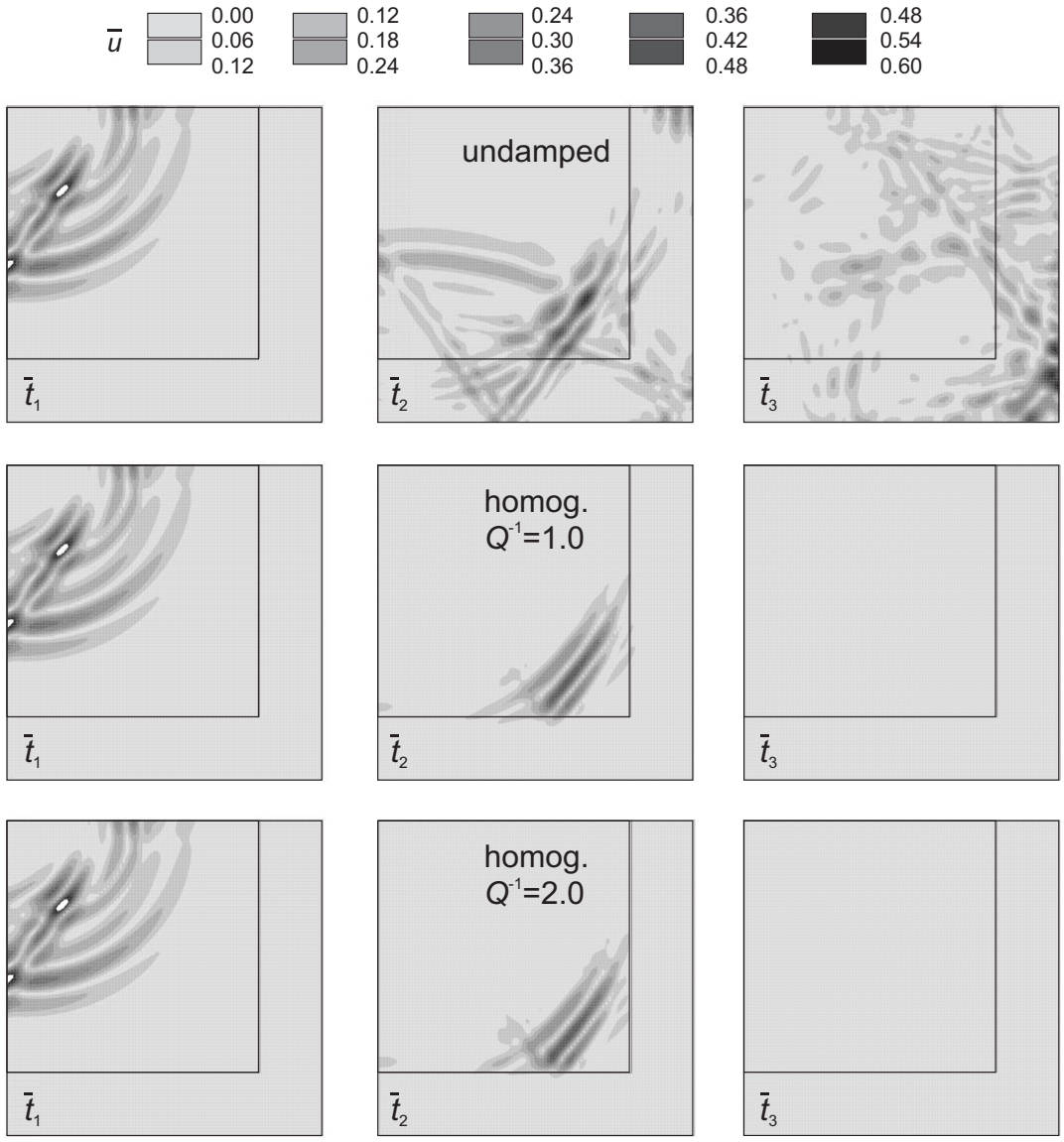

Figure 2.14: Comparison between the undamped 2D case (top) and the homogeneous 2D case ($Q_{min}^{-1} = 1.0$, middle; $Q_{min}^{-1} = 2.0$, bottom) at three different times: normalized displacement at $\overline{t}_1 = t_1/t_p = 4.15$ (left); $\overline{t}_2 = t_2/t_p = 9.13$ (centre); $\overline{t}_3 = t_3/t_p = 14.1$ (right).

The numerical results at time $\overline{t}_3$ are displayed in Fig.2.15 considering a displacement am-

plitude range $0.0 \leqslant \overline{u} \leqslant 0.02$ (some values above this range are displayed in white). In the homogeneous case (top), the relative amplitude of the reflected wave is small for $Q_{min}^{-1} = 0.5$ (2.48% of the maximum amplitude obtained in the undamped case (Fig.2.15 top left)). For larger damping values ($Q_{min}^{-1} = 1.0$: top centre and $Q_{min}^{-1} = 2.0$: top right), the homogeneously absorbing layer system leads to larger amplitudes of the reflected waves (4.67% and 10.4% respectively) probably due to the velocity contrast at the interface (see results from the 1D case).

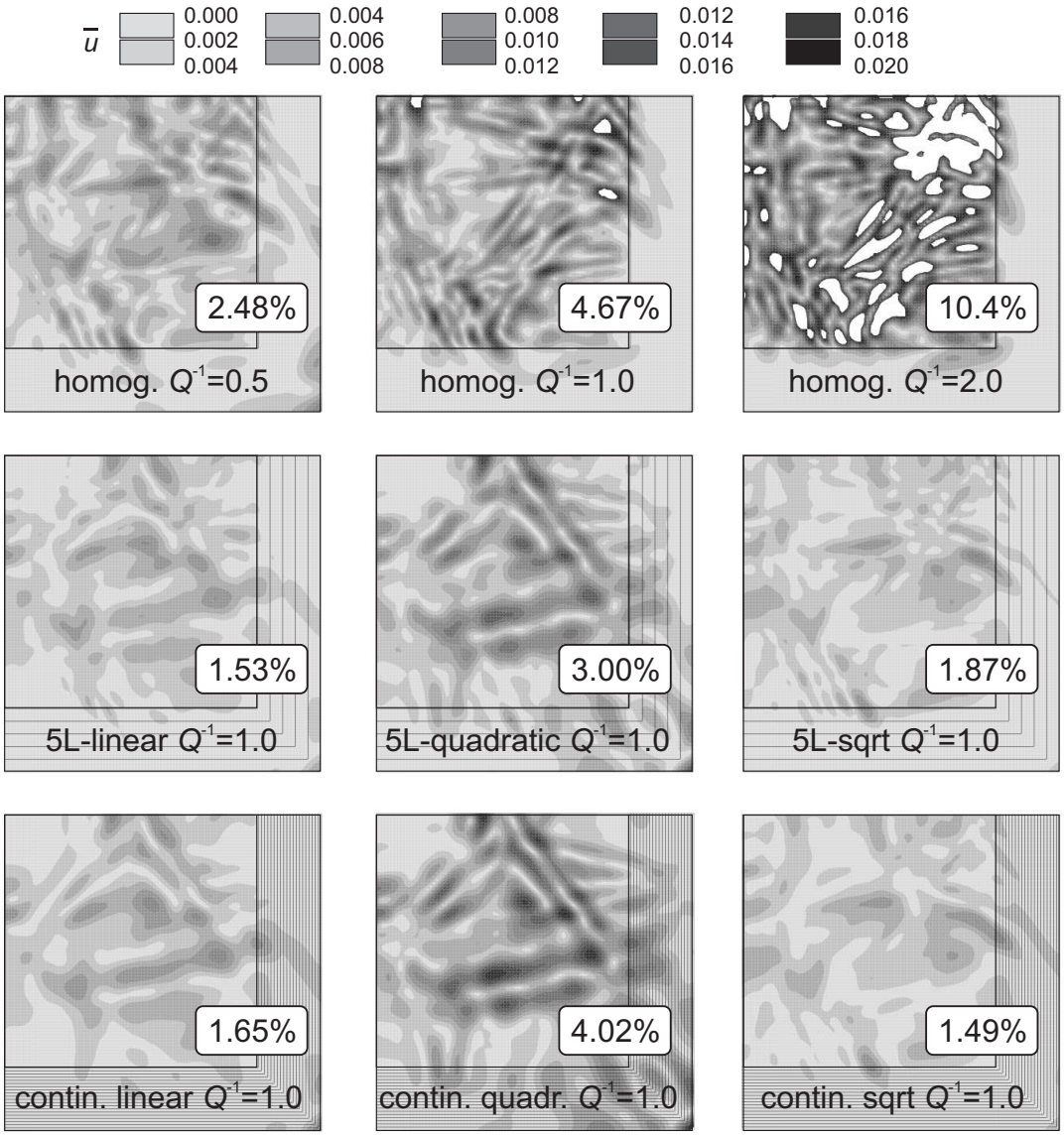

Figure 2.15: Comparison between homogeneous (top), heterogeneous (five layers, middle) and continuous (bottom) 2D cases at normalized time $\overline{t}_3 = t_3/t_p = 14.1$. Maximum relative amplitude of the reflected waves in %.

2.6.2 Efficiency of the heterogeneous absorbing layers

For the heterogeneous case, five absorbing layers are considered at the medium boundaries (bottom and right). In order to assess the influence of the damping variations, the linear increase (already studied in the 1D case) is now compared to a quadratic and a square root law. The numerical results of the heterogeneous cases at time are displayed in Fig.2.15 (middle). The amplitude of the reflected wave is very small for the linear and square root laws (1.53% and 1.87% respectively) and a bit larger for the quadratic law (3.00%). The discrepancy is due to

the slower increase of damping obtained with the latter.

2.6.3 Efficiency of the continuous absorbing layers

For the continuous case, the linear increase of damping is again compared to a quadratic and a square root law. The numerical results of the continuous cases at time $\overline{t}_3$ are displayed in Fig.2.15 (bottom). As for the heterogeneous case, the amplitude of the reflected wave is very small for the linear and square root laws (1.65% and 1.49% respectively) and a bit larger for the quadratic law (4.02%). The square root law leads to a faster damping increase near the interface and works better in the continuous case due to the regular increase of damping in the absorbing layer system (when compared to the piecewise constant damping in the heterogeneous case).

2.6.4 Influence of the damping variations in the continuous layers

To assess the influence of the damping variations in the continuous case for various maximum attenuation Q_{min}^{-1}, the maximum relative amplitude of the reflected waves are compared in Fig.2.16. The homogeneous case (a) for $Q_{min}^{-1} = 2.0$ leads to a large amplitude (10.4%). For $Q_{min}^{-1} = 1.0$ (b,c), the values were already discussed in the two previous paragraphs (best solutions with the linear and the square root laws). From additional simulations with $Q_{min}^{-1} = 2.0$ (d,e), the square root law appears as the worst solution (3.39% and 2.66% resp.) since the quadratic case gives much better results (2.30% and 2.20% resp.) than for $Q_{min}^{-1} = 1.0$ (3.00% and 4.02% resp.). The continuous case (e) improves significantly the results for the different laws (when compared to the heterogeneous case (d)) due to the smoother description of the damping variations in the absorbing layer.

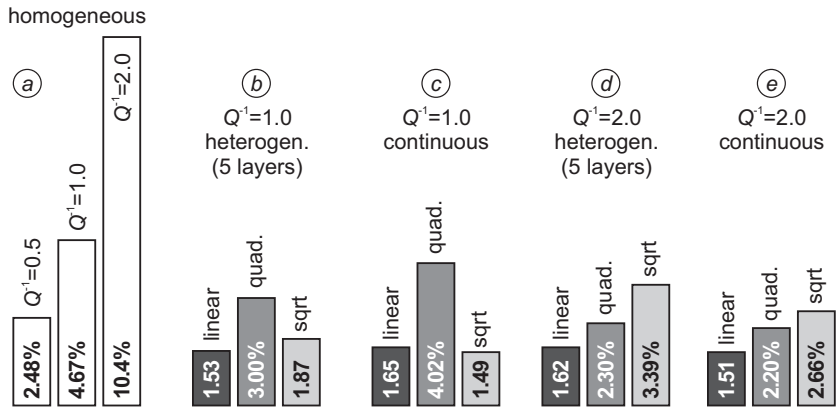

Figure 2.16: Comparison between homogeneous 2D cases (a), heterogeneous (b), (d) and continuous (c), (e) 2D cases with various laws at normalized time $\overline{t}_3 = t_3/t_p = 14.1$ in terms of maximum relative amplitude of the reflected waves.

2.6.5 Efficiency of Caughey absorbing layer for surface waves

To assess the efficiency of the Caughey Absorbing Layer Method for surface waves, the numerical results at point A are now displayed in terms of normalized displacement vs normalized time (Fig.2.17). All 2D cases are considered: homogeneous case (top); heterogeneous and continuous case for $Q_{min}^{-1} = 1.0$ (middle); heterogeneous and continuous case for $Q_{min}^{-1} = 2.0$ (bottom). As in the 1D case, the reflections at the interface and at the medium boundaries are quantified in terms of maximum relative amplitude.

In the homogeneous case (Fig.2.17, top), the reflected surface waves have large amplitudes when compared to the undamped case (5.60% to 22.9%).

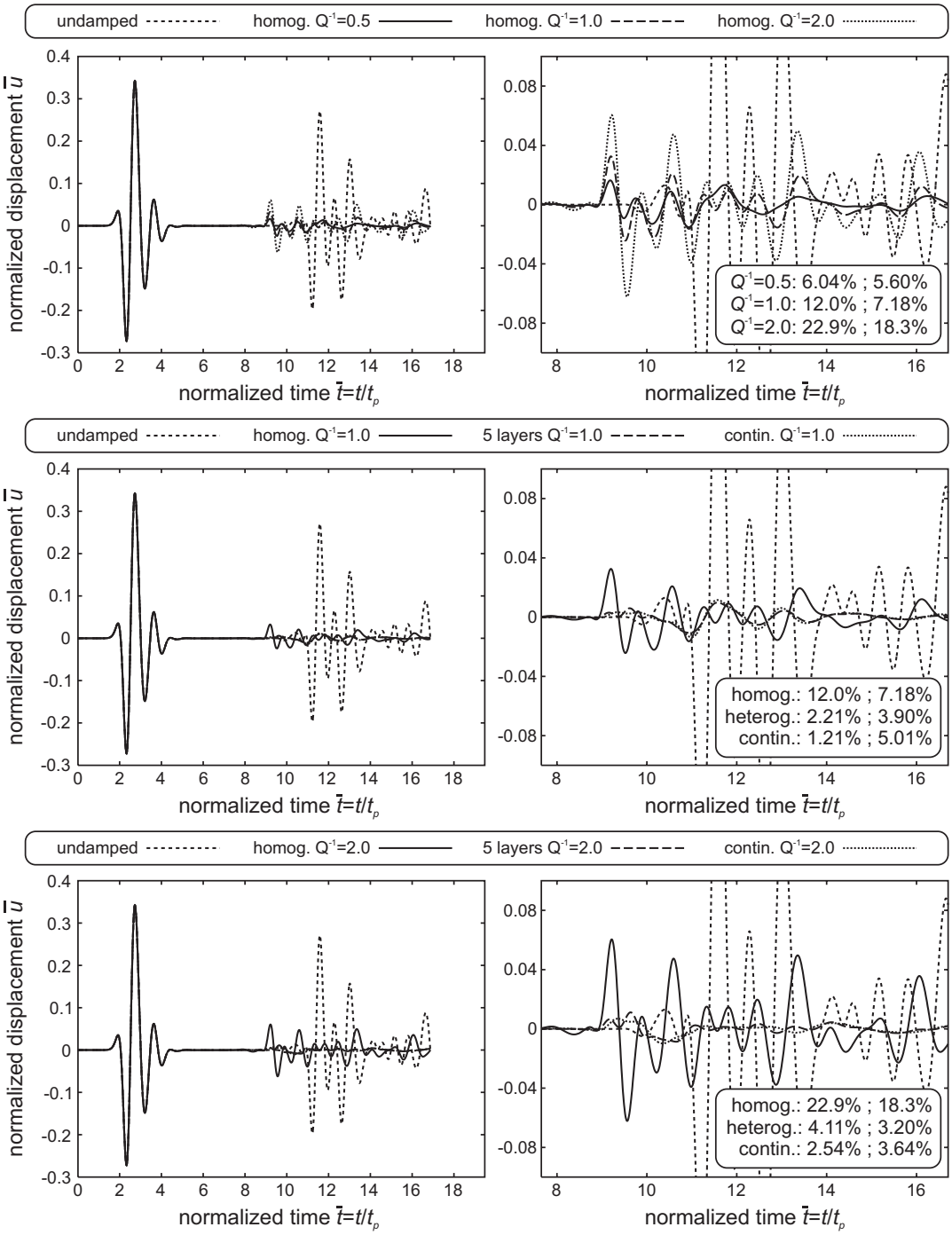

Figure 2.17: Comparison between homogeneous, heterogeneous and continuous 2D cases at point A (surface): curves and maximum relative amplitude of the reflected waves.

In the heterogeneous and continuous case for =1.0 (Fig.2.17, middle), the reflection at the interface leads to low amplitudes (2.21% and 1.21% resp.) whereas the reflections at the medium boundaries are a bit larger (3.90% and 5.01% resp.). As shown by the time histories, the variations with time are strong and it is difficult to quantify an overall maximum amplitude in both time (Fig.2.17) and space (Fig.2.15).

In the heterogeneous and continuous case for$Q_{min}^{-1} = 2.0$ (Fig.2.17, bottom), the reflection at the interface leads to low amplitudes (4.11% and 2.54% resp.) and the reflections at the medium boundaries are also small (3.20% and 3.64% resp.). For such a maximum damping value, the continuous case is more efficient than the heterogeneous case.

As this 2D case involves various incidences, polarizations and wave types, the overall efficiency of the proposed method may thus be considered as satisfactory.

2.7 Conclusion

The main conclusion of this chapter is that the *CALM* (at least the second-order *CALM* discussed herein) is reliable to reduce the spurious elastic wave reflections in Finite Element computations. Furthermore, when compared to PML techniques or viscoelastic mechanical models, it is very easy to implement (damping matrix directly computed from the stiffness and mass matrices) or even already available in most of general purpose Finite Element codes.

From the simple 2D simulations (pure P-waves), our results are at the same level as the 3rd order PML technique proposed by Festa and Vilotte (2005) but our method needs a larger additional storage (thicker absorbing layers). For more complex 2D wavefields, the efficiency of the Caughey Absorbing Layer Method is also shown to be satisfactory. In such complex cases, the best efficiency of the *CALM* is reached for a damping variation up to $Q_{min}^{-1} = 1.0$ defined by a linear function in the heterogeneous case (5 layers with piecewise constant damping) and linear as well as square root function in the continuous case (1.53%, 1.65% and 1.49% resp.).

In future work, it will be necessary to assess the efficiency of the *CALM* in 3D realistic cases and to make some detailed comparisons with other existing methods (e.g. PMLs). It may also be useful to consider higher order Caughey damping (Equation 2.5) leading to various types of damping-frequency variations. In addition to the Finite Element Method, the *CALM* may be considered in the framework of other numerical methods such as the Spectral Element Method (Faccioli et al., 1997; Komatitsch et al., 1999).

Chapter 3

Nonlinear behavior of soils and constitutive models

Contents

3.1 Introduction

Soils are complex materials whose dynamical behavior constitutes focus of attraction to several branches of nonlinear dynamics. The study of the evolution of the stress and strain during seismic events is important provided that the resulting ground motion at the surface can be strongly modified when passing from linear to nonlinear behavior.

The evidence of nonlinear soil behavior comes from experimental cyclic tests on soil samples where it is observed departure from the linear state as well as hysteresis when large strains are produced. While nonlinearity in seismic ground motion is often inferred, there are only few cases where nonlinearity has been directly observed in strong ground motion accelerograms. Among the clearest examples of nonlinear response are the Port Island borehole records of the 1995 Hyogoken Nanbu (Kobe) earthquake (Bonilla, 2000).

The goal of this work is to investigate the effect of soil nonlinearity on dynamic soil-structure interaction. Therefore, a nonlinear constitutive model is required for soil to represent this nonlinearity. This chapter is dedicated to the nonlinear behavior of soils and soil constitutive models.

A review of various existing soils constitutive models, from linear to nonlinear is presented in §3.2. In this section we will talk about different approaches to model the soil nonlinearity, and particularly the nonlinear model that is selected in this work. This nonlinear model was initially proposed by Iwan (1967). The theoretical aspects of this model and its implementation to the CESAR-LCPC numerical program are presented in §3.3. The implemented model is numerically verified by means of different analyses. The results are compared with other numerical tools in time and frequency domains (§3.4).

3.2 Review of various constitutive models

3.2.1 From linear to nonlinear behavior

Sediments were recognized to amplify earthquake ground motion at least 100 years ago but there is still a lingering uncertainty as to whether the degree of amplification varies with the level of the input motion. This issue remains as one of the most important questions related to the understanding and prediction of the earthquake ground motion (Field et al., 1998).

In accordance with the conservation of energy, seismic wave amplification generally increases in sediments due to lower densities and/or seismic velocities. In addition, resonance effects can occur where abrupt impedance contrast exist. If sediments were perfectly elastic, their response would be independent of the amplitudes of the incident wave. However, as with any real material, sediments begin to yield at some level of strain, and this violation of Hooke's law will give rise to a nonlinear response (Field et al., 1998).

The engineering community has long believed that soil nonlinearity is significant. This perspective was based almost entirely on laboratory studies such as cyclic tests on soil samples, where observed stress-strain loops imply a reduced effective shear modulus and an increased damping at higher levels of strain, e.g. Hardin and Drnevich (1972a), Hardin and Drnevich (1972b) and Vucetic (1990).

There are also evidences, that nonlinearity can be directly observed in acceleration time histories such as those recorded at the Wildlife Refuge and Kushiro Port downhole arrays from the 1987 Superstition Hills, California, and the 1993 Kushiro-Oki, Japan, earthquakes, respectively (Bonilla et al., 2005).

Since the late 1960's, considerable attention has been given to the development of constitutive equations for soils, but although many different models have been proposed, there is not yet firm agreement among researchers (Prevost and Popescu, 1996; Muravskii and Frydman, 1998). As stated by Chandrakant Desai: *Soil models are like religion. Everyone believes in his own but not in anyone-else's* (Pyke, 2004).

The first techniques used for dynamic soil analysis were linear and equivalent-linear methods. They utilized equivalent dynamic stiffness and hysteretic damping ratio as soil parameters. There are also the nonlinear elastic or viscoelastic models such as Delépine et al. (2009) as the attempts to improve the linear-equivalent models. Development of computational means promoted the use of powerful numerical techniques for dynamic soil analysis, such as a step-by-step integration or true nonlinear methods. These methods involve tangent dynamic stiffness rather than the equivalent (secant) value. The tangent stiffness dependency on the shear strain amplitude, γ, can, in principle, be obtained from the experimental equivalent (secant) stiffness-strain relationship (Puzrin and Shiran, 2000a). There is also nonlinear elastic models such as that are between

It is well established in geotechnical engineering that the soil response is nonlinear beyond a certain strain level (Beresnev and Wen, 1996). Once shear strains exceed about 10^{-5}(Assimaki et al., 2000) or 10^{-6}(Fahey, 1992) (referred to as the linear threshold), the stress-strain behavior of soils becomes increasingly nonlinear, and there is no unique way of defining shear modulus or damping. Therefore, any approach to characterize the soil for analyses of cyclic loading of larger intensity must account for the level of cyclic strain excursions. Figure 3.1 illustrates the limits of different analysis methods based on the cyclic strain.

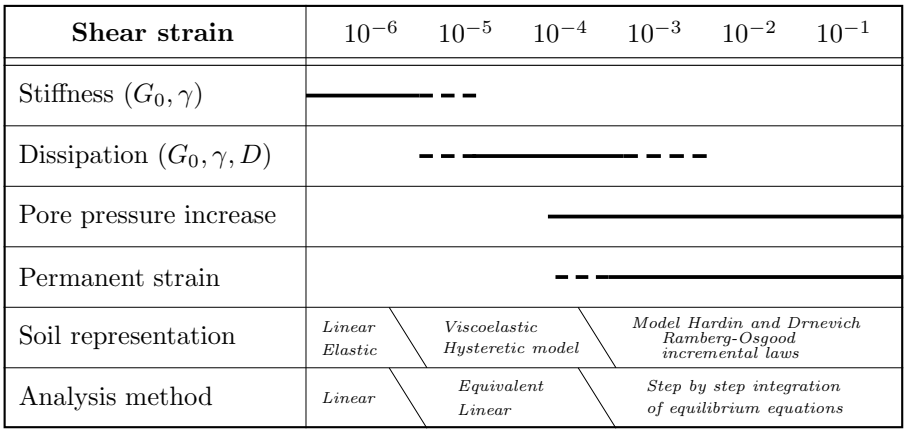

Figure 3.1: constitutive models and analysis methods function of cyclic strain (After Hujeux (1985))

3.2.1.1 Different approaches

In general, two approaches are conventionally used to model nonlinear cyclic soil stress-strain behavior: equivalent linear and truly nonlinear. The equivalent linear approach approximates a second-order nonlinear equation by a linear equation expressed in terms of an effective shear strain. This approach has the advantage of mathematical simplicity and the preservation of the principle of superposition, but has the disadvantage of giving poor predictions at large strains and inability to model plastic deformation and/or failure (Borja et al., 2000). The ability to represent the development or permanent strains is one of the most important advantages of cyclic nonlinear models over equivalent linear models. The ability to compute changes in pore pressure, hence also changes in effective stress, represents another significant advantage of cyclic nonlinear models (Kramer, 1996).

3.2.1.2 Different types of problem

Kramer (2006) believes that nonlinear site response analyses can be used to address the two main types of problems in geotechnical earthquake engineering, response problems and ground failure problems, which can be distinguished on the basis of permanent deformations. For response

problems, permanent deformations are insignificant and they deal with the estimation of the the amplitude, frequency content, phasing, and duration of ground motions. Response problems typically arise in sites with level ground surfaces and can be addressed with equivalent linear or nonlinear analyses.

Ground failure problems are those in which permanent deformations are significant and may control the performance of structures and facilities of interest. Ground failure problems involve initial, static stresses and therefore are frequently associated with sloping or irregular ground surfaces or with the presence of structures. Direct analysis of ground failure problems requires nonlinear analyses. Advances in the treatment of both types of problems will require the verification of nonlinear analyses.

3.2.1.3 Soil nonlinearity modeling

Most of the studies about soil nonlinearity can be investigated by simple state equations with few parameters to complex formulations with several parameters. In general these models can be divided into two groups. One group consists of true tensorial models (advanced constitutive models) which establish a relationship between the rates (or the increments) of the strain and stress tensors (for example Hujeux (1985)). The most accurate and general methods to model the soil behavior are based on advanced constitutive models that use basic principles of mechanics to describe the observed soil behavior for a) general initial stress conditions, b) a wide variety of stress paths, c) rotating principal stress axes, d) cyclic or monotonic loading, e) high or low strain rates, and f) drained or undrained conditions.

Such models generally require a yield surface that describes the limiting stress conditions for which elastic behavior is observed, a hardening law that describes changes in the size and shape of the yield surface as plastic deformation occurs, and a flow rule that relates increments of plastic strain to increments of stress.

Although advanced constitutive models allow considerable flexibility and generality in modeling the response of soils to cyclic loading, their description usually requires many more parameters than equivalent linear models or cyclic nonlinear models (mechanical models). Evaluation of these parameters can be difficult, and the parameters obtained from one type of test can be different from those obtained from another one (Kramer, 1996). For example, Fig.3.2 displays the shear modulus reduction curve obtained for Toyoura sand with different tests in various strain ranges (Andria-Ntoanina, 2011). Although the advanced models establish a tensorial strain-stress relationship, they are usually calibrated only against the coaxial or simple shear deformation (Osinov, 2003).

In many practical cases such as level ground response analyses, the problem under study is restricted to one spatial dimension, and the soil is deformed in simple-shear conditions. In such cases it may be more reliable to construct a constitutive model considering only the strain and stress components involved in the problem, rather than using the general tensorial representation. Such models (usually called nonlinear cyclic models or mechanical models) comprise the second group. Besides the fact that such models are usually simpler than tensorial ones, they have the advantage that the experimental data used for the calibration represent the same type of deformation (cyclic simple shear). In the two next sections we will review a brief history of these two model types.

3.2.2 Mechanical models or phenomenological models

The development and the use of these models for the dynamic site response analyses began in the 1970s and currently continues, but these models originate in the work of Masing (1926). Nonlinear site response studies have mostly been approached by using constitutive equations for the so-called Masing rules. The Masing rules describe the stress-strain path at any given time. His work was as early as 1926 to make some general statements about the behavior of materials subjected to cyclic loading. He suggested the following two rules (Pyke, 1979):

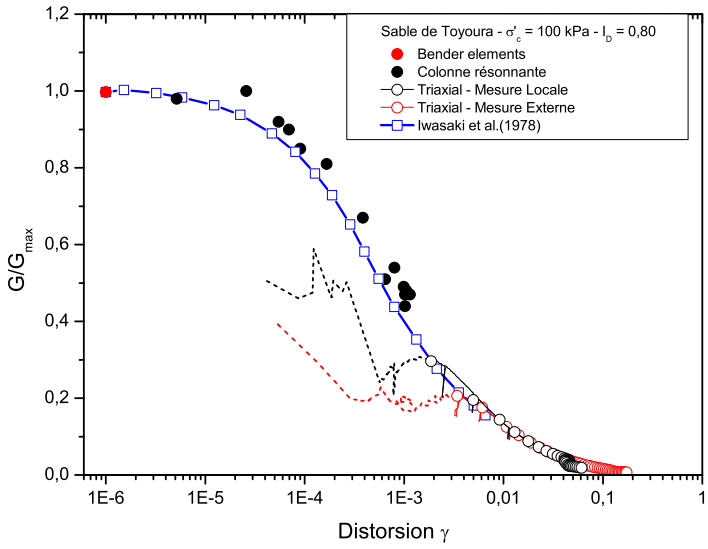

Figure 3.2: Shear modulus reduction curve obtained with different laboratory tests, After Andria-Ntoanina (2011)

- For the initial loading, the stress-strain curve follows the backbone curve (static monotonic stress-strain behavior, see §3.2.4). Fig.3.3
- The shape of the unloading or reloading curves is the same as that of the initial loading curve, except that the scale is enlarged by a factor of two. This operation is mathematically represented as

$$\frac{\tau - \tau_r}{2} = F_{bb}\left(\frac{\gamma - \gamma_r}{2}\right) \tag{3.1}$$

where τ_r and γ_r are the reversal stress and strain when passing from loading to unloading and vice-versa and F_{bb} is the backbone curve.

In Masing's original work, which was concerned with the value of the proportional limit of brass under cyclic loading, application of the second rule did not give an especially good fit to experimental data (Pyke, 1979). Also, if keeping the two previous rules for irregular loading, the computed stress may exceed the maximum shear stress τ_{max} (Bonilla, 2000). However, τ_{max} may be exceeded only at large strains, thus the equation is what happens at all strain levels.

Several authors tried to solve this problem by adding the so-called extended Masing rules (Bonilla, 2000) which state,

- The unloading and reloading paths follow the backbone curve if the previous maximum shear stress is exceeded (Fig.3.4).
- If the current unloading and reloading curve intersects the curve described by a previous loading or reloading process, the stress-strain path follows the previous curve.

Another solution is to use other factor than 2 in the second Masing rule, so

$$\frac{\tau - \tau_r}{c_H} = F_{bb}\left(\frac{\gamma - \gamma_r}{c_H}\right) \tag{3.2}$$

where c_H is the hysteresis scale factor. The first work on controlling the hysteresis scale factor is probably by Pyke (1979). He modifies the Masing rules such as the hysteresis scale

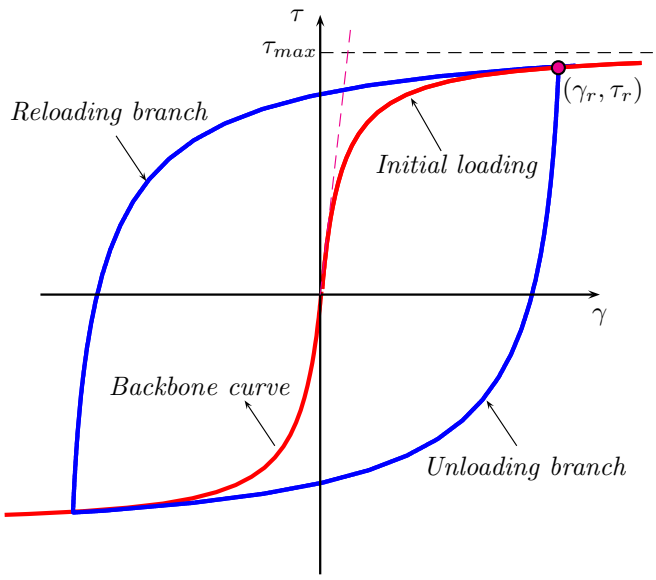

Figure 3.3: Hyperbolic model of a stress-strain curve for a soil under cyclic loads. The red line displays the monotonic stress-strain curve, known as the backbone curve and represents the hyperbolic model. The slope of the dashed magenta line represents G_0. The loading and unloading branches have also the same shape but translated as described by Masing rules. The point (γ_r, τ_r) displays the point where the path reverses from loading to unloading.

factor is no longer two, but instead it depends on the maximum strength of the material τ_{max} such as

$$c_H = \left| \pm 1 - \frac{\tau_r}{\tau_{max}} \right| \tag{3.3}$$

This operator is known as the Cundall-Pyke hypothesis (Bonilla, 2000). This hypothesis operator makes no use of the extended Masing rules. The stress is always bounded by the backbone so that it will never exceed τ_{max}. However, for large strains the amplitude of the computed stress may be considerably lower than the one predicted by the backbone curve.

The third and fourth rules require that the model memorizes the coordinates of the greatest excursion in either direction and the coordinates of all reversal points in a sequence with descending amplitudes (Pyke, 1979). In the Cundall-Pyke hypothesis, an element of soil is aware only of the last reversal point.

Bonilla (2000) developed a Generalized Masing rule, a constraint on c_H such as the computed stress trajectory is always bounded by $\pm\tau_{max}$. This model depends on one single parameter γ_{rj} (the strain where the reversal occurs at time t_j, which can be calibrated from laboratory data to account for realistic damping ratios at large strains. The original Masing rules and the Cundall-Pyke hypothesis are subsets of this model.

Idriss et al. (1978) proposed to consider the first two original Masing rules in conjunction with a cyclic degradation model, to take into account the effect of the cyclic stiffness degradation. Their model was based on the results of a series of uniform cyclic strain-controlled tests, that is, tests with a constant cyclic strain amplitude. This model was originally proposed for normally consolidated clays, and was later extended to over-consolidated clays.

In the case of clays, the above four rules are still not sufficient for a complete characterization (Vucetic, 1990). According to Vucetic, the combination of non-symmetric and nonuniform consecutive cycles show that one more rule is required for a complete characterization of the irregular cyclic behavior of clay. Therefore, he proposed that if the subsequent reloading curve goes beyond the maximum shear strain applied in the previous cycle, it will continue beyond

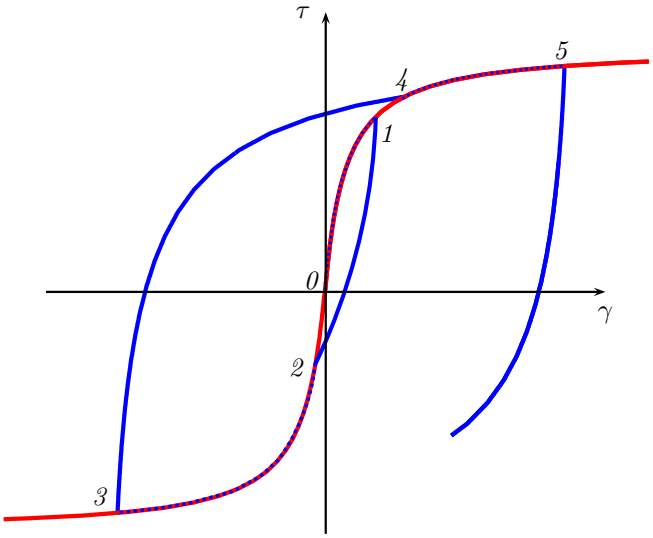

Figure 3.4: Effect of the first extended Masing rule when irregular loading is applied. The red line represents the backbone curve. The blue dashed line represents the computed stress following the backbone only. Note that during the intersections between the computed stress and the backbone curve (2-3 and 4-5 sections in dashed lines), both curves are the same.

the tip of the previous loop along the path that has a shape identical to the shape of a section of the associated degraded reloading curve. This section is defined by the following two steps :

- The associated degraded reloading curve is translated with its initial reversal point onto the initial point of the subsequent reloading curve, then,
- It is further translated horizontally so that it passes through the tip of the previous loop. The same applies to the subsequent unloading curve in connection with the previous unloading curve.

Muravskii (2001) shows in his work that experimental results on stiffness and damping corresponding to cyclic deformation of soils can be well approached theoretically on an interval of strain variation from zero to arbitrary large values of strains. For this purpose, the following two methods are recommended: a modification of the hysteretic model obeying Masing's rule by adding elastic stresses to pure hysteretic stresses that do not change the corresponding backbone curve; and, as the second method, a non-linear model with frequency independent loss of energy in periodic processes. It is shown that in the area close to the free surface of soil, normalized strains resulting from propagation of seismic waves can be very large, even in the case of an input motion of relatively low intensity.

Pyke (2004) demonstrated that not only the second Masing's rule is not correct, the first Masing hypothesis is also invalid. Through no fault of Masing, adoption of his hypotheses has been one of the obstacles to better modeling of the nonlinear behavior of soils. Because it was written in German, it seems that few modern workers have ever read his paper. It describes his hypothesis, a simple experiment to test it, and concludes that the hypothesis is not supported by the experiment! Pyke (2004) divided the limitation of early models in 4 parts:

- They tended to observe the Masing rules which not only make fitting of real soil behavior more difficult in general but specifically prevents the development of permanent strains in cases where there is an initial shear stress in the direction of the subsequent cyclic loading. This limitation is not critical in one-dimensional analyses whose sole purpose is to compute the site response, but it is critical in one, two or three-dimensional analyses that are intended to compute permanent deformations, which is one of the goals of nonlinear

analyses. In a nonlinear analysis in which the material model complies with the second Masing hypothesis, the computed deformations will result solely from the irregularities in the input motion rather than from the material behavior.

- They tended not to follow the degradation (flattening of the secant modulus) and degeneration (change of shape) that occurs in the stress-strain relationships of most soils under cyclic loading. Again, this may not be critical in analyses whose sole purpose is to compute site response as indicated by response spectra but it may be critical to the computation of displacement profiles and displacement histories, which are increasingly required as the input to more sophisticated soil-structure interaction analyses.

- They did not produce the small strain damping that is observed in element tests and implied by field measurements. This may not be significant in analyses of site response for strong ground motions but may be for analyses of weak motions.

- They almost universally produced more damping at moderate to large strains than is observed in element tests. However, it is not clear whether this is always a significant shortcoming in nonlinear analyses since some nonlinear models that generate higher damping than observed in element tests have performed well in back-calculations of the motions recorded in vertical arrays.

3.2.3 Advanced constitutive models based on plasticity theory

Iwan (1967) proposed a class of physically motivated models for the rate independent hysteretic behavior of both continuous and composite systems. It was shown that this class of models provides a bridge between empirical initial loading data and the analysis of the steady-state and transient cyclic behavior of hysteretic systems. A feature of the Iwan models under irregular loadings is that once the array of elements has been programmed, the model automatically does the bookkeeping required to comply with the third and fourth of the extended Masing rules (Pyke, 1979), i.e., the Iwan models inherently have the capacity to memorize relevant portions of the past loading history. When coupled with their flexibility to model arbitrary stress-strain curves to any desired degree of accuracy, this makes the Iwan models very attractive for nonlinear use in one-dimensional nonlinear analysis. Furthermore, the Iwan models can be extended to two and three dimensions within the framework of the incremental theory of plasticity to provide attractive models of more general stress-strain behavior under cyclic loading but according to Prevost and Popescu (1996) these theories suffer inherent limitations namely: storage requirements for the multi-surface theory. The Iwan model will be presented in details in §3.2.5.

Prevost (1978) presented a model for soils within the general framework of the formalism of the plasticity theory. The model combines the properties of isotropic and kinematic plasticity, and allows for the adjustment of the hardening rule to any kind of experimental hardening law by using a collection of nested yield surfaces. For any loading (or unloading) history, the instantaneous configuration of the field of yield surfaces is determined by calculating the translation and contraction (or expansion) of each yield surface during successive changes of loading. The material behavior can thus be determined for complex, and, in particular, for cyclic loading paths. Specific hardening rules are proposed to describe the soil behavior under both drained and undrained loading conditions. It is shown that the model parameters required to characterize the behavior of any given soil can be derived entirely from the results of conventional consolidation and axial undrained soil tests.

Ramsamooj and Alwash (1990) developed Prevost (1978) model. However, their model is simpler, uses fewer parameters, and introduces several new concepts. Specifically, the similarities include the use of multi-yield surfaces, volumetric strain hardening, the same expression for the plastic modulus, and a kinematic rule for the movement of the $x-$coordinates of the centers of the yield surfaces for undrained loading. The dissimilarities arise from the use of

isotropic hardening for drained loading and a combination of isotropic and kinematic hardening for undrained loading.

In 1985, a simple elastic-plastic constitutive model for cohesionless soils is proposed by Prevost (1985). The model retains the extreme versatility and accuracy of the simple multi-surface theory in describing observed shear nonlinear hysteretic behavior, shear stress-induced anisotropy; and reflects the strong dilatancy dependency on the effective stress ratio. The theory is applicable to general three-dimensional stress-strain conditions, its parameters can be derived entirely from the results of conventional laboratory soil tests. (Elgamal et al., 2003) also developed Prevost (1985) model. Motivated by experimental observations, they developed this plasticity model for capturing the characteristics of cyclic mobility. This model extends an existing multi-surface plasticity formulation with newly developed flow and hardening rules. The new flow rule allows for reproducing cyclic shear strain accumulation.

A stress-strain model for soil, called as multi-spring model, was proposed by Towhata and Ishihara (1985). It consists of an infinite number of nonlinear springs and can take into account the effects of principal stress axes rotation. The deformation characteristics of springs are related to the stiffness and strength of soil by the hyperbolic model (Kondner, 1963), enabling a prediction of soil behavior under plane-strain conditions.

Iai et al. (1990, 1992) proposed a cyclic mobility model based on Towhata and Ishihara (1985) model. The salient feature of this model is that the concept of the multiple mechanism, within the framework of plasticity theory defined in strain space, is used as a vehicle for decomposing the complex mechanism into a set of one dimensional mechanisms. They believed that the main problem of the previous proposed model to simulate the cyclic behavior of sand was the numerical vulnerability when the effective stress path becomes very close to the failure line. The purpose of their work was to solve this problem and to develop a useful tool for estimating earthquake induced deformation in soil structures and foundations due to the cyclic mobility (Iai et al., 1992).

In 1990, a comprehensive constitutive model for sand was formulated within the general framework of bounding surface hypoplasticity by Wang et al. (1990). The distinctive feature of this model is the dependence of the loading and plastic strain rate directions on the stress rate direction. This property renders the model hypoplastic. The model can simulate different features of sand behavior under various loading conditions, which range from simple monotonic to complex cyclic at different amplitudes and directions. Makdisi and Wang (2004) developed this model in three dimensions.

According to Prevost and Popescu (1996), an important theoretical development in plasticity was made simultaneously by Mroz and Iwan in 1967. They showed how continuous yielding could be represented by a set of nested yield surfaces in stress space. The notion, in combination with kinematic and isotropic hardening/softening plastic rules, can give rise to a material representation of considerable power and flexibility.

According to Muravskii and Frydman (1998), two basic approaches have commonly been employed for representing soil stress-strain behavior during cyclic loading, for application in site response analysis. The first, in which the soil is modeled by a series of springs and frictional elements (Iwan model), uses Masing's rules to establish the shape of the cyclic, hysteresis curves. This model does not normally simulate the degradation observed due to cyclic loading of soils, nor does it provide a good simulation of the observed strain dependence of the shear modulus and damping ratio. Furthermore, application of Masing's rules does not provide an adequate approximation simultaneously for shear modulus and damping ratio. In the second approach, damping is modeled as a viscous, rather than frictional, effect. This approach is adopted, for example, in SHAKE (Schnabel et al., 1972) analysis, which uses a pseudo-linear treatment, and applies an iterative procedure in order to account for the strain dependence of modulus and damping (Muravskii and Frydman, 1998).

Rao and Panda (1999) considered a different approach to modify Iwan's series-parallel model by incorporating the degradation index into it as suggested by Idriss et al. (1978). Their purpose

was to income the problem of this model that cannot take into account the stiffness degradation which is observed during cyclic loading of soft clays.

In 2000, a deviatoric bounding surface plasticity model that preserves Masing's rule and an algorithm that allows for the lack (or existence) of elastic range is formulated by Montáns (2000). This model inherits the advantages of multilayer models like Mroz's and the simplicity and continuity of the bounding surface plasticity.

In 2000, a three-dimensional bounding surface plasticity model with a vanishing elastic region capable of capturing the essential features of many one-dimensional non-linear soil models was proposed by Borja et al. (2000). The constitutive model was reformulated from a version presented previously by Borja and Amies, derived from the idea of Dafalias and Popov, and includes provisions for the translation of the bounding surface and decomposition of the response into inviscid and viscous parts. The model was formulated in terms of total stresses, and hence is appropriate for non-liquefiable soils such as partially saturated soils and clays (Borja et al., 2000).

Papadimitriou et al. (2001) proposed a plasticity constitutive model for sands. The 14-parameter model was proven to be independent of initial and drainage conditions, as well as the cyclic shear strain amplitude. Papadimitriou and Bouckovalas (2002) presented a multiaxial formulation of the aforementioned model, which is necessary for the implementation of the model in numerical codes used for solving general boundary value problems of geotechnical earthquake engineering. The model adopts a kinematic hardening circular cone as the yield surface and three non-circular conical surfaces corresponding to the deviatoric stress ratios at phase transformation, peak strength and critical state.

Osinov (2003) presented a mathematical model for the deformation of soil under irregular cyclic loading in the simple-shear conditions. The model includes the possible change in the effective pressure in saturated soil due to the cyclic shearing, the reciprocal influence of the effective pressure on the response of the soil to the shear loading, and the pore pressure dissipation due to the seepage of the pore fluid. The approach enables the constitutive functions involved in the model to be specified in various ways depending on the soil under study. The constitutive functions can be calibrated independently from the conventional cyclic shear tests. The main feature of this model is that the damping ratio produced by the hysteresis loops as a function of the strain amplitude can be prescribed independently of the form of the backbone curve (Osinov, 2003).

Bonilla et al. (2005) combined a general hysteresis formulation (Bonilla, 2000) and pore pressure generation following stress-strain constitutive models of Towhata and Ishihara (1985) and Iai et al. (1990); Iai (1991); Iai et al. (1992). These models were implemented in a nonlinear one-dimensional finite-difference code to understand the soil nonlinear behavior. This model represents the effect of rotation of principal stresses during cyclic behavior of anisotropically consolidated sands. Since the theory is a plane strain condition, it can be used to study the problems in two dimensions, for example, embankments, quay walls, among others (Bonilla et al., 2005).

Muravskii (2005) presented a modification of well known extended Masing's rules in order to provide more flexible description of stress-strain relationships of different materials. Particularly, this modification allows to control the dependence of the damping ratio on the strain amplitude in the process of cycle deforming of a material. The suggestion consists only in modifying the second Masing's rule. Classical Masing's model as well as such models as Pyke's model do not allow controlling damping ratio which in practice can be smaller than that predicted by the models. The model presented by Muravskii is intended for eliminating above shortcomings (Muravskii, 2005, 2009).

Mayama et al. (2007) presented a unified constitutive model for cyclic viscoplasticity and changes occurring in subsequent viscoplastic deformation due to the evolution of dislocation structures. This model was proposed for stainless steel.

Asik and Isbuga (2007) modified the model proposed by Joyner and Chen (1975) that is

originally based on Iwan model to include the response of the stiffer layer and additional mass placed on this layer. The response of the stiffer layer and the mass may be assumed to show the approximate behavior of a soil supporting a structure during earthquakes. Governing equations of the mathematical model can be obtained by applying variational principles and the resulting equations are solved by the finite difference procedure presented by Joyner and Chen (1975).

In 2007, a set of rules is proposed by Ashrafi and Smyth (2007), which is a generalization of the Masing rules and can capture the deteriorating (or nondeteriorating) response of distributed-element model (parallel-series Iwan model) with any distribution of element yield displacement thresholds to any arbitrary loading.

Segalman and Starr (2008) showed that for any material or structural model expressible as a Masing model, there exists a unique parallel-series (displacement-based) Iwan system that characterizes that model as a function of the displacement history. They extended the Masing hypothesis to accommodate general load/displacement histories by keeping track of excursions to new loads and of load reversals.

Lee et al. (2009) proposed a modified parallel Iwan model, which includes a cyclic hardening function. The proposed model consists of elastic-perfect plastic isotropic hardening elements. The model is able to predict cyclic hardening behavior through the adjustment of the internal slip stresses of its elements beyond the cyclic threshold, and satisfies Bauschinger's effect and the Masing rule with its own behavior characteristics. The cyclic hardening function is developed based on the irrecoverable plastic strain (accumulated shear strain) of dry sand during shearing, which is assumed to be a summation of shear strain beyond the cyclic threshold.

The ECP's elastoplastic multi-mechanism model (Aubry and Modaressi, 1992), commonly called Hujeux model (Hujeux, 1985) is used to represent the soil behaviour for investigating the dynamic soil response and nonlinear soil-structure interaction by Saez (2009). This model can take into account the soil behavior in a wide range of strains. The model is written in terms of effective stress. The representation of all irreversible phenomena is made by four coupled elementary plastic mechanisms: three plane-strain deviatoric plastic deformation mechanisms in three orthogonal planes and an isotropic one. The model uses a Coulomb type failure criterion and the critical state concept. The evolution of hardening is based on the plastic strain (deviatoric and volumetric strain for the deviatoric mechanisms and volumetric strain for the isotropic one). To take into account the cyclic behavior, a kinematic hardening based on the state variables at the last load reversal is used (Saez, 2009). The soil behavior is decomposed into pseudo-elastic, hysteretic and mobilized domains. This model has 21 parameters.

Boulanger (2010) presented a sand plasticity model for nonlinear seismic deformation analyses. The model follows the basic framework of the stress-ratio controlled, critical state compatible, bounding surface plasticity model for sand presented by Dafalias and Manzari in 2004. Modifications to the model were implemented to improve its ability to approximate the stress-strain responses important to geotechnical earthquake engineering applications; in essence, the model was calibrated at the equation level to provide for better approximation of the trends observed across a common set of experimentally and case history-based design correlations (Boulanger, 2010).

3.2.4 Representation of the shear modulus reduction curve

3.2.4.1 Definition

The locus of points corresponding to the tips of hysteresis loops of various cyclic strain amplitudes is called a *backbone* (or *skeleton*) curve (Kramer, 1996). Characterization of the stiffness of an element of soil requires consideration of both G_0 and the way the modulus ratio G/G_0 varies with cyclic strain amplitude and other parameters. The variation of the modulus ratio with shear strain is described by a modulus reduction curve. The nonlinear stress-strain behavior of soils can be represented more accurately by cyclic nonlinear models that follow the actual stress-strain path during cyclic loading. Such models are able to represent the shear strength

of the soil, and with an appropriate pore pressure generation model, changes in effective stress during undrained cyclic loading.

A variety of cyclic nonlinear models have been developed; all are characterized by 1) a backbone curve and 2) a series of rules that govern unloading-reloading behavior, stiffness degradation, and other effects (Kramer, 1996). Alternatively, backbone curves can be constructed from modulus reduction curves and vice versa.

3.2.4.2 Different types of representation

The backbone curve can be expressed in a variety of ways, either in terms of a mathematical function or in terms of discrete stress-strain coordinates. For purposes of applications in soils, several simple mathematical functions have been proposed. These include the bilinear, the multilinear, the hyperbolic, the Ramberg-Osgood and logarithmic formulations. Hyperbolic function was one of the earliest proposition presented by Kondner (1963) and Hardin and Drnevich (1972b,a). Kondner (1963) believed that the two-constant hyperbolic form of the stress-strain that he presented is such that the ultimate shear strength of the soil is contained within the general formulation and appears in the mathematical limit of the stress as the strain becomes excessive. According to Hardin and Drnevich, the original hyperbolic function of backbone curve is,

$$F_{bb}(\gamma) = \frac{G_0\gamma}{1 + (G_0/\tau_{max})|\gamma|} \tag{3.4}$$

which concludes the shear modulus reduction curve as follows,

$$G(\gamma) = \frac{G_0}{1 + |\gamma/\gamma_{ref}|} \tag{3.5}$$

where γ_{ref} is equal to τ_{max}/G_0. An example of the hyperbolic backbone curve and the shear modulus reduction curve are shown in Fig.3.5.

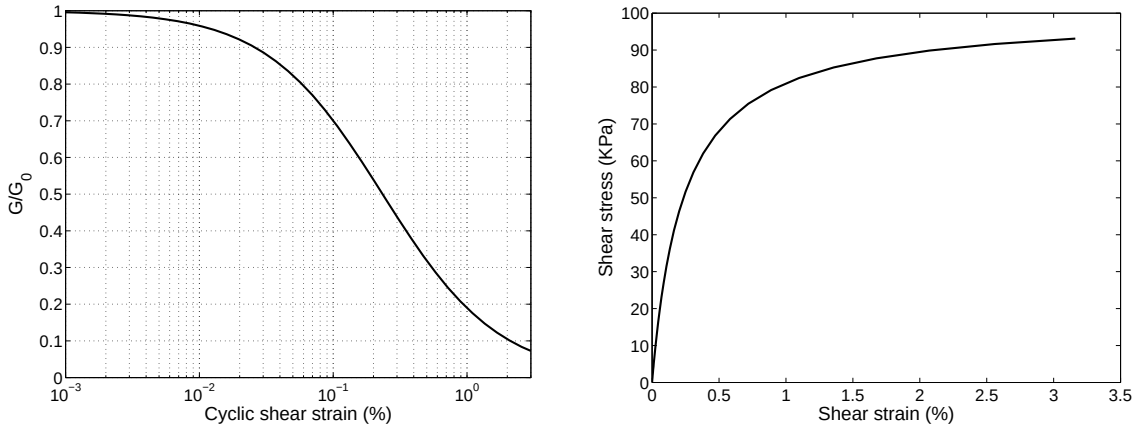

(a) G/G_0 vs. $\gamma\%$ (b) Backbone curve of the sample soil

Figure 3.5: Nonlinear properties of the soil layer including modulus reduction curve versus cyclic shear strain and monotonic loading stress-strain curve

The Ramberg-Osgood equation has been proposed to describe the nonlinear hysteretic constitutive relation of the one-dimensional elastoplastic behavior of many materials. It has been used by many researchers to model the dynamic soil behavior. Four parameters are needed in the Ramberg-Osgood equation to describe the nonlinear behavior of a material. These parameters are generally obtained based on the test data or typical relations in terms of modulus and damping ratios versus strain. The backbone (monotonic loading) strain-stress relation of the Ramberg-Osgood elastoplastic model can be expressed by (Ueng and Chen, 1992)

$$\frac{\gamma}{\gamma_{ref}} = \frac{\tau}{G_0\gamma_{ref}}\left(1+\alpha\left|\frac{\tau}{nG_0\gamma_{ref}}\right|^{r-1}\right) \tag{3.6}$$

where coefficient n is equal to 1 for initial loading and 2 for unloading and reloading (Pyke, 1979). Therefore, besides G_0, there are three parameters, γ_{ref}, α, and r to be determined for the Ramberg-Osgood model (LoPresti et al., 2006).

Idriss et al. (1978) developed a new stress-strain model based on Ramberg-Osgood model for soft clays subjected to one-dimensional undrained shear cyclic loading. This stress-strain model incorporates the nonlinear hysteretic behavior of the clay and accounts for degradation during cyclic loading. The parameters of the model can be obtained from controlled-strain tests and used to predict stress-strain response of controlled-stress tests, or an arbitrary cyclic history such as that occurring during earthquakes.

According to Pyke (1979), the Ramberg-Osgood model allows a reasonably good fit to be made to the stress-strain behavior of both soils and structural systems. However, because this model gives strains in terms of stresses and it can not be inverted, its use is somewhat inconvenient in many dynamic analysis procedures that require the stress to be expressed in terms of the strain. Another minor criticism of the Ramberg-Osgood model is that there is no bound placed on the stress for even initial loading Pyke (1979).

According to Prevost and Keane (1990), the best known and most widely used function to describe the backbone curve is hyperbolic. It is simple but unable to model failure accurately. To correct that deficiency, a modified hyperbolic function including a power term was proposed by Prevost and Keane (1990). This function was shown to offer more versatility for modeling stress-strain behavior in both monotonic and cyclic loading conditions, at both low and high strain levels.

Vucetic and Dobry (1991) performed a study on the influence of the plasticity index (PI) on the cyclic stress-strain parameters of saturated soils needed for site-response evaluations and seismic microzonation was presented. Based on the review of a number of available cyclic loading results, they concluded that the plasticity index is the main factor controlling the locations of the modulus reduction curve G/G_0 versus γ and material damping ratio curve, for a wide variety of saturated soils ranging from clays to sands. As the PI goes up, G/G_0 increases and damping is reduced.

Based on some experimental data obtained from a systematic test series of cyclic simple shear tests, Hayashi et al. (1994) showed that most of the previous hyperbolic or Ramberg-Osgood models have some specific limitations and are not versatile when applying to a) both monotonic and cyclic loading conditions, b) a wide variety of geotechnical materials including clays, sands and gravels, and c) a wide range of strain, say from 0.0001% to that at the peak of the order of 10%. Therefore, they proposed a new model based on a hyperbolic law, which is much more flexible and accurate than the above-mentioned models in fitting to the data obtained under widely varying conditions and in generating stress-strain relations under various cyclic loading conditions (Hayashi et al., 1994).

In the case of dry cohesionless soils, the physical origin of the variation in modulus and damping with cyclic strain is now well understood. Both parameters are related to the frictional behavior at the interparticle contacts and the rearrangement of the grains during cyclic loading (Ng and Dobry, 1994). The approach by Seed and Idriss in 1970 assumes that the G/G_0 and damping curves are essentially the same for sands, gravels, and cohesionless silts (Assimaki et al., 2000). Their generic response curves assume that the degradation curves are independent of the cycle number considered as well as the void ratio (or relative density, sand type, and confining pressure). However, it should be noted that all the aforementioned factors do significantly affect the maximum shear modulus G_0. Laboratory measurements provide evidence in support of some of these simplifying assumptions. They show that void ratio, overconsolidation, sand type, and cycle number do indeed have relatively small influence on the measured backbone curves.

However, the influence of the confining pressure is significant and cannot possibly be ignored, specially when performing dynamic analyses for deep soil deposits.

A number of laboratory studies on hydrostatically consolidated sands have shown by Assimaki et al. (2000) that their stress-strain response becomes more linear as the confining pressure increases. In addition, large confining pressures lead to substantial reductions in material damping at small strain. Assimaki et al. (2000) presented a simple four-parameter model that can represent the shear modulus factors and damping coefficients for a granular soil subjected to horizontal shear stresses imposed by vertically propagating shear waves. The input parameters are functions of the confining pressure and density.

The experimental data on equivalent stiffness and hysteretic damping dependency on strain amplitude has accumulated so far. Its utilization in solution of dynamic geotechnical problems requires a reliable stress-strain relationship with easily determined parameters capable of fitting experimental curves accurately. Successful search for such a relationship requires some important decisions to be made (Puzrin and Shiran, 2000a),

- in what strain range the maximum accuracy should be achieved;
- in what form the experimental stress-strain data should be presented for the curve fitting;
- what are the means to achieve, in the selected strain range, accurate predictions simultaneously for experimental data in turns of stress-strain and damping ratio.

Puzrin and Shiran (2000a) examined some existing relationships, in particular the Ramberg-Osgood relationship, mainly as an attempt to understand the reasons for its inability to provide an accurate fit to cyclic stress-strain and damping ratio data at small to medium strains. It appeared that the main reason for the limitations of the existing functions is that they fail to satisfy the specific small strain condition formulated for soils on a basis of the analysis of the small strain data from the pseudo-static cyclic tests. As an alternative, they studied a possibility to use the logarithmic function for fitting experimental relationships. Its fitting ability was evaluated against the high quality experimental data found in the literature covering a wide range of soils, sample disturbance, drainage conditions and level of strain hardening or cyclic degradation (Puzrin and Shiran, 2000a). Constructed to satisfy the formulated small strain condition for soils, this function has proven to be free from the limitations of the Ramberg-Osgood and other relationships. When applied in combination with the Masing rules to predict damping ratios, it gives a good prediction in the small to medium strain range, where the Masing hypothesis is supported by experimental evidence. They also compared the results dealing with effects of constitutive modeling on site amplification (Puzrin and Shiran, 2000b).

As damping characteristics of Masing's model result completely from the backbone curve, they cannot be regulated independently. This leads, in most cases, to an improper prediction of damping, specially for large strain amplitudes. Indeed, maximum experimental values of damping ratio (for very large amplitudes of strain) are equal approximately to 30% for different types of soils, whereas Masing's rule leads to the limit value $2/\pi$ for infinite strains and limited strength of the material (Muravskii, 2001). It should be noted that in the domain of small strain amplitudes, slight deviations in ordinates of a stress-strain curve can lead to large relative changes in values of damping ratio determined with the help of Masing's rule.

Applications of other functions known in literature such as the logarithmic function (Puzrin), function suggested by Ramberg and Osgood and Davidenkov for analytical representation of experimental data meet difficulties when the strain interval under consideration is large enough (because of insufficient number of parameters) (Muravskii, 2001). It should be noted also that, according to experimental data, the values of reference strain $\gamma_{ref} = \tau_{max}/G_0$, which are used for obtaining the normalized strain $x = \gamma/\gamma_{ref}$, tend to zero for non-cohesive soils when approaching the surface of a soil (τ_{max} is proportional to depth and G_0 is proportional to the square root of depth). Therefore, in order to be able to consider arbitrarily large values of normalized

strains, which can be encountered in seismic response analysis, Muravskii (2001) recommended to perform the normalization proposed by Hardin and Drnevich (1972b) using the failure stress τ_f instead of the stress τ_{max} (as above) and to continue the backbone curve in the area of infinite strains.

According to Osinov (2003), the model proposed by Muravskii (2001) allows us to prescribe independently the shear modulus and the damping ratio as functions of the strain amplitude. A shortcoming of this model is that the behavior of the material is not rate independent. As a consequence, the shape of a hysteresis loop for stationary cycles, when the strain $\gamma(t)$ oscillates between some γ_a and $-\gamma_a$, is determined not only by the amplitude γ_a but also by the actual shape of the function $\gamma(t)$.

Different types of monotonic stress-strain curve presented here can be used in nonlinear models. In the next section, a brief review of the cyclic nonlinear model selected in this work to investigate the soil nonlinearity is presented. Later, we will shown that the backbone curve presented in this part is the only input nonlinear property of the selected nonlinear model.

3.2.5 Iwan model (MPII model)

3.2.5.1 Presentation of the initial model

Iwan (1967) presented a class of physically motivated models for the rate independent hysteretic behavior of both continuous and composite systems. It will be shown that this class of models provides a bridge between empirical initial loading data and the analysis of the steady-state and transient cyclic behavior of hysteretic systems and, at the same time, provides a basis for comparing many of current purely empirical formulations. Since the models in their basic form are one-dimensional, they will lead to considerable simplification for problems of this type. However, the concepts of the models can easily be incorporated into the general three-dimensional incremental theory of plasticity, and it will be shown that this leads to a very straightforward method of accounting for a realistic Bauschinger effect.

Masing used the parallel-series model as early as 1926 to make some general statements about the behavior of materials, and Prandtl used a physically different but mathematically equivalent model as a vehicle for the application of kinetic theory to a rather wide range of problems associated with rate effects (Iwan, 1967). Drucker has also discussed this model and has indicated some of its advantages and shortcomings. The series-parallel model has received only little attention in the literature.

The class of models which will be considered consists of a collection of perfectly elastic and rigid-plastic or slip elements (Coulomb friction elements) arranged in either a series-parallel (Fig.3.6a) or a parallel-series (Fig.3.6b) combination. The distribution of these properties will then dictate the particular form that the hysteretic behavior will take.

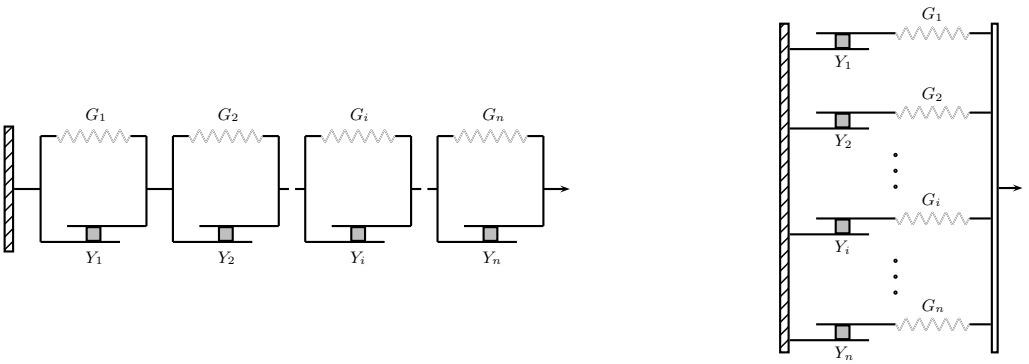

(a) Series-parallel Iwan model

(b) Parallel-series Iwan model

Figure 3.6: One dimensional Iwan rheological model

The friction elements remain locked until the stress on them exceeds the yield stress. Then, they yield, and the stress across them during yielding is equal to the yield stress. At any given time, all the elements up to a certain index number will be yielding and all those above will not. Generally, the yield stress of the first element is set to zero to generate the elastic behavior of the material. By appropriate specification of the spring constants G_i and the yield stresses Y_i, we can model a very broad range of material behavior as dictated by laboratory experiments. The accuracy of the modeling depends upon the number of elements. Iwan model leads to a very simple and efficient method of calculation and offers considerable flexibility for incorporating laboratory data on soil behavior (Joyner and Chen, 1975).

The Iwan model can be used to represent, to any desired accuracy, the behavior of any material whose hysteresis loops satisfy the Masing criterion and do not depend on the number of cycles of loading. The whole set of four extended Masing's rules is satisfied by Iwan model (Puzrin and Shiran, 2000a). Joyner and Chen (1975) believes that even if a soil does not exactly meet the Masing criterion, its behavior might still be approximately represented by an Iwan model. If also the shape of the loop changed with the number of loading cycles, the Iwan model might still be used, provided the changes were not too drastic. In evaluating the constants of the model, one would simply use the loop generated after a certain number of cycles (Joyner and Chen, 1975). The number would be chosen to be representative of the number expected during the postulated earthquake.

The Iwan model is used to present the behavior of different type of materials such as Taylor and Larkin (1978), Iwan and Cifuentes (1986), Belyaev and Irschik (1996), Song et al. (2004), Miller and Quinn (2009), Asik and Isbuga (2007) and Shiryayev et al. (2007). There exist also several developments of the Iwan model that are presented as follows.

3.2.5.2 Model developments

To take into account the effect of cyclic stiffness degradation, Puzrin et al. (1995) have considered the influence of the changing mean effective stress on the parameters of the Iwan's series-parallel model which leads to the concept of a normalized non-degrading backbone curve and predicts the cyclic simple shear behavior of soft Nile clay consistent with the Masing rules.

As already discussed, the Iwan model in its original form cannot take into account the stiffness degradation which is observed during cyclic loading of soft clays. The degradation index proposed by Idriss et al. (1978) has been incorporated into Iwan's series-parallel model as a single fatigue parameter to account for the degradation during cyclic loading by Rao and Panda (1999).

According to Muravskii (2001), as damping characteristics of Masing's models, such as Iwan model, result completely from the backbone curve, they cannot be regulated independently. This leads, in most cases, to an improper prediction of damping, specially for large strain amplitudes. Therefore, in order to be able to consider arbitrarily large values of normalized strains, which can be encountered in seismic response analysis, Muravskii (2001) recommended to make the normalization of backbone curve proposed by Hardin and Drnevich (1972b), using the failure stress τ_f instead of the maximum stress τ_{max} and to continue the backbone curve in the area of infinite strains.

Segalman modified the parallel-series Iwan model to use it in structural dynamics for joint elements (Segalman, 2001, 2002; Segalman and Starr, 2004). He demonstrated that being Iwan representations, the Segalman models are also Masing models. According to Segalman and Starr (2008) what are now often referred to as Iwan might correctly be called Masing-Prandtl-Ishlinskii-Iwan (MPII) models. Also in the early 1990s, Lubarda et al. (1993) demonstrated that the Prandtl-Ishlinskii-Iwan models could be constructed from Preisach models, connecting them to the rich mathematics built around the Preisach formalism within the physics community (Segalman and Starr, 2008).

According to Gutta et al. (2003), one of the shortcomings of Masing's model (such as Iwan

model) is that they can be computationally very expensive as it is necessary to retain in memory each and every surface during the entire loading history.

According to Ashrafi and Smyth (2007) the Iwan parallel-series model is widely used and is also known as the distributed-element model. They proposed a set of rules, which is a generalization of the Masing's rules and can capture the deteriorating (or nondeteriorating) response of distributed-element model (parallel-series Iwan model) with any distribution of element yield displacement thresholds to any arbitrary loading.

Lee et al. (2009) modified the parallel Iwan model to represent the cyclic hardening behavior of dry sand by the inclusion of isotropic hardening elements connected in parallel. The advantages of the parallel Iwan model are that it is able to predict hysteretic behavior, including Bauschinger's effect, with its own behavior characteristics without any additional behavior rules, and it obeys Drucker's stability postulate even if a system comes into localized failure modes. The behavior of the isotropic hardening elements is controlled by the cyclic hardening function, which uses accumulated shear strain as a control parameter. Material parameters of the proposed model can be determined from symmetric-limit cyclic loading tests (torsional shear tests).

The parallel-series formulation always lead to stress-strain relations in a form which gives stress as a function of strain. This is probably the most convenient form for the dynamicist since strains or displacements are normally taken as the independent variables in the equations of motion (Iwan, 1967). On the other hand, most of the equations of the incremental theory of plasticity are based upon the idea that the strain should be separable into an elastic and a plastic part, the total strain being just the sum of these two. The series-parallel models are more acceptable from this point of view. Therefore in this work we use the Iwan series-parallel model to investigate the soil nonlinearity and its effects on dynamic soil-structure interaction problem.

3.3 Selected soil constitutive model

3.3.1 Introduction

The stress-strain model used here is the elastoplastic cyclic model presented by Iwan (1967). The model is composed of simple linear springs and Coulomb friction units arranged as shown in Fig.3.7. The friction units remain locked until the stress on them exceeds the yield stress Y_i. Then, they become active and the stress inside them during yielding remains the yield stress. The yield stress at the first friction unit is equal to zero so we are capable to reproduce the elastic behavior of the soil.

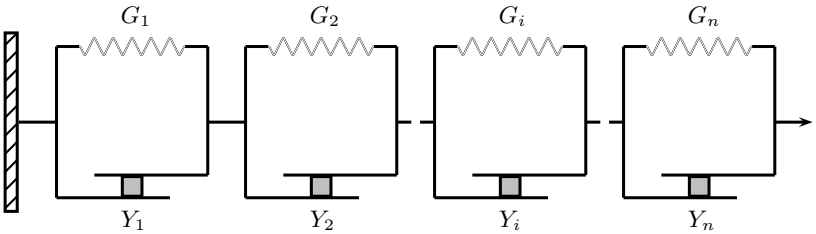

Figure 3.7: One dimensional Iwan rheological model

The spring constants G_i are chosen so as to represent the stress-strain behavior measured in the laboratory. An example of stress-strain loops computed by such a model are shown in Fig.3.8. It depicts the cyclic response of a single soil element subject to a single component sinusoidal loading of increasing amplitude. The model of Fig.3.8 contains 50 springs and 50 friction units.

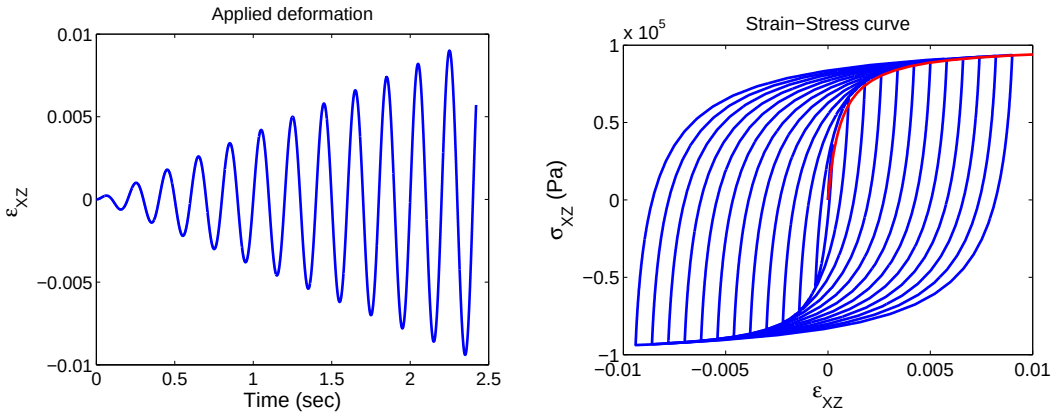

Figure 3.8: Applied single component sinusoidal loading of increasing amplitude (left) and Hysteresis loops produced by the Iwan model (right)

In order to extend the model to three dimensions, Iwan (1967) introduced an extension of the standard incremental theory of plasticity. The only difference between the Iwan formulation and the classical approach is the introduction of a collection of yield surfaces in place of the usual single surface. Each of these surfaces individually obey a linear hardening law of the type developed by Prager but their combined action, in general, gives rise to a nonlinear hardening law for the material.

3.3.2 Theoretical aspects

3.3.2.1 Theoretical formulation

The theoretical aspects and formulations presented here are initially introduced by Iwan (1967) and developed by Joyner and Chen (1975) and Joyner (1975).

The relationship between mean stress and mean strain is presumed elastic so that

$$de_M = d\sigma_M/3K$$

where K is the bulk modulus. Let the state of deviatoric stress of an element of the yielding material be represented by a point, p, in the nine-space by s_{ij} and let the corresponding total deviatoric strain by e_{ij}. The total deviatoric strain e_{ij} is supposed to consist of the sum of an elastic deviatoric strain e_{Eij} plus plastic deviatoric strain components e_{Pnij}. Following the suggestion of Prager, a family of yield surfaces is supposed and represented by the yield functions,

$$F_n(s_{ij} - \alpha_{nij}) = k_n^2 \tag{3.7}$$

where k_n is a constant characteristic of the nth yield surface that can be obtained by laboratory tests and α_{nij} represents the "origin" of the yield surfaces (n used here as a subscript always denotes the nth yield surface). Kinematic hardening of the Prager type is assumed so that,

$$d\alpha_{nij} = C_n de_{Pnij} \tag{3.8}$$

where C_n is a constant associated with the nth surface.

The yield surface translates in a direction parallel to the increment of plastic strain at any point in the stress history of the material, therefore, the plastic strain increments should be normal to the corresponding yield surfaces. Consequently,

$$de_{Pnij} = L_n h_n \frac{\partial F_n}{\partial s_{ij}} \tag{3.9}$$

where L_n is the index of the activity of the nth friction unit. This means if L_n is equal to zero the related friction unit is inactive and equal to 1 for an active one. L_n can be equal to zero when,

$$F_n < k_n^2 \quad or \quad \frac{\partial F_n}{\partial s_{ij}} ds_{ij} < 0$$

and L_n is equal to 1 when

$$F_n = k_n^2 \quad and \quad \frac{\partial F_n}{\partial s_{ij}} ds_{ij} \geq 0$$

The requirement that loading from a plastic state must lead to another plastic state can be used to determine h_n. According to Fung and Tong (2001), if the material obeys the associated flow rule we have,

$$de_{Pnij} = \frac{n_{ij} n_{rs} ds_{rs}}{C_n} \tag{3.10}$$

where n_{ij} is a unit normal to yield surface equal to

$$n_{ij} = \frac{\partial F_n}{\partial s_{ij}} \left(\frac{\partial F_n}{\partial s_{kl}} \frac{\partial F_n}{\partial s_{kl}} \right)^{-1/2} \tag{3.11}$$

Therefore substituting equation 3.11 into equation 3.10 and finally comparing by equation 3.9, we can easily obtain :

$$h_n = \frac{(\partial F_n / \partial s_{rs}) ds_{rs}}{C_n (\partial F_n / \partial s_{kl})(\partial F_n / \partial s_{kl})} \tag{3.12}$$

Since the total plastic strain is the sum of plastic strains associated with each individual surface, the overall work-hardening behavior of the material depends on the combined action of a number of separate surfaces. Since the work-hardening law of each individual surface has been assumed to be linear, the form of the overall work-hardening behavior will only be a function of the distribution of these surfaces (Iwan, 1967). If there is a finite number of individual surfaces, the overall work-hardening relation will be piecewise linear. On the other hand, if the yield surfaces are distributed continuously throughout some region of stress space, the overall work-hardening will also be continuous and nonlinear.

When the yield surfaces are distributed continuously, it may be shown that the total incremental plastic strain at any point along the loading path of the element will be

$$d\epsilon_{Pij} = \frac{1}{2C} \left(\int^{k^*} \frac{(\sigma_{ij} - \alpha_{ij}(k) - \frac{1}{3}(\sigma - \alpha(k))\delta_{ij})(\sigma_{lm} - \alpha_{lm}(k) - \frac{1}{3}(\sigma - \alpha(k))\delta_{lm})}{k^2} \Gamma(k) dk \right) d\sigma_{lm}$$

where σ_{ij} is the total stress, C and k are the continuous form of C_n and k_n. $\alpha_{ij}(k)$ is the α_{nij} for all of those surfaces with $k_n = k$, $\sigma = \sigma_{ii}$, $\alpha(k) = \alpha_{ii}(k)$, and $\Gamma(k)dk$ is the fraction of the total number of yield surfaces with a value of k between k and $k + dk$. In this work we use a finite number of friction elements, therefore, the formulation is based on this hypothesis.

The elastic deviatoric strain is given by

$$e_{Eij} = s_{ij} / 2G_0$$

where G_0 and E are respectively the low-strain shear modulus and Young moduli.

Summing elastic and plastic strain increment components and substituting from equation 3.9 and 3.12 gives the total deviatoric strain increment,

$$de_{ij} = Q_{ijrs} ds_{rs} + de_{Eij} \tag{3.13}$$

where

$$Q_{ijrs} = \sum_n \frac{L_n(\partial F_n/\partial s_{ij})(\partial F_n/\partial s_{rs})}{C_n(\partial F_n/\partial s_{kl})(\partial F_n/\partial s_{kl})} \tag{3.14}$$

Equation 3.13 should be solved for ds_{rs} in terms of de_{ij}. It should be mentioned that only five components of ds_{rs} are independent. These five independent components are selected, and using the relationships,

$$s_{rs} = s_{sr}$$

and

$$s_{11} + s_{22} + s_{33} = 0$$

Equation 3.13 is rewritten in terms of the independent components,

$$de_{ij} = P_{ij11}ds_{11} + P_{ij12}ds_{12} + P_{ij13}ds_{13} + P_{ij23}ds_{23} + P_{ij33}ds_{33} \tag{3.15}$$

where (i, j) takes the values $(1, 1)$, $(1, 2)$, $(1, 3)$, $(2, 3)$ and $(3, 3)$. The coefficients are given by,

$$P_{1111} = \sum_n^N \frac{L_n(\partial F_n/\partial s_{11})(\partial F_n/\partial s_{11} - \partial F_n/\partial s_{22})}{C_n(\partial F_n/\partial s_{kl})(\partial F_n/\partial s_{kl})} + \frac{1}{E} \tag{3.16}$$

$$P_{1112} = \sum_n^N \frac{L_n(\partial F_n/\partial s_{11})(\partial F_n/\partial s_{12} + \partial F_n/\partial s_{21})}{C_n(\partial F_n/\partial s_{kl})(\partial F_n/\partial s_{kl})}$$

$$P_{1113} = \sum_n^N \frac{L_n(\partial F_n/\partial s_{11})(\partial F_n/\partial s_{13} + \partial F_n/\partial s_{31})}{C_n(\partial F_n/\partial s_{kl})(\partial F_n/\partial s_{kl})}$$

$$P_{1123} = \sum_n^N \frac{L_n(\partial F_n/\partial s_{11})(\partial F_n/\partial s_{23} + \partial F_n/\partial s_{32})}{C_n(\partial F_n/\partial s_{kl})(\partial F_n/\partial s_{kl})}$$

$$P_{1133} = \sum_n^N \frac{L_n(\partial F_n/\partial s_{11})(\partial F_n/\partial s_{33} - \partial F_n/\partial s_{22})}{C_n(\partial F_n/\partial s_{kl})(\partial F_n/\partial s_{kl})}$$

$$P_{1211} = \sum_n^N \frac{L_n(\partial F_n/\partial s_{12})(\partial F_n/\partial s_{11} - \partial F_n/\partial s_{22})}{C_n(\partial F_n/\partial s_{kl})(\partial F_n/\partial s_{kl})} \tag{3.17}$$

$$P_{1212} = \sum_n^N \frac{L_n(\partial F_n/\partial s_{12})(\partial F_n/\partial s_{12} + \partial F_n/\partial s_{21})}{C_n(\partial F_n/\partial s_{kl})(\partial F_n/\partial s_{kl})} + \frac{1}{2G_0}$$

$$P_{1213} = \sum_n^N \frac{L_n(\partial F_n/\partial s_{12})(\partial F_n/\partial s_{13} + \partial F_n/\partial s_{31})}{C_n(\partial F_n/\partial s_{kl})(\partial F_n/\partial s_{kl})}$$

$$P_{1223} = \sum_n^N \frac{L_n(\partial F_n/\partial s_{12})(\partial F_n/\partial s_{23} + \partial F_n/\partial s_{32})}{C_n(\partial F_n/\partial s_{kl})(\partial F_n/\partial s_{kl})}$$

$$P_{1233} = \sum_n^N \frac{L_n(\partial F_n/\partial s_{12})(\partial F_n/\partial s_{33} - \partial F_n/\partial s_{22})}{C_n(\partial F_n/\partial s_{kl})(\partial F_n/\partial s_{kl})}$$

$$P_{1311} = \sum_n^N \frac{L_n(\partial F_n/\partial s_{13})(\partial F_n/\partial s_{11} - \partial F_n/\partial s_{22})}{C_n(\partial F_n/\partial s_{kl})(\partial F_n/\partial s_{kl})} \tag{3.18}$$

$$
\begin{aligned}
P_{1312} &= \sum_{n}^{N} \frac{L_n(\partial F_n/\partial s_{13})(\partial F_n/\partial s_{12} + \partial F_n/\partial s_{21})}{C_n(\partial F_n/\partial s_{kl})(\partial F_n/\partial s_{kl})} \\
P_{1313} &= \sum_{n}^{N} \frac{L_n(\partial F_n/\partial s_{13})(\partial F_n/\partial s_{13} + \partial F_n/\partial s_{31})}{C_n(\partial F_n/\partial s_{kl})(\partial F_n/\partial s_{kl})} + \frac{1}{2G_0} \\
P_{1323} &= \sum_{n}^{N} \frac{L_n(\partial F_n/\partial s_{13})(\partial F_n/\partial s_{23} + \partial F_n/\partial s_{32})}{C_n(\partial F_n/\partial s_{kl})(\partial F_n/\partial s_{kl})} \\
P_{1333} &= \sum_{n}^{N} \frac{L_n(\partial F_n/\partial s_{13})(\partial F_n/\partial s_{33} - \partial F_n/\partial s_{22})}{C_n(\partial F_n/\partial s_{kl})(\partial F_n/\partial s_{kl})} \\
P_{2311} &= \sum_{n}^{N} \frac{L_n(\partial F_n/\partial s_{23})(\partial F_n/\partial s_{11} - \partial F_n/\partial s_{22})}{C_n(\partial F_n/\partial s_{kl})(\partial F_n/\partial s_{kl})} \\
P_{2312} &= \sum_{n}^{N} \frac{L_n(\partial F_n/\partial s_{23})(\partial F_n/\partial s_{12} + \partial F_n/\partial s_{21})}{C_n(\partial F_n/\partial s_{kl})(\partial F_n/\partial s_{kl})} \\
P_{2313} &= \sum_{n}^{N} \frac{L_n(\partial F_n/\partial s_{23})(\partial F_n/\partial s_{13} + \partial F_n/\partial s_{31})}{C_n(\partial F_n/\partial s_{kl})(\partial F_n/\partial s_{kl})} \\
P_{2323} &= \sum_{n}^{N} \frac{L_n(\partial F_n/\partial s_{23})(\partial F_n/\partial s_{23} + \partial F_n/\partial s_{32})}{C_n(\partial F_n/\partial s_{kl})(\partial F_n/\partial s_{kl})} + \frac{1}{2G_0} \\
P_{2333} &= \sum_{n}^{N} \frac{L_n(\partial F_n/\partial s_{23})(\partial F_n/\partial s_{33} - \partial F_n/\partial s_{22})}{C_n(\partial F_n/\partial s_{kl})(\partial F_n/\partial s_{kl})} \\
P_{3311} &= \sum_{n}^{N} \frac{L_n(\partial F_n/\partial s_{33})(\partial F_n/\partial s_{11} - \partial F_n/\partial s_{22})}{C_n(\partial F_n/\partial s_{kl})(\partial F_n/\partial s_{kl})} \\
P_{3312} &= \sum_{n}^{N} \frac{L_n(\partial F_n/\partial s_{33})(\partial F_n/\partial s_{12} + \partial F_n/\partial s_{21})}{C_n(\partial F_n/\partial s_{kl})(\partial F_n/\partial s_{kl})} \\
P_{3313} &= \sum_{n}^{N} \frac{L_n(\partial F_n/\partial s_{33})(\partial F_n/\partial s_{13} + \partial F_n/\partial s_{31})}{C_n(\partial F_n/\partial s_{kl})(\partial F_n/\partial s_{kl})} \\
P_{3323} &= \sum_{n}^{N} \frac{L_n(\partial F_n/\partial s_{33})(\partial F_n/\partial s_{23} + \partial F_n/\partial s_{32})}{C_n(\partial F_n/\partial s_{kl})(\partial F_n/\partial s_{kl})} \\
P_{3333} &= \sum_{n}^{N} \frac{L_n(\partial F_n/\partial s_{33})(\partial F_n/\partial s_{33} - \partial F_n/\partial s_{22})}{C_n(\partial F_n/\partial s_{kl})(\partial F_n/\partial s_{kl})} + \frac{1}{E}
\end{aligned}
\tag{3.19}
\tag{3.20}
$$

By solving equation 3.15, the stress increments are obtained from the strain increments. Gaussian elimination can be used to solve equation 3.15. The coefficients in equation 3.15 depend on $\partial F_n/\partial s_{ij}$, C_n and L_n. The yield condition of Von Mises is used so that,

$$
\begin{aligned}
F_n =& \frac{1}{2}\left[(s_{11} - \alpha_{n11})^2 + (s_{22} - \alpha_{n22})^2 + 2(s_{12} - \alpha_{n12})^2 \right. \\
&\left. +2(s_{13} - \alpha_{n13})^2 + 2(s_{23} - \alpha_{n23})^2 + (s_{33} - \alpha_{n33})^2\right]
\end{aligned}
\tag{3.21}
$$

and

$$\frac{\partial F_n}{\partial s_{ij}} = s_{ij} - \alpha_{nij} \tag{3.22}$$

With that choice, the parameter k_n used in the description of the yield surface represents the initial yield stress (backbone curve) in simple shear. The values of k_n and C_n are chosen in order to fit laboratory data on the stress-strain behavior of the material.

In order to control the activity of each unit, we need to know the value of F_n and the sign of $(\partial F_n/\partial s_{ij})ds_{ij}$. To obtain F_n, there is no problem because it depends on s_{ij} and α_{nij} that are known at the beginning of each increment. But for the second, $(\partial F_n/\partial s_{ij})ds_{ij}$, ds_{ij} is unknown in equation 3.14. Therefore, this difficulty is avoided by a procedure which is the equivalent of choosing L_n, in accordance with the sign of $(\partial F_n/\partial s_{ij})ds_{ij}$ during the previous time step. The accuracy of this approximation has been checked by Joyner (1975) by comparing with the results of one-dimensional calculations for which the approximation was not made.

If during a given time step yielding takes place on the nth surface, the quantities α_{nij} are changed. In order to ensure that the stress point always remains exactly on a yielding surface, equation 3.8 is not used to calculate the change in α_{nij}. Coincidence of the stress point and the yielding surface is mentioned by using the following equation,

$$\alpha'_{nij} = s'_{ij} - \frac{k_n(s'_{ij} - \alpha_{nij})}{T_n} \tag{3.23}$$

where T_n is equal to

$$T_n = \left[1/2(s'_{kl} - \alpha_{nkl})(s'_{kl} - \alpha_{nkl})\right]^{1/2}$$

where unprimed quantities represent values at current time step and the primed quantities values at previous time step.

3.3.2.2 Schematic interpretation of the model

In order to demonstrate more precisely what the previous formulation implies, consider the special case where the yield surfaces are given by the von Mises condition. Then these surfaces will be cylinders in the principal stress space, and their projections on the $\pi-$plane of this space will be circles. Figure 3.9a represents the distribution of the yield surfaces (in case of a finite number of units) for the virgin material. Then, as the element is initially loaded, the stress point p reaches the first yield surface and then another one. As a result of the kinematic hardening, each surface is carried along with p so long as $L_n h_n > 0$, as depicted schematically in Fig.3.9b. Now the original distribution of the yield surfaces will be alerted by the loading to point A. Thus, even if the element is unloaded along the same path as the initial loading, the stress-strain relation and the overall work-hardening behavior will be changed. This is indicated schematically in Fig.3.9c. On loading to A, the stress point p would have encountered four separate yield surfaces resulting in four slope discontinuities in the stress-strain relation. However, on unloading, the stress point would only have encountered two surfaces with only two resulting discontinuities. It can readily be seen that this would lead to a piecewise linear work-hardening behavior exhibiting a Bauschinger effect.

3.3.2.3 Algorithm for the resolution

As the formulations of the model are presented, now, the sequence of computations used in this work is given below, where the primed quantities are computed in the current time step and the unprimed quantities are inherited from the previous time step.

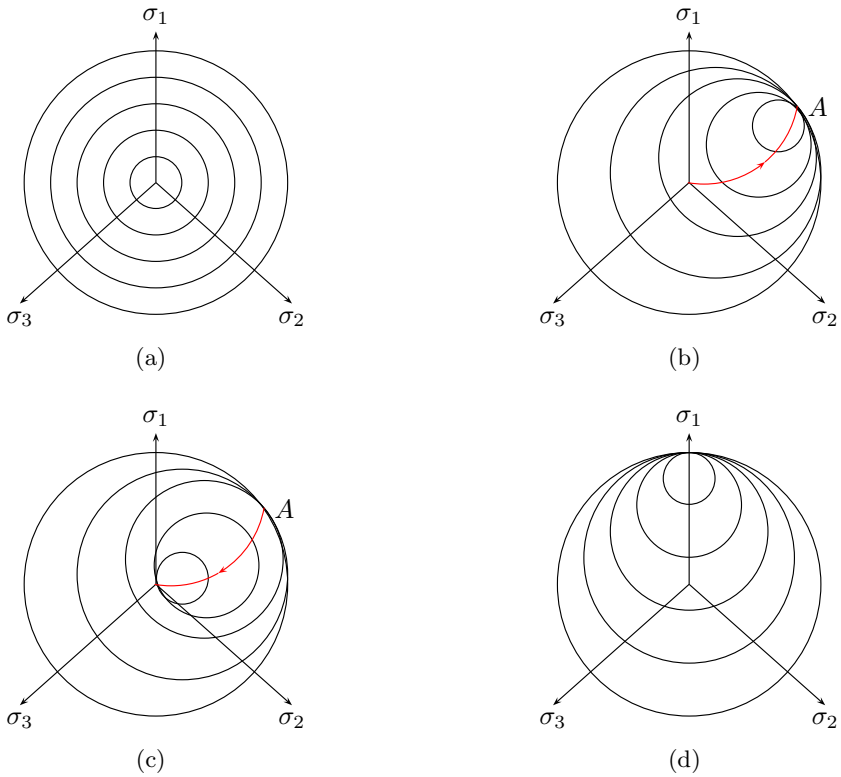

Figure 3.9: Schematic behavior of yield surfaces of Iwan model in π-plane

- New values of the stress components $s_{ij}^{'}$ are obtained from,

$$s_{ij}^{'} = s_{ij} + ds_{ij}$$

- F_n is calculated by equation 3.21 and consequently $T_n = F_n^{\frac{1}{2}}$.
- By means of the previous incremental strain that we save from the previous time step, $\partial F_n / \partial s_{ij}$ can be obtained by combining equation 3.22 and 3.24.

$$\frac{\partial F_n}{\partial s_{ij}} = \frac{k_n}{T_n}\left(s_{ij}^{'} - \alpha_{nij}\right) \tag{3.24}$$

- State of the yield surfaces is verified to obtain the units that are activated (L_n).
- P_{ijkl} can be obtained by the equation 3.16 to 3.20 by means of equation 3.24.

$$P_{ijkl} = \begin{bmatrix} P_{1111} & P_{1112} & P_{1113} & P_{1123} & P_{1133} \\ P_{1211} & P_{1212} & P_{1213} & P_{1223} & P_{1233} \\ P_{1311} & P_{1312} & P_{1313} & P_{1323} & P_{1333} \\ P_{2311} & P_{2312} & P_{2313} & P_{2323} & P_{2333} \\ P_{3311} & P_{3312} & P_{3313} & P_{3323} & P_{3333} \end{bmatrix}$$

- Now equation 3.15 is solved by inverting the P_{ijkl} matrix to give the new stress increments ds_{ij}. Factors of (k_n/T_n) from 3.24 appearing in the numerator and denominator of the expressions for the coefficients of equation 3.15 cancel out and simplify the calculations.
- The yield surface, F_n, is calculated to check the state of the yield surfaces comparing to k_n to control if there is any new unit that is activated. The previous levels are repeated if there is any change for the point at stress space by updating the yield surfaces.

- Equation 3.24 is also used to evaluate α'_{nij} and so on.

We need to determine the parameter C_n that is used to compute equations 3.16 to 3.20. The determination of the constants C_n is performed by considering the behavior of the system in simple shear. Iwan (1967) showed that the behavior of the three-dimensional model in simple shear is equivalent to the behavior of the one-dimensional model. It is assumed that the loading curve from an initial state of zero deviatoric stress and strain is known. In principle it could be determined from laboratory measurements. With the proper choice of coordinate axes, the non vanishing components of stress and strain in simple shear are,

$$s_{13} = s_{31} \quad , \quad e_{13} = e_{31}$$

The parameter k_n represents the yield stress in simple shear for the nth yielding surface. A set of values of k_n is chosen to cover the range of stress the system is expected to encounter, and the values are distributed so that the initial loading curve can be faithfully represented (Joyner, 1975). From the initial loading curve a set of values $e_n(n = 1, N)$ is obtained for the shear strain corresponding to the stress values k_n. A stress value s_{N+1} is chosen larger than any stress that is expected to occur. A corresponding strain value e_{N+1} is obtained from the loading curve. For the case of simple shear (example of yield surfaces in Fig.3.9d), equation 3.13 becomes,

$$de_{13} = \frac{ds_{13}}{2G_0} + Q_{1313}ds_{13} + Q_{1331}ds_{31} \tag{3.25}$$

Evaluating Q_{1313} and Q_{1331} with the aid of equation 3.15, gives,

$$de_{13} = \left(\frac{1}{2G_0} + \sum_{n=1}^{j}\frac{1}{C_n}\right)ds_{13} \tag{3.26}$$

where j is the index of the surface with the largest yield stress of all the surfaces that are in the yielding state. This equation leads to a simple recursion relationship for determining C_j,

$$\frac{1}{C_j} = \frac{e_{j+1} - e_j}{k_{j+1} - k_j} - \frac{1}{2G_0} - \sum_{n=1}^{j-1}\frac{1}{C_n} \tag{3.27}$$

The evaluation of C_N is the same except that s_{N+1} is used in place of the undefined k_{N+1}.

3.3.3 FEM implementation of the MPII model into the CESAR-LCPC code

During this thesis, the MPII model (Iwan model) presented in details in §3.3.1 and §3.3.2 is implemented into CESAR-LCPC numerical program. This program is presented in §1.6.1 in details. The MCCI calculation module (see §1.6.2) is selected for this purpose. The mathematical formulations of the nonlinear model are programmed in FORTRAN and implemented to the code. The implemented model is verified by different numerical tests. In the next section, the results of two test cases are compared with other numerical programs.

3.4 Verification of the implemented model

3.4.1 Model definition

Two one-dimensional soil columns are considered to verify the behavior of the implemented Iwan model into CESAR-LCPC program. The results are compared with other computer programs, considering linear and nonlinear soil behavior during the wave propagation through the soil columns in time and frequency domains. The first example (#1) consists of a one-dimensional single soil layer based on a rigid base. The second one (#2) consists of a one dimensional three-layer soil column, also based on a rigid base. The elastic properties of both soil columns are

presented in table 3.1. The first example is a homogeneous $50m$ soil column (Fig.3.10a). The second example is shown in Fig.3.11 and composed of three layers of 30, 25 and $60m$.

In general, to avoid the numerical dispersion, more than 10 nodes per wavelength should be considered. Therefore, a uniform spatial discretization is performed for the two cases and the vertical size of each element is equal to $1m$. The numerical dispersion in nonlinear materials will be discussed in details in §4. The tied boundaries with periodic condition at the two lateral sides of the model are considered.

	Layer N.	$\rho(Kg/m^3)$	$V_s(m/s)$	ν
#1	1	1900	150	0.3
#2	1	1900	150	0.3
	2	2000	300	0.3
	3	2100	350	0.3

Table 3.1: Elastic properties of the two soil columns for the verification of the implemented model

The Newmark algorithm with unconditional stable condition is assumed with the two constants $\alpha = 0.5$ and $\beta = 0.25$. Therefore, no more numerical dissipation will be induced to the model in order to investigate the nonlinear behavior of the soil only.

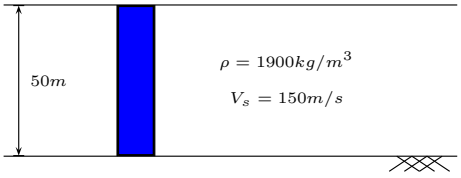

(a) One layer soil profile (#1)

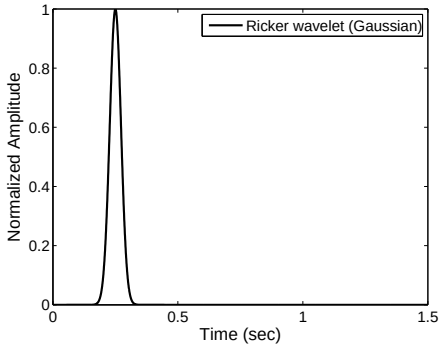

(b) Ricker wavelet of order zero (Gaussian wavelet)

Figure 3.10: One dimensional soil layer on a rigid base and applied Ricker wavelet

The comparison of the results is presented in §3.4.3 for linear case and in §3.4.4 for nonlinear one.

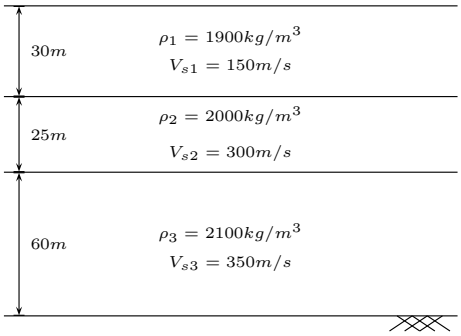

Figure 3.11: One dimensional 3-layer soil profile (#2) based on a rigid base

3.4.2 Other methods and programs

The results of the implemented model are compared to other methods and programs. The first program is EERA (**E**quivalent-linear **E**arthquake site **R**esponse **A**nalyses of Layered Soil Deposits, Bardet et al. (2000)) which shares the same procedure as SHAKE (Schnabel et al., 1972) both performing equivalent-linear earthquake response analysis. The equivalent linear model represents the soil stress-strain response based on Kelvin-Voigt model. The shear stress τ depends on the shear strain γ and its rate $\dot{\gamma}$. The second computer program is NERA (**N**onlinear **E**arthquake site **R**esponse **A**nalyses of Layered Soil Deposits, Bardet and Tobita (2001)). This code follows the Iwan (1967) model. Concepts similar to those in NERA have been used by Joyner and Chen (1975); Prevost (1989) and others. The third program is a finite differences program based on the work of Bonilla (2000) and uses the elastoplastic Iwan model. These three computer programs are based on the finite difference method and are capable to simulate one dimensional wave propagation.

To investigate linear behavior of soil, we use another calculation module of the CESAR-LCPC program, named DYNI. It serves for resolution of the dynamic problems in time domain, considering elastic behavior of the materials. This calculation module has been widely used and already validated (Humbert et al., 2005).

3.4.3 Linear behavior

Considering elastic behavior of soil, transfer function (ratio of the acceleration at the surface of the soil and the input acceleration at the base of the soil column) of the first example defined in §3.4.1 is compared between theory and different programs. The theoretical transfer function, $F(\omega)$, for a homogeneous elastic soil layer can be obtained by means of following equation (Kramer, 1996),

$$|F(\omega)| = \frac{1}{|\cos(\omega H/V_s)|} \tag{3.28}$$

where H is the depth and V_s the velocity of shear waves of the soil column.

The results are compared between the calculation modules MCCI (MPII model), DYNI (CESAR-LCPC), EERA program and the theory. The Ricker wavelet of order zero (Fig.3.10b) is imposed at the base of the soil column. Figures 3.12a and 3.12b display the comparison of the resulting transfer functions for the two examples (#1 and #2).

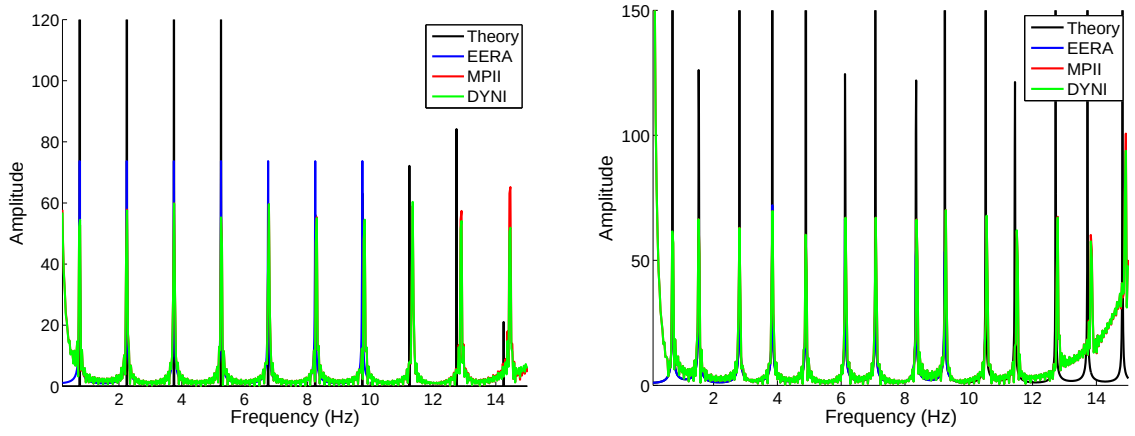

(a) Transfer function of acceleration, #1

(b) Transfer function of acceleration, #2

Figure 3.12: Transfer function of the acceleration (ratio of the acceleration at the surface of the soil and input acceleration at the base of the soil column) for the examples #1 and #2

The theoretical transfer function of the three-layer elastic soil can be obtained by equation 3.29.

$$|F(\omega)| = \frac{4}{\begin{array}{l}|(1+\alpha_1)(1+\alpha_2)\cos(\omega h_1/V_{s1}+\omega h_2/V_{s2}+\omega h_3/V_{s3})+ \\ (1-\alpha_1)(1+\alpha_2)\cos(-\omega h_1/V_{s1}+\omega h_2/V_{s2}+\omega h_3/V_{s3})+ \\ (1-\alpha_1)(1-\alpha_2)\cos(\omega h_1/V_{s1}-\omega h_2/V_{s2}+\omega h_3/V_{s3})+ \\ (1+\alpha_1)(1-\alpha_2)\cos(-\omega h_1/V_{s1}-\omega h_2/V_{s2}+\omega h_3/V_{s3})|\end{array}} \tag{3.29}$$

where α is the impedance ratio as

$$\alpha_1 = \frac{\rho_1 V_{s1}}{\rho_2 V_{s2}} \qquad \alpha_2 = \frac{\rho_2 V_{s2}}{\rho_3 V_{s3}}$$

It is shown in Fig.3.12, that there is a very good agreement between the results. Only for the high frequencies there are some differences between the theory and the computer programs. This shows clearly the limit of the numerical programs. The domain should be discretized for the numerical programs. Therefore, relating to the level of the discretization the program can solve the problem up to a specified frequency. Consequently, the obtained results should be filtered for the frequencies more than the capacity of the numerical program.

There is also a little difference between the results of the programs in high frequencies. The spatial and temporal discretization of the model for the different programs may be the reason of such differences.

3.4.4 Nonlinear behavior

The two examples of §3.4.1 are used to compare the dynamic responses of the nonlinear soil with different approaches. The same elastic properties are used here and a Ricker wavelet of order zero as input displacement is applied at the base of the soil layer (Fig.3.10b). The modulus reduction curve vs. cyclic shear strain and the stress-strain curve obtained by monotonic shear loading known as backbone curve are shown in Fig.3.13. These properties represent a weak nonlinear soil that can be a good test to verify the implemented nonlinear model. In the two next sections the results of the computer programs (§3.4.2) are compared in time (§3.4.4.1) and frequency (§3.4.4.2) domain.

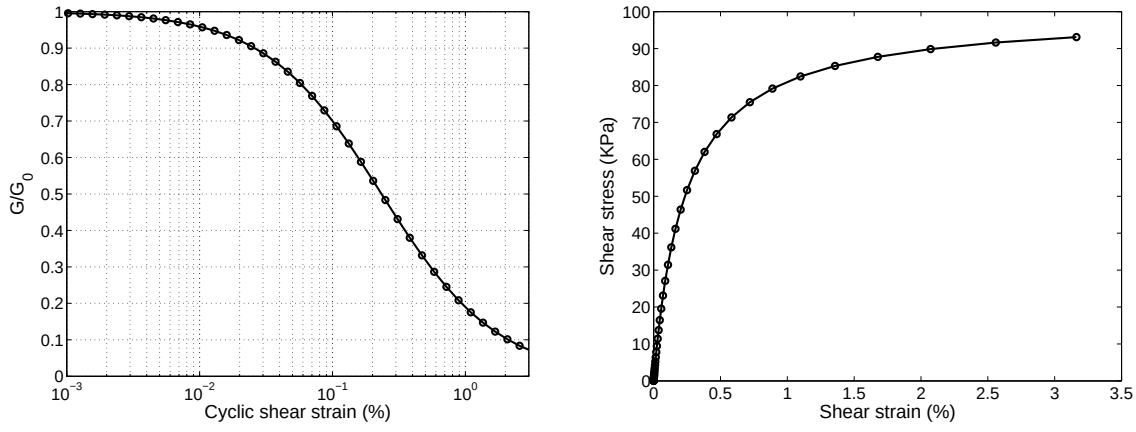

(a) G/G_0 vs. $\gamma\%$ (b) Backbone curve of the sample soil

Figure 3.13: Nonlinear properties of the soil layer including modulus reduction curve versus cyclic shear strain and monotonic loading stress-strain curve

3.4.4.1 Verification in time Domain

The acceleration at the surface of the soil is compared between these three programs (named as EERA, NERA and Bonilla) with our implemented program (named as MPII). Figure 3.14 illustrates the acceleration at the surface of the soil column for two different strain levels, equivalent to 0.015g and 0.3g outcrop PGA. In this case, the rigid behavior is considered at the base of the soil layer, therefore the wave continues to propagate in the soil layer and its energy dissipates through the propagation.

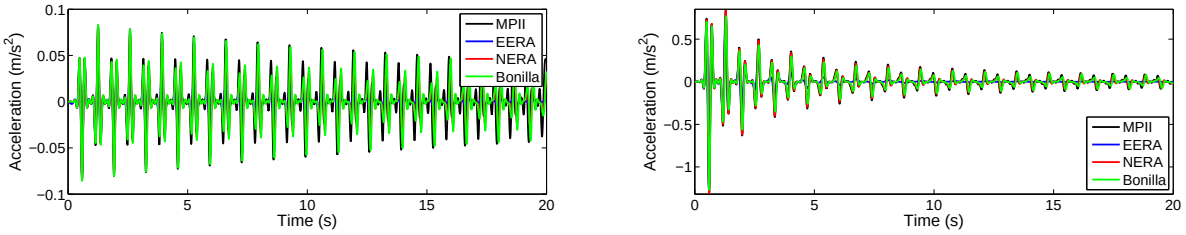

(a) Acceleration at ff (outcrop PGA :0.015g) (b) Acceleration at ff (outcrop PGA :0.3g)

Figure 3.14: Acceleration at the surface of the soil column excited by a Ricker wavelet of order zero at the base of the soil layer for two different input levels (equivalent to 0.015 and 0.3g outcrop PGA)

To have a better comparison, the first second of the propagation (first acceleration peak) is shown in Fig.3.15. The results for weak and moderate strain levels show a very good agreement for various codes. Specially, the MPII model and NERA give almost the same results.

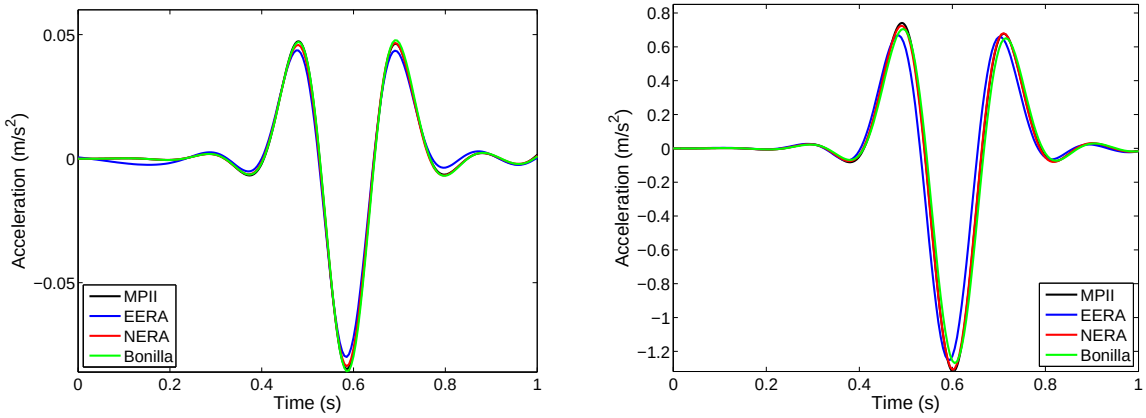

(a) Acceleration at ff (outcrop PGA :0.015g) (b) Acceleration at ff (outcrop PGA :0.3g)

Figure 3.15: First second of the acceleration obtained at the surface of the soil column for applied Ricker wavelet of order zero at the base of the soil layer for two different input levels (equivalent to a 0.015 and 0.3g outcrop PGA)

Now, we try to compare the results for a stronger motion. The same Ricker wavelet (Fig.3.10b) is applied at the base of the model with an equivalent outcrop PGA equal to 1.0g. The acceleration at the surface of the soil layer is shown in Fig.3.16. For this strain level, we can have a better comparison between these programs.

The equivalent-linear program (EERA) gives a higher amplitude but, after the second acceleration peak, the acceleration amplitude decreases very quickly and the energy dissipation is much larger with this model. Figure 3.17 displays the first second of the free field acceleration peak. Very good agreement exists, comparing our implemented model (MPII model) and NERA program, the results are almost the same. Bonilla program is also very close to MPII model and NERA, but more nonlinearity is induced into the soil.

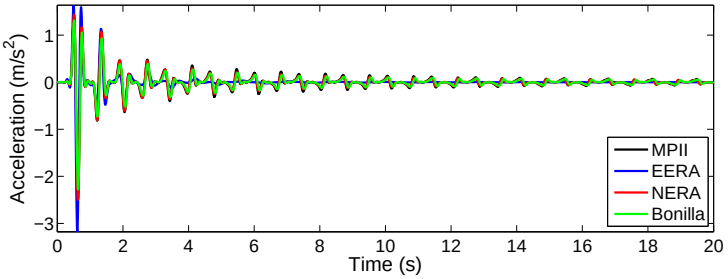

Figure 3.16: Acceleration obtained at the surface of the soil column for applied Ricker wavelet of order zero at the base of the soil layer equivalent to a 1.0g outcrop PGA

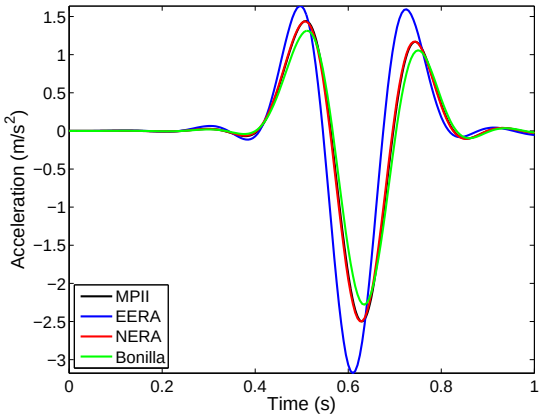

Figure 3.17: First second of the acceleration obtained at the surface of the soil column for applied Ricker wavelet of order zero at the base of the soil layer equivalent to a 1.0g outcrop PGA

The equivalent-linear model (EERA) predicts higher acceleration values for the peak acceleration, this means lower nonlinearity. Hence, the arrival time of the waves computed with this model is smaller than the nonlinear ones. Consequently, the apparent wave velocity during the propagation is higher with the equivalent-linear model than the fully nonlinear one.

The results of the second case, #2, are also compared between different programs. This model consists of a one dimensional three-layer soil on a rigid base (Fig.3.11). The model is composed of three layers, therefore, the wave propagation can be influenced by the stiffness contrast between the layers.

The same Ricker wavelet of order zero is applied at the base of the soil column for three different strain levels (Equivalent to a 0.015g, 0.3g and 1.0g outcrop PGA's). The acceleration at free field for 0.015g and 0.3g outcrop PGA's is compared between MPII model, EERA, NERA and Bonilla programs in Fig.3.18. For weak motion (0.015g outcrop PGA), the MPII model and Bonilla program demonstrate lower nonlinearities than the two other programs.

The first second of the propagation in the soil column is also compared in Fig.3.19 for 0.015g and 0.3g outcrop PGA. The MPII model, NERA and Bonilla programs are in very good agreement for weak and moderate motions. However, the difference between these three fully nonlinear programs and linear-equivalent model (EERA) is significant compared to the one-layer soil column. This is due to the contrast effect in the three-layer model and the amplification that takes place in the soil.

The results for a strong motion, 1.0g outcrop PGA, are shown in Fig.3.20. It is observed that the acceleration at the surface of the soil is almost the same for NERA and MPII until the end of the wave propagation ($20sec$).

The linear-equivalent method gives a higher amplitude for the first arrival at free field comparing to the fully nonlinear program but after that, higher dissipation takes place using this

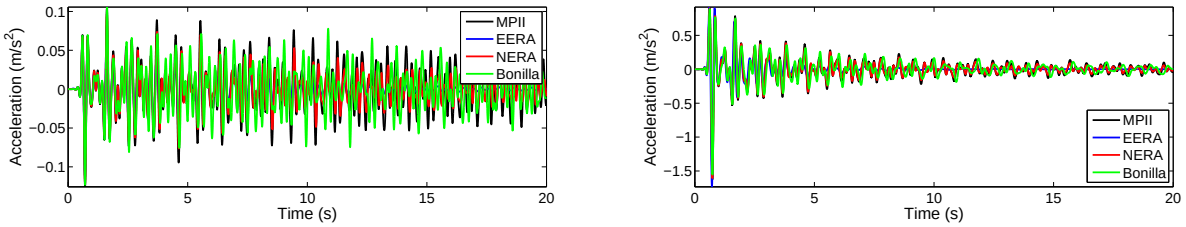

(a) Acceleration at ff (outcrop PGA :0.015g) (b) Acceleration at ff (outcrop PGA :0.3g)

Figure 3.18: Acceleration at the surface of the three-layer soil column for applied Ricker wavelet of order zero at the base of the soil layer (boundary condition in displacement) for two different input levels (equivalent to 0.015 and 0.3g outcrop PGA)

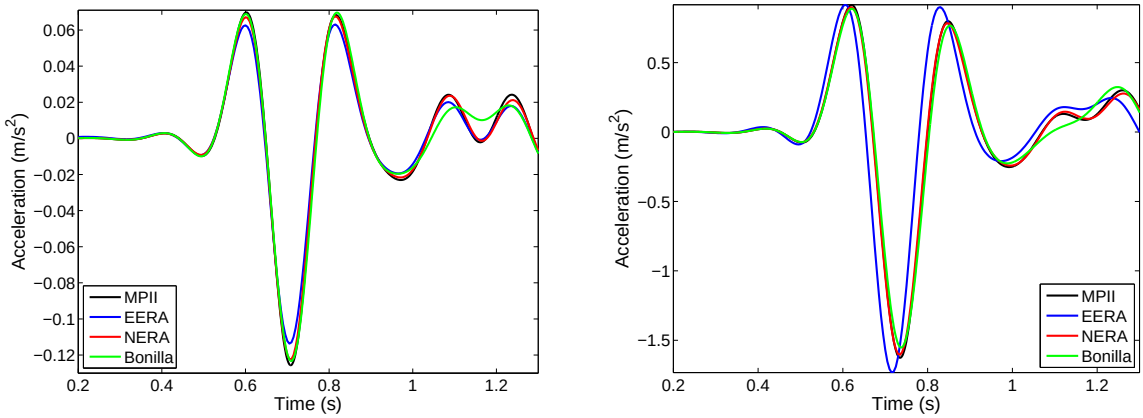

(a) Acceleration at ff (outcrop PGA :0.015g) (b) Acceleration at ff (outcrop PGA :0.3g)

Figure 3.19: First second of the acceleration obtained at the surface of the soil column for applied Ricker wavelet of order zero at the base of the soil layer (boundary condition in displacement) for two different input level (equivalent to 0.015 and 0.3g outcrop PGA)

model. We can conclude that, for weak motion, the equivalent linear method is more dissipative than fully nonlinear programs, but for moderate and strong motions, it is the contrary. Comparing Fig.3.15a, Fig.3.15b, Fig.3.17, Fig.3.19a and Fig.3.19b confirm this remark.

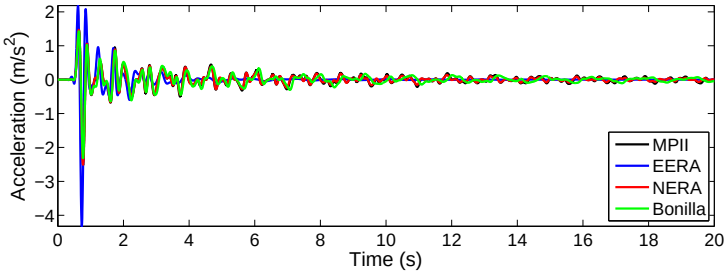

Figure 3.20: Acceleration obtained at the surface of the three-layer soil column for applied Ricker wavelet of order zero at the base of the soil layer (boundary condition in displacement) equivalent to 1.0g outcrop PGA

Figure 3.21 displays the first second of wave propagation of Fig.3.20. The MPII model and NERA use the same nonlinear model and the results perfectly agree. The results of Bonilla program are also very close to these two programs. However, in this case, the results of EERA are twice the results of nonlinear model. The choice of the damping curve for EERA should be the reason of this difference.

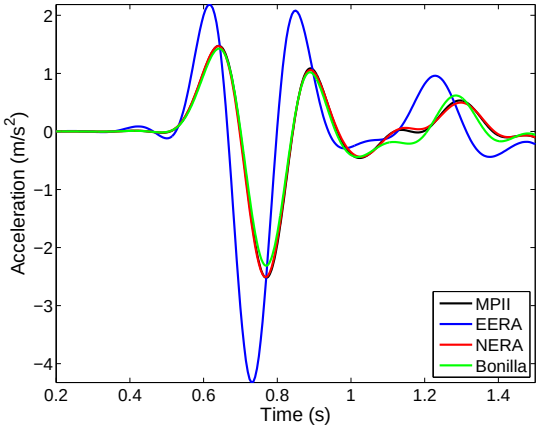

Figure 3.21: First second of the acceleration obtained at the surface of the three-layer soil column for applied Ricker wavelet of order zero at the base of the soil layer (boundary condition in displacement) equivalent to 1.0g outcrop PGA

In the next section the results of these two examples are compared in frequency domain.

3.4.4.2 Verification in frequency domain

The transfer functions (ratios of the Fast Fourier Transform of the free field acceleration and the outcropping bedrock motion) are also compared between the programs presented in §3.4.4. Figures 3.22 and 3.23 display the results for the single soil layer (#1) for two different strain levels equivalent to 0.015g and 1.0g outcrop PGA. The results are in very good agreement for natural frequencies of the soil layer.

For 0.015g outcrop PGA, the amplification of MPII model and Bonilla program are very close. The amplification obtained by NERA program is also close to these two programs. However, the amplification obtained by EERA program are smaller than the three fully nonlinear programs. This shows, the high level of dissipation of equivalent-linear model for weak motions.

For the strong motion, the results in amplitude and natural frequencies of the soil column are very close between the three fully nonlinear programs. However, the amplification obtained by EERA program is larger than other programs. This confirms the larger acceleration in time domain obtained for 1.0g outcrop PGA. This also shows one more time that the equivalent-linear method exhibits less nonlinearity for strong motion than fully nonlinear models. We should mentioned also that there is a little difference of natural frequencies between EERA and other nonlinear programs.

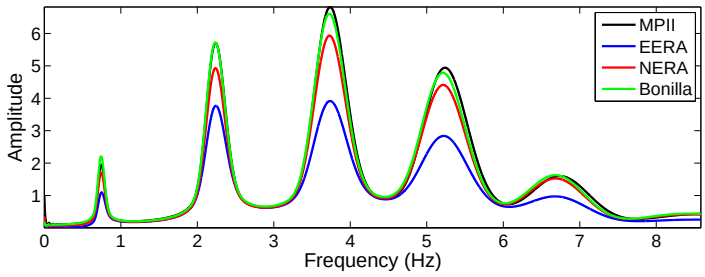

Figure 3.22: Transfer function of the acceleration between the surface of the one-layer soil column (#1) for applied Ricker wavelet of order zero at the base of the soil layer (boundary condition in displacement) equivalent a to 0.015g outcrop PGA

The same comparison are performed for three-layer soil column (#2) in Fig.3.24 and Fig.3.25. For the weak motion, the natural frequencies of the soil column obtained by all the programs are

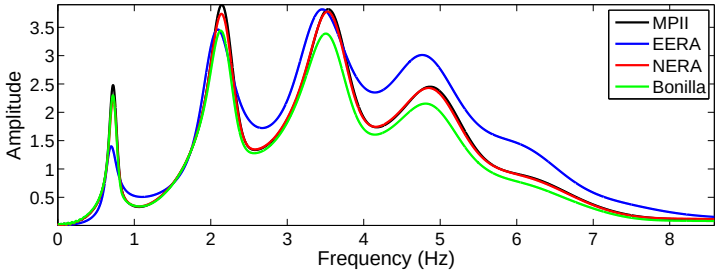

Figure 3.23: Transfer function of the acceleration between the surface of the one-layer soil column (#1) for applied Ricker wavelet of order zero at the base of the soil layer (boundary condition in displacement) equivalent to a 1.0g outcrop PGA

the same. For the strong motion (1.0g outcrop PGA) there is a very good agreement between the fully nonlinear models.

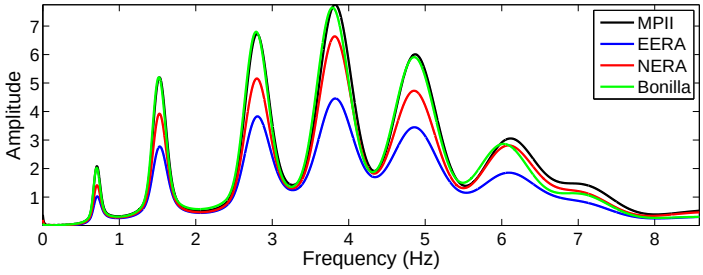

Figure 3.24: Transfer function of the acceleration between the surface of the three-layer soil column (#2) for applied Ricker wavelet of order zero at the base of the soil layer (boundary condition in displacement) equivalent to a 0.015g outcrop PGA

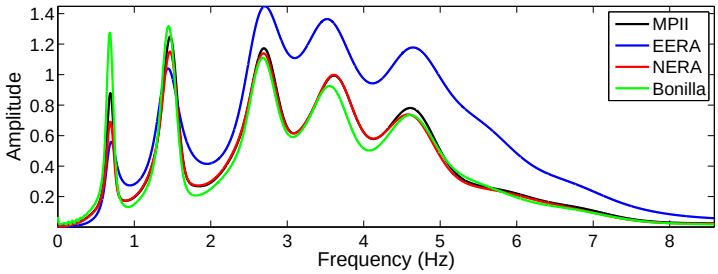

Figure 3.25: Transfer function of the acceleration between the surface of the three-layer soil column (#2) for applied Ricker wavelet of order zero at the base of the soil layer (boundary condition in displacement) equivalent to a 1.0g outcrop PGA

In general, there is a very good agreement between the results particularly for the natural frequencies of the soil columns and the level of amplification in both test cases (#1 and #2) between the fully nonlinear models.

3.5 Concluding remarks

A review of various existing soils constitutive models, from linear to nonlinear, is presented in this chapter. Different approaches of modeling of the soil nonlinearity are discussed. The Iwan nonlinear model (MPII model) is selected in this work and presented in detail. The model accounts for the nonlinear hysteretic behavior of soils and only needs the shear modulus

degradation curve to characterize the soil behavior. This feature is very important since complex constitutive models generally involve numerous mechanical parameters difficult to characterize experimentally.

The Iwan model is implemented in the framework of the Finite Element method into the CESAR-LCPC numerical program. Finally, the implemented model is numerically verified by comparing to other different codes.

Chapter 4

Numerical dispersion of waves in nonlinear soils

Contents

4.1 Introduction

Over the past decades, numerous researches have been dedicated to various numerical methods such as finite elements, finite differences and boundary elements in order to investigate wave propagation phenomena. Many of these methods are based on space and time discretization, which is the origin of the numerical approximation of the exact solution. The discretization error is related to the approximate representation of the physical phenomena, namely dispersion, anisotropy and reflection, decreasing with the mesh refinement (Harari, 1997). Numerical dispersion may increase the numerical error during the propagation process as the wave velocity (phase and group) depends on the features of the numerical model (Semblat and Brioist, 2000). The propagation of numerical waves causes a significant challenge in scientific computing (Complex geometries, boundary conditions, etc.). Many alternatives have been explored in the quest for a stable method that can efficiently solve the wave problem without large numerical dissipation or dispersion, particularly in the context of high frequency applications (Ainsworth, 2004).

Some of the more promising domain based approaches involve the use of higher order elements (Dauksher and Emery, 1999; Semblat and Brioist, 2000), higher order standard Galerkin finite element methods (Ihlenburg and Babuška, 1995a; Harari, 1997; Babuška et al., 1997b; Ihlenburg and Babuška, 1995b; Babuška et al., 1997a; Deraemaeker et al., 1999; Steffens and Dez, 2009), spectral elements (Faccioli et al., 1996, 1997; Komatitsch et al., 1999), stabilizing techniques referred to as Galerkin least-squares (GLS) and Galerkin/gradient least-squares (GGLS), (Thompson and Pinsky, 1995; Harari, 1997; Harari and Nogueira, 2002), higher order discontinuous Galerkin finite element methods (Ainsworth, 2004; Ainsworth et al., 2006; Sarmany et al., 2007), and, more recently, isogeometric analysis (Hughes et al., 2008).

The study of the dispersive and dissipative properties of a method provides insight into its ability to accurately propagate a wave. Indeed, the order of accuracy of the discrete dispersion relation is often used as a basis for ranking different methods. For most of these methods, the number of nodal points per wavelength is usually kept constant, therefore, the knowledge of the dispersive properties of the numerical solution is very important. A *rule of thumb* to apply the standard Galerkin FEM is to resolve the wavelength by 10 elements (Ihlenburg and Babuška, 1995a), but it may not be sufficient especially for high frequencies or for large propagation distances, for instance 5 or 10 wavelengths (Semblat and Brioist, 2000). Each numerical method requires a different number of points per wavelength and it is possible only in linear media, to determine the dispersion error mathematically. However, are these rules sufficient to obtain good results in the case of nonlinear constitutive laws? Considering the nonlinear elastic and elastoplastic behavior of materials, more parameters may be involved in numerical dispersion than in the elastic case.

In general, the numerical implementation of the theoretical constitutive laws is not able to exactly follow the behavior of the materials; consequently, it is not simple to separate dispersion and constitutive law errors. In addition, in nonlinear media, the results and consequently the errors depend on the amplitude of the input motion, which makes the problem more complicated.

In this chapter, numerical dispersion is investigated in the case of waves propagating in nonlinear elastoplastic materials. Finite element method and initially simple behavior models such as bilinear model and then MPII (Masing-Prandtl-Ishlinskii-Iwan) hysteretic model, (Iwan, 1967; Segalman and Starr, 2008), is considered. A 1D parametric analysis is performed to investigate the number of points per wavelength in various nonlinear cases. The more important features of nonlinear numerical dispersion are discussed. In §4.2, some efforts in quantifying the dispersion considering linear materials are reviewed. The importance of the material nonlinearity in numerical dispersion and the nonlinear constitutive law used in this work are presented in §4.3 and §4.4. The numerical dispersion of waves in nonlinear solids is then studied in §4.5. Finally, several recommendations are proposed in §4.6.

4.2 Linear numerical dispersion: a brief review

For a viscoelastic solid, the one-dimensional wave equation in the frequency domain can be written as follows (Semblat and Pecker, 2009):

$$\frac{\partial^2 u(x,\omega)}{\partial x^2} + \frac{\rho\omega^2}{M^*(\omega)} u(x,\omega) = 0 \tag{4.1}$$

where u is the displacement, x the distance, ω the circular frequency, ρ the density and M^* the complex modulus.

The numerical solution of equation 4.1 can be written in the form of,

$$u_h(x,\omega) = u(0,\omega).e^{ik^h(\omega)x} \tag{4.2}$$

where u_h and k^h are the approximate displacement and discrete wavenumber depending on the frequency that is different from the exact values.

In general, the numerical wave propagation depends on the physical wavenumber, k, and the numerical properties h, element size, p polynomial order of approximation (Ihlenburg and Babuška, 1995a). For finite elements at polynomial order p, the approximate solution of the problem is written from the fundamental system of equation,

$$\cos k^h h = -\frac{S_p(K)}{T_p(K)} \tag{4.3}$$

which determines the discrete wavenumber k^h as a function of k, h and p. Where K is the normalized frequency equal to kh. S_p and T_p are rational polynomial functions of K. For example, for linear interpolation ($p = 1$), we have,

$$S(K) = 1 - \frac{K^2}{3} \qquad T(K) = -1 - \frac{K^2}{6} \tag{4.4}$$

If the exact solution is a propagating wave, the numerical solution is propagating only for normalized frequencies K below K_0, named the cutoff frequency. The magnitude of the cutoff frequency grows with the increase of approximation order.

Also, after Harari (1997), the wave resolution is measured by the number of nodal points in a wavelength and for one-dimensional linear elements it is,

$$G = \frac{2\pi}{kh} \tag{4.5}$$

In practice, one usually follows a "rule of thumb" of the form $kh = const.$. In computations with lower wavenumbers, this rule leads to sufficiently correct results. However, the quality of numerical results, deteriorates when the wavenumber k increases (Ihlenburg and Babuška, 1995b).

Babuška et al. (1997b) used an asymptotic analysis of the error, they predicted the optimal element degree distribution in sets of geometrically graded meshes. They also searched the entire class of meshes that can be created by subdivision and found the hp meshes (An adaptive hp finite element method is a method which can achieve an exponential rate of convergence through an optimal selection of the mesh size h and the degree p of the elements) with minimal error for each number of degrees of freedom, thus obtaining the sequence of true optimal meshes.

For high wavenumbers, the Helmholtz equation suffers the so-called "pollution effect". This effect is directly related to the dispersion. Deraemaeker et al. (1999) presented a method to measure the dispersion on any numerical method related to the classical Galerkin FEM. They proposed different approaches leading to solutions that do not suffer from the pollution effect in one dimension but in two and three dimensions, they proved that the pollution cannot be avoided.

Steffens and Dez (2009) proposed a simple strategy to assess the error in the numerical wavenumber of the FE solution of the Helmholtz equation. The error assessment paradigm is reverted in the sense that the exact value of the wavenumber, k, is known (it is part of the problem data) and the effort produced in the error assessment technique aims at obtaining the numerical wavenumber, k^h, as a postprocess of the numerical solution, u_h.

Harari and Hughes have applied Galerkin least-squares (GLS) technology to the Helmholtz equation for one-dimensional model problems (Thompson and Pinsky, 1995). An important feature of GLS methods is the introduction of a local mesh parameter into the variational equation that may be designed to provide accurate solutions with relatively coarse meshes. Thompson and Pinsky (1995) also developed a GLS finite element method, in which residuals in least-squares form are added to the standard Galerkin variational equation, to solve the Helmholtz equation in two-dimensions. In general problems, the direction of propagation is not known a priori. In this case, an optimal GLS parameter is found which reduces the phase error for all possible wave vector orientations over the elements.

The Galerkin/gradient least-squares is an alternative modification of the basic Galerkin formulation in which the least-squares terms contain residuals of the gradient of the governing differential equation. The performance of Galerkin/least-squares and Galerkin/gradient least-squares for problems of time-harmonic acoustics was compared on the basis of spurious numerical representation of physical phenomena by Harari (1997).

The performance of Galerkin/gradient least-squares deteriorates on non-uniform meshes. However, Galerkin/least-squares maintains its enhanced performance, exhibiting low sensitivity to transitions in mesh size, thereby reducing spurious dispersion, anisotropy and reflection in finite element analysis of time-harmonic acoustics. Based on GLS method, Harari and Nogueira (2002) proposed a method parameter that may be used for computation with both linear triangular and bilinear quadrilateral elements that improves the performance of FE computations at high wavenumbers.

Ainsworth (2004) analyzed the dispersive behavior of high order discontinuous Galerkin finite element (DGFEM) methods. For the small wavenumber limit, $hk \to 0$, he showed that the discontinuous Galerkin gives a higher order of accuracy than the standard Galerkin procedure. If the mesh is fixed and the order p is increased, he showed that the dissipation and dispersion errors decay at a super-exponential rate when the order p is much larger than hk.

Ainsworth et al. (2006) investigated two popular DGFEM schemes: the interior penalty discontinuous Galerkin finite element method applied to the second-order wave equation and a more general family of schemes applied to the corresponding first order system and they derived the dispersion error for various schemes and conjectured on the generalization to higher order approximation in space. Another example of dispersion analysis is presented by Sarmany et al. (2007).

Higher order finite elements may also reduce the numerical dispersion. Dauksher and Emery (1999) have shown that Chebyshev finite elements possess significant advantages in accuracy and in computational efficiency with respect to p-elements for an equivalent number of nodes in engineering structures.

Semblat and Brioist (2000) compared the accuracy of higher order finite elements with linear and quadratic elements. Considering the same number of degrees of freedom in the direction of propagation, the accuracy and efficiency of higher order finite elements appeared much better than that of linear and even quadratic elements.

Other methods are also capable to reduce the dispersion. Bao et al. (2004) explored the feasibility of a local spectral method, the discrete singular convolution (DSC) algorithm for solving the Helmholtz equation with high wavenumbers. Their analysis of dispersive errors indicated that the DSC algorithm yields a dispersion vanishing scheme and is accurate and efficient for solving the Helmholtz equation with high wavenumbers.

Park and Kausel (2004) characterized the numerical dispersion for both anti-plane (SH) and in-plane ($SV - P$) body waves in an unbounded medium by means of the thin-layer method

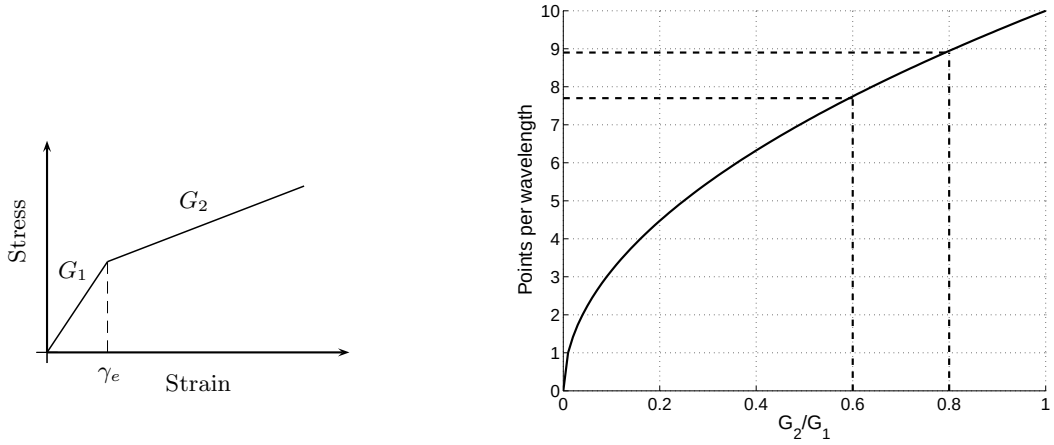

Figure 4.1: Bilinear constitutive law for elastoplastic materials (left), Number of points per wavelength vs G_2/G_1 assuming 10 points per element in the elastic behavior range (right)

(TLM) which is an effective numerical tool for the analysis of wave motions in laminated media. They developed optimal factors for this method, with the aid of which the numerical dispersion error is minimized and the accuracy of the solution improved.

Zhou and Zhou (2007) presented a time integration method with two control parameters for solving initial-value problems in dynamics that can achieve lower numerical amplitude dissipation and period dispersion than some of the existing methods, e.g. the Newmark method and Zhais approach, when the same time step size is used. Askes et al. (2008) give the recommendations for the finite element size and the time step size by means of continuum theories with additional higher-order inertia terms in order to be able to describe dispersive wave propagation.

4.3 Simple nonlinear cases

For strong dynamic loading, the maximum strains can often reach the elastic limit of the material behavior. For an elastoplastic soil behavior, the apparent wave velocity is less than that in elastic soils. Generally, we use *a rule of thumb* for numerical modeling of wave propagation where the number of points per wavelength is kept constant. Considering soil nonlinearity, with respect to the strain level, the wavelength will be decreased and the accuracy of the results will deteriorate.

4.3.1 Bilinear model

We first consider a bilinear stress-strain curve (bilinear constitutive law, Fig.4.1). In general, we chose a_1 points per wavelength in the elastic range, but if the strain level exceeds the elastic limit (γ_e), the wave velocity decreases and consequently, the wavelength is reduced. The number of points per wavelength will thus not be equal to a_1.

Assuming a constant frequency range for the wave, we can obtain the number of points per wavelength a_2 for the bilinear case in a simple manner,

$$a_2 = a_1\sqrt{\frac{G_2}{G_1}} \tag{4.6}$$

Assuming 10 points per wavelength in the elastic range, the number of points per wavelength in the plastic region are shown in Fig.4.1 (right) depending on the ratio of G_2/G_1. It means considering $a_1 = 10$ and for example, the ratio of G_2/G_1 being 0.8 or 0.6, the number of points per wavelength will be 8.9 and 7.7 respectively. Consequently, the accuracy of the results reduces and for a constant accuracy, we need more points than the classical number of points per "elastic wavelength".

4.3.2 Hyperbolic model

The hyperbolic function was one of the earliest proposition by Kondner (1963) and Hardin and Drnevich (1972b,a) to represent the relation between the shear stress and the shear strain. Kondner (1963) believed that the two-constant hyperbolic form of the stress-strain relationship that he presented is such that the ultimate shear strength of the soil is contained within the general formulation and appears in the mathematical limit of the stress as the strain becomes excessive. According to Hardin and Drnevich, the original hyperbolic function is,

$$F(\gamma) = \frac{G_0 \gamma}{1 + (G_0/\tau_{max})|\gamma|} \tag{4.7}$$

which derives in the following the shear modulus reduction curve,

$$G(\gamma) = \frac{G_0}{1 + |\gamma/\gamma_{ref}|} \tag{4.8}$$

where G_0 and τ_{max} are the low-strain shear modulus and maximum shear strain of the material and γ_{ref}, the reference strain equal to τ_{max}/G_0.

Assuming a constant frequency range for the wave, we can obtain the number of points per wavelength a_2 for this plastic behavior as,

$$a_2 = a_1 \sqrt{\frac{G_2}{G_1}} = a_1 \frac{\sqrt{1 + \frac{\gamma}{\gamma_{ref}}}}{1 + \frac{\gamma}{\gamma_{ref}}} \tag{4.9}$$

where, in this equation, γ is the strain level and γ_{ref} the reference strain level.

Figure 4.2 (left) displays the hyperbolic shear modulus reduction curves for three different materials. We assume 10 points per wavelength for the numerical simulation. For each strain level, we are able to easily obtain the wave velocity and wavelength. Figure 4.2 (right) illustrates the number of points per wavelength for different shear strain levels of these materials. For example, for the second material (number 2), less than 7 points per wavelength will be considered instead of 10 points for 0.1% of shear strain. Also, only 5 points per wavelength will be taken into account for 0.09, 0.25 and 0.7 percent of the strain respectively for the materials 3, 2 and 1.

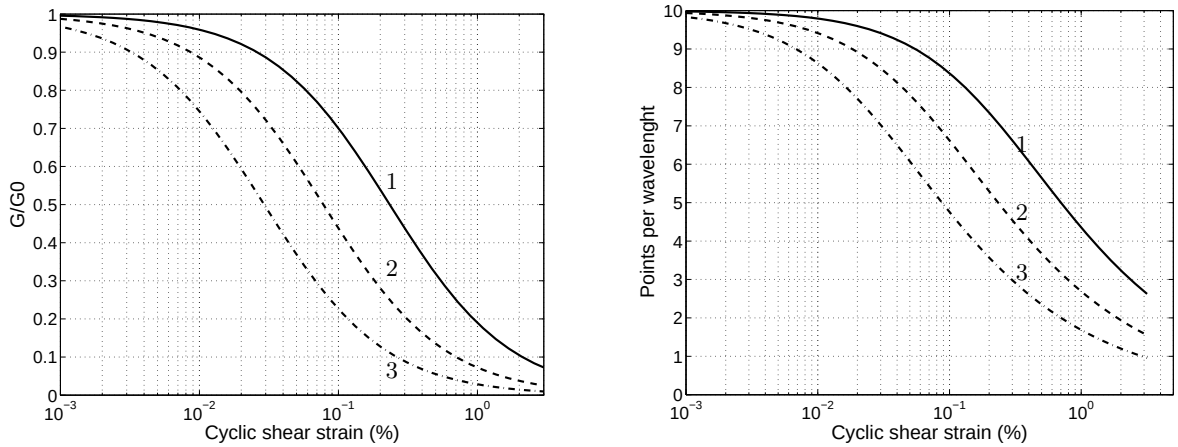

Figure 4.2: Shear modulus reduction curve for three materials 1, 2 and 3 (left) and the number of points per wavelength for materials 1, 2 and 3 (right) vs cyclic shear strain

Therefore, for a given excitation level, one should take into account more points per "elastic wavelength" (limit of elastic behavior) to reach a target error in the dynamic response of

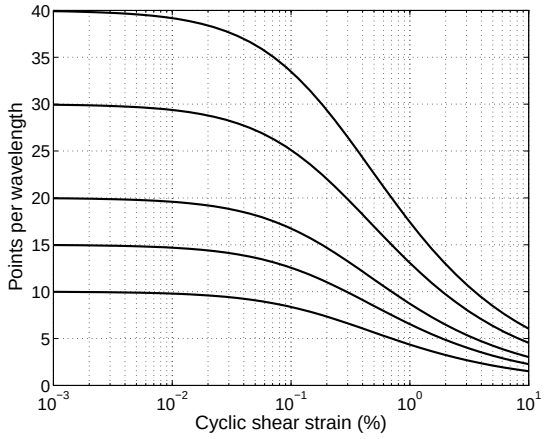

Figure 4.3: Different numbers of the points per "elastic wavelength" for different shear strain levels

elastoplastic materials. For instance, Fig.4.3 displays five different choices of initial "elastic wavelength" and their modifications with respect to the strain level for material 2.

In each case, we reach 10 points per wavelength for 0.3, 0.7, 1.8 and 3 percent of the strain level respectively for the choices of the 15, 20, 30 and 40 points per elastic wavelength. Also, the initial choices (the initial number of the points per elastic wavelength equal to the 10, 15, 20, 30 and 40 points) are divided by two at approximately 0.7% of the strain level. As mentioned, it is difficult to know the best element size in advance. If a very small one is chosen, the numerical cost will be large, therefore, an optimum element size should be considered. This optimum value depends on the constitutive law of the material and the strain or excitation level. For each material and each dynamic loading, it may be different and it is not possible to give a general rule for all materials.

This simple demonstration motivates this study to investigate the effect of the material nonlinearity on the numerical dispersion. Different meshes with respect to the number of points per wavelength are considered. The effect of the level of nonlinearity on the results is studied. In the next section the elastoplastic nonlinear model applied in this work is presented.

4.4 Nonlinear constitutive model

The nonlinear stress-strain behavior of soils can be represented more accurately by cyclic nonlinear models that follow the actual stress-strain path during cyclic loading (Kramer, 1996). Such models are able to represent the shear strength of the soil. A variety of cyclic nonlinear models have been developed (see also §3.2); all are characterized by a backbone curve and a series of rules that govern unloading-reloading behavior, stiffness degradation, and other effects. The stress-strain model used in this work was originally proposed by Iwan (1967) and used by Joyner and Chen (1975) to compute the nonlinear ground response in earthquakes (see also §3.2.5). They presented a method based on the Iwan model that accounts for the nonlinear, hysteretic behavior of soils and offers considerable flexibility for incorporating laboratory data on soil behavior (Joyner, 1975). Joyner et al. (1981) improved the model to be capable of generating the energy dissipation in small strain levels.

This form of model has a rich history of applications to model the material plasticity, structural dynamics and vibrations, control systems and magnetics. After Segalman and Starr (2008), what are now often referred to as Iwan model might correctly be called Masing-Prandtl-Ishlinskii-Iwan (*MPII*) models. They showed that for any material or structural model able to be presented as a Masing model, there exists a unique parallel-series (displacement based) Iwan system that

characterizes that model as a function of displacement history.

The MPII model (see also §3.3) is used and implemented in the framework of the Finite Element method to investigate the effect of soil nonlinearity on wave propagation and numerical dispersion. The model is composed of simple linear springs and Coulomb friction elements arranged as shown in Fig.4.4.

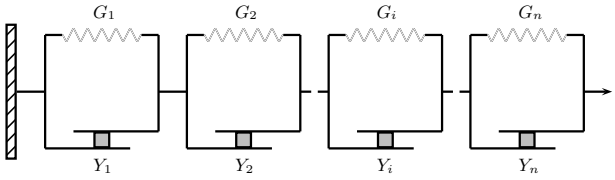

Figure 4.4: One dimentional constitutive MPII model

The friction elements remain locked until the stress exceeds the yield stress Y_i. Generally, the yield stress of the first element, Y_1, is set to zero for simulating the elastic behavior of the soil. By appropriate specification of the spring constants G_i and the yield stresses Y_i, we are able to model a broad range of material behavior as dictated by laboratory experiments (Joyner and Chen, 1975).

The accuracy of the model depends on the number of elements, N, but it affects the calculation duration and an optimal value should be found. At any given time, all the elements up to a certain index yield and all those above will not. The Y_i are chosen to cover the range of stresses that the system is expected to experience and are distributed so that the initial loading curve can be faithfully recovered. It should be noted that the rheological model used here does not involve any viscous damping, and as a result the stress depends on the strain (and strain history) but not on the strain rate. Therefore, the energy dissipation per cycle does not depend upon the frequency.

The relationship between the mean stress and the mean strain is assumed elastic. The deviatoric stress σ_{ij} is considered as a vector in a nine-dimensional space, and a family of yield surfaces is postulated, represented by the yield functions,

$$F_n(\sigma_{ij} - \alpha_{nij}) = k_n^2 \tag{4.10}$$

where k_n is a constant characteristic of the nth surface and α_{nij} represents the origin of the surfaces. The total deviatoric strain e_{ij} is the sum of an elastic strain e_{Eij} and the plastic strain components e_{Pij} each associated with the nth yield surface. Kinematic hardening of the Prager type is also assumed (More details are presented in §3.3).

The parameter k_n describes the yield surface and represents the initial yield stress in simple shear. The values of k_n are chosen in order to fit laboratory data. Knowing the increment of deviatoric strain, the incremental deviatoric stress may be obtained directly by this model. The MPII model (see also §3.3 and §3.3.3) is implemented and numerically validated (Gandomzadeh et al., 2010) in the framework of the FEM in the CESAR-LCPC numerical tool (Humbert et al., 2005) and is used to investigate the numerical dispersion in case of the nonlinear materials, soils in this case.

Figure 4.5 illustrates the stress-strain curve obtained by this model for a single component sinusoidal strain with increasing amplitude (Simple shear loading). It means that only the ε_{xz} and ε_{zx} members of the strain matrix are nonzero. The red line shows the monotonic loading curve, known as the backbone curve.

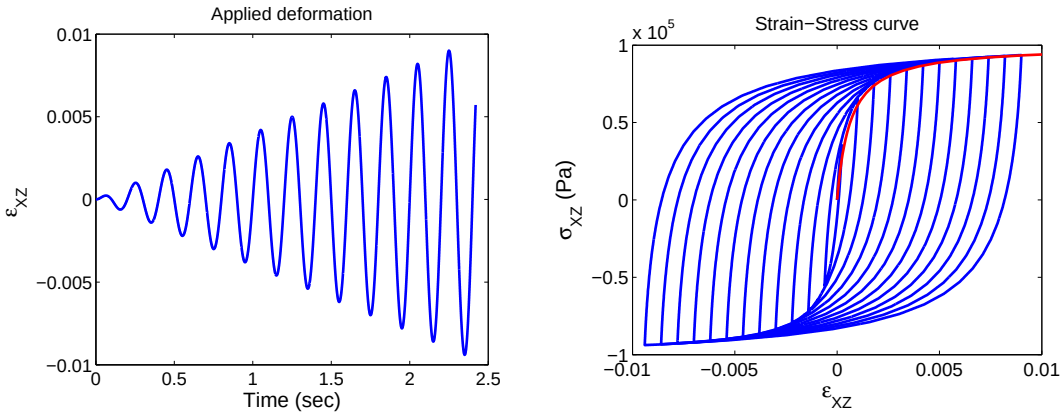

(a) Applied single component sinusoidal strain (b) stress-strain curve

Figure 4.5: Applied single component sinusoidal strain (left) and the stress-strain curve obtained using the implemented MPII model (right)

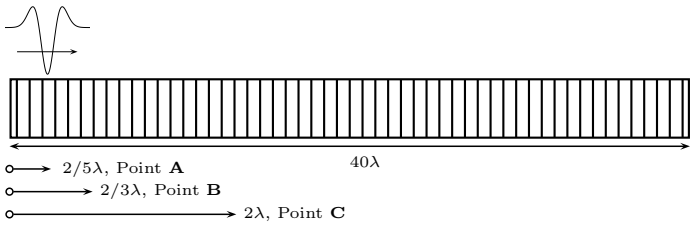

Figure 4.6: Finite element model and the position of the three control points (A, B and C)

4.5 Numerical dispersion in nonlinear soils

4.5.1 Features of the Finite Element model

The Finite Element method (Hughes, 1987) is used to investigate the numerical dispersion for wave propagation. The second order implicit Newmark scheme is used to integrate the equation of motion in time (CESAR-LCPC software, Humbert et al. (2005)). The unconditional stability coefficients are considered in all the simulations (0.25 as β and 0.5 as α). The Newton-Raphson algorithm is combined to Newmark scheme to solve the nonlinear dynamic problem. In this work, we are focusing on one dimensional wave propagation. A 40λ (λ : wavelength) long medium is considered for this purpose (Fig.4.6).

A 2^{nd}-order Ricker wavelet is applied at the left boundary of the model for different strain levels. The central period of the wavelet is $0.2sec$. The time duration of the input motion is enough for the wave to reach the end of the 40λ model.

Eight different meshes are considered for this model. The element size per wavelength ratios are shown in table 4.1 for these eight meshes. To investigate the numerical dispersion and compare the results, three control points are considered at $2/5\lambda$, $2/3\lambda$ and 2λ from the left of the model. Henceforth, they are named respectively, points A, B and C (Fig.4.6).

Model number	1	2	3	4	5	6	7	8
$\frac{\Delta h}{\lambda}$	$\frac{2}{3}$	$\frac{1}{3}$	$\frac{1}{5}$	$\frac{1}{6}$	$\frac{2}{15}$	$\frac{1}{10}$	$\frac{1}{15}$	$\frac{1}{30}$

Table 4.1: Element size per wavelength ratio for 8 different meshes

The density, shear wave velocity and the Poisson coefficient of the soil are respectively

$1900Kg/m^3$, $150m/s$ and 0.3. The shear strain modulus reduction curve of the soil is similar to the material 2 presented in §4.3.2 and shown in Fig.4.2.

In the next section we will study the wave propagation with respect to the element size per wavelength ratio.

4.5.2 Wave propagation along the model

The MPII model presented in §4.4 is used to investigate the numerical dispersion in nonlinear media. For the eight meshes of Table 4.1, different dynamic analyses are performed. First, a 50-spring constitutive model is used. Figure 4.7 displays the wave form (displacement) at different times, during the wave propagation. These curves clearly show that the solution changes significantly depending on the mesh grid. Comparing the amplitude and the apparent velocity, we can conclude that by selecting a lower number of points per wavelength, the model underestimates the amplitude and overestimates the apparent velocity. In nonlinear media, the residual displacement can be produced and makes the numerical dispersion more complicated than in linear media. Figure 4.7 shows that the models with less elements underestimate the residual displacement. This means that they tend to work like a linear model. But, the dissipation is more important for coarse meshes, because they dissipate the energy of the motion faster, and lower energy remains during the wave propagation, and it could be the reason of lower residual displacement. Therefore, one may conclude that the coarse meshes behave more nonlinear than fine meshes. Consequently, as it is observed, it is not easy to understand exactly which model acts more nonlinearly.

The frequency content of the waves is also different between meshes that makes the problem more complicated. In this example, the model with 30 points per wavelength gives the lowest numerical error. We observe that even for 15 points per wavelength, at the end of the propagation a little disturbance may be observed.

We can also investigate the effect of the number of springs in the constitutive model. Two other analyses are performed considering 10- and 5-spring constitutive models. The same input motion is applied and the same meshes are used. The wave forms during the propagation for 10-spring and 5-spring models are shown respectively in Fig.4.8 and Fig.4.9. Comparing the wave forms with 50-spring constitutive model, the residual displacement decreases. Also, the amplitude in the negative part is underestimated compared to Fig.4.7, but in the positive part, specially for the 5-spring model, the amplitude increases. In addition, the reduction of the wave amplitude during the propagation through the media is stronger for the 50-spring model than for the two other models. This suggests that when the number of springs in the constitutive law decreases, the result is more linear.

Changing the amplitude of the input motion, the level of nonlinearity will be modified in the media. The wave form (displacement) during the propagation is compared for another input motion with smaller amplitude. As the amplitude of the input motion decreases, a lower level of nonlinearity is expected. The results are shown in Fig.4.10 for a 50-spring model. Comparing Fig.4.7 and 4.10, the residual displacement decreases, and the apparent velocity increases. We can also qualitatively conclude that the numerical error and consequently the numerical dispersion is more important for higher levels of nonlinearity.

The question is now “what could be the origin of these differences in the results for different models?”. In nonlinear models, the strain level and the dissipated energy during the propagation play an important role that could be critical. In the following, we will investigate this issue.

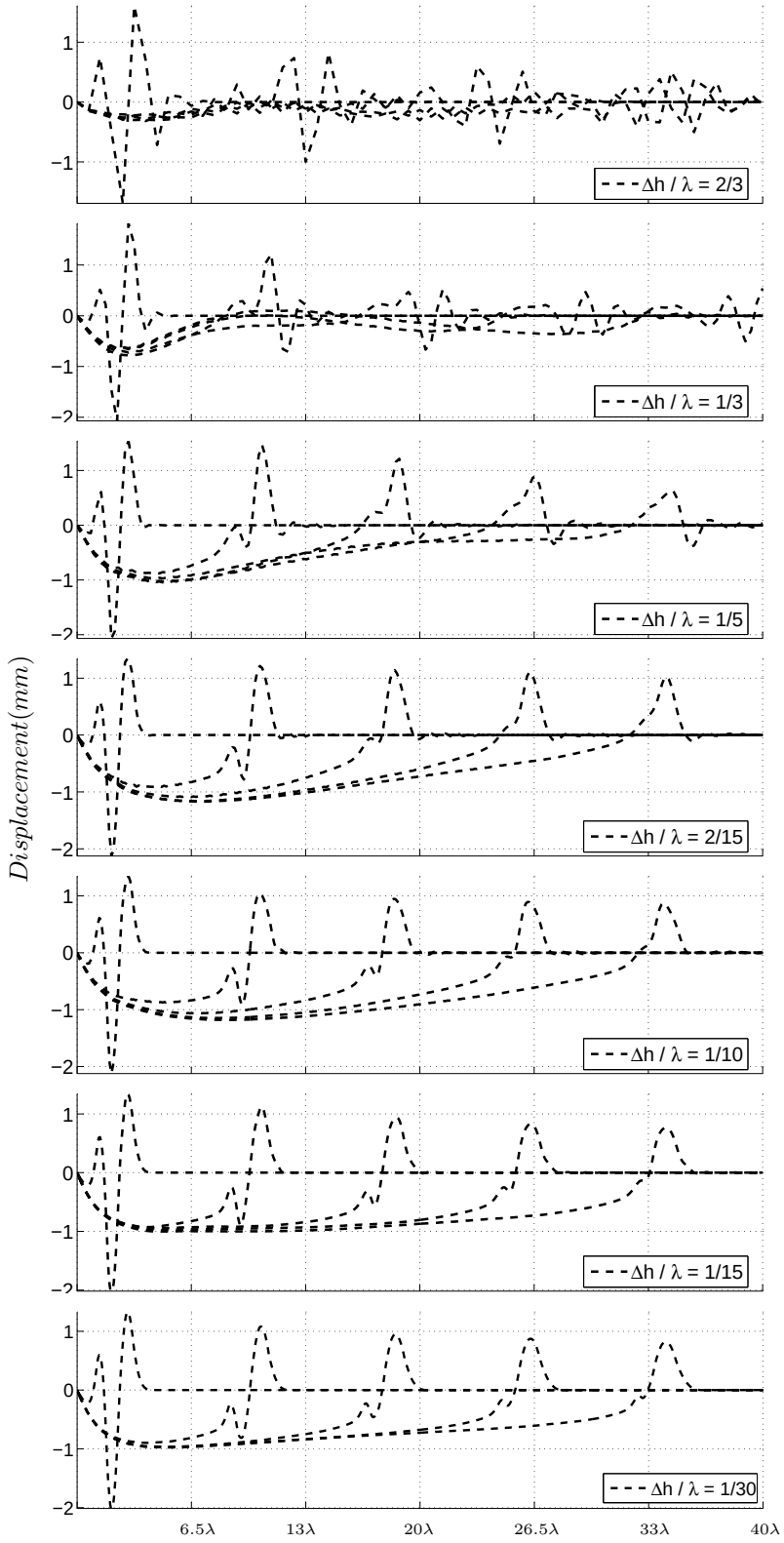

Figure 4.7: Wave forms (displacements) for different models at various times in the 40λ nonlinear medium considering a 50-spring MPII model

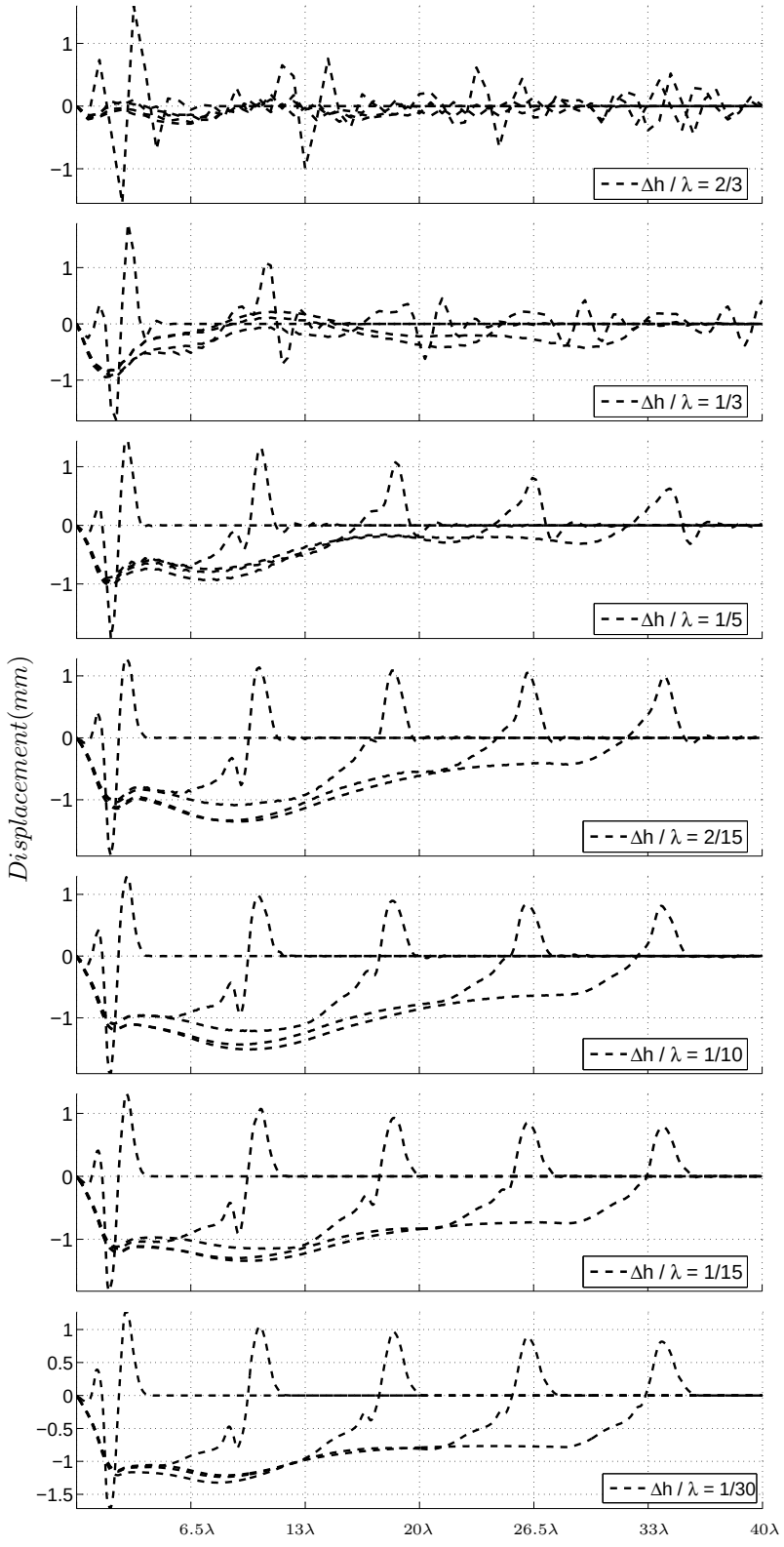

Figure 4.8: Wave forms (displacements) for different models at various times in the 40λ nonlinear medium considering a 10-spring MPII model

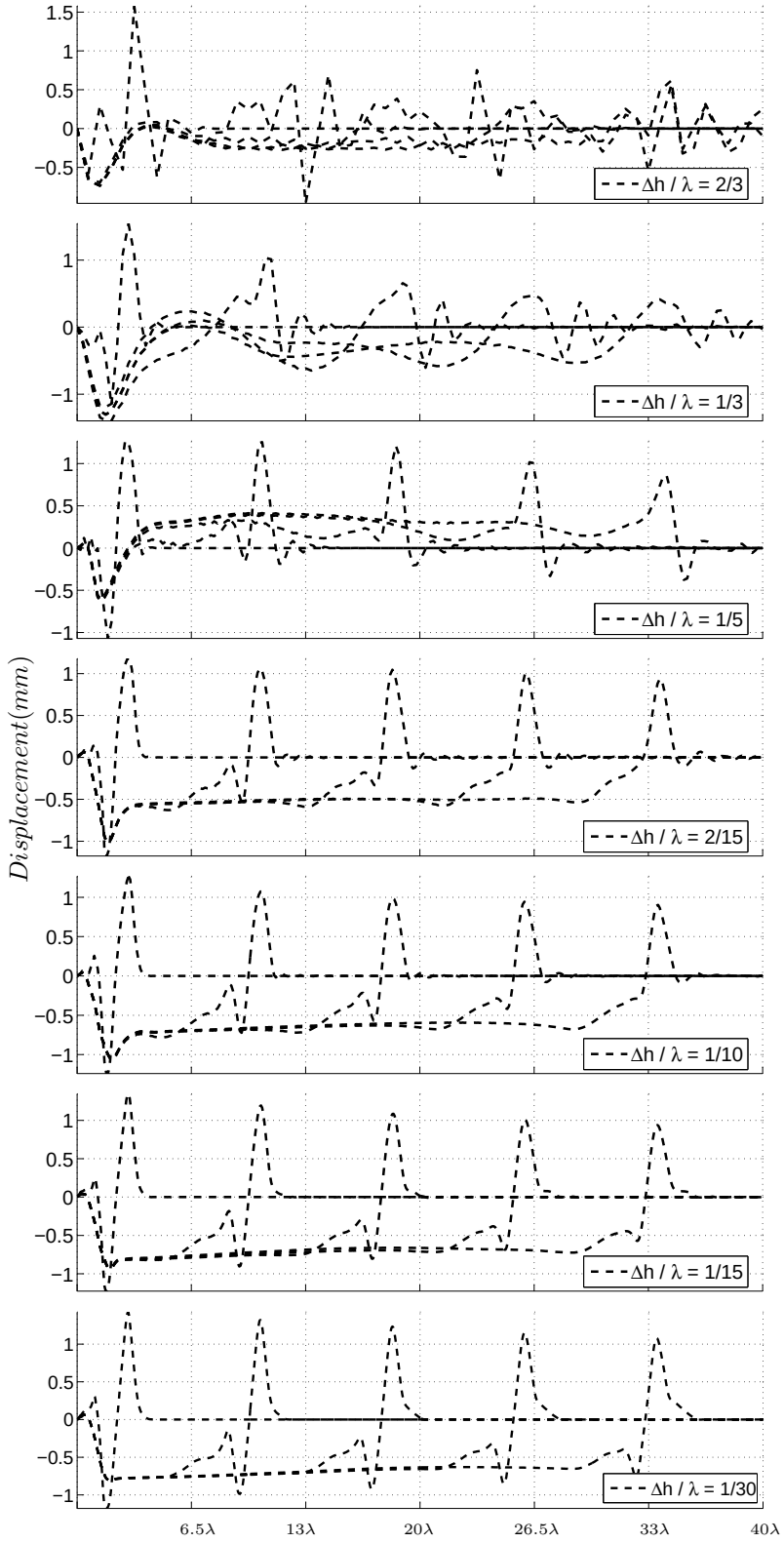

Figure 4.9: Wave forms (displacements) for different models at various times in the 40λ nonlinear medium considering a 5-spring MPII model

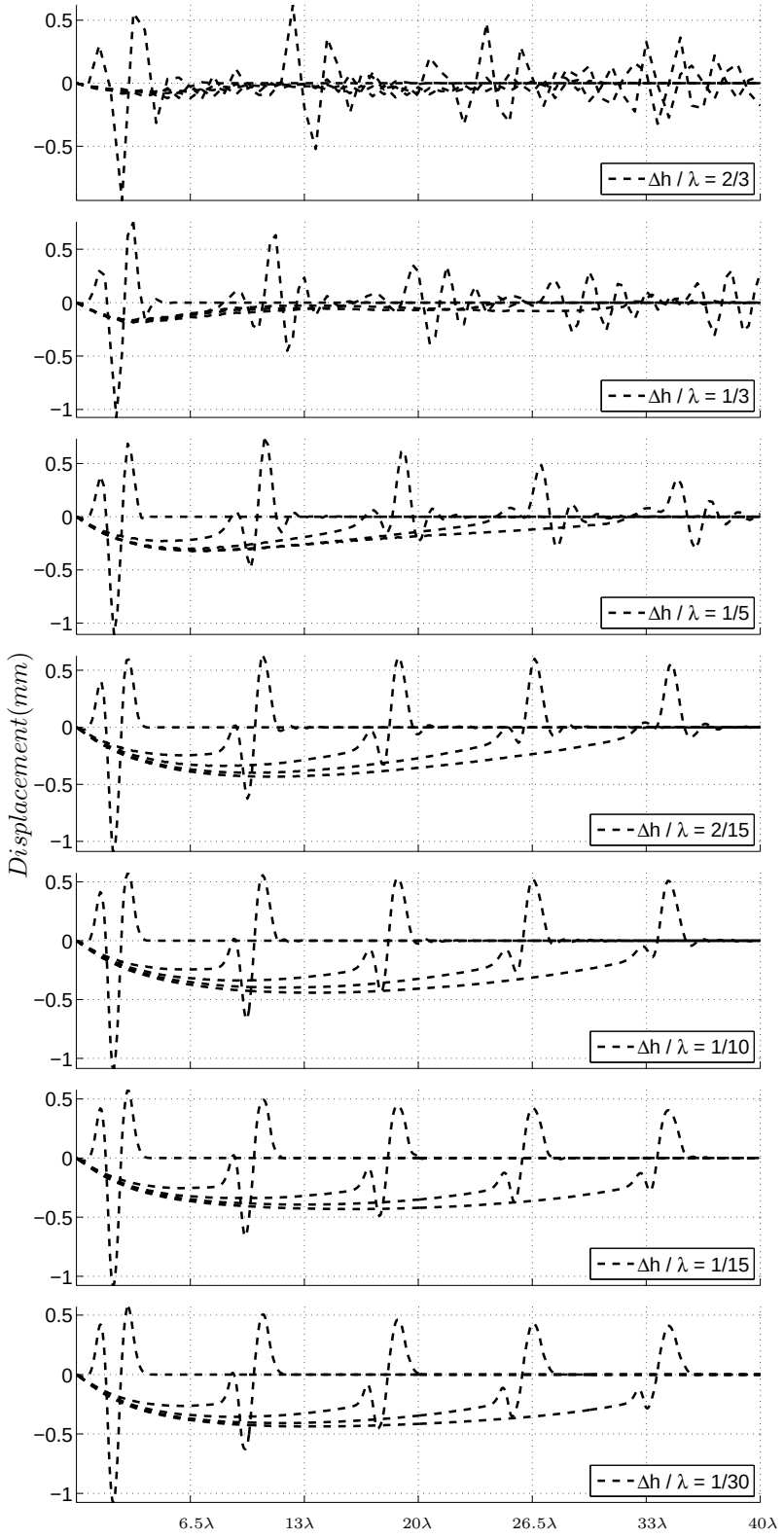

Figure 4.10: Wave forms for different models at various times in the 40λ nonlinear medium considering a 50-spring MPII model (the strain level is smaller than three previous figures)

4.5.3 Effect of the nonlinear dispersion on the stress-strain loops

The model introduced in §4.4 is used to investigate the numerical dispersion. The stress-strain curves are compared between different models presented in (Table 4.1). In this section, the input Ricker wavelet and its amplitude are the same for all meshes. The maximum amplitude of the input motion is equivalent to a 0.5g PGA.

As the meshes are different, it is difficult to find a point at the same coordinate for all these meshes. But, we try to compare the results at least at the three control points A, B and C, already presented in Fig.4.6.

4.5.3.1 50-spring MPII model

First, we try to choose a point at $2/3\lambda$ (point B) from the left boundary of the model (Fig.4.6). In this part, the number of springs of the constitutive model is considered to be 50 in spite of being sure that the results obtained by the constitutive model are stabilized. The results are compared to the 100-spring model and the differences are negligible. It should be mentioned that Joyner and Chen (1975) also used 50 springs for their computations. The stress-strain curve at the point $4/3\lambda$ (left) and the control point B (right) for the meshes with $\Delta h/\lambda$ equal to 2/3 and 1/3 are shown in Fig.4.11.

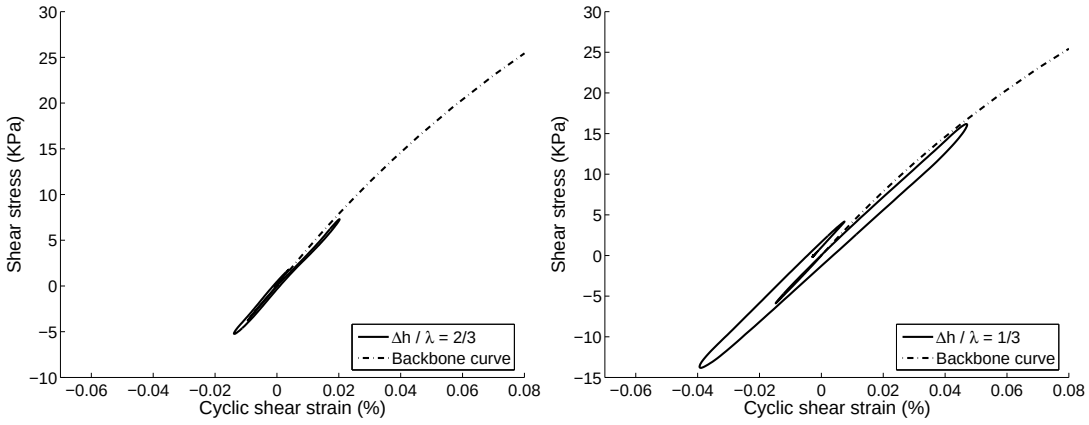

Figure 4.11: Stress-strain curve for the 50-spring model at the control point $4/3\lambda$ for $\Delta h/\lambda$ equal to 2/3 (left) and at the control point B for $\Delta h/\lambda$ equal to 1/3 (right)

The same curves are presented in Fig.4.12 for the meshes with $\Delta h/\lambda$ equal to 1/5 and 1/6. We observe that the shape and the maximum strain change with the number of elements. It means that the level of non linearity depends on the way that the model is discretized. Therefore, the discretization is more important for nonlinear material than for linear ones.

The stress-strain curves for the meshes with $\Delta h/\lambda$ equal to 2/15 and 1/10 are presented in Fig.4.13 and for the most finest meshes, $\Delta h/\lambda$ equal to 1/15 and 1/30, the curves are displayed in Fig.4.14.

Comparing the maximum positive and negative strains, the level of non linearity increases by increasing $\Delta h/\lambda$. It means, the coarse meshes are more dissipative than fine meshes, because the amplitude that arrives at the control point in coarse meshes is less than in fine ones. Specially, in the negative region of strain, the strain level discrepancy is totally different and keeps stabilizing for fine meshes. Figure 4.15 displays the maximum positive and negative strains for all the 8 meshes at the control point B. As already mentioned, the choice of the control point is not easy, because it is necessary to have a node for all the meshes at the same place. It should not also be too far from the source of the input motion as the material is non linear (the amplitude of the wave decreases rapidly). The same synthesis is done for two other control points A and C.

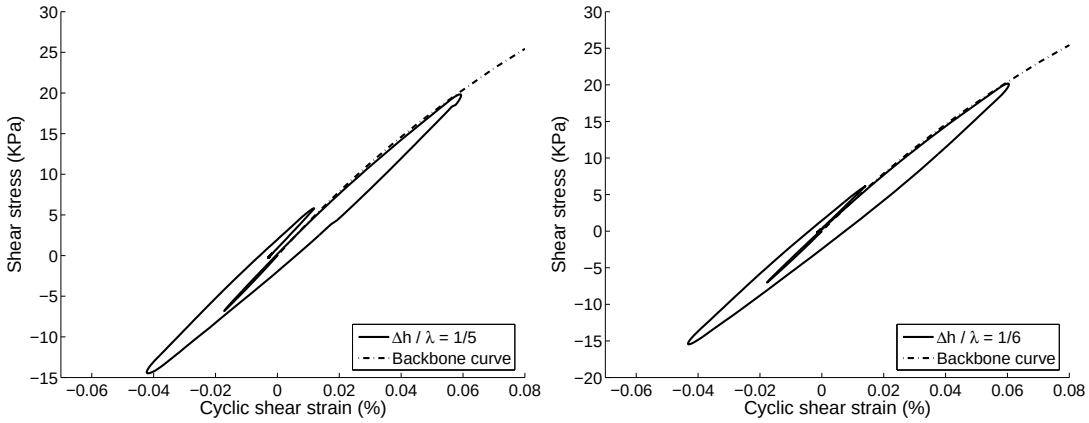

Figure 4.12: Stress-strain curve for the 50-spring model at the control point $3/5\lambda$ for $\Delta h/\lambda$ equal to 1/5 (left) and at the control point B for $\Delta h/\lambda$ equal to 1/6 (right)

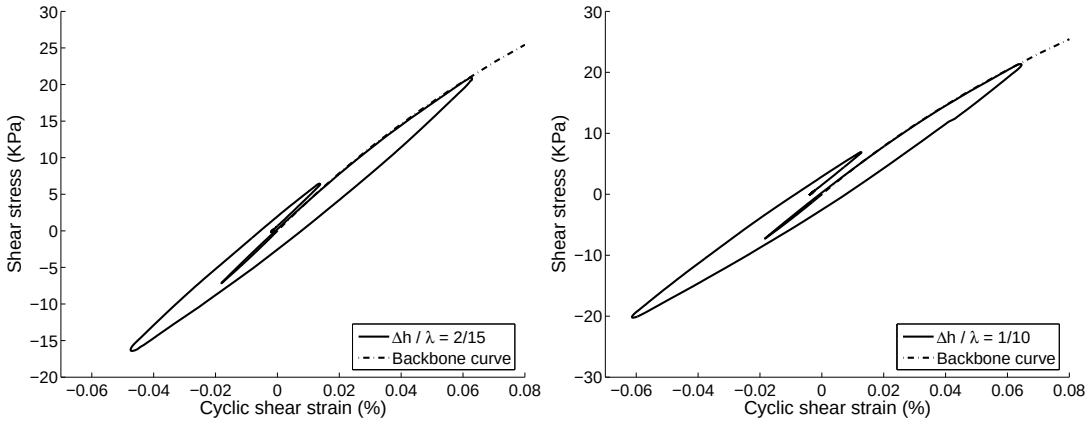

Figure 4.13: Stress-strain curve for the 50-spring model at the control point B for $\Delta h/\lambda$ equal to 2/15 (left) and 1/10 (right)

It is clear that at the control point A, we do not have nodes for all meshes.

Based on the literature, for linear materials, the minimum number of points per wavelength should be 6 and the recommended value is 10. We observe in Fig.4.15 (right) that at the control point B there is a 29% difference between 6 and 10 points per wavelength, 36% between 6 and 30 points per wavelength and finally 9% between 10 and 30 points. This means that the 6 points per wavelength condition is not acceptable for non linear materials. The difference between 10 and 30 points per wavelength is also non negligible. A similar discrepancy is seen at the other control point A for the positive and negative strains between 10 and 30 points per wavelength. At the control point C, neglecting the $\Delta h/\lambda$ more than 0.3, we observe that the results are closer comparing to other control points, specially for the negative strain. As this control point is far from the source, the amplitude decreases before reaching this point and the results are less sensitive to the number of points per wavelength.

In general, the maximum strain is obtained at a given time and depends on the shape of the input motion. Therefore, another criterion should be found to compare the results. The total dissipated energy (see §5 for the way the energy dissipation is computed) during the wave propagation may be a better criterion to compare the results. Figure 4.16 illustrates the dissipated energy at each control point during the wave propagation for different meshes. At point A, the difference between 10 and 30 points per wavelength ($\Delta h/\lambda$ equal to 1/10 and 1/30)

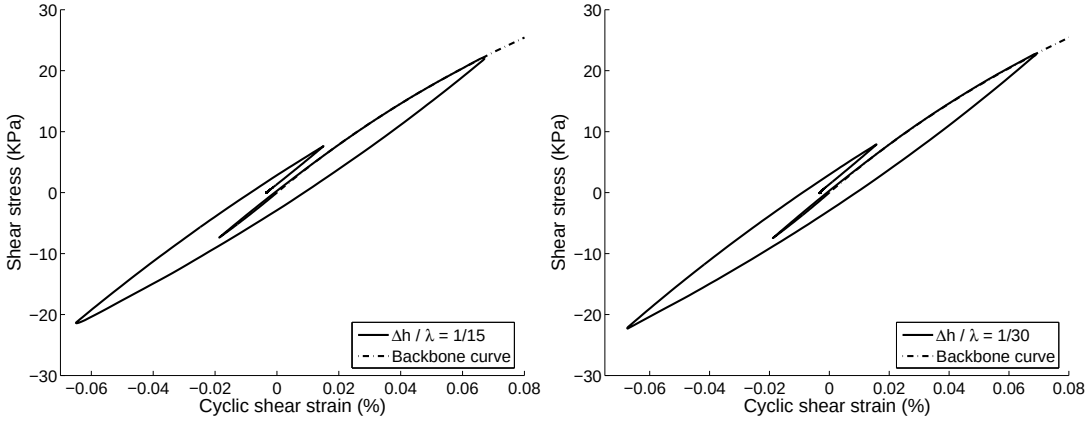

Figure 4.14: a) Stress-strain curve for the 50-spring model at the control point B for $\Delta h/\lambda$ equal to 1/15 (left) and 1/30 (right)

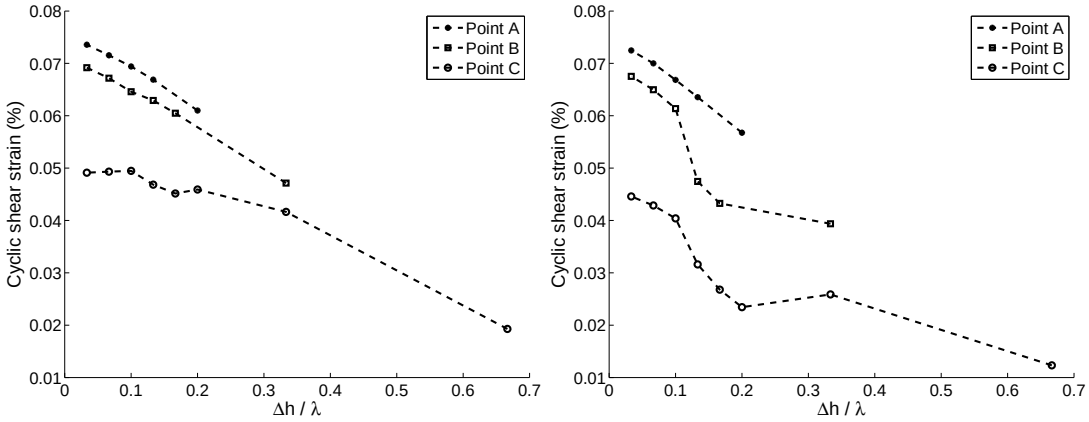

Figure 4.15: Maximum positive (right) and negative (left) strains at 3 different control points of the model (A, B and C) for all the meshes

is 12%, and between 15 and 30 points per wavelength it is 6%. This means that 10 points per wavelength is not sufficient and one should use finer meshes. At the control point B, the differences are more significant. A 16% discrepancy between 10 and 30, 33% between 6 and 30, 20% between 6 and 10 and finally 5% between 15 and 30 points per wavelength are observed. Once again, we observe that 10 points per wavelength is not enough.

These results are only for the selected material and the input motion level and will be different for other materials. It is not possible to drive a general rule in case of non linear materials. Afterward, in §4.5.4, we will look at other levels of excitation to investigate the effect of the strain level on numerical dispersion. Another possible approximation or simplification of this type of constitutive model may be the number of springs or on the other hand the number of discretization of the shear modulus reduction curve for the used constitutive model. In nonlinear problems, the total time of the analysis is very important. Increasing the number of springs will increase the calculation duration. So, in many cases we decrease the number of springs, consequently, the results will be modified. In the next section, we will focus on this type of approximation.

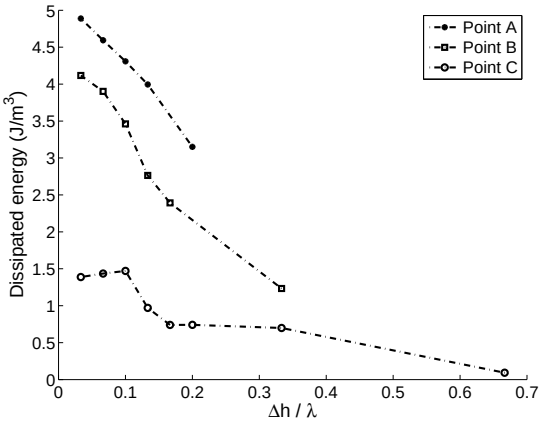

Figure 4.16: Dissipated energy for each stress-strain curves of 8 meshes at three different control points (A, B and C)

4.5.3.2 Effect of the spring numbers of the MPII model

First, 10 springs are considered instead of 50 springs in the MPII model. The input motion is unchanged in order to compare the results with various numbers of springs. Figure 4.17 presents the stress-strain curves at the control point B for 3 (left) and 6 (right) points per wavelength.

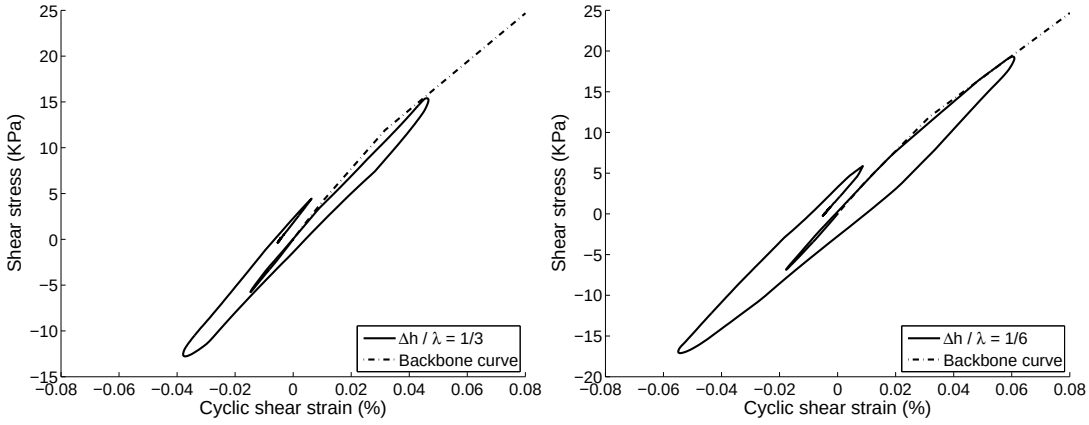

Figure 4.17: Stress-strain curves for the 10-spring model at the control point B, for $\Delta h/\lambda$ equal to 1/3 (left) and 1/6 (right)

Comparing to the 50-spring model, similar results are obtained here. When the number of points per wavelength increases the level of non linearity increases. The stress-strain curves for $\Delta h/\lambda$ equal to 1/10 and 1/30 are displayed in Fig.4.18. Comparing the maximum shear strain for 30 points per wavelength between the 50-spring and the 10-spring models, it seems that considering more springs increases the level of non linearity.

The results of the 10-spring model are summarized in Fig.4.19. In this case, we have approximately the same trend comparing to the 50-spring model. For example, there is a 8% discrepancy between 10 and 30 points per wavelength at the second control point B for the maximum positive strain and 12.5% for the negative one. This means that the material non linearity decreases for a larger number of points per wavelength.

Figure 4.20 displays the stress-strain curves of a 5-spring MPII model at point A.

Similar analyses are performed with a 5-spring model applying the same Ricker wavelet with the same amplitude and finally the results are summarized in Fig.4.21. The first difference is

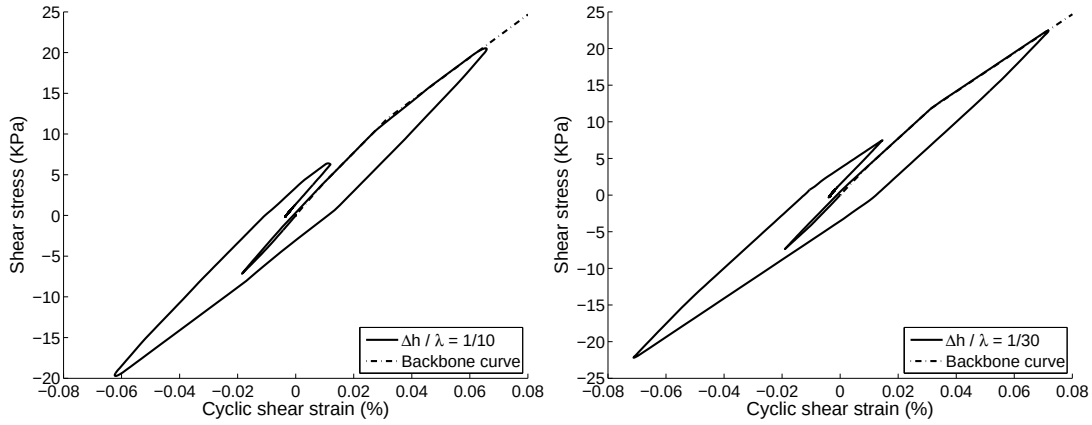

Figure 4.18: Stress-strain curves for the 10-spring model at the control point B, for $\Delta h/\lambda$ equal to 1/10 (left) and 1/30 (right)

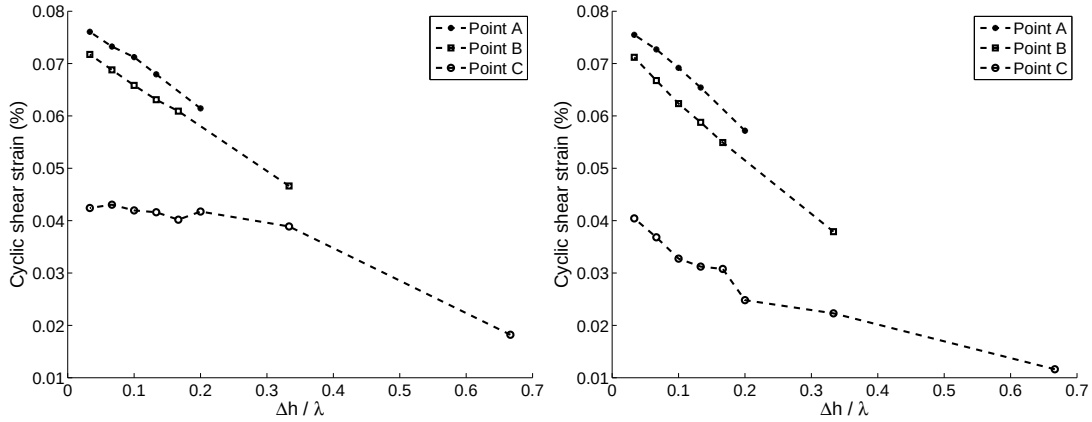

Figure 4.19: Maximum positive (left) and negative (right) strain at the three different control points of the model (A, B and C) for all the meshes and the 10-spring constitutive model

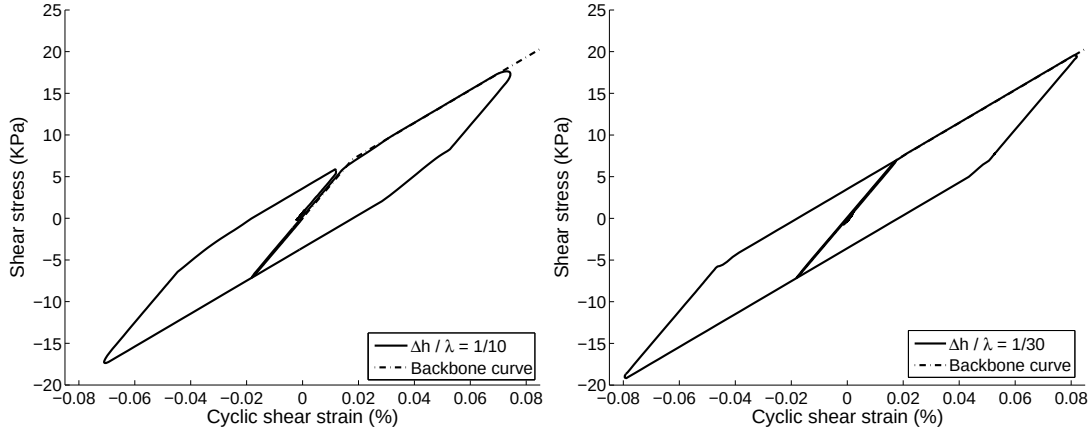

Figure 4.20: Stress-strain curves for the 5-spring model at the control point A, for $\Delta h/\lambda$ equal to 1/10 (left) and 1/30 (right)

the maximum shear strain with comparing the results to the 10 and 50-spring models. This means that the material seems less non linear. The second is that the slope of the lines are more severe than for the 10 and 50-spring models. Consequently, the numerical dispersion is more important in this case.

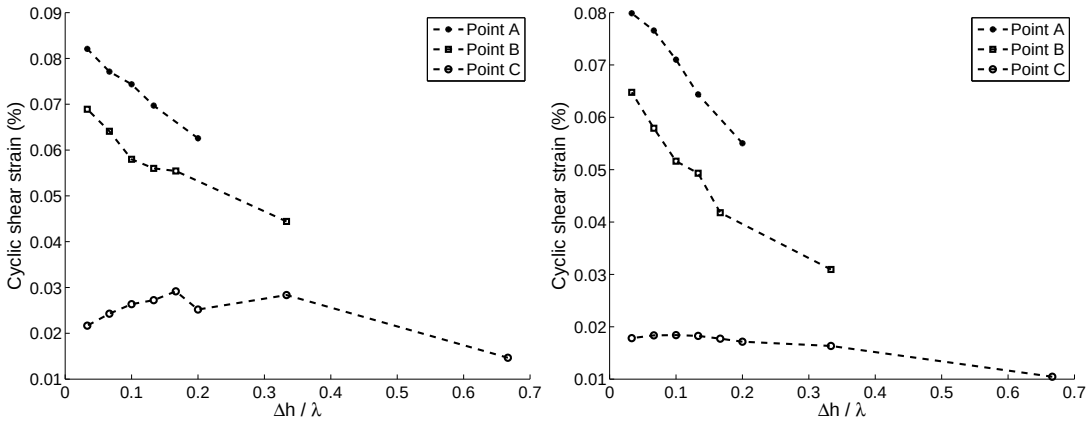

Figure 4.21: Maximum positive (left) and negative (right) strain at the three different control points of the model (A, B and C) for all the meshes and the 5-spring constitutive model

For example, there is 16% discrepancy between the 10 and 30 points per wavelength meshes for the negative strain at the control point B and 20% at the same control point for the positive strain. Consequently, one should be aware of the discretization of the model and the choice of the constitutive law. We can also take a look at the dissipated energy during the propagation at the three control points. Figure 4.22 illustrates the energy dissipation during the wave propagation for all the 8 meshes. Comparing with Fig.4.16, it shows that the dissipated energy increases when decreasing the number of the springs of the MPII model. For example, at the control point A, 4.1 J/m^3 energy is dissipated with 50-spring model and 5.45 and 8.2 J/m^3 with 10 and 5-spring models. This means more energy reaches this point in case of 5-spring model, consequently the material behavior is less non linear decreasing the number of springs.

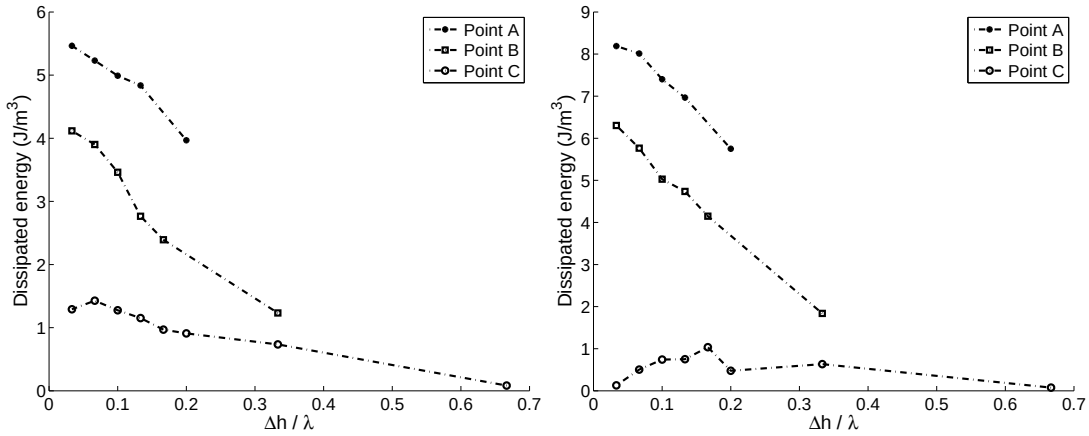

Figure 4.22: Dissipated energy for each stress-strain curve of the 8 meshes at the three different control points (A, B and C) for the 10-spring (left) and the 5-spring (right) models

Input strain level	L.1	L.2	L.3	L.4	L.5
Equivalent PGA	0.7g	0.5g	0.2g	0.1	0.05g

Table 4.2: Equivalent PGA of different selected strain levels

4.5.4 Numerical dispersion in nonlinear media for various input strain levels

4.5.4.1 50-spring constitutive model

In this section, different input strain levels are applied to the selected numerical model to investigate the effect of the strain level on numerical dispersion in nonlinear media. It is obvious that the larger the amplitude of the input motion, the stronger the level of nonlinearity. Five different input strain levels are considered (Table 4.2). All the results in the previous sections are obtained considering the second input strain level (L.2).

The procedure detailed in §4.5.3 is repeated for these five different input strain levels and for various numbers of springs in the nonlinear model. The maximum positive strain during the wave propagation is shown in Fig.4.23 at the three different control points (A, B and C) and the five different input strain levels (L.1 to L.5).

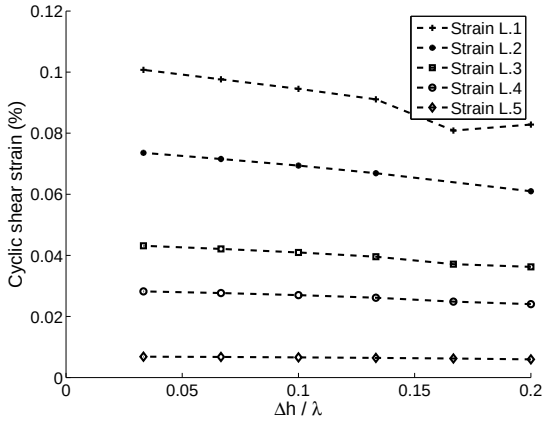

(a) Maximum positive strain at the control point A for all the meshes

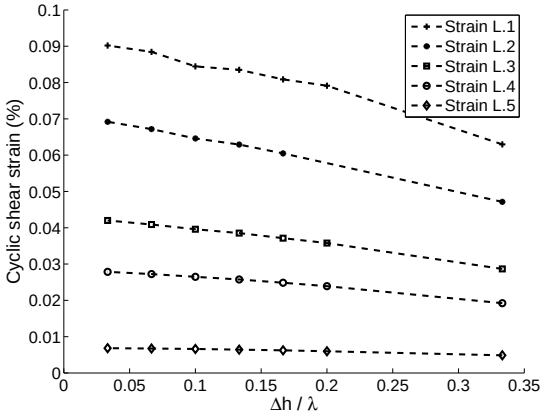

(b) Maximum positive strain at the control point B for all the meshes

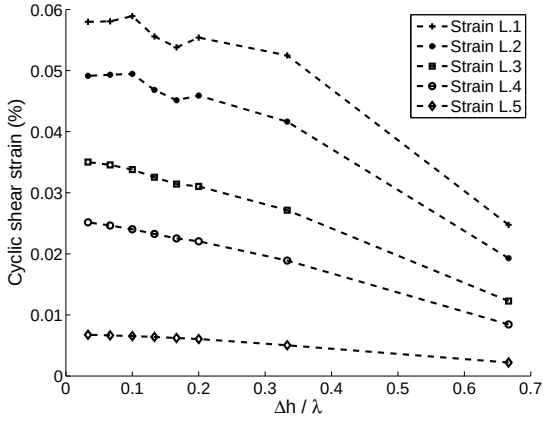

(c) Maximum positive strain at the control point C for all the meshes

Figure 4.23: Maximum positive strain at the three different control points of the model (A, B and C) for all the meshes for the 50-spring constitutive model and the various input strain levels

We observe that for larger input strain levels, the discrepancy between the different meshes

increases. This means the slope of each line increases by increasing the input strain level. This trend is observed for all the control points. Consequently, the larger the nonlinearity, the stronger the numerical dispersion.

The same results are illustrated in Fig.4.24 for the maximum negative strain. The slopes of the lines for the negative strain are stronger than for the positive one. Some irregularities are observed for high strain levels results especially at the control point C. The distance is the same but depending on the number of points per wavelength, the energy dissipation is different and irregular maximum strains are obtained at the control point C.

To have a better comparison, the difference between the results of the 10 and 30 points per wavelength models are calculated for various inputs at different control points. The difference is called here the "error". To estimate this error, the difference between the maximum strain with 10 and 30 points per wavelength models is calculated and is divided by the maximum strain with 30 point per wavelength model (reference case). Figure 4.25 displays the computed error of the maximum positive and negative strain at the three control points A, B and C. In the horizontal axis, the related input acceleration of each analysis is shown.

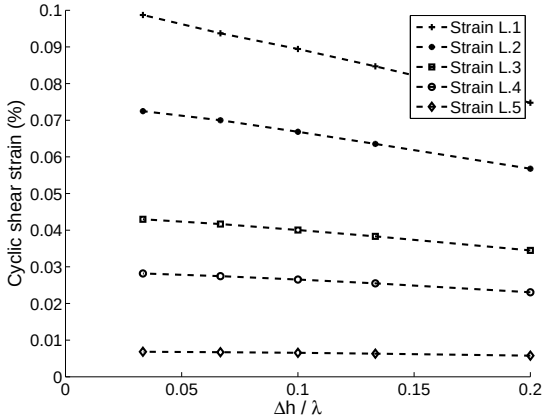

(a) Maximum negative strain at the control point A for all the meshes

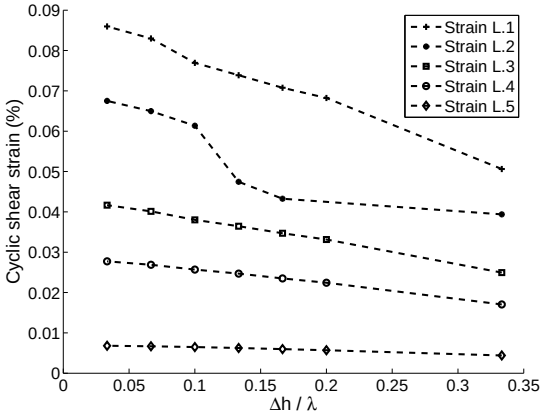

(b) Maximum negative strain at the control point B for all the meshes

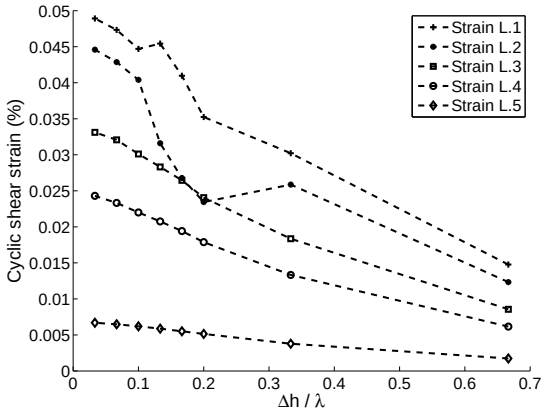

(c) Maximum negative strain at the control point C for all the meshes

Figure 4.24: Maximum negative strain at the three different control points of the model (A, B and C) for all the meshes for the 50-spring constitutive model and the various input strain levels

According to the results shown in Fig.4.25, the related error reach 11% for the maximum negative strain in the investigated range of acceleration. At the control points A and B, the error keeps increasing and the numerical dispersion is stronger.

It is obvious that increasing shear strain, the shear modulus decreases. This issue becomes more important depending on the form of the shear modulus reduction curve. In this work,

a hyperbolic model (Fig.4.2) is chosen to describe the shear modulus reduction curve, but any experimental curve can be used. As we observe in Fig.4.2, any difference in the strain level could change strongly the shear modulus. Consequently, the numerical dispersion may be critical.

Related to any change in the strain level, a new shear modulus is obtained and the wave velocity is modified. Consequently, this modification changes the wavelength and then the initial selected number of points per wavelength will be changed. Therefore, one should be aware of the choice of the number of elements.

At the control point C, the computed error is stabilized but is not negligible. Part of the energy is dissipated before reaching this point. Therefore, the level of nonlinearity decreases and the material behaves less nonlinear. Consequently, the results are less sensitive to the amplitude of the input motion.

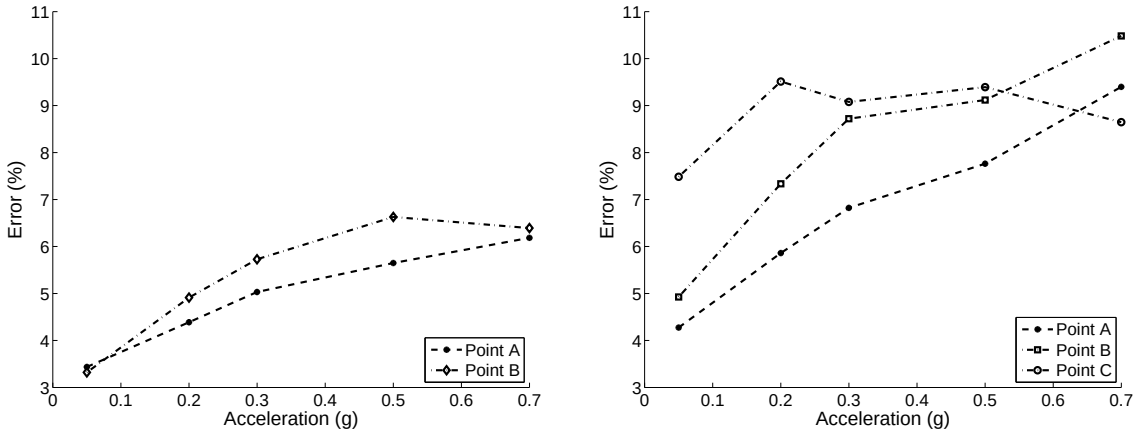

Figure 4.25: Computed error between maximum positive (left) and negative (right) strain of 10 and 30 points per wavelength models at the three different control points (A, B and C) for different input levels (shown as acceleration) for the 50-spring constitutive model

The dissipated energy can also be compared for various strain levels at the three control points (Fig.4.26). In this case, the choice of the number of points per wavelength is more important comparing to the results of the maximum strain level criterion, because the slope of the lines is stronger. The dissipated energy is directly related to the surface of the stress-strain loops. It is obtained during the total propagation duration, therefore, it could be a better criterion to compare the results. The dissipated energy is also more sensitive to the input strain level than the maximum strain. The difference between the dissipated energy, named here as "error", for 10 and 30 points per wavelength models at the two control points A and B, are shown in Fig.4.26d. Similar to the maximum strain criterion, the results of the 30 points per wavelength model are considered as the reference case. The error at the control point C is not computed because an important part of the energy is dissipated before reaching this point and the dissipated energy for different strain levels at this point is very irregular. It is not easy to find a general rule for the computed error but comparing the results, it is shown that the computed error is very high and varies between 12 and 36%. The error of the dissipated energy is more than the maximum strain error. The dissipated energy criterion is thus more sensitive to the numerical dispersion. The error of the dissipated energy is strong for all the input ranges, which makes the numerical dispersion more critical.

It was said before that it is impossible to give a general rule for the choice of the number of points per wavelength in nonlinear media. It depends on many parameters such as the amplitude of the input motion, the material properties, the form of the input motion, the material constitutive model and etc. Increasing the number of elements, the results could be more accurate, but we increase the total time of the analysis. The computation time is one of most important factors in nonlinear dynamic analyses. Increasing the number of elements, the

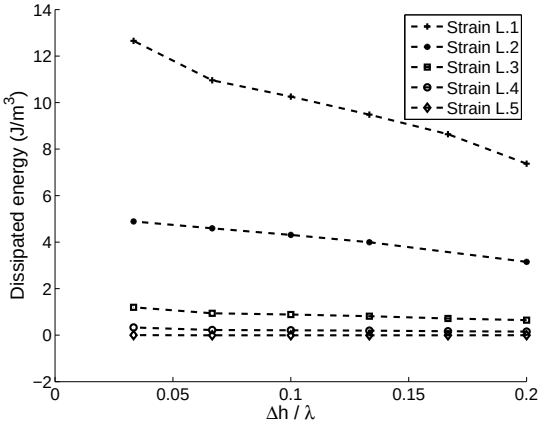

(a) Dissipated energy during the propagation at the control point A for all the meshes and various input strain levels

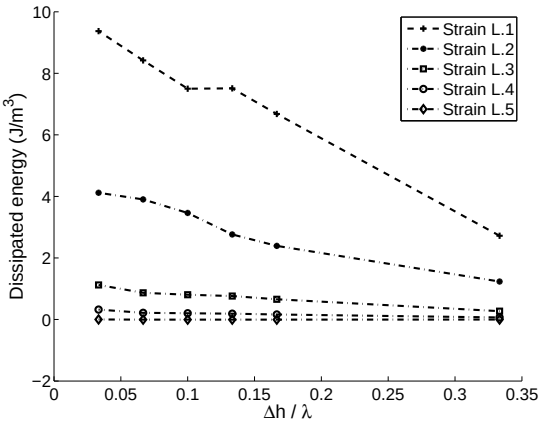

(b) Dissipated energy during the propagation at the control point B for all the meshes and various input strain levels

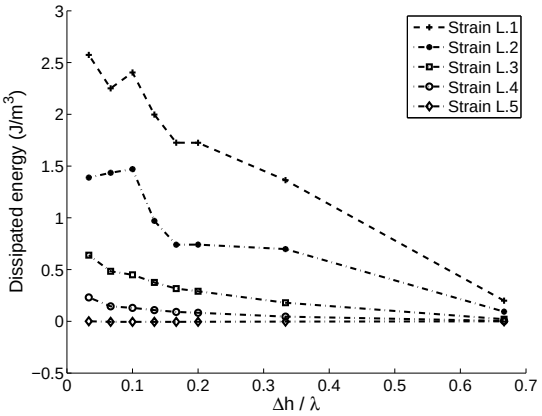

(c) Dissipated energy during the propagation at the control point C for all the meshes and various input strain levels

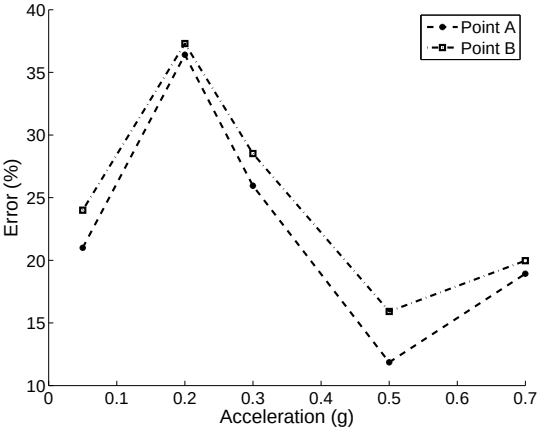

(d) Computed error between dissipated energy of 10 and 30 points per wavelength models at the control points A and B

Figure 4.26: Dissipated energy for each stress-strain curves of 8 meshes at the three different control points (A, B and C) for the 50-spring model for 5 different strain input levels and the calculated error between dissipated energy of 10 and 30 points per wavelength models at the control points A and B versus related input maximum acceleration (bottom-right)

total number of degrees of freedom increases in one side and in the other side, we have to decrease the time step because the number of the points per wavelength is modified. Consequently, an optimum number of elements should be considered.

In our case, we try to find the number of points per wavelength to have a desirable maximum error in the results. For instance, the maximum negative strain and the dissipated energy for all the input strain levels are illustrated in Fig.4.27. Assuming that the results of 30 points per wavelength are the reference results, we chose two different levels of target maximum error, for example 5 and 10 percent. In Fig.4.27, the blue lines display the 95% of the reference results for the two strain levels L.1 and L.2. The red lines show the 90% of the reference results for similar strain levels. These lines help us to find, in an approximate way, the required number of points per wavelength to have 5 and 10% maximum errors at the maximum strain and the dissipated energy. These lines are shown only for the strain levels L.1 and L.2. For example, 15 points per wavelength is needed to have a 5% maximum error in the maximum negative strain for the input strain level L.1 and 13 points per wavelength for the same condition and the input strain level L.2. In the same situation, 10 and 9 points per wavelength are needed to have a

10% maximum error.

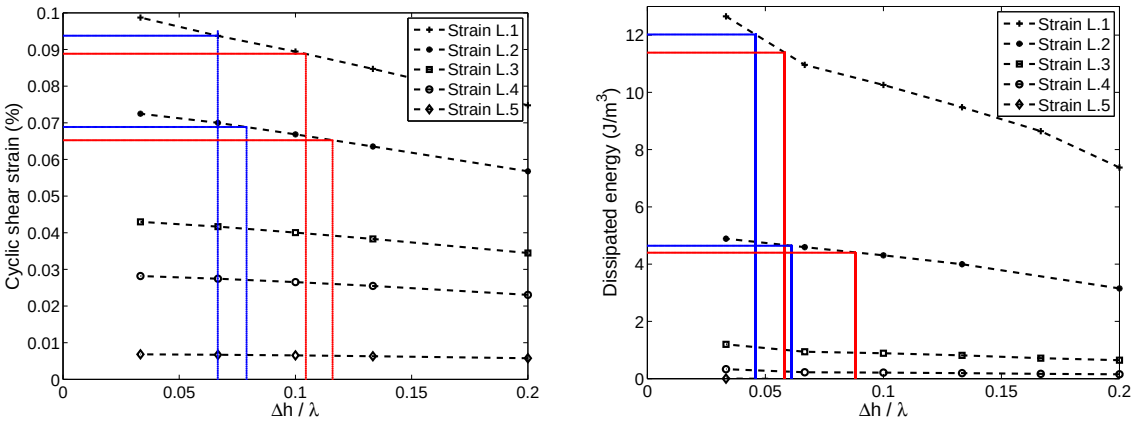

Figure 4.27: Maximum negative strain (left) and the dissipated energy (right) during the propagation for different meshes at the control point A for the 50-spring model and the five different input strain levels

For the dissipated energy criteria, more points per wavelength are needed to keep the error below 5 and 10%. For example, 21 points per wavelength is needed to have a 5% maximum error in the dissipated energy for the input strain level L.1 and 17 points for the input strain level L.2. In the same condition, 17 and 11 points per wavelength are needed to have a 10% maximum error, respectively for the input strain levels L.1 and L.2. As an example, Fig.4.28 illustrates the required number of points per wavelength to have a maximum 5 and 10 percent error in the maximum negative strain and the dissipated energy. These results are computed for a 50-spring constitutive model and for the five selected input strain levels. It is observed that especially for the dissipated energy criteria, the required number of points per wavelength is larger than the recommended 10 points per wavelength in linear media.

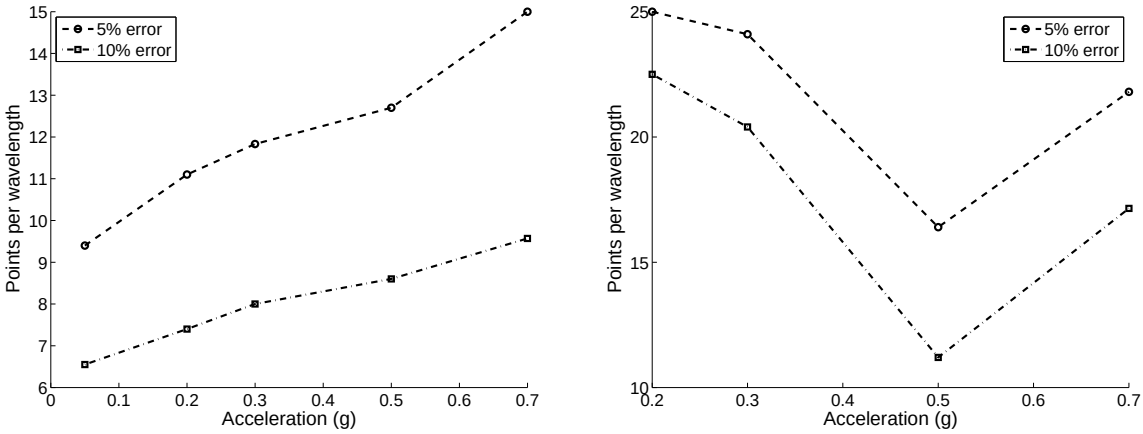

(a) Applied single component sinusoidal strain

(b) stress-strain curve

Figure 4.28: Maximum negative strain (left) and the dissipated energy (right) during the propagation for different meshes at the control point A for the 50-spring model and the five different input strain levels

It is possible to find the optimal number of points per wavelength for each input strain level for any target maximum error and find a general rule. Nevertheless, this rule would be only valid for each case, depending on the material properties and the nature of the input motion.

The goal of this part was to aware the users of the numerical tools to the choice of the

number of elements that they use in their models to investigate nonlinear dynamic problems. The linear rules are not valid anymore in nonlinear media, therefore, the number of points per wavelength could strongly influence the accuracy of the results.

4.5.4.2 Effect of the number of springs in the constitutive model

All the analyses in §4.5.4.1 are repeated for the 5- and 10-spring constitutive models. The maximum positive and negative strains are computed for the same five different input motions (L.1 to L.5). Also, the dissipated energy is calculated for these five different input motions for the 8 different meshes. To avoid too many figures, only the computed errors, obtained in the same way as Fig.4.25 and Fig.4.26d, are presented here. Fig.4.29a illustrates the computed error between 10 and 30 points per wavelength models for the maximum negative strain versus the related input acceleration for the 10-spring constitutive model. The computed error of the dissipated energy error during the propagation for the same models is shown in Fig.4.29b.

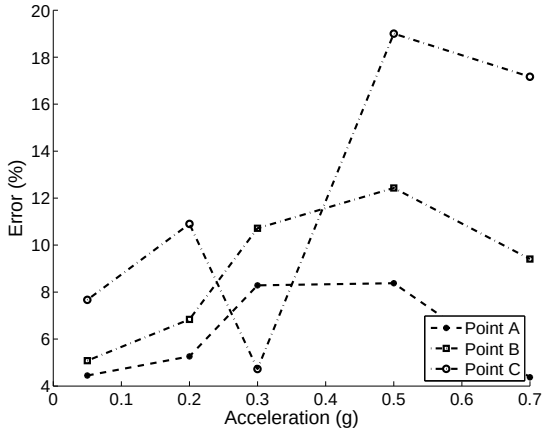

(a) Computed error between the maximum negative strain of the 10 and 30 points per wavelength models

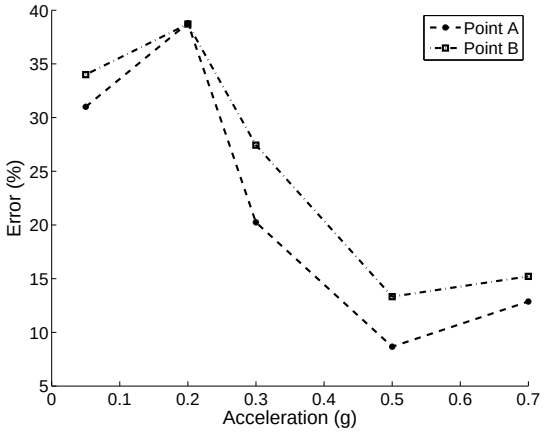

(b) Computed error between the dissipated energy of the 10 and 30 points per wavelength models

Figure 4.29: Computed error of the maximum negative strain (left) and the dissipated energy (right) during the propagation of the 10 and 30 points per wavelength models versus the five different input motions (acceleration) for the three selected control points (A, B and C) and the 10-spring constitutive model

Finally, the computed error of the maximum negative strain and the dissipated energy are shown in Fig.4.30 for a 5-spring constitutive model.

Comparing Fig.4.25, Fig.4.29a and Fig.4.30a, the computed error between the 10 and 30 points per wavelength models for the maximum negative strain increases, considering a smaller number of springs in the constitutive model. For example, at the control point B, the computed error is equal to 10.5, 12.2 and 20 percent respectively for the 50-, 10- and 5-spring constitutive models for the second input strain level (L.2). This means that the numerical dispersion is stronger if one consider lower number of springs in the constitutive model.

We can also compare Fig.4.27 with Fig.4.29b and Fig.4.30b for the dissipated energy at different control points. It is observed that, decreasing the number of springs in the nonlinear model, the error of the dissipated energy tends to decrease, but it also depends on the level of the input motion. As we already said in the previous sections, considering lower number of springs, the rheological model behaves less nonlinear. Therefore, it is logical in general that the computed error decreases considering lower number of the spring in the constitutive model. But this is not respected in the case of the maximum strain criteria. As we observe, it is difficult or maybe impossible to derive a general rule.

In the same way presented for the 50-spring model, we can obtain the number of points per

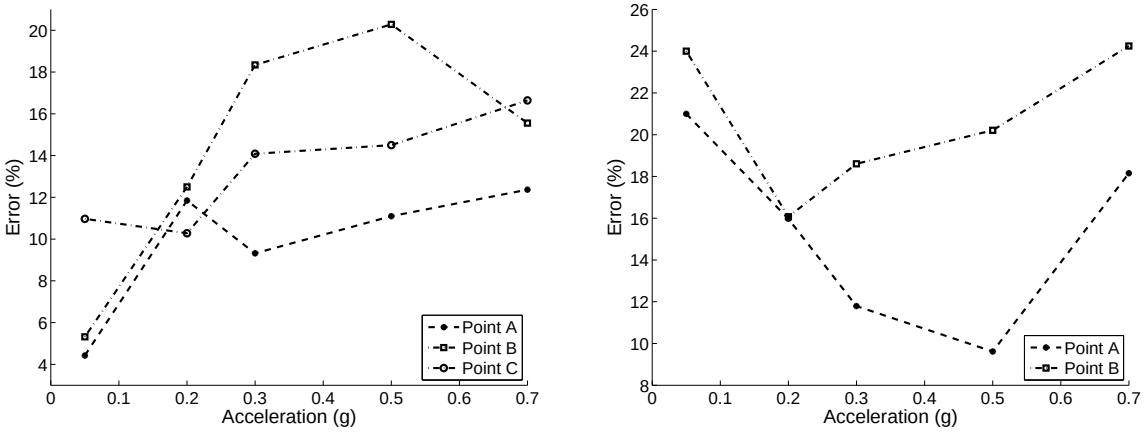

(a) Computed error between the maximum negative strain of the 10 and 30 points per wavelength models

(b) Computed error between the dissipated energy of the 10 and 30 points per wavelength models

Figure 4.30: Computed error of the maximum negative strain (left) and the dissipated energy (right) during the propagation of the 10 and 30 points per wavelength models for the three selected control points (A, B and C) for a 5-spring constitutive model versus the five different input motions (acceleration)

wavelength to obtain a specific accuracy of the results. The procedure being the same, we do not repeat it.

4.6 Concluding remarks and recommendations

The idea of this chapter was to aware the user of the numerical tools on the spatial discretization of the nonlinear media. It is shown that the 10 points per wavelength rule, recommended in the literature for the elastic media is not sufficient in nonlinear case. It was explained that when the material is nonlinear, during the propagation of the shear waves, the shear modulus of the material reduces and then the shear velocity decreases. Therefore, the wavelength changes and the initial number of points per wavelength decreases.

It was shown that comparing the energy dissipation in the media, it seems that the coarse meshes are more dissipative than fine meshes.

The choice of the number of points per wavelength could influence significantly the results such as displacement or strain-stress curves. The effect of the input strain level was also investigated and as we expected the numerical dispersion is stronger when the nonlinearity increases.

The nonlinear constitutive model used in this work requires only the shear modulus reduction curve as nonlinear property. The manner which this curve (or in other hand the number of the springs) is discretized can influence the results. We showed that when the number of the springs decreases the nonlinearity in the media also decreases.

Defining the reference results corresponding to the ones computed within the finest mesh, all other results are compared. The required number of points per wavelength to have a maximum target error (in this case 5 and 10 percent) is computed. Nevertheless, it is not possible to derive a general rule for nonlinear media, because the results depend on numerous parameters. In any case, we present some recommendations to assess the precision of the results.

We can use finer meshes for the region where there is a potential nonlinear behavior. Using a complete and fully fine mesh can significantly increase the calculation time. Consequently, we can adapt different meshes for different regions, coarser meshes for the linear parts of the media and finer meshes for the nonlinear parts of the media.

It could be better to perform each nonlinear analysis two times. At the first time, we obtain a general idea about the level of the nonlinearity in each part of the media. For the second

analysis, we try to adjust the appropriate mesh for each region with respect to the nonlinearity levels estimated from the first analysis. This helps us to obtain more reliable results from the numerical simulation.

We should also pay attention to the regions where there is an energy concentration. This concentration could be more critical for numerical dispersion in case of nonlinear media than for linear ones. Because it can increase the strain level and it influences directly the numerical dispersion. Therefore, finer meshes should be used for this parts. For the dynamic soil-structure interaction problem, this region could be around the foundation where there is a strong energy concentration. For example, the mesh can progressively be coarser when moving away from the foundation.

Chapter 5

Effect of soil nonlinearity on dynamic SSI : Parametric study

Contents

5.1 Introduction

In the following, we will investigate the effect of soil nonlinearity on soil-structure interaction using the finite element approach described in previous chapters (CESAR-LCPC code).

Through a parametric study, different features of the nonlinear DSSI are discussed. In this chapter we study the effect of the soil nonlinearity on the amplitude of the structural response in time and frequency domains. Its effect on the modification of the frequency content of the responses is studied as well.

Different structures, soil profiles, input motions and case studies will be presented in §5.2. We will study in §5.3 the soil response for different soil profiles and different excitation levels. In §5.4, we will investigate different features of the structural response due to the soil nonlinearity. The energy dissipation in the soil and its effect on the DSSI and vice versa will be presented in §5.5 and §5.6. This chapter will be completed by presenting some concluding remarks in §5.7.

5.2 Description of the model

A parametric study is performed to investigate nonlinear dynamic soil-structure interaction. Three different structures with different fundamental frequencies are considered. Three different soil profiles are also assumed. The soil-structure models are excited by different input motion levels.

5.2.1 Studied buildings

The purpose of our parametric study is to investigate the effect of soil nonlinearities on dynamic soil-structure interaction. Therefore, an elastic behavior is considered for the structural materials. The first structure is an idealization of a twelve story reinforced concrete frame with a foundation covering a surface area of $12m$-by-$30m$, founded in Bucharest, Romania (Pitilakis, 2006). The total height of the residential building is approximately $38m$. The effective height of the idealized structure is equal to $25.4m$. The total mass of the structure is approximately $6628t$, and 85% is attributed to the first natural mode, giving $5634t$ at the top of the frame. The fundamental frequency of the structure based on a rigid base is equal to 0.56Hz. For the sake of simplicity, the foundation is rigid, massless, rectangular plate resting on the soil surface. The geometric properties of this structure are shown in Fig.5.1a.

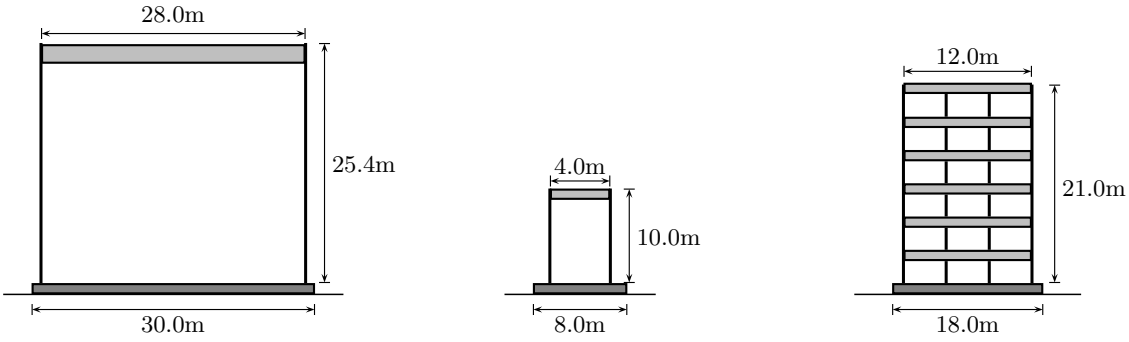

(a) Building #1 (b01) (b) Building #2 (b02) (c) Building #3 (b03)

Figure 5.1: Geometric properties of three selected buildings

The second structure is a $10m$ high tower (Pitilakis, 2006). This conceptual case may represent a water tower, having a mass of $72t$ fixed at the height of $10m$ above the foundation surface (Fig.5.1b). The foundation is considered massless and rigid, covering a $8m$-by-$8m$ surface. The fundamental frequency of the structure on a rigid base is equal to 3.51Hz.

The third structure is a six-story frame with three spans. The total height of the structure is $18m$. The foundation is massless and rigid with a rectangular shape of $18m$-by-$12m$. The

total mass of the structure is equal to $182t$ and its fixed base fundamental frequency is 2.32Hz. The geometrical properties of the third structure are presented in Fig.5.1c.

The properties of these three structures are summarized in Tab.5.1. Beam elements are used to model the columns and beams of the selected reinforced concrete buildings.

Building	Total height (m)	Total mass (ton)	First fixed base frequency (Hz)	Length of Foundation (m)
b01	25.4	5634	0.56	30
b02	10	72	3.51	8
b03	21	180	2.32	18

Table 5.1: Properties of the three selected buildings

5.2.2 Soil profiles

5.2.2.1 Elastic properties

Three different soil profiles are considered to represent different level of nonlinearities. The soil consists of $50m$ of three different layers. The geometry and elastic properties of these soil profiles are displayed in Fig.5.2.

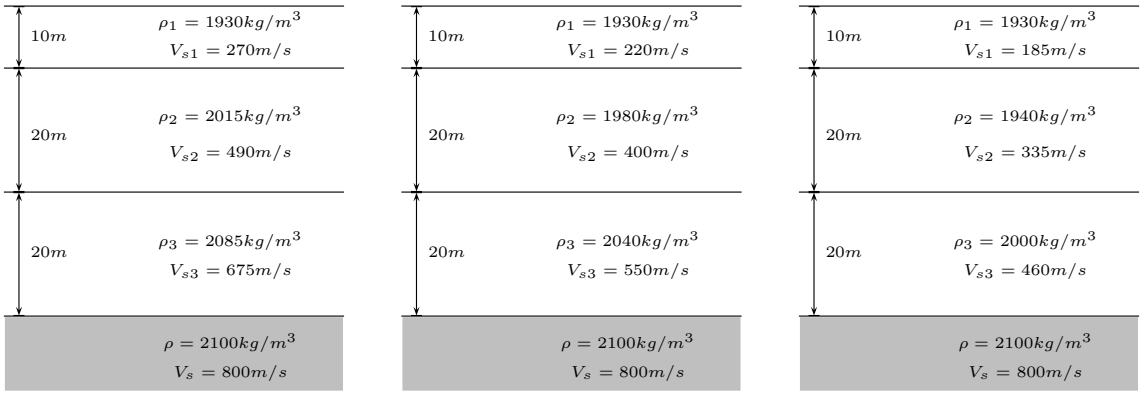

(a) Soil profile (#1) (b) Soil profile (#2) (c) Soil profile (#3)

Figure 5.2: Geometric and material properties of the three selected soil profiles

To obtain these soil profiles specially their shear wave velocities we used the strategy presented by Cotton et al. (2006). The soil densities of the profiles are obtained by following David Boore's notes ($http://www.daveboore.com/daves\_notes.php$). He presented the necessary formulation to obtain the density depending on S and P waves velocities. The total height of the soil profiles is $50m$, consists of three different layers of 10, 20 and $20m$. These soil profiles are laying on an elastic bedrock. The effect of the stiffness increasing with the confinement is taken into account by a nonlinear elastic approach considered as,

$$G = G_{ref} \left(\frac{P}{P_{ref}} \right)^n \tag{5.1}$$

where the elastic shear moduli, G, is a function of the mean compressive stress P. The G_{ref} is the elastic shear moduli measured at the mean pressure P_{ref} and n depends on the soil type. It is usually 0.5 for granular soils and close to 1 for clays. Therefore, the low-strain shear moduli increases with depth. The low-strain shear moduli and elastic shear wave velocity of the soil profiles are shown in Fig.5.3.

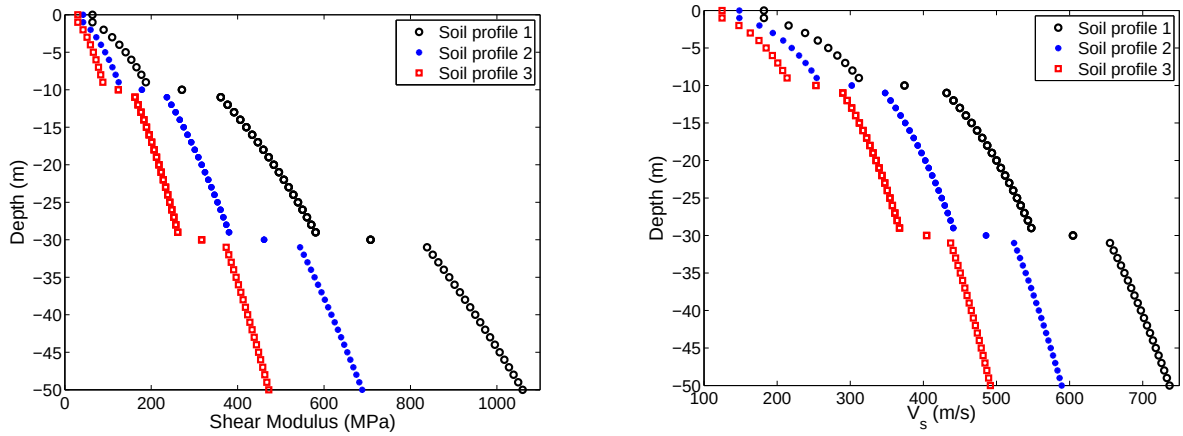

(a) Low-strain shear moduli of the profiles

(b) Low-strain shear wave velocity of the profiles

Figure 5.3: Low-strain shear moduli and elastic shear wave velocity of the studied soil profiles

Figure 5.4 displays the results of the elastic frequency analyses of the three studied soil profiles. The first and the second elastic natural frequencies of soil profile #1 are respectively 2.96 and 7.05Hz. For the second soil profile, they are 2.4 and 5.74Hz. Finally, for the third studied soil profile, the frequencies are equal to 1.98 and 4.82Hz. The relative position of the fixed base frequency of the three selected buildings are also shown in Fig.5.4. The buildings are selected in a way to form different combinations of the fundamental and natural frequencies of the soil and structure. For example, the fundamental frequencies of buildings b01 and b03 are lower than the first natural frequency of the soil profile #1 (Fig.5.4a). For the same soil profile, the fundamental frequency of the second building is greater than the soil natural frequency for other soil profiles. Consequently, the effect of the ratio of the natural and fundamental frequencies of the soil and structure can be investigated.

5.2.2.2 Nonlinear properties

The implemented nonlinear constitutive model (§3.3) requires the shear modulus reduction curve. The reference strain, γ_{ref}, for the first layer of the first, second and third soil profile are respectively 0.1%, 0.058% and 0.033% (Fig.5.5a). This means the level of nonlinearity of the first soil profile is less than two other soil profiles. On the other hand, for the same level of shear strain, the shear modulus reduction is larger for soil profile #3 than for the first and second one. The reference strains of the three soil profiles are displayed in table 5.2.

	Soil Profile #1	Soil Profile #2	Soil Profile #3
Layer 1	0.10	0.058	0.033
Layer 2	0.12	0.069	0.038
Layer 3	0.14	0.072	0.043

Table 5.2: Reference strain (%) of the three studied soil profiles

The bedrock behavior is elastic. A Young's modulus of $E = 3.7632GPa$, a density of $\rho = 2100Kg/m^3$ and a Poisson's ratio of $\nu = 0.4$ are considered for the bedrock. Similar Poisson's ration is considered for the soil.

5.2.3 Input motion

In the CESAR-LCPC software, the input motion can be introduced into the model either as a displacement or as a force. For displacement input, we are limited to the borehole condition.

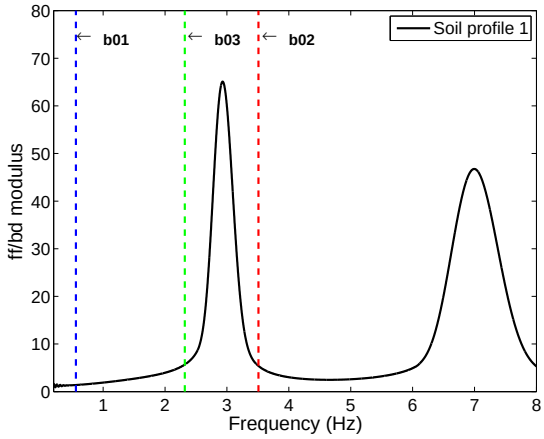

(a) Transfer function of the free field and bedrock responses (ff/bd) for soil profile #1

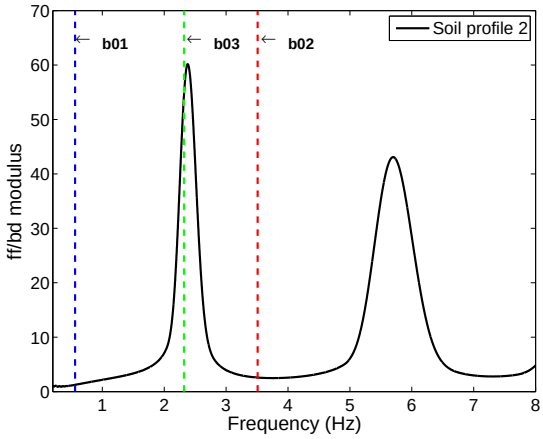

(b) Transfer function of the free field and bedrock responses (ff/bd) for soil profile #2

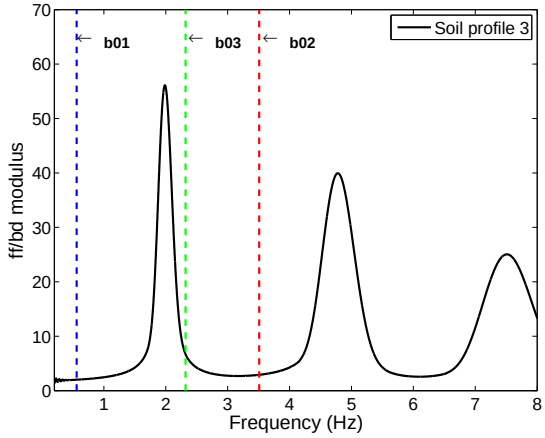

(c) Transfer function of the free field and bedrock responses (ff/bd) for soil profile #3

Figure 5.4: Low-strain transfer function between free field and bedrock responses (ff/bd) for the three selected soil profiles

This means the total displacement at the nodes where the input motion is applied, is equal to the incident motion and not the downgoing waves. Therefore, we are not able to excite our models by any earthquake, measured at the outcropping bedrock. The input motion can also be applied as a force. In this case, the total displacement is the sum of the incident and the downgoing waves but the program is not able to separate these two movements. Consequently, the input motion should be short enough not to mix the incident and downgoing waves.

For the reasons mentioned above, we selected a Gabor wavelet as a force input motion. We had to extend in depth the elastic bedrock to avoid any conflict with the waves. The total duration of the Gabor wavelet is less than one second. Therefore, a $250m$ elastic bedrock is considered between the $50m$ nonlinear soil and the absorbing layers.

An important feature of the Gabor wavelet is that it covers a wide range of the frequencies that are important in our study. Therefore, the parameters of the wavelet are selected to cover the range between zero and 12Hz with approximately the same amplitude in the frequency domain. The Gabor wavelet used in this work is shown in Fig.5.6 in time and frequency domains.

The Gabor wavelet is used as the outcropping motion and scaled to different values. Four levels of the input motions are equivalent to $0.1g$, $0.25g$, $0.5g$ and $0.7g$ outcropping PGA's. These input motions are divided by two before applying at the base of the model in order to account for the free surface effect in the previous values.

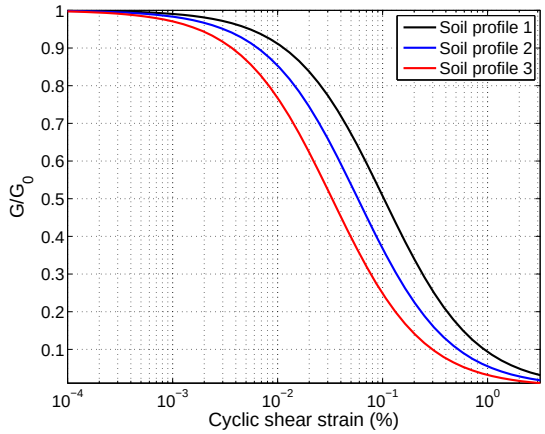

(a) Shear modulus reduction curve of the first soil layer #1

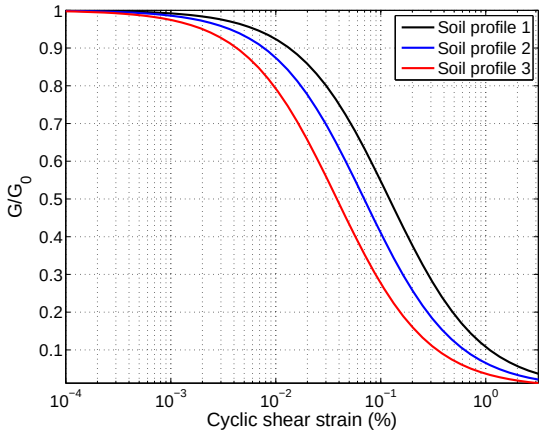

(b) Shear modulus reduction curve of the second soil layer #2

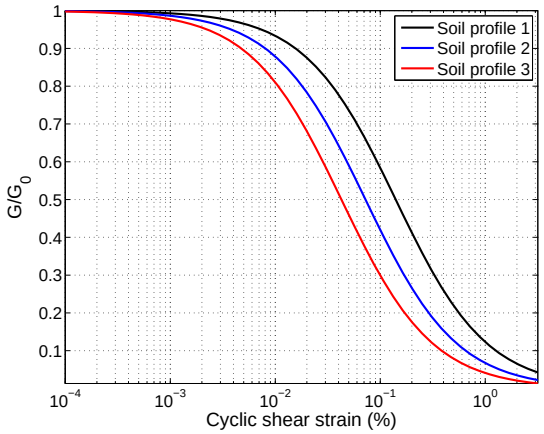

(c) Shear modulus reduction curve of the third soil layer #3

Figure 5.5: Shear modulus reduction curve for the three selected soil profiles

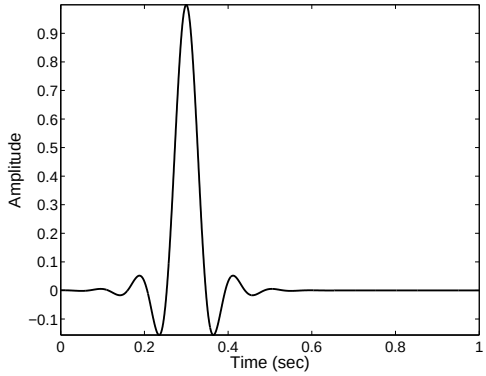

(a) Gabor wavelet in time domain

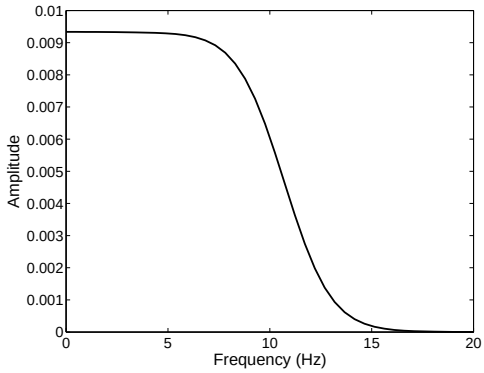

(b) Gabor wavelet in frequency domain

Figure 5.6: Normalized Gabor wavelet in time and frequency domains used in the study of DSSI

5.2.4 Finite element model

The finite element model is composed of: the structure, the foundation, the contact elements (at the interface of the foundation and the soil), the nonlinear soil, the elastic bedrock and finally the absorbing layers. An example of the finite element mesh used to model the SSI is shown in Fig.5.7. The incident waves, defined at the outcropping bedrock are introduced into the model between the elastic bedrock and the absorbing layers. Only vertically incident shear waves are

studied.

The initial static condition is not taken into account in this work, but the effect of the weight of the superstructure on the low-strain shear moduli of the soil is considered (for more details see §1.6.4).

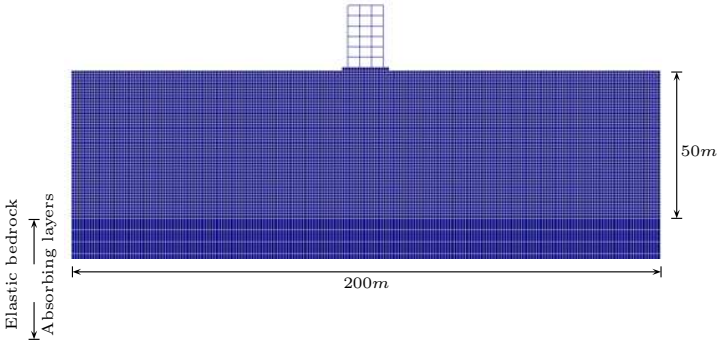

Figure 5.7: Example of the finite element mesh used to model SSI

The second order implicit method (Newmark algorithm), known for its performance and its unconditional stability is used. Here, we select $\beta = 0.25$ and $\alpha = 0.5$ for which the scheme is unconditionally stable and does not induce any numerical damping to the system. Therefore, the dissipation at the system will be originated by the elastoplastic behavior of the soil and the radiation damping.

5.2.4.1 Boundary condition

The elastic absorbing condition presented in §2 is used. Ten absorbing layers are considered at the bottom of the elastic layer. The properties of these layers are presented in Table 5.3. The elastic properties of these layers are similar to the elastic soil layer (§5.2.2.1). A progressive increasing damping (Q^{-1} from 0.1 to 1.0) is considered. Therefore, the efficiency of the method improves. A small damping close to the elastic soil layer avoids the reflection of the downgoing waves.

Layer number	$\rho(Kg/m^3)$	$E(GPa)$	ν	a_0	a_1	Q^{-1}
1	2100	3.7632	0.4	2.18859E-3	1.1423	0.1
2	2100	3.7632	0.4	4.37719E-3	2.2846	0.2
3	2100	3.7632	0.4	6.56579E-3	3.4268	0.3
4	2100	3.7632	0.4	8.75439E-3	4.5691	0.4
5	2100	3.7632	0.4	1.09429E-2	5.7114	0.5
6	2100	3.7632	0.4	1.31316E-2	6.8537	0.6
7	2100	3.7632	0.4	1.53202E-2	7.9960	0.7
8	2100	3.7632	0.4	1.75088E-2	9.1383	0.8
9	2100	3.7632	0.4	1.96974E-2	10.2805	0.9
10	2100	3.7632	0.4	2.18859E-2	11.4228	1.0

Table 5.3: Properties of the ten absorbing layers at the bottom of the elastic soil layer (a_0 and a_1) are the Rayleigh coefficients

Each layer has $25m$ depth. This value is a little exaggerated in order to have the minimum parasite waves coming through the absorbing layers.

The periodic condition is assumed at the two lateral sides of the finite element model (see §1.6.4). Therefore, we had to take a greater domain around the structure to avoid the reflected

waves. However, the reflected waves coming from the sides of the model dissipate during the propagation as the soil behavior is nonlinear.

5.2.4.2 Soil-foundation interface

In order to prevent the apparition of traction between the foundation and the surrounding soil, the contact elements presented in Appendix §A have been positioned at the soil-foundation interface. The contact element properties are selected in order to reduce stress concentration at the foundation corners but not to alter the dynamic response by excessive sliding. The contact elements are able to represent the uplift condition but for sake of simplicity the uplift is neglected in this work.

Since the soil-foundation interface consists of modeling an artificial material for contact elements, to numerically ensure the continuity of the displacement the value of the Young modulus of the contact is equal to the lower value of the Young modulus of two materials in contact, this means the soil. The properties of the contact elements are shown in Table 5.4.

Parameter	Value
E	185-261.5-394(MPa)
G	92.5-131-197(MPa)
ϕ	27
c	4(kPa)

Table 5.4: Soil-foundation interface parameters depending on the soil profile

5.2.5 Case studies

Three different structures and three different soil profiles are considered. Consequently, we have 9 different case studies. For each case, one linear and four nonlinear analyses (with the input motions presented in §5.2.3) are performed. Therefore, our parametric study consists of 45 different analyses. Table 5.5 displays the properties of each case study.

For each case study, the soil response and the soil-structure interaction are studied. The soil response of the three different soil profiles are presented in §5.3. The soil-structure interaction is studied in §5.4. Different indexes and control points are defined to simplify the way the results are displayed. Figure 5.8 shows these indexes and the control points in the model.

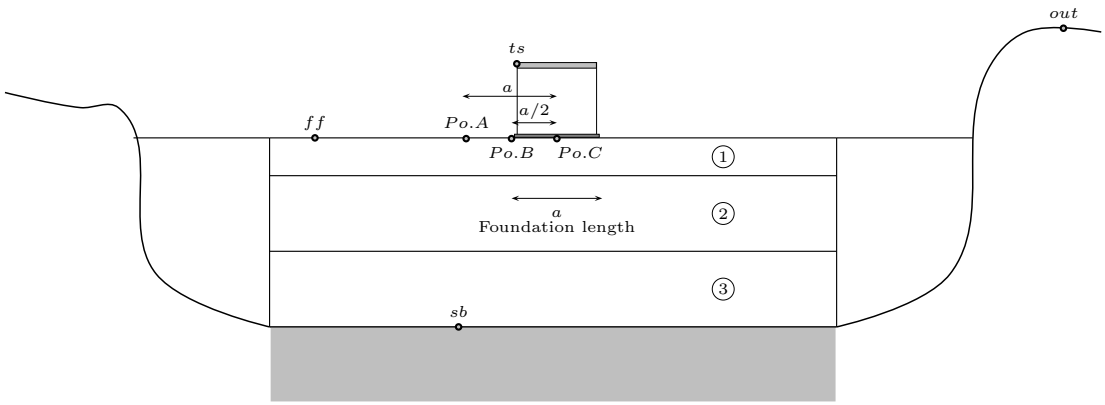

Figure 5.8: Definition of the control points of the soil-structure models

ff represents the free field, ts the top of the structure, out the outcropping and sb the base of the soil profile. The control points $Po.A$, $Po.B$ and $Po.C$ represents the points where we will study the soil and structure responses. The parameter a is the length of the foundation.

Case number	Soil profile	Structure	Outcropping PGA	Soil behavior
1	1	1	0.1g	linear
			0.1g	nonlinear
			0.25g	nonlinear
			0.5g	nonlinear
			0.7g	nonlinear
2	2	1	0.1g	linear
			0.1g	nonlinear
			0.25g	nonlinear
			0.5g	nonlinear
			0.7g	nonlinear
3	3	1	0.1g	linear
			0.1g	nonlinear
			0.25g	nonlinear
			0.5g	nonlinear
			0.7g	nonlinear
4	1	2	0.1g	linear
			0.1g	nonlinear
			0.25g	nonlinear
			0.5g	nonlinear
			0.7g	nonlinear
5	2	2	0.1g	linear
			0.1g	nonlinear
			0.25g	nonlinear
			0.5g	nonlinear
			0.7g	nonlinear
6	3	2	0.1g	linear
			0.1g	nonlinear
			0.25g	nonlinear
			0.5g	nonlinear
			0.7g	nonlinear
7	1	3	0.1g	linear
			0.1g	nonlinear
			0.25g	nonlinear
			0.5g	nonlinear
			0.7g	nonlinear
8	2	3	0.1g	linear
			0.1g	nonlinear
			0.25g	nonlinear
			0.5g	nonlinear
			0.7g	nonlinear
9	3	3	0.1g	linear
			0.1g	nonlinear
			0.25g	nonlinear
			0.5g	nonlinear
			0.7g	nonlinear

Table 5.5: 9 case studies characteristics of the parametric study

Therefore, $Po.A$ has the distance a from the middle of the foundation. $Po.B$ is at the foundation corner and finally, $Po.C$ represents the middle of the foundation.

5.3 Soil response

The soil response of the selected soil profiles are presented in this section. For each soil profile, the free field responses are compared among models with different input motions in the linear and nonlinear cases.

5.3.1 Soil profile #1

The elastic properties of this soil profile are presented in Fig.5.2a. Its shear modulus reduction curve is also shown in Fig.5.5. When compared to the two other soil profiles, soil profile #1 should behaves more linearly. The free field response of this soil in terms of acceleration, velocity and displacement is depicted in Fig.5.9. The residual displacements computed at free field (ff) are very small as we expected since the soil exhibits rather a linear behavior even for strong motions.

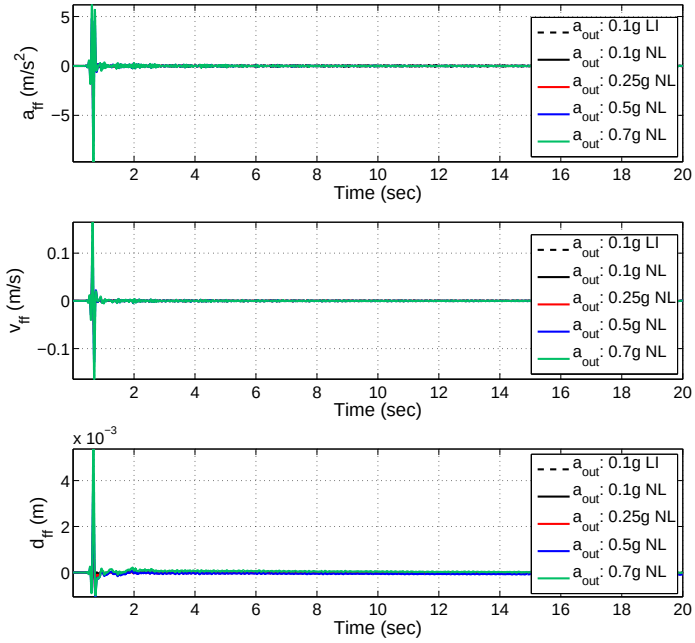

Figure 5.9: Free field acceleration (top), velocity (middle) and displacement (bottom) of the soil profile #1 excited by different input motion levels

It is observed that the absorbing layers work very well and the reflected waves coming back to the media are negligible. To have a better idea about the difference between the results with various input motions, the first second of the response is shown in Fig.5.10. Comparing the results, for all the input motions, the amplifications are observed. Also, the arrival time of the peak acceleration, velocity and displacement does not considerably vary.

The results are also compared in the frequency domain. Figure 5.10d displays the transfer function between the free field response and the outcropping motion. The behavior of this soil profile is rather linear but it is observed that the peaks shift a little to the low frequencies. In this case, the maximum amplification factor reaches up to 3 with soil linear behavior and up to 2.6 for soil nonlinear behavior. But, the first arrives at around 7Hz and the second at around 3.5Hz.

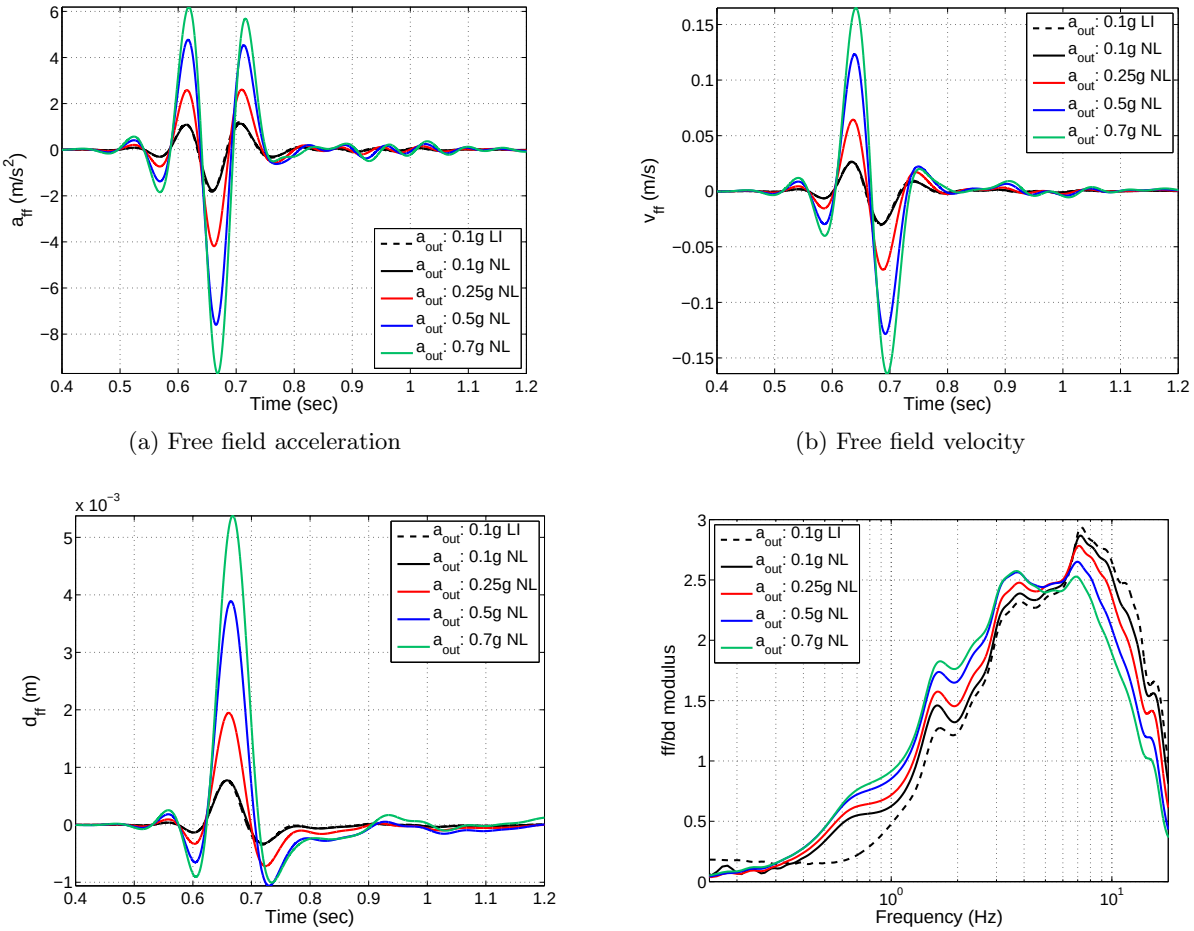

(a) Free field acceleration

(b) Free field velocity

(c) Free field displacement

(d) Transfer function between ff and out. response

Figure 5.10: First second of the response in terms of free field acceleration, velocity and displacement for the soil profile #1 and the transfer function between the free field response and the outcropping bedrock for different input motions

5.3.2 Soil profile #2

Figure 5.11 illustrates the results of the second soil profile. This soil behaves more nonlinearly than the previous one. Residual displacements are also produced and they are larger for increasing input motion level.

The results are shown in Fig.5.12 for the first second of the response. Comparing the arrival time in terms of peak acceleration, velocity and displacement, the apparent wave velocity decreases as the input motion level increases. The soil nonlinearity is evidenced in the time domain thus the arrival times are larger for increasing input motion levels.

Comparing the peak acceleration at free field and at the outcrop, the amplification is observed for all the input motions except for the $0.5g$ and $0.7g$ PGA's. The transfer function between the acceleration at free field and the outcropping bedrock is computed and displayed in Fig.5.12d. It is observed that the nonlinearity is stronger in the soil profile #2 compared to the first one. The transfer function peaks shift to the lower frequencies. We observe that for the frequencies lower than 2Hz the amplification is larger for the $0.5g$ and $0.7g$ outcropping PGA's than for the other cases. For the high frequencies, the results are reverse. This means that the amplification reduces for the high level input motions and even deamplication may occur. The maximum amplification factor reaches up to 3.5 for linear behavior and up to 2.4 for the strongest input motion with soil nonlinear behavior. However, in each case the related frequency is totally different. For linear behavior it happens at 6Hz and for the strongest input motion with nonlinear soil behavior at

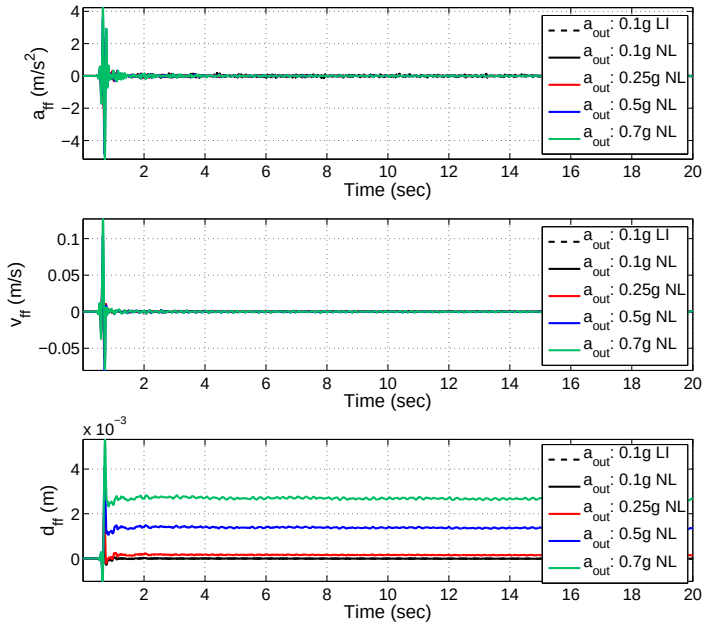

Figure 5.11: Free field acceleration (top), velocity (middle) and displacement (bottom) of the soil profile #2 excited by different input motion levels

2Hz.

5.3.3 Soil profile #3

The results of the third soil profile are presented in Fig.5.13. As we expected the soil nonlinearity is stronger than for the two other soil profiles. Comparing the peak accelerations at free field, for almost all the input motions, there is no amplification for the soil profile #3. The apparent wave velocity significantly decreases, increasing strain level. Despite the difference between the input motions, the acceleration at free field are very close. The residual displacements also strongly increase. For the strongest motion, the residual displacement is very close to the maximum displacement.

Finally, the transfer function between free field and the outcropping bedrock is depicted in Fig.5.13d. In this case, the transfer function of the input motion of $0.25g$ outcropping PGA is closer to the $0.5g$ and $0.7g$ ones comparing to two other soil profiles. Comparing to soil profiles #1 and #2, the amplification factor continues to increase, due to its weaker elastic properties. For the $0.7g$ outcropping PGA, the maximum amplification factor reaches up to 2.6 with nonlinear soil behavior, this is equal to the results of the first soil profile. This means that the weak elastic properties and the strong nonlinearity neutralize each other in this case.

The obtained amplification for low frequencies is also very interesting. For the $0.1g$ PGA with elastic and inelastic soil behavior, there is no amplification approximately below 1Hz, however, for the medium and strong motions, amplification reaches more than 1 even up to 2.5.

5.3.4 Comparison of the soil profiles responses

To have a better idea, the results of the three selected soil profiles are compared in one figure. Figure 5.14 illustrates the acceleration computed at free field for two different input motions, $0.1g$ and $0.7g$ outcropping bedrock PGA's. For the $0.1g$ outcropping PGA, despite the difference between the elastic properties, the peak accelerations at free field are very close to each other. This is due to the soil nonlinearity effect that decreases the soil response. However, the apparent velocities are totally different. On the other side, for the the $0.7g$ PGA motion, the peak accelerations are completely different between the soil profiles. For example, the peak acceleration

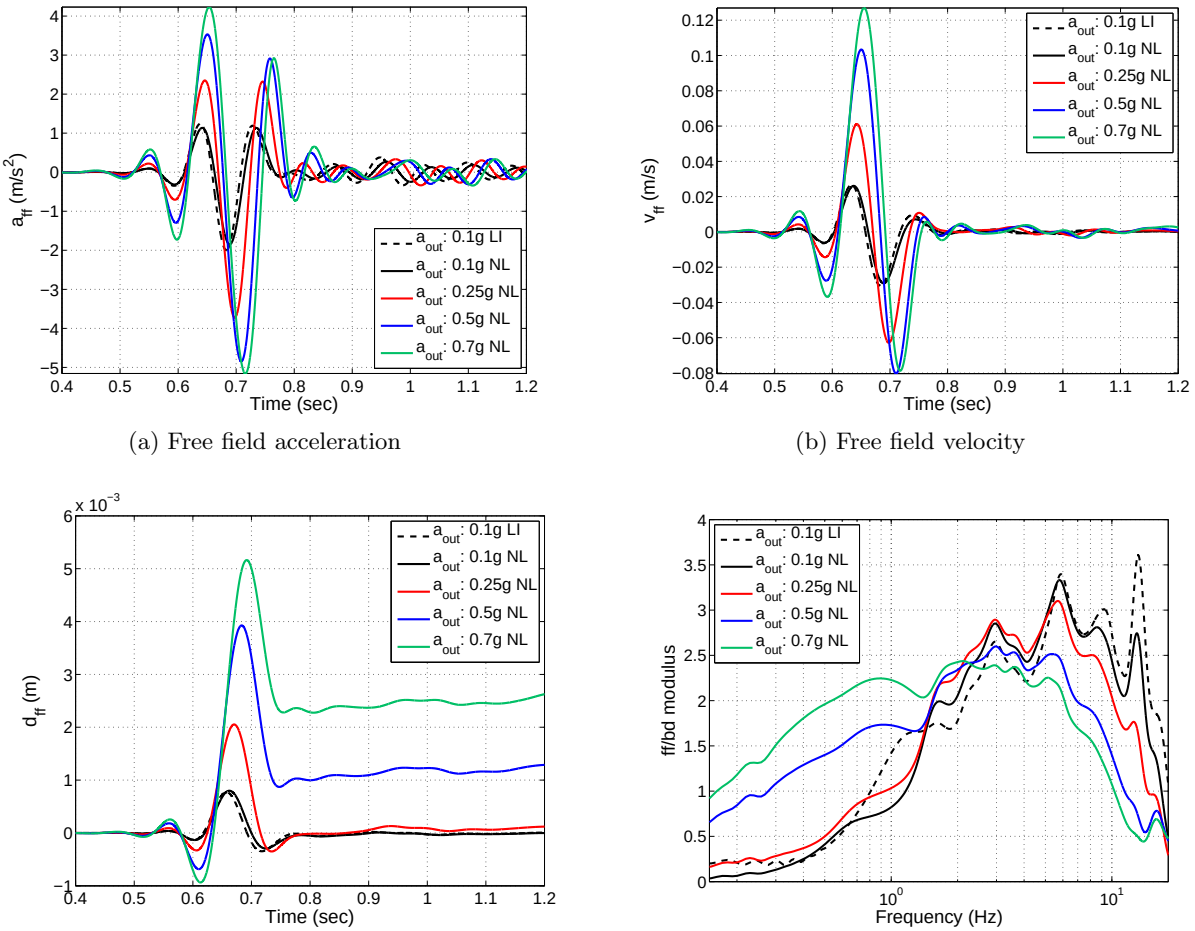

(a) Free field acceleration

(b) Free field velocity

(c) Free field displacement

(d) Transfer function between ff and out. response

Figure 5.12: First second of the response in terms of free field acceleration, velocity and displacement for the soil profile #2 and the transfer function between the free field response and the outcropping bedrock for different input motions

of the soil profile #1 is approximately 5 times the third one. For this case, the arrival time of the peak acceleration changes from 0.67 to 0.77*sec*. We observe that depending on the soil properties and input motion the effect of soil nonlinearity can be very significant.

Finally, the results are summarized in Fig.5.15a and Fig.5.15b. The acceleration of the outcropping motion is compared with the one of the free field for the three soil profiles in Fig.5.15a for all the input motions. The black solid line displays the boundary of the amplification and de-amplification between the free field and outcropping results. The dashed lines illustrate the tendency curve for the peak ground acceleration of the soil profiles with respect to the PGA of the outcropping motions. For the first soil profile, there is always amplification for the range of the strain levels that are considered. For the second soil, the amplification increases for the weak motion but for moderate and strong input motions the amplification decreases and even de-amplification is observed for strong motions. Finally, for soil profile #3 even for weak motions the amplification decreases and de-amplification is observed for moderate and strong motions. De-amplification is due to the energy dissipation that is related to the surface of each hysteresis loops in the stress-strain curve. Therefore, a part of energy dissipates through the soil before reaching the surface and the response at free field decreases. The more the soil behaves nonlinear, larger the energy dissipation.

In addition, the Arias intensity (Arias, 1970) of the accelerations at free field and the outcropping bedrock is obtained and shown in Fig.5.15b. The Arias intensity can be computed through the following equation:

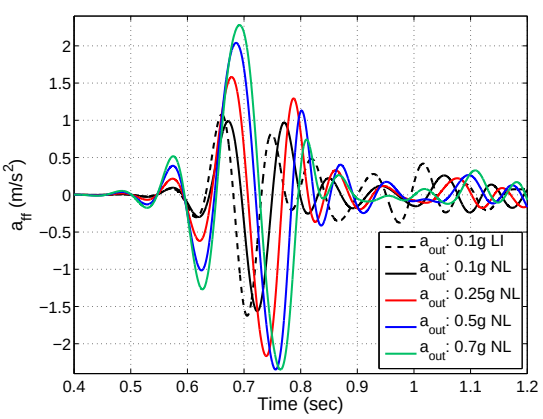

(a) Free field acceleration

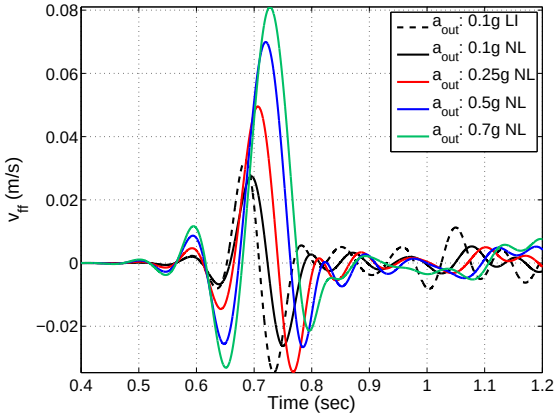

(b) Free field velocity

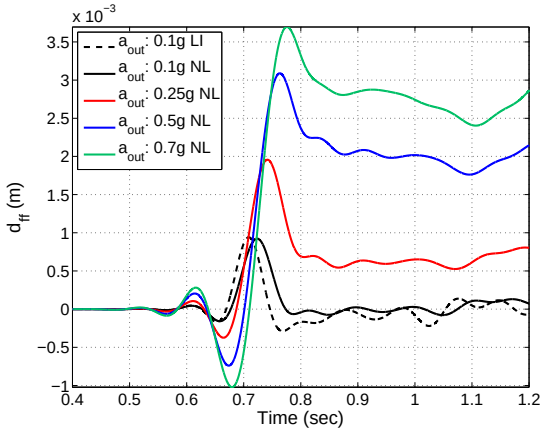

(c) Free field displacement

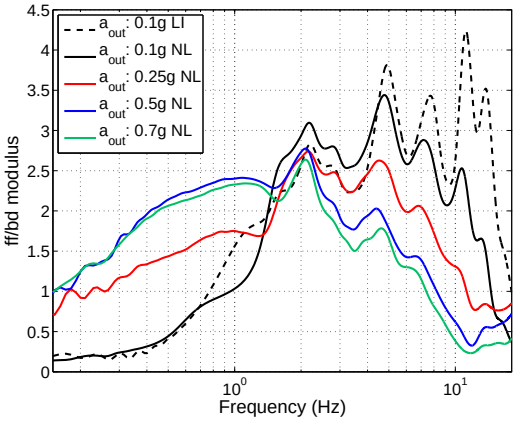

(d) Transfer function between ff and out. response

Figure 5.13: First second of the response in terms of free field acceleration, velocity and displacement for the soil profile #3 and the transfer function between the free field response and the outcropping for different input motions

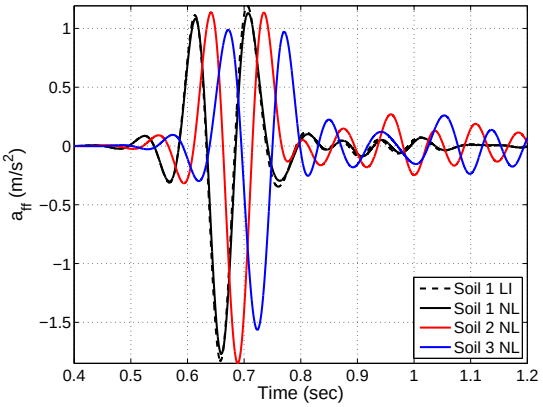

(a) Acceleration at the free field for the three soil profiles with $0.1g$ PGA

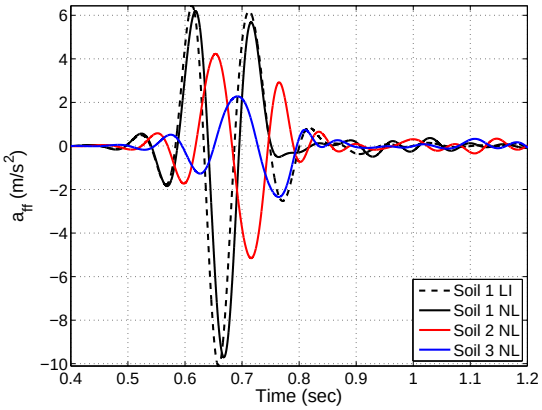

(b) Acceleration at the free field for the three soil profiles with $0.7g$ PGA

Figure 5.14: Acceleration at free field for the three selected soil profiles with $0.1g$ (left) and $0.7g$ (right) outcropping PGA's

$$AI = \frac{\pi}{2g}\int_0^t a(t)^2 dt \qquad (m/s) \tag{5.2}$$

where $a(t)$ is the acceleration in time domain. The Arias intensity is a better criterion than the PGA to compare the results, because it is related to the total duration of the wave and not only the maximum value. Comparing the results in Fig.5.15b, the same trend as the PGA shown in Fig.5.15a is observed between the results of the three selected soil profiles.

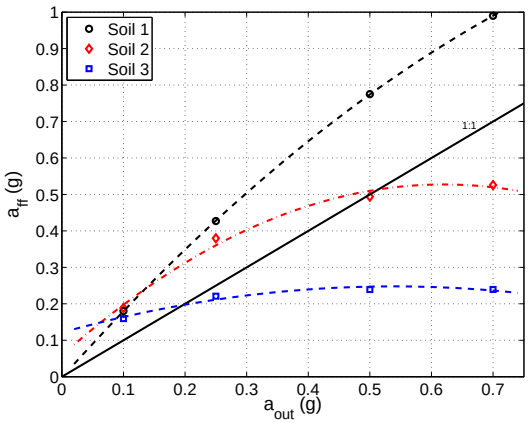

(a) Comparison between the peak acceleration at the outcropping and free field

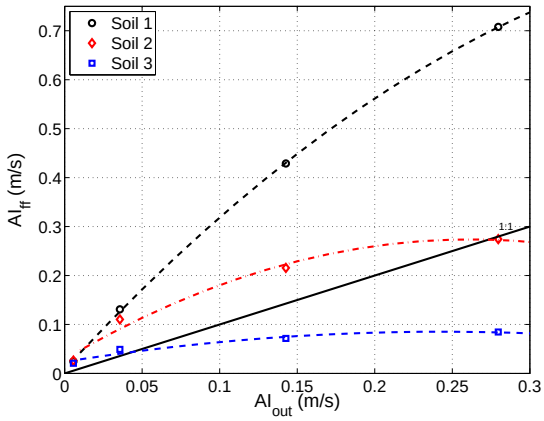

(b) Comparison between the Arias intensity of the acceleration at the outcropping and free field

Figure 5.15: Comparison between free field and outcropping bedrock in terms of peak acceleration (left) and Arias intensity of the acceleration (left) for the three soil profiles

We also compared the transfer function between the free field (ff) response and the base of the soil profile (sb). This transfer function gives the natural frequencies of the soil profiles and their variations depending on the level of the soil nonlinearity. The results are presented in Fig.5.16. It is observed that due to the soil nonlinearity, the natural frequencies of the soil profiles shift to the lower frequencies. This shift is stronger for soil profile #3 than for the two other soil profiles. We observe that the change in frequency is stronger for the second and the third natural frequencies than the first one. For example, for the second soil profile, the first natural frequency shifts from 2.41Hz with linear soil behavior to 2.33Hz with nonlinear soil behavior at $0.1g$ outcropping PGA and 2.12Hz at $0.5g$ outcropping PGA. This means 3.3 and 12 percent. For the second soil profile these values change from 5.76Hz to 5.57Hz and 5.03Hz, respectively. This means 3.3 and 12.6 percent. We observe that the changes are almost similar in the two cases, but, as the second natural frequency is larger than the first one, this change is more significant.

Also, the amplitude of the transfer function decreases by increasing the soil nonlinearity where this reduction is stronger for the third soil profile. This is the effect of soil nonlinearity that filters the high frequencies.

As the natural frequencies of the soil are modified during the propagation, their interaction with the fundamental frequencies of the structure could be interesting. This will be studied in the next sections.

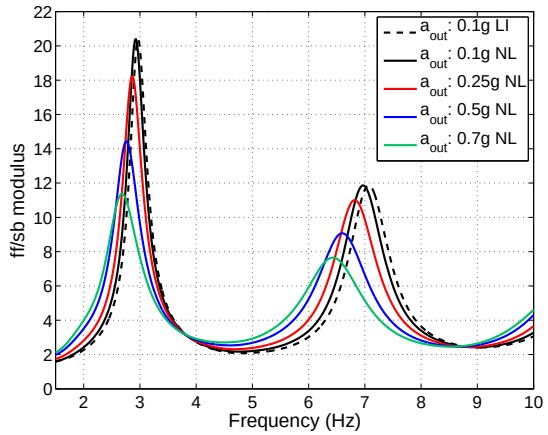

(a) Transfer function of ff/bs for soil profile #1

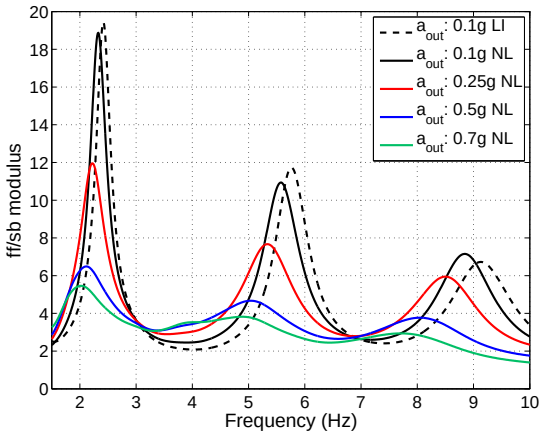

(b) Transfer function of ff/bs for soil profile #2

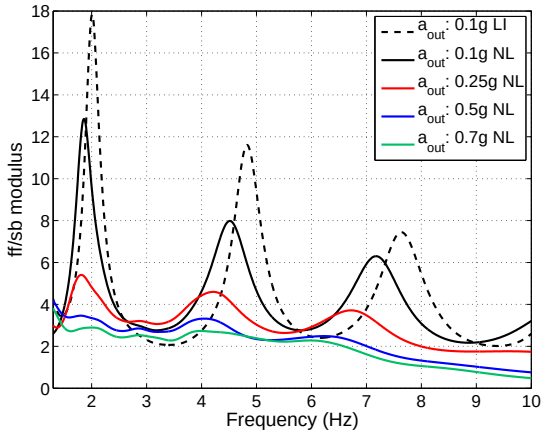

(c) Transfer function of ff/bs for soil profile #3

Figure 5.16: Transfer function between the free field response and the base of the soil profile (ff/bs) for the three different soil profiles and different input motion levels

5.4 Structural response

45 analyses are performed combining different types of structures and soil profiles. These analyses are divided in 9 case studies (§5.2.5). In the following, we try to investigate the effect of soil nonlinearity on the dynamic soil-structure interaction. First, the response of each structure is studied separately and then the results are compared with each other.

5.4.1 Structure b01

5.4.1.1 Structural response

The first structure is an idealization of a twelve story reinforced concrete frame presented in §5.2.1. The fundamental frequency of this structure on a fixed base is equal to 0.56Hz. The fundamental frequency of the structure is always lower than the natural frequency of the soil profile even with nonlinear behavior. In the following, the response of the structure based on the three selected soil profiles is studied in time and frequency domains.

The first case study is the combination of the structure b01 and the soil profile #1. The acceleration computed at the top of the structure is shown in Fig.5.17a. As the soil behavior is approximately linear even for the strong motions, there is no difference between the apparent wave velocities of the peak accelerations at the top of the structure. The acceleration at free field is much larger than that at the top of the structure. One of the reason could be the effect of the contact elements. They allow the sliding with a nonlinear behavior, therefore, a part of the energy does not pass to the structure. Another reason could be the filtering effect of the structure and its flexibility. The fundamental frequency of the structure is small and the structure is composed of a heavy mass at $25.4m$ height that moves very slowly, consequently, it filters the frequencies different to its fundamental frequency and its response reduces.

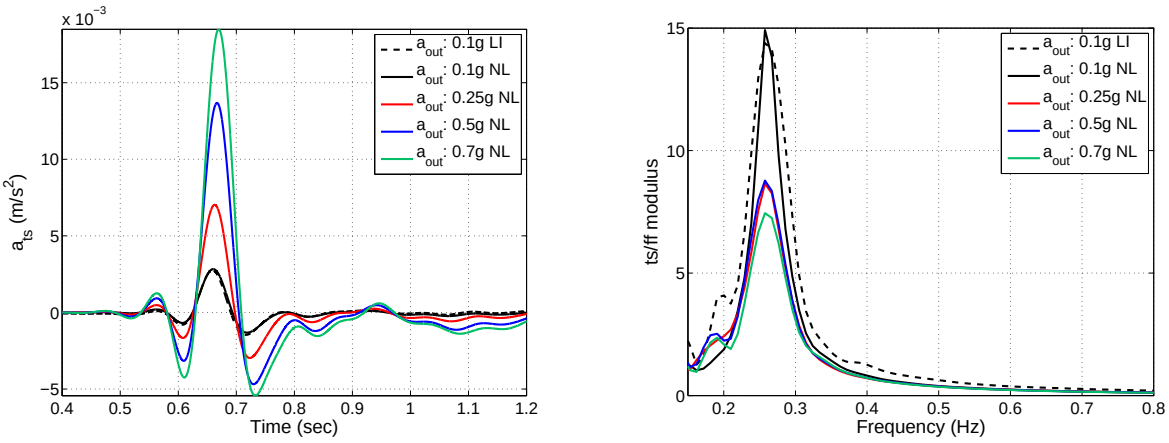

(a) Acceleration at the top of the structure

(b) Transfer function (ts/ff)

Figure 5.17: Acceleration at the top of the structure (left) and the transfer function (right) between the acceleration at the top of the structure (ts) and free field (ff) for the case study 1 (see Table 5.5)

Transfer function between the acceleration at the top of the structure (ts) and the free field (ff) is shown in Fig.5.17b. The fundamental frequency of the soil-structure system decreases significantly and shifts from 0.56Hz on a fixed base to 0.26Hz, this means more than 50%. It is observed that there is no difference between the the computed fundamental frequency of the soil-structure system for different levels of the soil nonlinearity. However, the amplitude of the transfer function is different for various input motions. The soil nonlinearity and different energy dissipation relating to the strain level are the origin of these discrepancies.

The acceleration at the top of the structure and the transfer function between the response of the top of the structure (ts) and the free field (ff) are shown in Fig.5.18 for the case study 2.

Comparing to the first case, the acceleration at the top of the structure decreases. This seems logic because the second soil profile exhibits more nonlinearity than the first one.

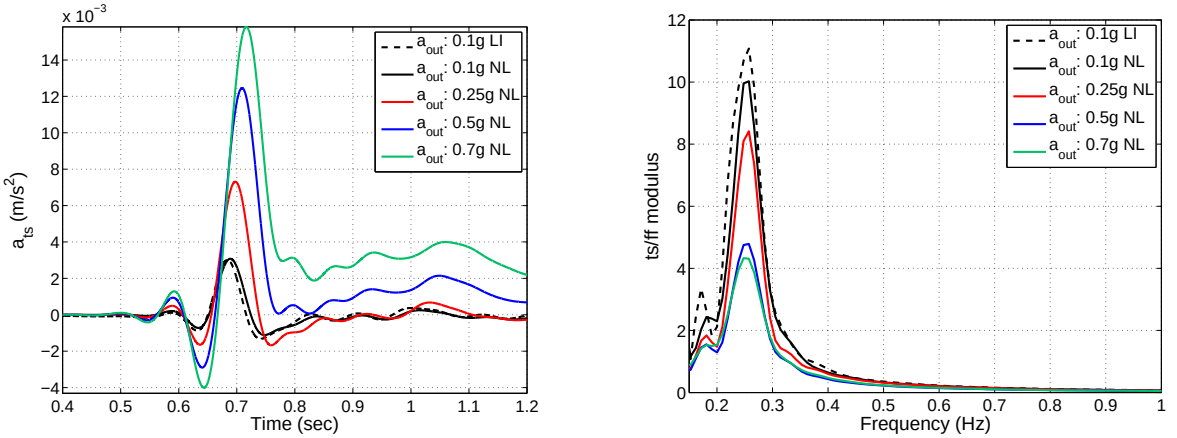

(a) Acceleration at the top of the structure

(b) Transfer function (ts/ff)

Figure 5.18: Acceleration at the top of the structure (left) and the transfer function (right) between the acceleration at the top of the structure (ts) and free field (ff) for the case study 2 (see Table 5.5)

Comparing the transfer function of the ts/ff, the computed fundamental frequency of the soil-structure system decreases to 0.26Hz. There is no difference between the fundamental frequency of the case study #1 and #2 despite the dissimilarity between the soil profiles. Only the amplitude of the transfer function decreases due to the larger nonlinearity in the soil.

We also take a look at the acceleration at the top of the structure during the total propagation duration (Fig.5.19). We observe that the structure keeps vibrating almost freely, after the passage of the induced wave at a single harmonic form which is fading out slowly.

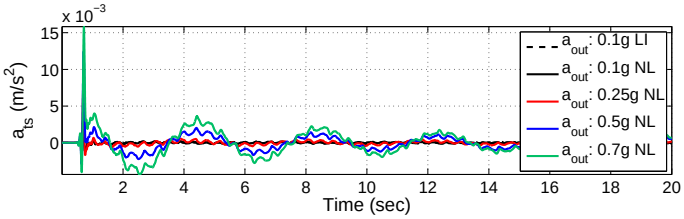

Figure 5.19: Top structure acceleration computed for the second case study with different input motion levels

Structure b01 founded on the third soil profile that contains the most nonlinear characteristics comparing to other soil profiles. The acceleration at the top of the structure and the transfer function between the acceleration at the top of the structure (ts) and free field (ff) are shown in Fig.5.20. Despite the significant nonlinearity in the soil, the fundamental frequency of the soil-structure system remains constant.

5.4.1.2 Discussion of the results

Figure 5.21 illustrates a comparison between the transfer function of the acceleration at the top of the structure and the free field for different soil profiles. The results are displayed for $0.1g$ and $0.5g$ outcropping PGA's. The fundamental frequency of the structure b01 on a fixed base is equal to 0.56Hz. Despite the difference between the behavior of the three soil profiles, there is no significant discrepancy between the fundamental frequency of the soil-structure systems. All are around 0.26Hz. This means the type of soil profile, even its behavior, does not change the soil-structure fundamental frequency. It seems that when the fundamental frequency of

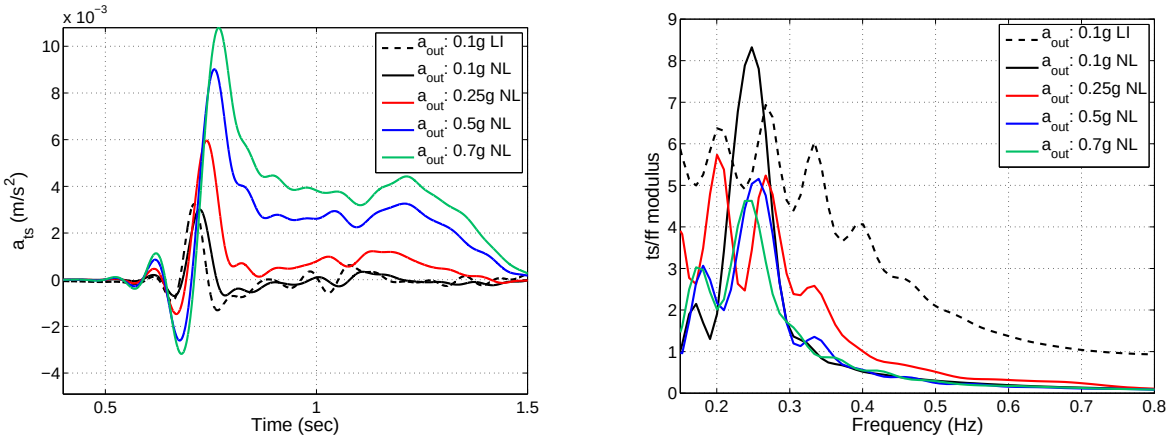

(a) Acceleration at the top of the structure

(b) Transfer function (ts/ff)

Figure 5.20: Acceleration at the top of the structure (left) and the transfer function (right) between the acceleration at the top of the structure (ts) and free field (ff) for the case study 3 (see Table 5.5)

the structure on a fixed base is smaller than the natural frequency of the soil, the effect of soil-structure is not significant. This agrees with the studies of Pitilakis (2006) and Saez (2009).

However, the modification of the fundamental frequency of the soil-structure system compared to the structure on the fixed base should be due to its weight compared to the weight of the soil around the foundation. Since the structure b01 is the idealization of another structure, many combinations of the element material densities and their stiffness gives the same fundamental frequency. Consequently, different analyses with various structures but all with similar fundamental frequency should be performed to find the reason of this large variation.

Concerning the amplitude of the transfer function, the results are different. The amplitude of the transfer function decreases due to the nonlinearity in the soil and its effect on the energy dissipation.

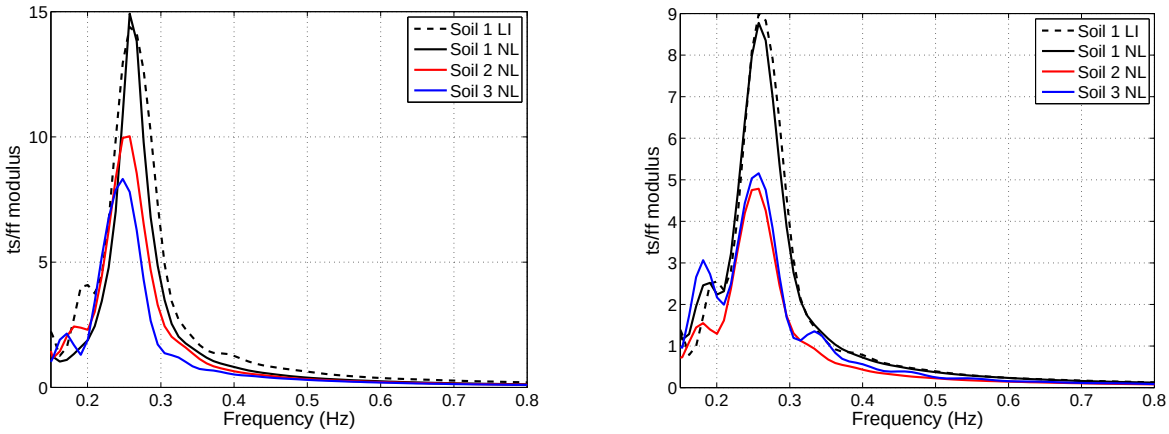

(a) Transfer function (ts/ff)

(b) Transfer function (ts/ff)

Figure 5.21: Transfer function between the acceleration at the top of the structure and the free field for 0.1g (left) and 0.5g (right) outcropping PGA's for three different soil profiles with linear and nonlinear soil behaviors

5.4.2 Structure b02

5.4.2.1 Structural response

The second structure is a $10m$ high tower, having a mass of $72t$ at the height of $10m$ above the foundation surface. The fundamental frequency of this structure on a fixed base is equal to 3.51Hz. We observe in Fig.5.4 that the fundamental frequency of this structure on a fixed base is always between the first and second natural frequencies of the soil profiles.

The acceleration at the top of the structure considering the soil profile #1 (case study 4) is shown in Fig.5.22a. The weight of the first structure is much larger than the second one, therefore, due to the inertial effect, the acceleration at the top of the second structure (5.22a) is more than the first one (5.17a).

The transfer function between the response of the top of the structure and free field for the soil-structure system of the case study 4 is displayed in Fig.5.22b for different input motion levels. Similarly to the results in the time domain, the amplitude of the transfer function (ts/ff) for the second structure is larger than the first one. The fundamental frequency of the soil-structure system with a linear soil behavior is equal to 1.6Hz. The shift of the fundamental frequency to the low frequencies is very significant, around 54%. There is also a little difference between the fundamental frequency of the soil-structure system with linear and nonlinear soil behavior.

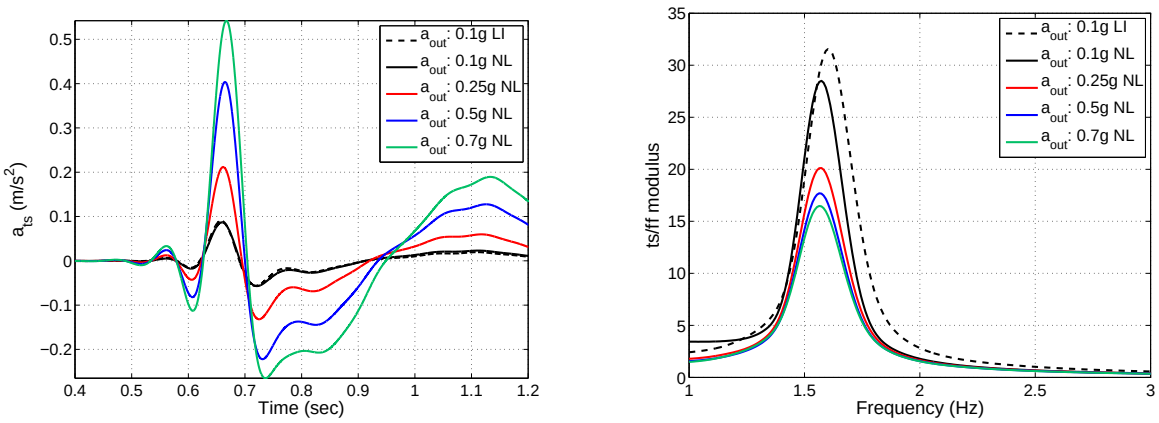

(a) Acceleration at the top of the structure

(b) Transfer function (ts/ff)

Figure 5.22: Acceleration at the top of the structure (left) and the transfer function (right) between the acceleration at the top of the structure (ts) and the free field (ff) for the case study 4 (see Table 5.5)

The results of the fifth case study are shown in Fig.5.23. This consists of the second structure based on the second soil profile. The soil is softer than the first soil profile, consequently, the acceleration at the top of the structure (Fig.5.23a) decreases. Also, the fundamental frequency of the soil-structure system is different from the case study 4. It is equal to 1.53Hz for linear soil behavior, and it continues to decrease down to 1.48Hz for the nonlinear soil behavior. However, the effect of the soil nonlinearity is not more than 3.3%. We observe that the effect of soil nonlinearity on the amplitude of the structural response is more than its effect on decreasing the fundamental frequency of the soil-structure system.

Similar results are computed for case study 6 in Fig.5.24. The fundamental frequency of the soil-structure with linear and nonlinear soil behaviors is 1.43Hz and 1.38Hz, respectively. This means the difference is equal to 3.5%.

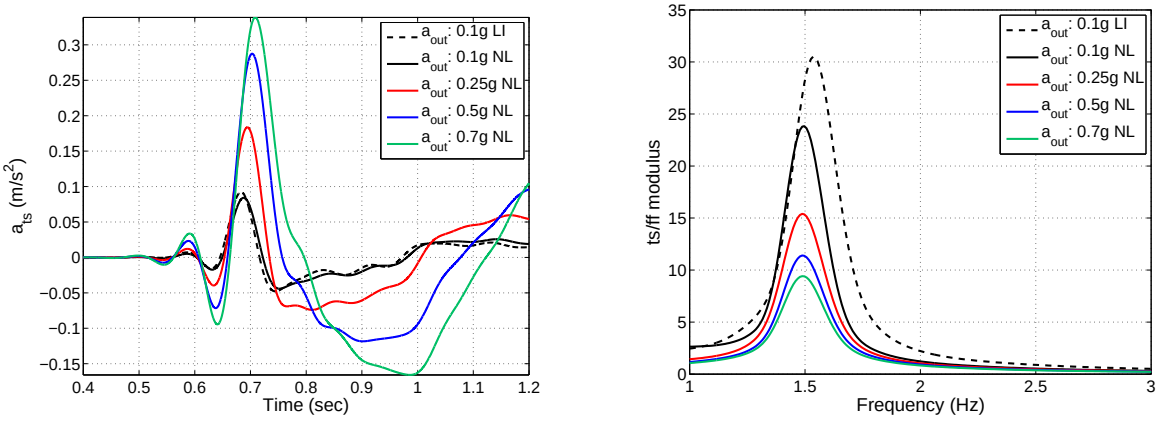

(a) Acceleration at the top of the structure (b) Transfer function (ts/ff)

Figure 5.23: Acceleration at the top of the structure (left) and the transfer function (right) between the acceleration at the top of the structure (ts) and the free field (ff) for the case study 5 (see Table 5.5)

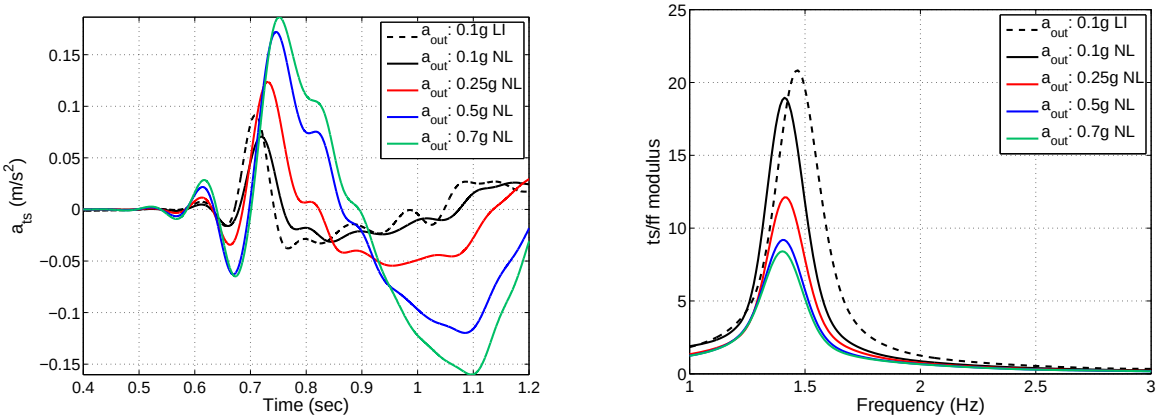

(a) Acceleration at the top of the structure (b) Transfer function (ts/ff)

Figure 5.24: Acceleration at the top of the structure (left) and the transfer function (right) between the acceleration at the top of the structure (ts) and the free field (ff) for the case study 6 (see Table 5.5)

5.4.2.2 Discussion of the results

Finally, the second structural responses are compared in Fig.5.25. This figure illustrates the transfer function between the acceleration at the top of the structure and free field for weak and strong input motions. The fundamental frequency of the soil-structure is dependent on the soil profile and we observe the soil-structure interaction effects. The fundamental frequency changes from 1.6Hz to 1.4Hz, this means 12.5%. The amplitude of the transfer function also changes significantly. It seems that for structures with fixed base fundamental frequency more than the first natural frequency of the soil, the soil-structure interaction is significant. However, the reduction of this frequency from the fixed base condition is very strong, similar to the structure b01. This is a tall slender structure having a strong rocking motion, which should be the reason of this significant reduction on fundamental frequency. The results obtained for this structure are in coherence with ones obtained by Pitilakis (2006) that studied the same one. Rocking of the foundation-structure system on a soft soil depends mostly on the characteristics of the system itself and less on the linear or nonlinear behavior of the soil. Nevertheless, the rocking effect influences the energy dissipation around the foundation and increases the soil-structure interaction. This rocking effect also changes the soil response that we will study in the next

sections.

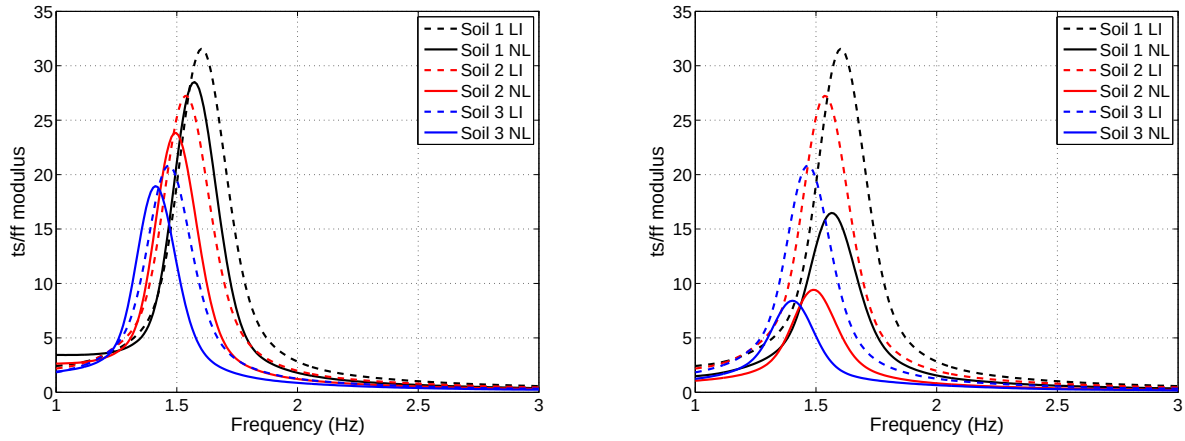

(a) Transfer function (ts/ff)

(b) Transfer function (ts/ff)

Figure 5.25: Transfer function between the acceleration at the top of the structure and the free field for 0.1g (left) and 0.7g (right) outcropping PGA's for three different soil profiles with linear and nonlinear soil behaviors

5.4.3 Structure b03

5.4.3.1 Structural response

The third structure is a six-story frame with three spans. The total height of the structure is $18m$. The total mass of the structure is equal to $182t$ and its fixed base fundamental frequency is 2.32Hz. Similarly to the two previous structures, the third structure is based on three selected soil profiles, in order to investigate the effect of soil nonlinearity on DSSI. The fundamental frequency of the structure on the fixed base is lower than the natural frequency of the first soil profile, approximately equal to the natural frequency of the second soil profile and larger than the one of the third soil profile, all with the hypothesis of the linear soil behavior. When the soil nonlinear behavior is assumed, the problem becomes complicated since the natural frequencies of the soil also reduces and the relation between these frequencies, the ones of the structure and the frequency content of the input motion may change compared to the linear behavior.

Figure 5.26a presents the first second of the acceleration at the top of the structure based on the first soil profile. This structure is more realistic than both other structures, and its weight is distributed between the stories. Acceleration at the top of the structure reaches up to $5.5m/s^2$ for an outcropping PGA equal to $0.7g$. More oscillations are observed for this structure than two other structures. The two first structures were approximately SDOF systems, but the third structure is a multi degree of freedom system (MDOF), therefore the response of the top of the structure is a combination of various structural modes.

Figure 5.26b displays the transfer function between the acceleration at the top of the structure and the free field. We observe that the fundamental frequency of the soil-structure system decreases from 2.32Hz for the fixed base condition to 1.56Hz for the structure based on the first soil profile with linear behavior. It keeps decreasing with nonlinear soil behavior down to 1.54Hz, but the difference between linear and nonlinear behaviors is only 1.3%. The first soil profile is rather a hard soil, consequently, increasing the input motion level, the difference between linear and nonlinear soil behavior on the structural response is smaller than for the two other soil profiles. Despite the effect of soil nonlinearity, the amplitude of the transfer function (TF) for the $0.7g$ outcropping PGA is more than the $0.5g$ outcropping PGA. Figure 5.16a may help us to find the reason. The natural frequency of the soil profile decreases, increasing the input motion. Therefore, the natural frequency of the soil gets closer to the frequency of the structure which

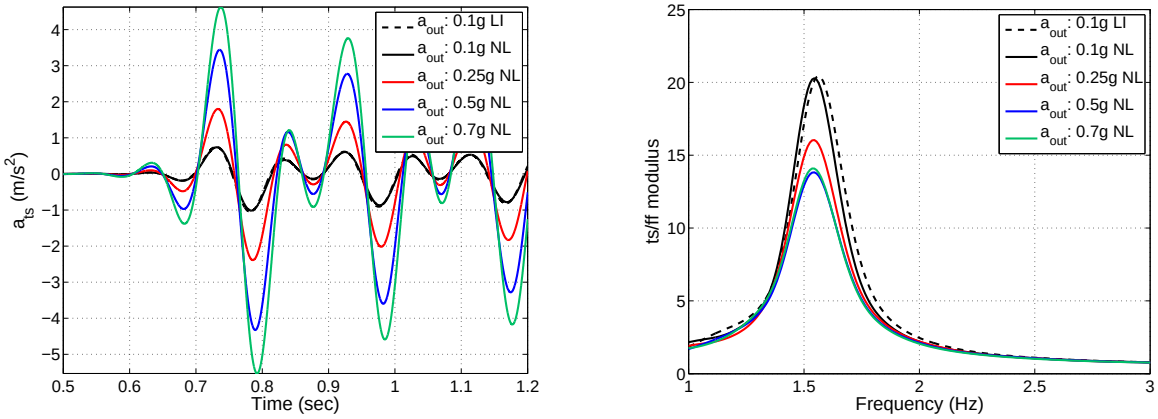

(a) Acceleration at the top of the structure (b) Transfer function (ts/ff)

Figure 5.26: Acceleration at the top of the structure (left) and the transfer function (right) between the acceleration at the top of the structure (ts) and the free field (ff) for the case study 7 (see Table 5.5)

produces a type of resonant condition that increases the structure response.

The second soil profile exhibits more nonlinearity than the first one. The acceleration at the top of the structure based on the second soil profile is shown in Fig.5.27a. As we expected, the amplitude of the accelerations is smaller than for the case study 7. The transfer function between the acceleration at the top of the structure (ts) and the free field (ff) is shown in Fig.5.27b. Comparing to the case study 7, the fundamental frequency of the soil-structure system of case study 8 is smaller, because of the weaker properties of the soil profile.

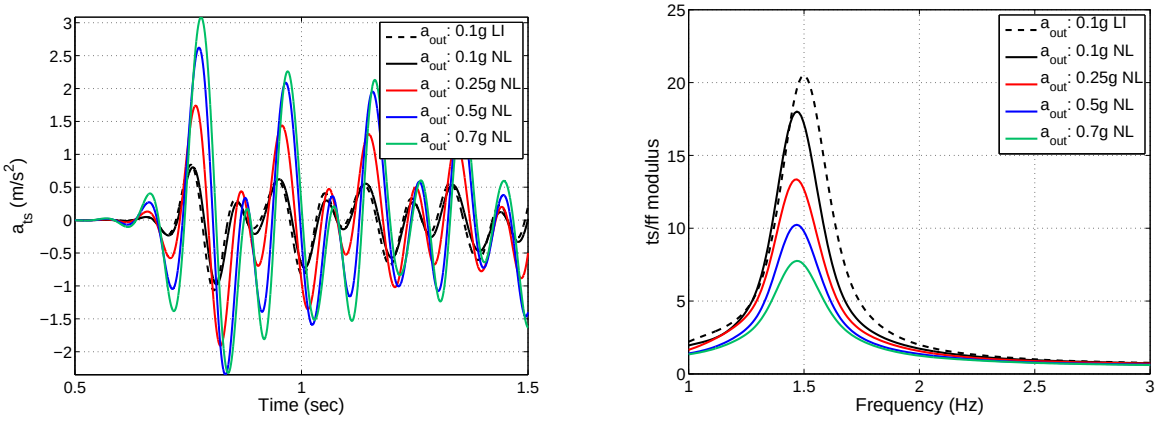

(a) Acceleration at the top of the structure (b) Transfer function (ts/ff)

Figure 5.27: Acceleration at the top of the structure (left) and the transfer function (right) between the acceleration at the top of the structure and the free field for the case study 8 (see Table 5.5)

The fundamental frequency of the soil-structure system decreases from 2.31Hz for the fixed base structure to 1.5Hz (35%) with the soil linear behavior, and 1.47Hz considering nonlinear behavior.

Finally, the results of the structure based on the third soil profile are presented in Fig.5.28. The nonlinearity is so strong that the acceleration at the top of the structure is almost the same for two different outcropping PGA's of $0.5g$ and $0.7g$ or even $0.25g$. Figure 5.15a illustrates the reason. For the third soil profile, the tendency curve of the acceleration at free field is almost linear for moderate and strong motions. This means, despite the larger amplitude of the input motion, the soil nonlinearity neutralizes the effect of higher input motions. The effect of soil

nonlinearity on the apparent wave velocity is also very clear in this example.

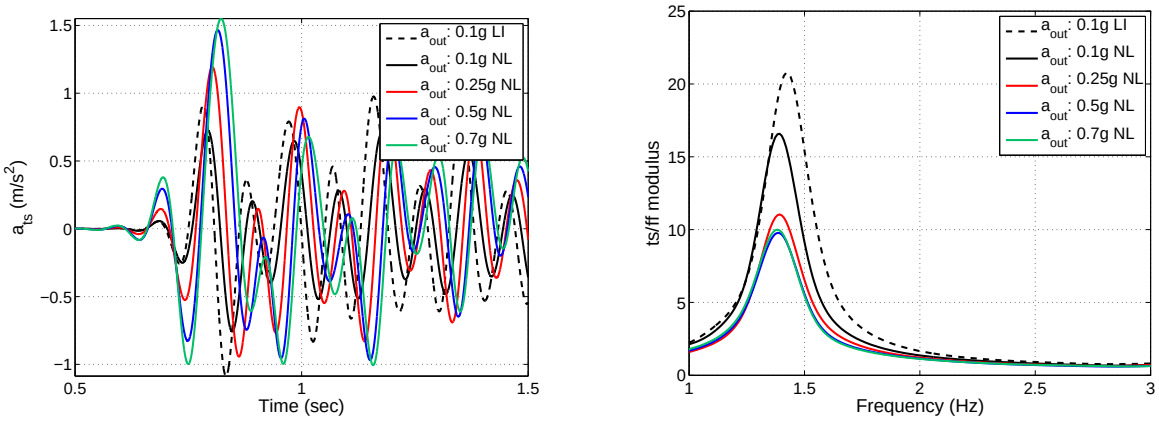

(a) Acceleration at the top of the structure

(b) Transfer function (ts/ff)

Figure 5.28: Acceleration at the top of the structure (left) and the transfer function (right) between the acceleration at the top of the structure and the free field for the case study 9 (see Table 5.5)

The fundamental frequency of the soil-structure system is equal to 1.43Hz with linear soil behavior and 1.38Hz with nonlinear soil behavior. The difference does not exceed 3.5%. From all the obtained results, we may conclude that the effect of soil nonlinearity on the reduction of the fundamental frequency of the soil-structure system is not significant.

Figure 5.29 illustrates the displacement at the top of the structure for the third structure based on the softest soil profile. We observe the production of the residual displacements in the soil and their effects on the response of the structure.

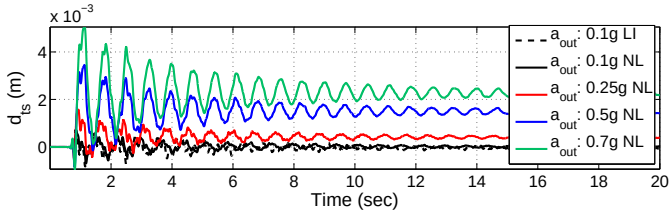

Figure 5.29: Displacement at the top of the structure for the case study 9 (see Table 5.5)

5.4.3.2 Discussion of the results

Results of the third structure are summarized in Fig.5.30 for two input motions ($0.1g$ and $0.7g$ outcropping PGA's). We observe that the fundamental frequency of the structure changes from 2.31Hz on a fixed base to 1.56, 1.5 and 1.43Hz considering linear soil behavior. This means 32, 35 and 38%. This values are equal to 33, 36 and 40% with nonlinear soil behavior.

Depending on the frequency content of the input motion and the soil properties, this shift to the low frequencies can be beneficial or detrimental. The response spectrum helps us in general to find out this effect.

For the $0.7g$ outcropping PGA, the transfer function amplitude of the second nonlinear soil profile is smaller than the third one despite the weaker properties of the third soil profile. The response spectrum of the arrival waves below the structure may help us to find the reason.

The acceleration at the top of the structure is compared between the case studies 7, 8 and 9 in Fig.5.29. The accelerations are computed for the $0.7g$ outcropping PGA. Due to the soil nonlinearity and the energy dissipation in the soil, the energy that reaches the structure reduced when the soil is softer. The top structure acceleration of the linear soil behavior case is also

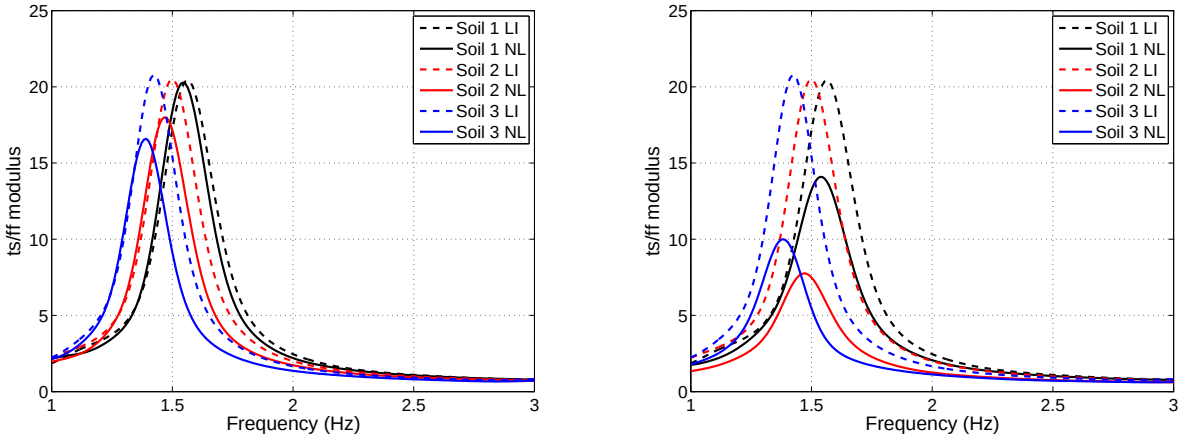

(a) Transfer function (ts/ff)

(b) Transfer function (ts/ff)

Figure 5.30: Transfer function between the acceleration at the top of the structure and the free field for 0.1g (left) and 0.7g (right) outcropping PGA's for three different soil profiles with linear and nonlinear soil behaviors

reduces. This is due to the geometric or radiation damping where the energy that reaches from the soil to the structure comes back to the soil during its oscillation and vanishes into the soil.

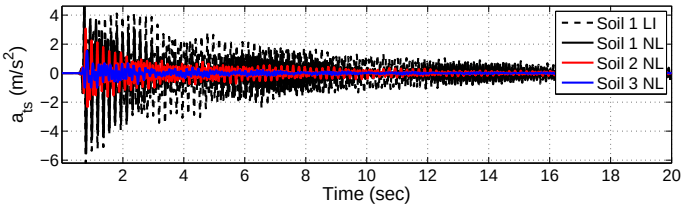

Figure 5.31: Acceleration at the top of the structure for the case study 9 (see Table 5.5) for the $0.7g$ outcropping PGA

Also, the acceleration at the end of the propagation is different between these cases. This is due to the different nonlinear properties of the soil profiles that are related to their shear modulus reduction curve. For each case, the strain level and the related shear moduli is different and consequently, the response of the soil will be different.

In general, the shift of the fundamental frequency of the soil-structure system when soil nonlinear behavior is acting is quite low. Numerical simulations show this is not a good index to discriminate linear from nonlinear behavior. However, the amplitude may be more discriminant. The structural material behavior is assumed linear, consequently, the aforementioned remark may change considering a nonlinear structure.

5.5 Energy dissipation in the soil and maximum strain during the propagation

5.5.1 Energy dissipation

In order to identify the role of the different energy dissipation mechanisms in the problem and assess the effects of soil nonlinearity on SSI, the dissipated energy due to the hysteresis behavior of the soil can be computed during the wave propagation. For the soil, an energy dissipation index can be computed by

$$I_{soil} = \frac{1}{\Omega}\int_{\Omega}\int_{t}\underline{\underline{\sigma}}(\underline{x},t) : d\underline{\underline{\epsilon}}(\underline{x},t)dV \tag{5.3}$$

with $\underline{\underline{\sigma}}$ and $\underline{\underline{\epsilon}}$ the stress and strain tensors induced in the soil during the dynamic loading in an interior material point $\underline{x}$. This integration is performed over a control volume Ω. In our plane-strain problem, the above equation takes the form:

$$I_{soil} = \frac{1}{\Omega} \int_{\Omega} \int_{t} [\sigma_{xx} d\epsilon_{xx} + \sigma_{yy} d\epsilon_{yy} + 2\sigma_{xy} d\epsilon_{xy}] \, dV \tag{5.4}$$

The contribution of each term to the total value of I_{soil} depends on the characteristics of the loading. As a result of the horizontal seismic motion (in xy) applied in our case, the contribution of the $\sigma_{xx} d\epsilon_{xx}$ is negligible. According to our results, the shear term represents the most part of the total value of I_{soil}. For the heavier buildings, relatively larger variations of vertical stress and strains are induced by the superstructure rocking. Consequently, the contribution of the vertical term $\sigma_{yy} d\epsilon_{yy}$ increases.

The necessary developments are performed during this work in order to compute the energy dissipation due to all the components of stress and strain shear tensors or due only to the shear components. For example, Figure 5.32 displays the iso-values of the cumulative dissipated energy in the soil, for three soil-structure systems (Case studies 2, 5 and 8) at the end of the computation. The dissipated energy presented here is only due to the shear terms. These structures are based on the second soil profile, and the input motion of $0.25g$ outcropping PGA is applied at the base of the model after its division by two.

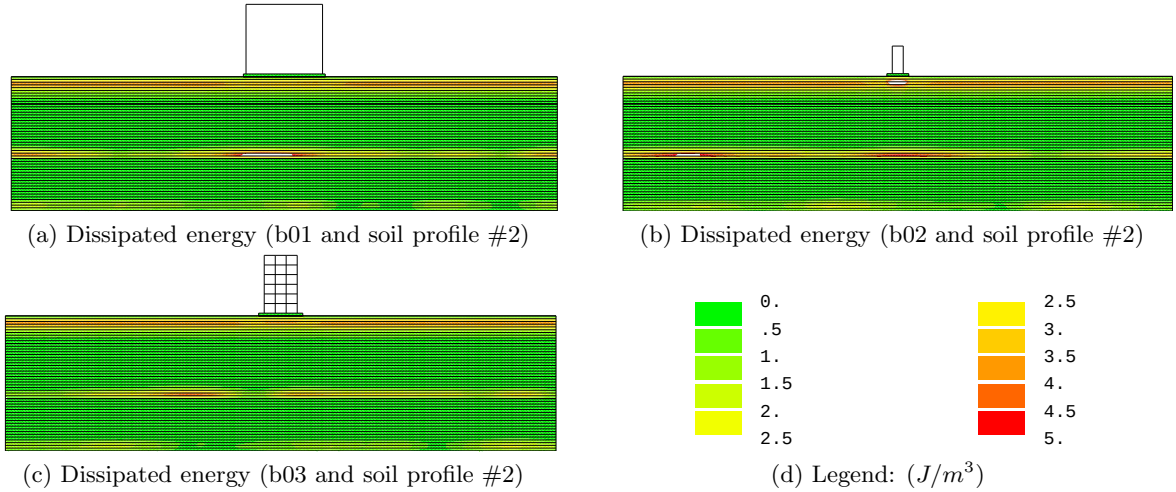

(a) Dissipated energy (b01 and soil profile #2)

(b) Dissipated energy (b02 and soil profile #2)

(c) Dissipated energy (b03 and soil profile #2)

(d) Legend: (J/m^3)

Figure 5.32: Cumulative dissipated energy at the end of the wave propagation due to the shear components of the stress and strains for case studies 2, 5 and 8 obtained for the $0.25g$ outcropping PGA

These graphs help us to find the parts of the soil medium that dissipate more energy during the wave propagation. The parts that are white in this figure dissipate more than $5J/m^3$ energy. We observe that the soil energy is strongly dissipated at the bottom boundary of each layer and also close to the surface where the up and downgoing waves are combined. Firstly, the shear modulus reduction curve is related to the confinement stress (equation 5.1), therefore the soil becomes softer by getting closer to the surface. Secondly, the properties of each layer is weaker than the one below it. Consequently, more energy dissipation is observed at the bottom boundary of each soil layer. Thirdly, the impedance contrast is higher at the boundary between layers, thus amplification is also produced, which competes with nonlinear effects.

The effect of the structure weight on the low-strain shear modulus is taken into account (see 1.6.4). This may change the nonlinear behavior of the soil particularly around the foundation. In this work, we neglected the effect of initial static condition. This effect changes the behavior of the soil before applying the dynamic loading. In addition, the weight of the structure and soil produces the settlement in the media that we did not study in our work. Therefore, the effect

of the structure weight on the low-strain shear modulus could be beneficial for the soil medium around the foundation. Figure 5.32 illustrates that different behaviors could take place around the foundation depending on the structure weight and the size of the foundation.

We observe in Fig.5.32a that for the first structure (having a considerable weight) the energy dissipation around the foundation is less than other parts of the medium in the same deep level. This should be the effect of additional confinement stress due to the weight of the structure and its effect on shear modulus. The second structure has a small foundation and a small weight. Therefore, it does not change significantly the shear modulus adjacent the foundation. But we observe that the energy dissipation below the center of the foundation is more than other parts at the same deep level. It may be from the rocking of the structure due to its tall and slender geometry. The third case behavior is in between the two other cases. It will be discussed later.

In order to quantify the energy dissipation in the soil, a surface of $2a \times 2a$ is defined below the foundation, where a is the foundation length. Then the total dissipated energy in this control surface is computed and compared between different soil-structure systems excited by different input motion levels (Fig.5.33). It is not easy to compare the results between different structures because the foundation length is different for each case. However, we observe that the dissipation for the first soil-structure system is larger than the second and the third ones due to its larger control surface.

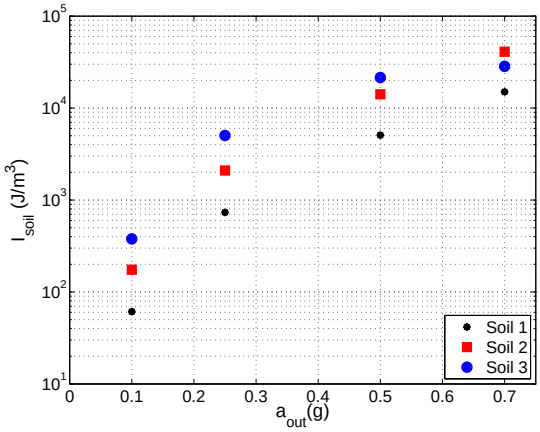

(a) Dissipated energy in term of (J/m^3) for soil-structure system with b01 building

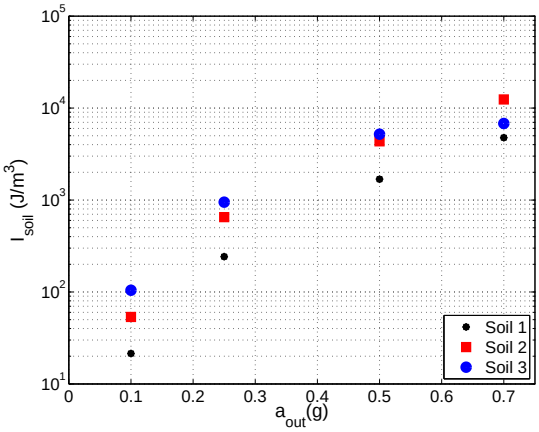

(b) Dissipated energy in term of (J/m^3) for soil-structure system with b02 building

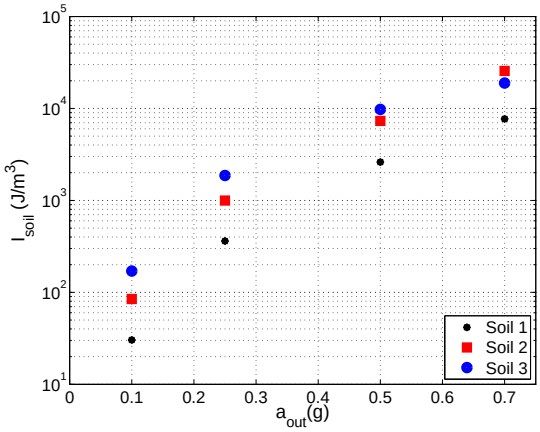

(c) Dissipated energy in term of (J/m^3) for soil-structure system with b03 building

Figure 5.33: The dissipated energy in the control surface due to the shear components of the stress and strain tensors for 3 different structures and various input motion levels

The first soil profile has less nonlinear behavior than the two other soil profiles, consequently, lower energy is dissipated in the soil. We observe that by increasing the input motion level, from

$0.1g$ to $0.7g$ outcropping PGA's, the energy dissipation of the soil-structure system with different soil profiles get closer to each other especially for the third soil profile. This means, for example, the blue points are getting closer to the red and black points. This trend is observed for the three soil-structure systems. For the third soil profile, the energy dissipation at $0.7g$ outcropping PGA is even lower than the second soil profile. The third soil profile is the softest soil between the three soil profiles, and we observe that the dissipated energy of the soil-structure system composed of the third soil profile tends to stabilize (This is due to the saturation effect, as when comparing PGA's, PGA tends to a single value-asymptotic behavior). This trend is in accordance with the work of Saez (2009). The energy dissipation computed here is the sum of different components such as soil nonlinearity, radiation damping, kinematic and inertial dynamic soil-structure interactions. Consequently, different analyses should be performed to distinguish the contribution of each one. This is beyond the scope of this work, however this could be the subject of future researches.

5.5.2 Maximum shear strain in the soil

The maximum shear strain during wave propagation could be an interesting indicator of soil nonlinearity and could be useful especially for site effects studies. In general, the energy dissipation due to the shear components of the stress and strain tensors and the maximum shear strain should be in accordance. Figure 5.34 illustrates the maximum shear strain obtained in the soil during the total calculation time. We observe that similarly to the dissipated energy, the maximum shear strain of the second soil-structure system (Fig.5.34c) is more than that of the two other systems and it takes place below the foundation. As it is said previously, since the uplift is not permitted, the rocking effect should be the reason of this energy concentration.

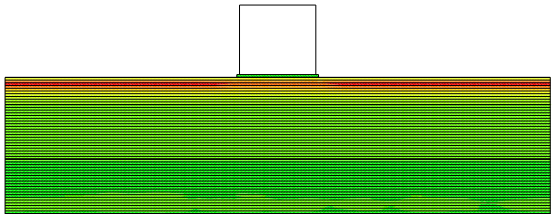

(a) Maximum shear strain (b01 and soil profile #2)

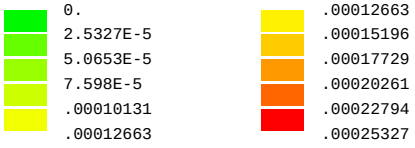

(b) Legend

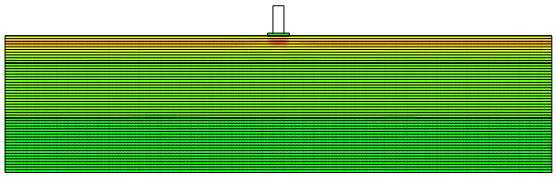

(c) Maximum shear strain (b02 and soil profile #2)

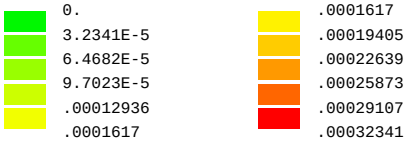

(d) Legend

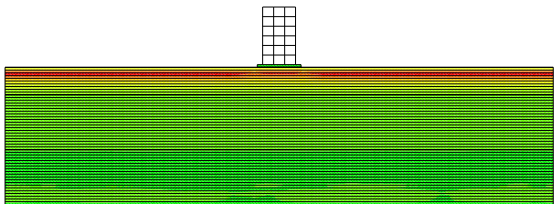

(e) Maximum shear strain (b03 and soil profile #2)

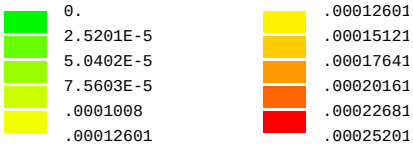

(f) Legend

Figure 5.34: Maximum shear strain in the soil during the propagation for three different soil-structure systems (Case studies 2, 5 and 8) where all the structures are based on the second soil profile and all are excited by the $0.25g$ outcropping PGA

In all cases, the maximum shear strain occurs in the first soil layer close to the free surface, where we have the combination of up and downgoing waves. With these values we are able to

obtain the minimum shear modulus that occurs during the calculation. For example, for the third soil-structure system (Fig.5.34e), the maximum shear strain reaches up to 0.0252% in the first soil layer. By means of the shear modulus reduction curve presented in Fig.5.5a, the value of G/G_0 for this level of input motion decreases approximately down to 0.7. This means around 30% of the low-strain shear moduli of the soil. Increasing the input motion level, the G/G_0 will continue to decrease. For instance, Fig.5.35 illustrates the same soil-structure system of the Fig.5.34e excited by a larger input motion as $0.7g$ outcropping PGA. The maximum shear strain reaches up to 0.071%. It gives a 0.45 G/G_0 value, this means 55% decrease on the elastic shear moduli.

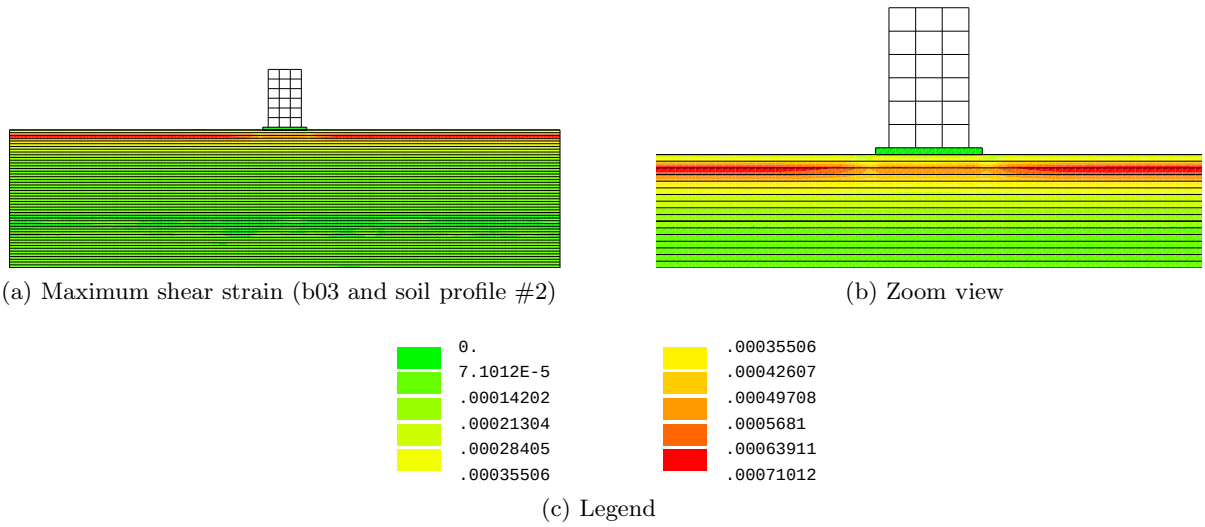

(a) Maximum shear strain (b03 and soil profile #2)

(b) Zoom view

(c) Legend

Figure 5.35: Maximum shear strain in the soil during the propagation for the third soil-structure system (case study 8) excited by $0.7g$ outcropping PGA

Figure 5.35b presents a closer view of the structure and the surrounding soil medium. This figure clearly shows the effect of the structure oscillation and the radiation effect around the structure. This can also help us to find the area in the soil which is influenced by the presence of the structure, however, the dissipated energy gives us better results where we can compare the effect of the stress and strain components on the energy dissipation. For example, the ratio of the dissipated energy in the soil due to the shear stress and strain components and the dissipated energy due to all stress and strain components (equation 5.4) gives approximately the influence area of the structure or soil-structure interaction. The difference between the two computed energy dissipation is due to the normal component of the stress and strain tensors. This ratio will be equal to 1 where the structure does not have any influence. An example of this ratio is presented in Appendix B, through a parametric study on the DSSI. This figure (B.10) illustrates the aforementioned area, that presents the structure influence zone.

5.6 Effect of SSI on energy dissipation and maximum shear strain in the soil

A detailed study on the energy dissipation and the maximum shear strain is performed in this section. Four soil columns are considered. The columns are below the control points where the indexes are shown in Fig.5.8. These columns are placed at free field (ff), below the middle of the foundation (Po.C), below the corner of the foundation (Po.B) and finally close to the foundation with a foundation length distance from the middle of the foundation (Po.A).

Figure 5.36 displays the maximum shear strain happening during the calculation and the dissipated energy due to the stress and strain shear components for the case study 2 applying $0.1g$ and $0.7g$ outcropping PGA's. The reason that there is more energy dissipation at the

bottom boundary of the soil layers and also close to the surface was described before in §5.5.1. We observe that at these areas the maximum shear strain is in accordance with the dissipated energy and is larger than other parts.

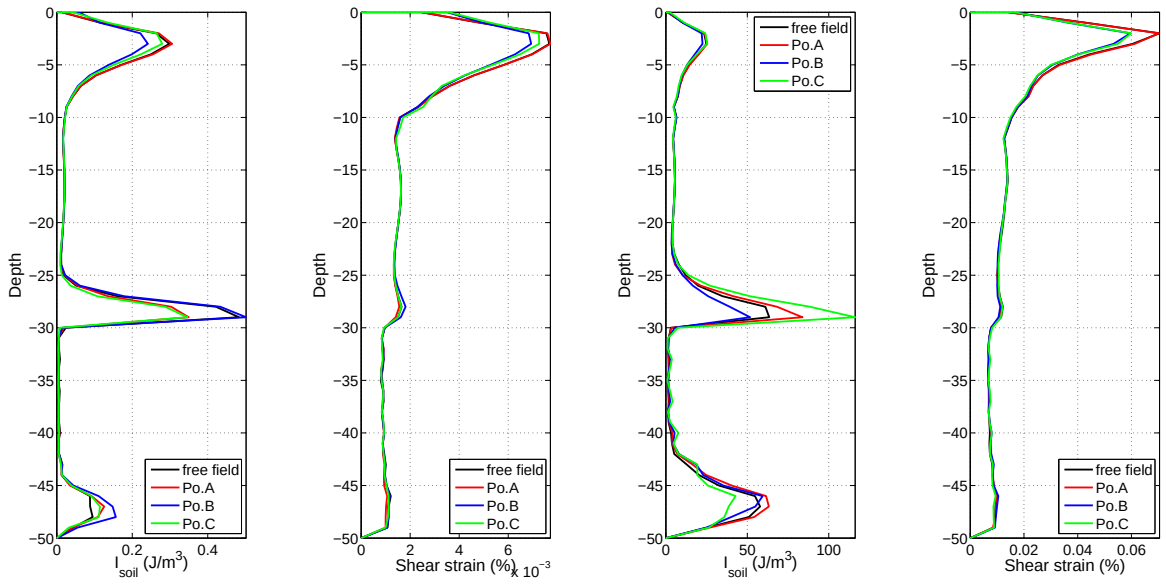

(a) Dissipated energy (b) Maximum shear strain (c) Dissipated energy (d) Maximum shear strain

Figure 5.36: Maximum shear strain reached during the calculation and the dissipated energy due to the stress and strain shear components for the case study 2 with two $0.1g$ (two left figures a and b) and $0.7g$ (two right figures c and d) outcropping PGA's, the results are compared between four soil columns presented in Fig.5.8

Following the waves that come from the elastic bedrock (below the $50m$ soil layer), a part of energy dissipates very fast at the beginning of the nonlinear soil (third layer). Before reaching the second layer, the energy dissipation and maximum shear strain remain constant. Due to the confinement stress, the soil becomes softer but at the same time the response amplitude also decreases since the soil behaves nonlinearly. Therefore, as an hypothesis, these effects neutralize each other and the energy dissipation and maximum shear strain remain constant. The waves reach the second soil layer with lower stiffness, therefore it is amplified on one side and on another side, the second soil layer is softer than third one. Consequently, a significant part of the energy is dissipated through the propagation at the bottom of the second soil layer. However, the maximum shear strain and the dissipated energy in the second layer are greater than the third one. The reason is the weaker soil properties. Also, the second soil layer is closer to the surface, therefore the energy of the downgoing waves and the radiated waves due to the structure oscillation continue to be dissipated. Finally, the energy dissipation and the maximum shear strain increase close the free surface due to the combination of the up and downgoing waves.

For this case study, because of the significant weight of the structure the dissipated energy and the maximum shear strain in the soil column at Po.B and Po.C close to the free surface is lower than the free field and Po.A columns.

The aforementioned results are computed for the case study 5 (Fig.5.37). We observe that for all cases the soil column Po.C exhibits the greatest maximum shear strain and the dissipated energy for the points close to the surface. We explained previously that this may be due to the rocking motion of the slender structure b02. Especially, the uplift is not allowed in our study, therefore, the rocking effect becomes more important.

Finally, the maximum shear strain and the dissipated energy in the soil are presented in Fig.5.38 for the $0.1g$ and $0.7g$ outcropping PGA's. We observe that the results of different soil

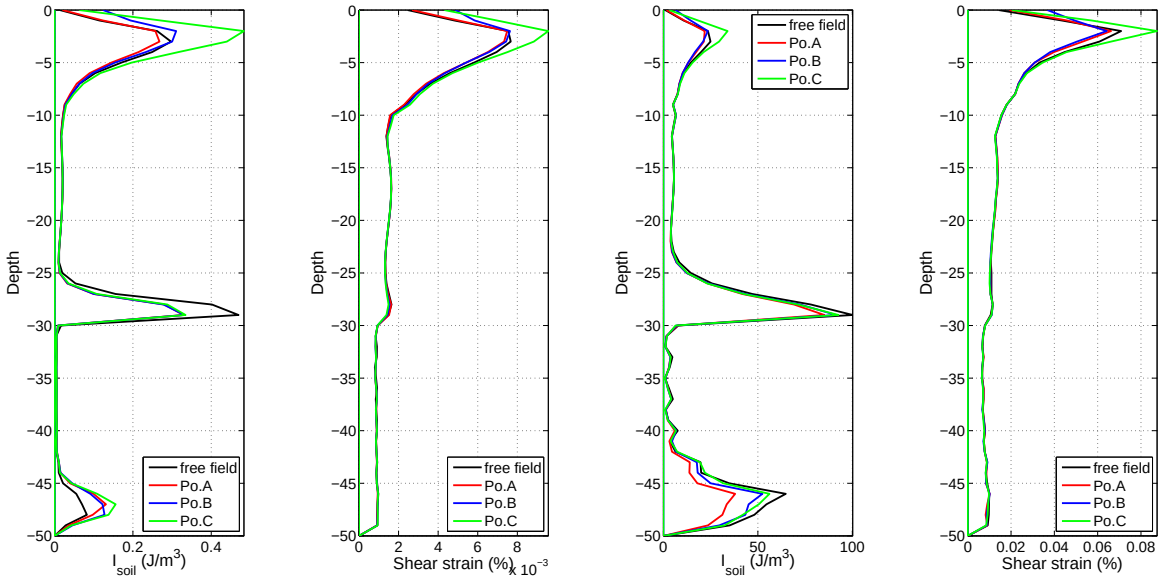

(a) Dissipated energy (b) Maximum shear strain (c) Dissipated energy (d) Maximum shear strain

Figure 5.37: Maximum shear strain reached during the calculation and the dissipated energy due to the stress and strain shear components for the case study 5 with two $0.1g$ (two left figures a and b) and $0.7g$ (two right figures c and d) outcropping PGA's, the results are compared between four soil columns presented in Fig.5.8

columns are very close to each other especially close to the surface where the maximum shear strain occurs.

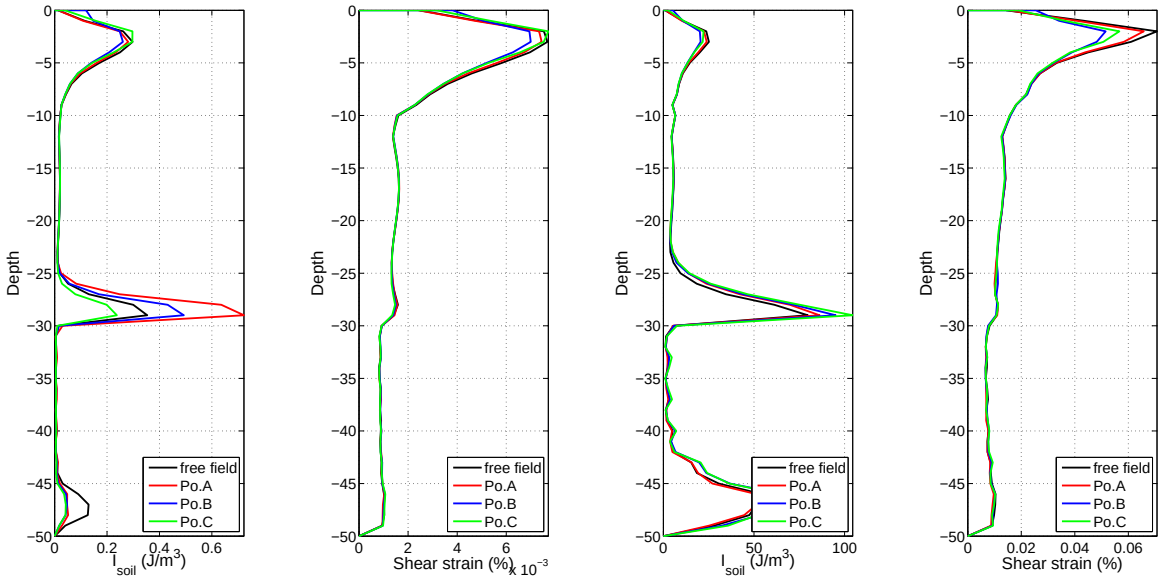

(a) Dissipated energy (b) Maximum shear strain (c) Dissipated energy (d) Maximum shear strain

Figure 5.38: Maximum shear strain reached during the calculation and the dissipated energy due to the stress and strain shear components for the case study 8 with two $0.1g$ (two left figures a and b) and $0.7g$ (two right figures c and d) outcropping PGA's, the results are compared between four soil columns presented in Fig.5.8

This soil-structure system characteristic is between case studies 2 and 5, where its weight is not large enough to change completely the shear modulus around the foundation like as the case study 2, and its geometry does not produces the significant rocking effect such as the case study 5.

5.7 Concluding remarks

Through a parametric study, different features of the nonlinear dynamic soil-structure interaction are discussed using the Finite Element formulation (CESAR-LCPC code) described in previous chapters. Different combinations of the fundamental frequency of the structure and natural frequency of soil are considered.

Depending on the soil properties, the frequency content of the soil response could change significantly due to the soil nonlinearity. The peaks of the transfer function between free field and outcropping responses shift to the lower frequencies and amplification occurs in this frequency range. Amplification reduces for the high frequencies and even de-amplification may happen for high level input motions. These changes influence the structural responses.

We observed that when the fundamental frequency of the structure on a fixed base is smaller than the natural frequency of the soil, the effect of soil-structure is not significant. However, the effect of structure weight and rocking of the superstructure could change the results. For structures with a fixed base fundamental frequency above the first natural frequency of soil, the soil-structure interaction is significant.

Considerable changes in amplitude of the structural response were seen due to soil nonlinearity. For the selected structures and soil profiles of this work, the performed numerical simulations showed that the shift of the fundamental frequency is not a good index to discriminate linear from nonlinear soil behavior. However, the structural response amplitude may be more discriminant.

Dissipated energy in the soil and maximum shear strain during the propagation are used in order to quantify the soil nonlinearity and its effect on dynamic soil-structure interaction. In general, because of soil nonlinearity, part of energy dissipates into the soil during the propagation before reaching the structure and consequently, the response of the structure is different.

It was shown that the weight of the structure plays an important role on energy dissipation into the soil and influences the soil and structure responses.

Chapter 6

Wave propagation on a heterogeneous nonlinear media and DSSI

Contents

6.1 Introduction

In the previous chapters the implemented nonlinear model is used for simple soil profiles, where the layers are perfectly horizontal. In this chapter, the model is now used to investigate site effects and dynamic soil-structure interaction for a real site with complex geometry. The Nice basin is considered to reach this goal.

This basin is analyzed considering a linear and nonlinear soil behavior for the basin layers and for different input motions to investigate the effect of soil nonlinearity on site effect. In addition, a structure is placed on the basin in order to study the dynamic soil-structure interaction and soil nonlinearity.

6.2 Description of the studied case

The Cote d'Azur is not Japan, neither California, neither Turkey, neither Algeria and neither Indonesia. Its seismic risk is not also so high. However, it is part of the recognized seismic areas and if tomorrow an earthquake with magnitude around 6 takes place no seismologist will be surprised (GEMGEP, 2005).

6.2.1 Site characterization and finite element model

The city of Nice is located in the south eastern part of France, between the Alps and the Mediterranean sea. The regional seismicity is moderate but not negligible. Five RAP (French Permanent Accelerometric Network) stations are located in the city, four in the quaternary sedimentary basin of Nice (stations NLIB, NPOR, NROC, NLAS) and one at rock (station NBOR). Experimental measurements of site effects, that used microtremors and earthquake recordings, clearly indicated that site amplification occurs in Nice (Duval, 1996; Gelis et al., 2008).

The 2D model of Nice basin, where the NLIB station is located, is used to investigate the effect of soil nonlinearity on site amplification and dynamic soil-structure interaction. The NLIB station is shown in Fig.6.1. This site is modeled by means of finite element code, CESAR-LCPC.

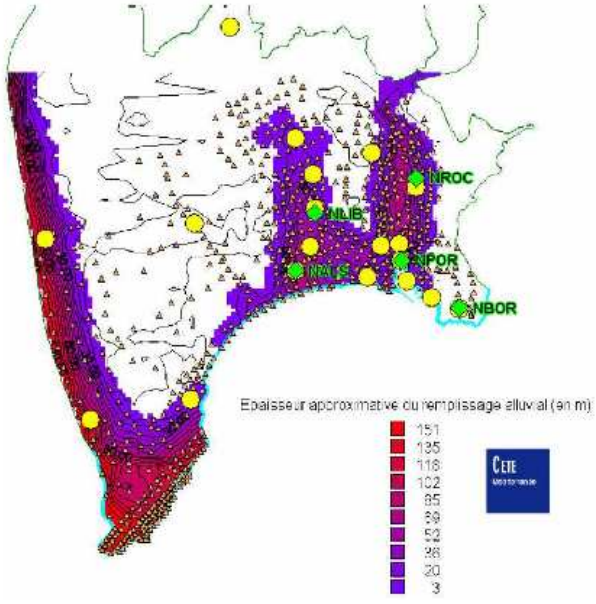

Figure 6.1: Depth of the Nice basin and the location of the stations in green after GEMGEP (2005)

The model has $1.3Km$ length. The minimum and maximum shear wave velocity are $180m/s$ and $1000m/s$ in the sediments and bedrock, respectively. The geometric properties of the basin are given in Fig.6.2. Table 6.1 presents the material properties of all the layers of the basin.

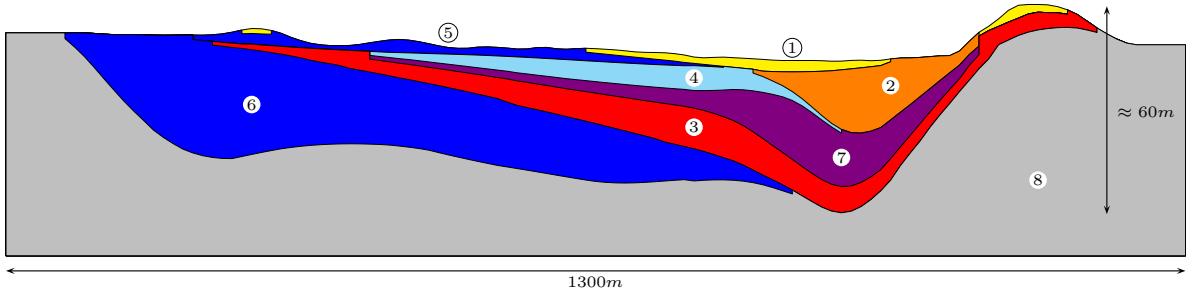

Figure 6.2: Geometry of 2D Nice basin

In the absence of P-wave velocity, we assumed a Poisson's coefficient of 0.4. As the rock station (NBOR) in not included in our model, the reference point is assumed to be the rock outcrop of the 2D model at the two edges.

Layer	$V_s(m/s)$	$\rho(Kg/m^3)$	$G_0(MPa)$	ν	$\tau_{max}(KPa)$	$\gamma_{ref}(\%)$
1	180	1900	61.57	0.4	43.73	0.027-0.06-0.067
2	200	1700	68.00	0.4	135.40	0.18
3	220	1800	87.11	0.4	231.61	0.035-0.25
4	250	1800	112.50	0.4	167.24	0.125
5	290	1900	159.78	0.4	54.68	0.034
6	290	2000	168.21	0.4	242.21	0.018-0.144
7	300	2100	189.00	0.4	224.66	0.119
8	1000	2100	2100.00	0.4	-	-

Table 6.1: Material properties of different soil layers of Nice basin

6.2.2 Input motion

Gelis et al. (2008) used a synthetic accelerogram simulating a M6 earthquake located at $8Km$ hypocentral distance having a PGA of $0.2g$. As we are limited to borehole condition, two Gabor wavelets with $0.1g$ and $0.2g$ outcropping PGA's are applied to the base of the model (SV vertical) after dividing by two to remove the free surface effect. The Gabor wavelet and its Fourier transform are shown in Fig.5.6.

6.3 Linear and nonlinear site effects in the Nice basin

Two different analyses are performed. First, a dynamic analysis in the Nice basin considering an elastic behavior for different soil layers. For the second one, the nonlinear properties presented in Table 6.1 are used. The time step is 2.10^{-4}. The absorbing layers (§2) are used at the base of model to avoid the reflection of the waves to the basin. The same absorbing layer presented in previous chapter for the parametric study on nonlinear dynamic soil-structure problem is used here. Its properties are displayed in Table 5.3. The computation is carried out up to 12Hz. Two $0.1g$ and $0.2g$ outcropping PGA's are used.

6.3.1 Data processing

All time series were low-pass filtered with a 2 poles with a non-causal Butterworth filter at 10Hz. Furthermore, the time series were tapered using a 2.5% Hanning window and the computed Fourier amplitudes were smoothed using a Konno-Ohmachi filter (Konno and Ohmachi, 1998) with a bandwidth of 40 before computing the spectral ratios.

6.3.2 Basin response in the time domain

The velocity wavefield at the surface of the basin for the first $5sec$ with linear and nonlinear rheology is shown in Fig.6.3. Since the input motion is a Gabor wavelet which lasts less than one second, it is distinguished during the first second of propagation in Fig.6.3. As the basin has a complex geometry and material properties, the arrival time of the peak velocity is different depending on the position of the control point.

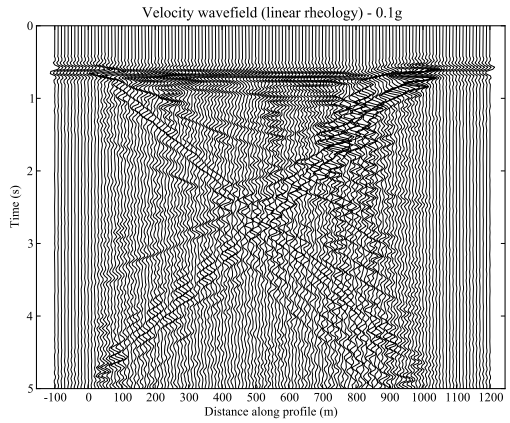

(a) Linear rheology ($0.1g$ outcropping PGA)

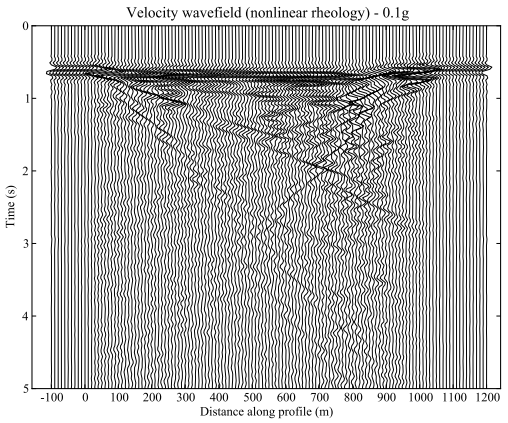

(b) Nonlinear rheology ($0.1g$ outcropping PGA)

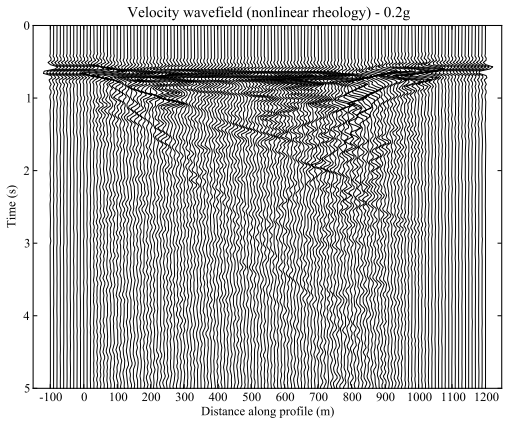

(c) Nonlinear rheology ($0.2g$ outcropping PGA)

Figure 6.3: First $5sec$ surface velocity wavefield of the Nice basin (A Gabor wavelet having a PGA of $0.1g$ and $0.2g$ is applied at the base of the model)

We observe the complex wavefield due to the geometry. The inclined layering at the left and the deeper basin at the right are clearly mapped by the ground motion. For both nonlinear cases, the wavefield is rapidly attenuated after 1.5 - 2.0sec.

The kinetic energy in the basin is also computed through the following equation,

$$E_k = \int_t \rho V_s^2 dt \quad (J) \tag{6.1}$$

The cumulative kinetic energy in logarithmic scale is shown in Fig.6.4, for linear and nonlinear soil behaviors and $0.1g$ and $0.2g$ outcropping PGA's. We observe the concentration of the kinetic energy in the basin, particularly for linear soil behavior.

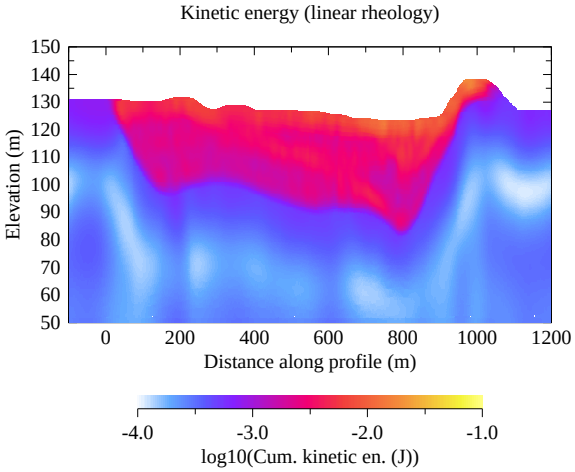

(a) Linear rheology (0.1g PGA)

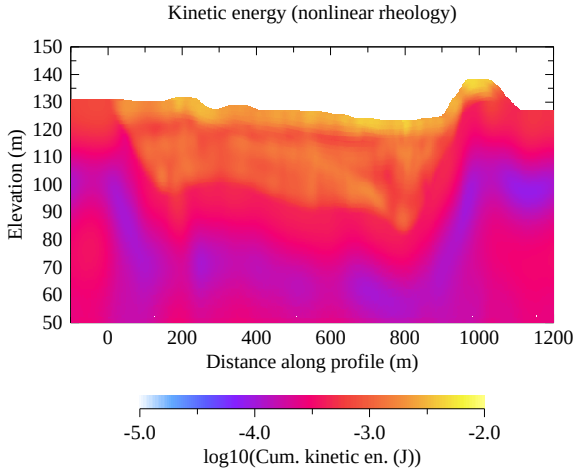

(b) Nonlinear rheology (0.1g PGA)

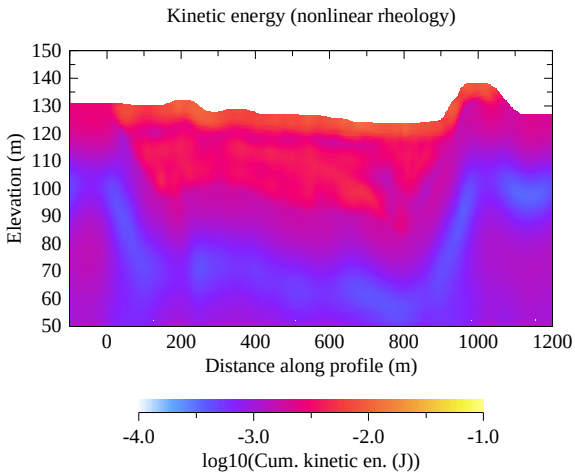

(c) Nonlinear rheology (0.2g PGA)

Figure 6.4: Cumulative kinetic energy (J) obtained for different rheology and different input motions

Comparing Fig.6.4a and 6.4b, since the wave velocity decreases due to the soil nonlinearity, the kinetic energy is decreased. The kinetic energy at $0.2g$ outcropping PGA (Fig.6.4c) is close to the results of linear soil behavior even with its double amplitude of the input motion. This is in accordance with the results of wavefield shown in Fig.6.3.

6.3.3 Basin response in the frequency domain

The transfer function of the acceleration at free surface of the basin is computed and shown in Fig.6.5 for linear and nonlinear material behaviors at $0.1g$ and $0.2g$ outcropping PGA's. Figure 6.5a illustrates the transfer function assuming linear soil behavior. Through this figure we obtain the resonance frequencies of the basin at different positions. The resonance frequency of the basin is between 2 and 2.5Hz for most of the profiles along the basin. For the hill at the right

of the basin, its resonance frequency is totally different and ranges between 8 and 10Hz. The resonance frequency of the soil profile is equal to $f = V_s/4H$ after the experimental results, where V_s is the shear wave velocity and H the height of the soil profile. We can verify the resonance frequency of the hill by means of this equation. The hill is composed of two different layers with 180, $220m/s$ shear wave velocities and approximately 2 and $4m$ height. The mean shear wave velocity is $207m/s$. Therefore, from the aforementioned equation, the resonance frequency is equal to 8.6Hz, which is in accordance with the obtained frequency calculated by the finite element model.

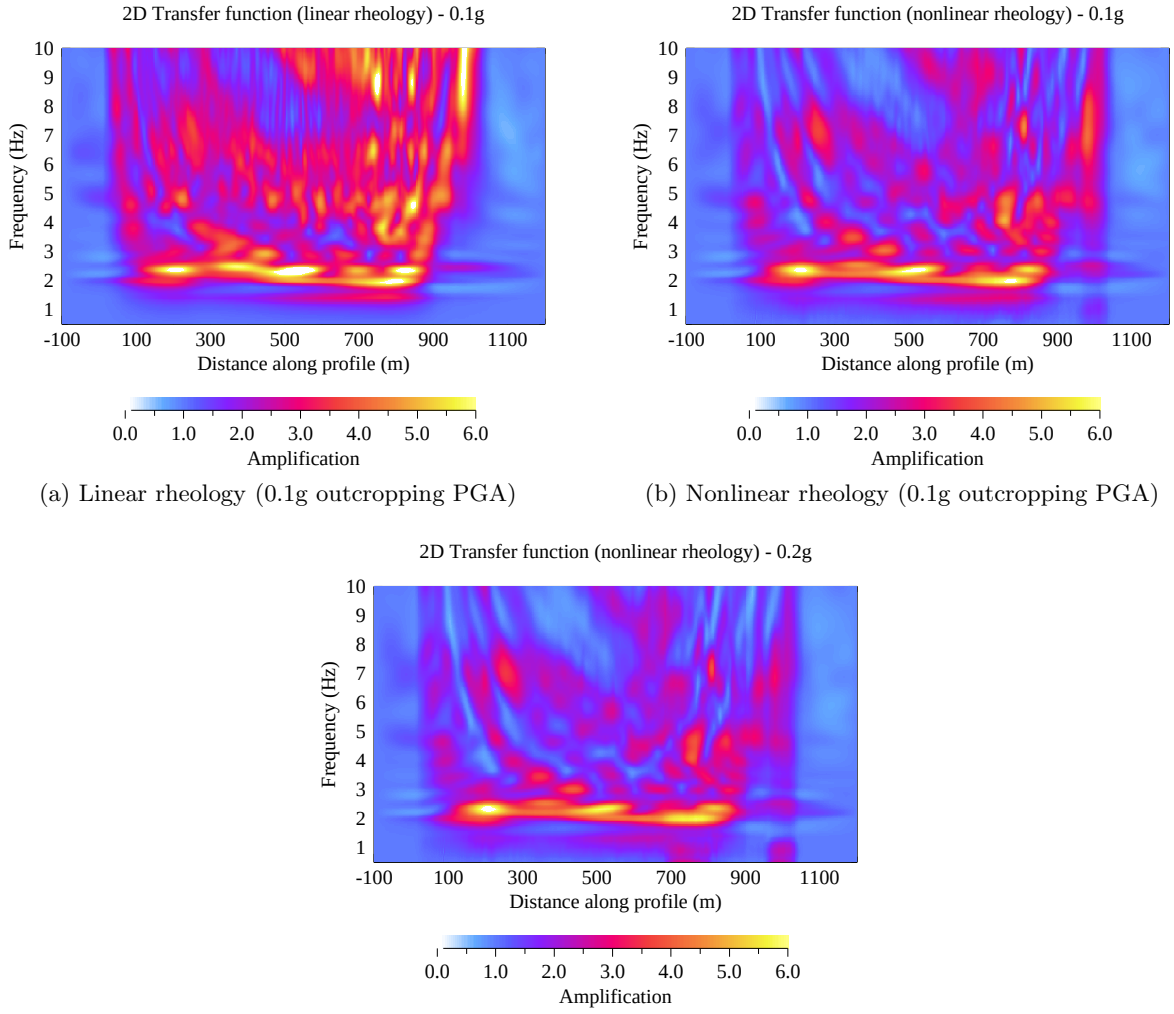

(a) Linear rheology (0.1g outcropping PGA)

(b) Nonlinear rheology (0.1g outcropping PGA)

(c) Nonlinear rheology (0.2g outcropping PGA)

Figure 6.5: Transfer function of acceleration at free surface of Nice basin for linear and nonlinear material behaviors at $0.1g$ and $0.2g$ outcropping PGA's

The maximum amplification reaches up to 6 for linear soil behavior between 500 and $600m$. This is in very good accordance with the work of Gelis et al. (2008). Comparing the results of linear and nonlinear soil behaviors, the amplification of the high frequencies decreases significantly, particularly at $0.2g$ outcropping PGA. For example, with linear soil behavior, between 700 and $900m$, strong amplification occurs for frequencies above 5 or 6Hz. However, with nonlinear soil behavior, the amplification strongly decreases and even deamplification takes place for some high frequencies.

We have, in addition, the apparition of amplification in low frequencies, for example, at the hill, the amplification between 3 and 4 happens for the frequencies around 1Hz.

The Fourier spectrum of the acceleration is also computed in the Nice basin for linear and

nonlinear soil profiles at different outcropping PGA's for 1, 2, 3, 6, 8 and 10Hz (Fig.6.6, 6.7 and 6.8). However, the effect of soil nonlinearity on the basin response is more important for us. Consequently, the ratio between nonlinear and linear soil behaviors is computed for two different input motions in Fig.6.9 and 6.10.

The two figures show that deamplification occurs at frequencies higher than 3Hz. Furthermore, these figures also show that the high frequencies are mostly affected within the basin. This results are in agreement with the results of the soil profile response obtained in the previous chapter, namely deamplification of high frequencies.

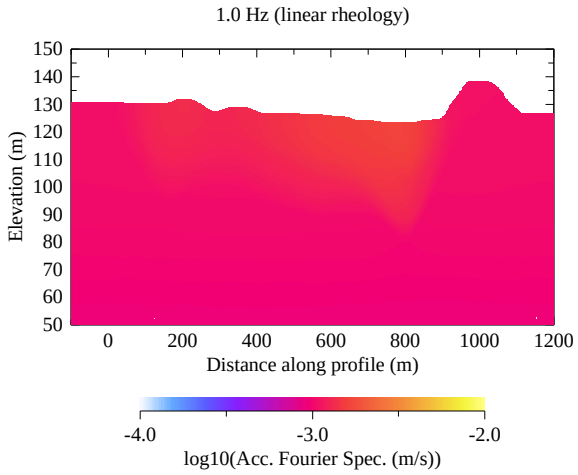

(a) Linear rheology (0.1g outcropping PGA)

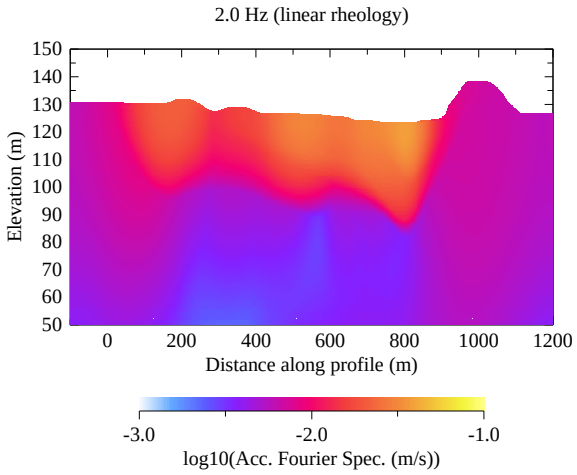

(b) Linear rheology (0.1g outcropping PGA)

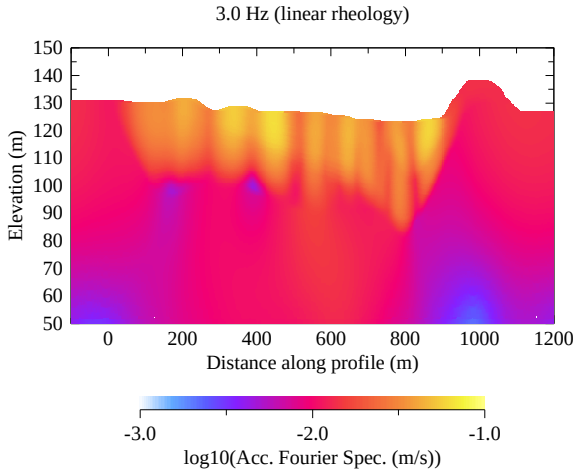

(c) Linear rheology (0.1g outcropping PGA)

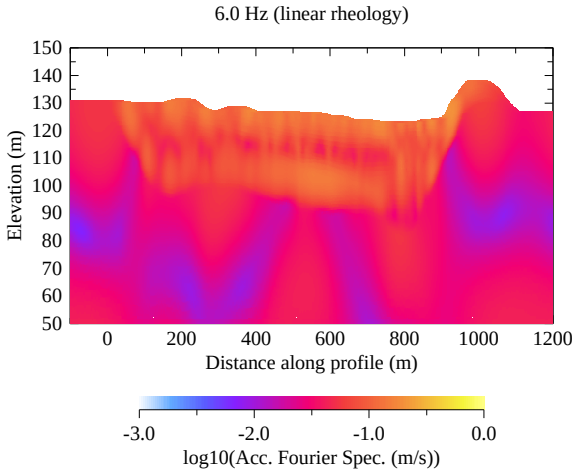

(d) Linear rheology (0.1g outcropping PGA)

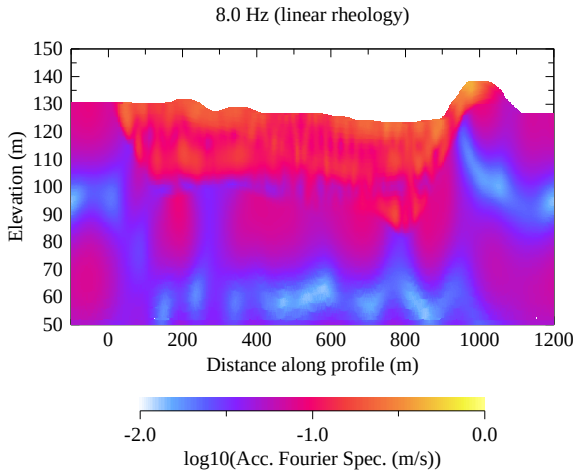

(e) Linear rheology (0.1g outcropping PGA)

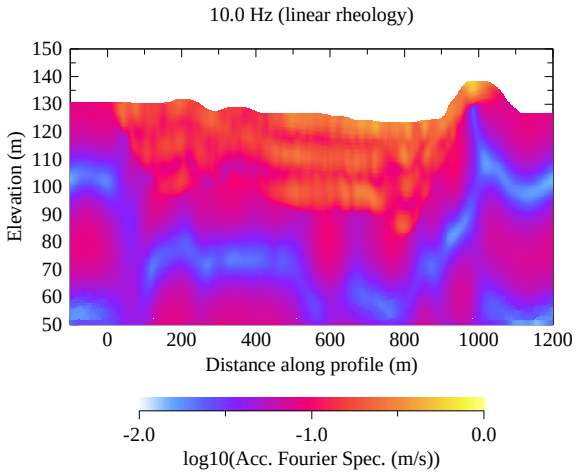

(f) Linear rheology (0.1g outcropping PGA)

Figure 6.6: Acceleration Fourier spectrum for linear soil rheology at $0.1g$ outcropping PGA's

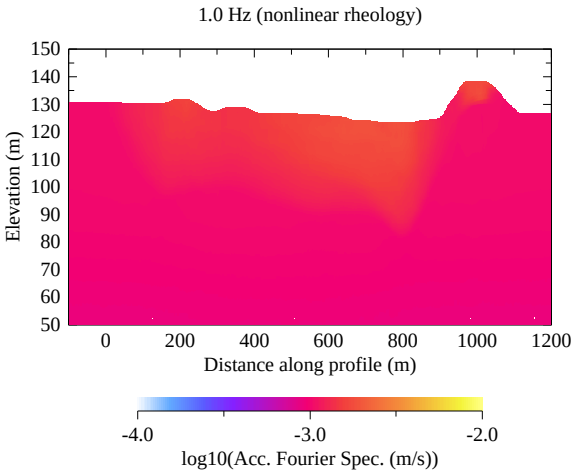

(a) Nonlinear rheology (0.1g outcropping PGA)

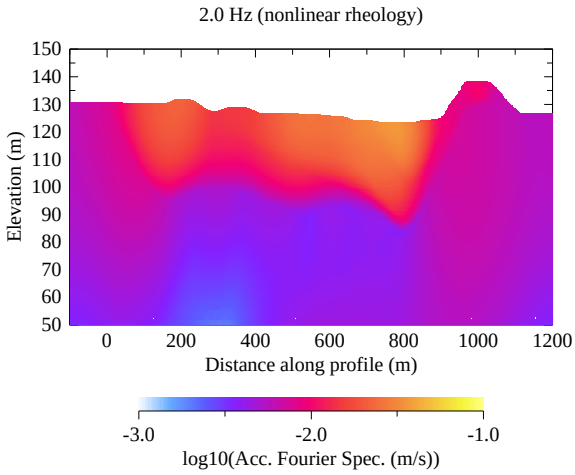

(b) Nonlinear rheology (0.1g outcropping PGA)

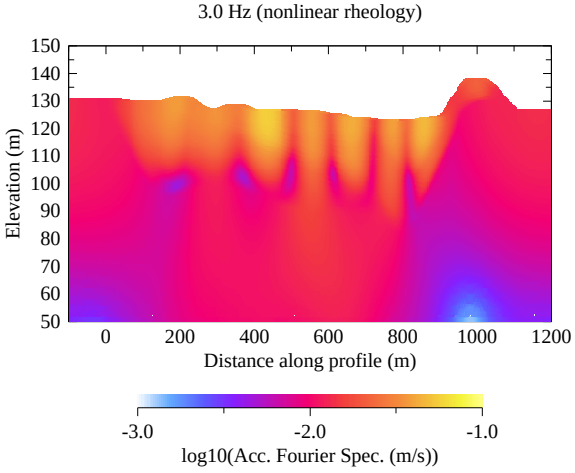

(c) Nonlinear rheology (0.1g outcropping PGA)

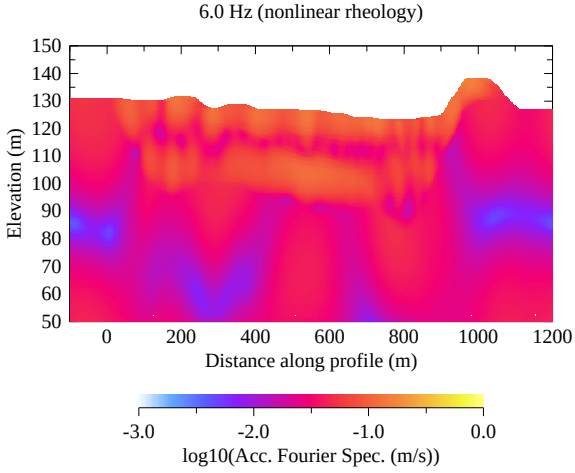

(d) Nonlinear rheology (0.1g outcropping PGA)

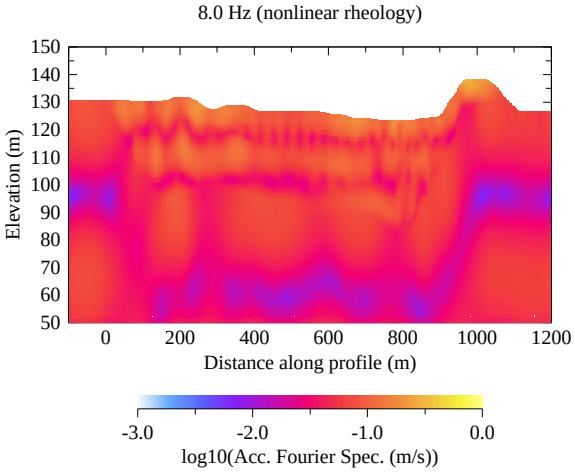

(e) Nonlinear rheology (0.1g outcropping PGA)

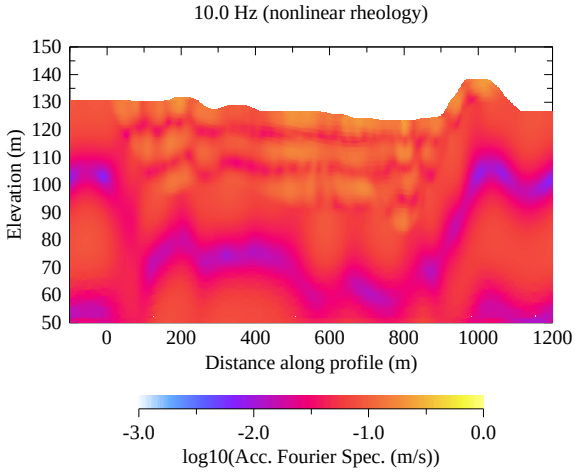

(f) Nonlinear rheology (0.1g outcropping PGA)

Figure 6.7: Acceleration Fourier spectrum for nonlinear soil rheology at 0.1g outcropping PGA's

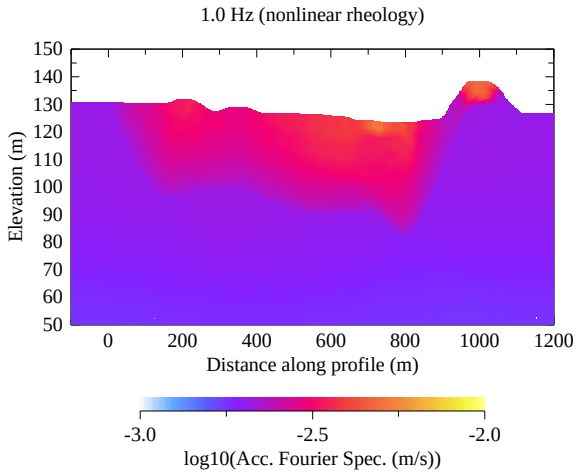

(a) Nonlinear rheology (0.2g outcropping PGA)

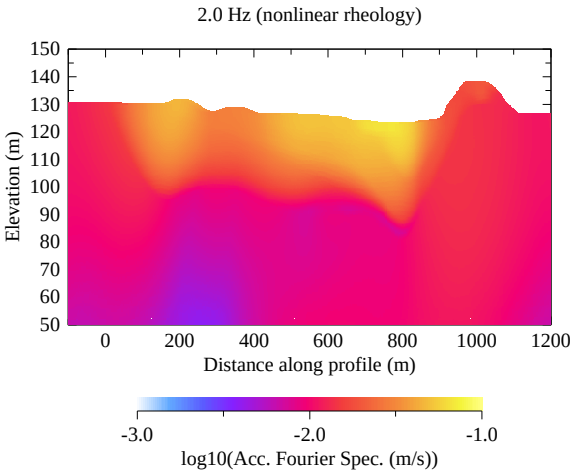

(b) Nonlinear rheology (0.2g outcropping PGA)

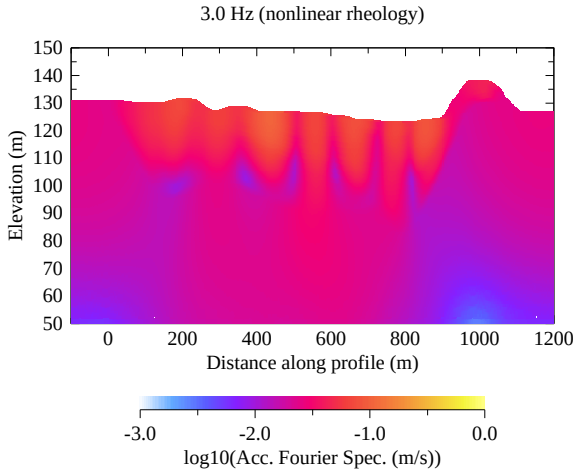

(c) Nonlinear rheology (0.2g outcropping PGA)

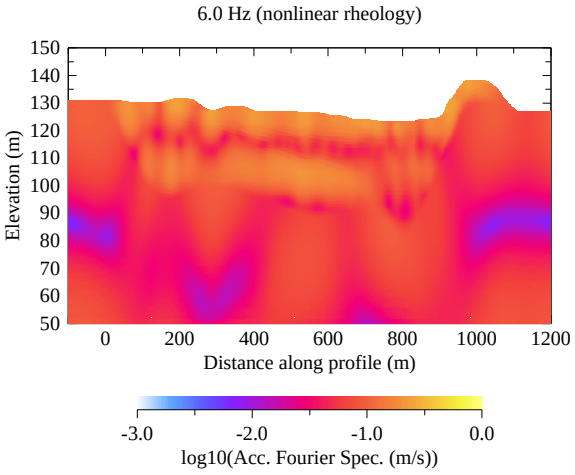

(d) Nonlinear rheology (0.2g outcropping PGA)

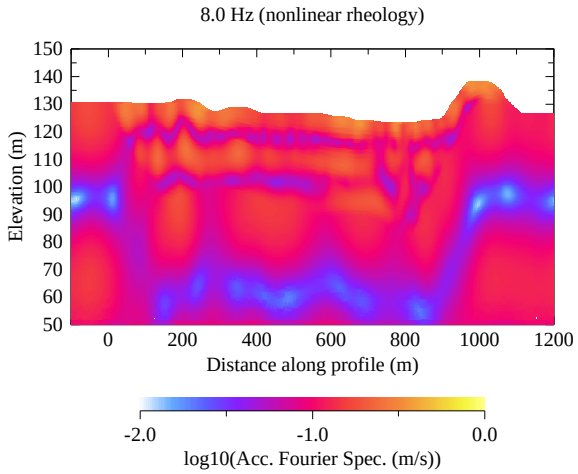

(e) Nonlinear rheology (0.2g outcropping PGA)

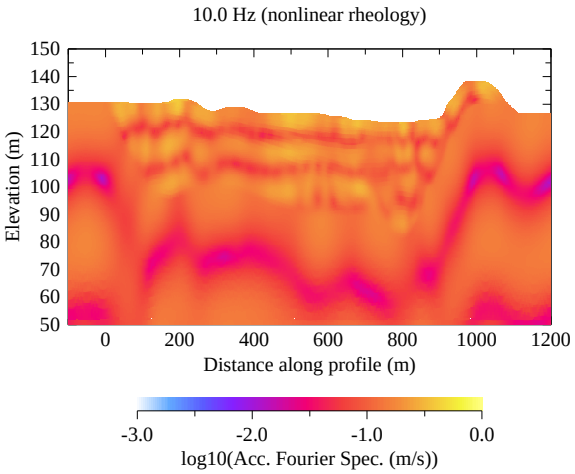

(f) Nonlinear rheology (0.2g outcropping PGA)

Figure 6.8: Acceleration Fourier spectrum for nonlinear soil rheology at $0.2g$ outcropping PGA's

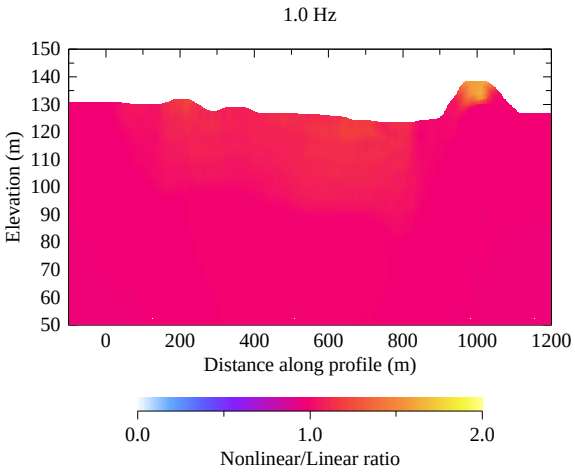

(a) Nonlinear/linear ratio (0.1g outcropping PGA)

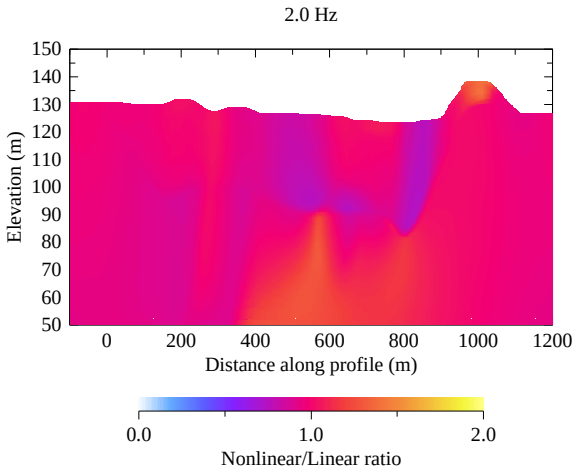

(b) Nonlinear/linear ratio (0.1g outcropping PGA)

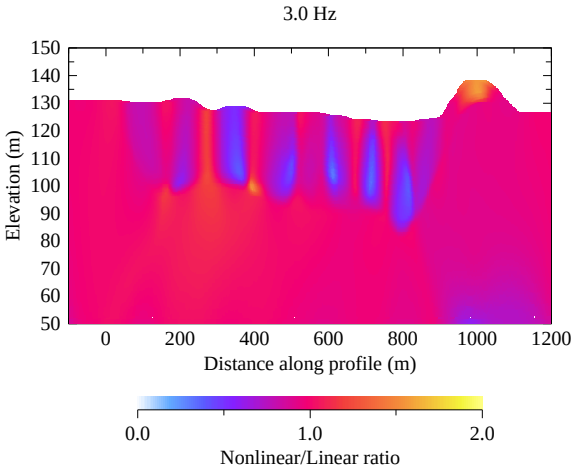

(c) Nonlinear/linear ratio (0.1g outcropping PGA)

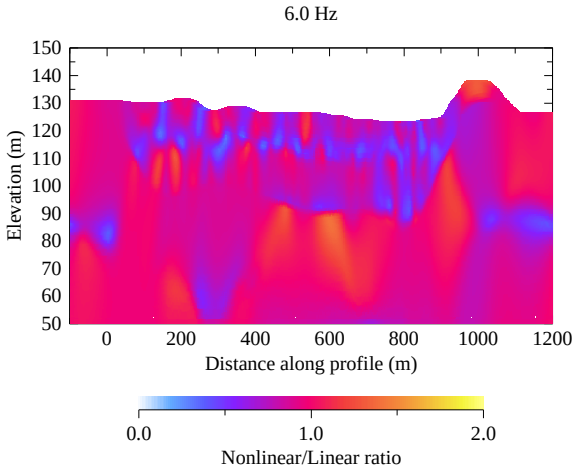

(d) Nonlinear/linear ratio (0.1g outcropping PGA)

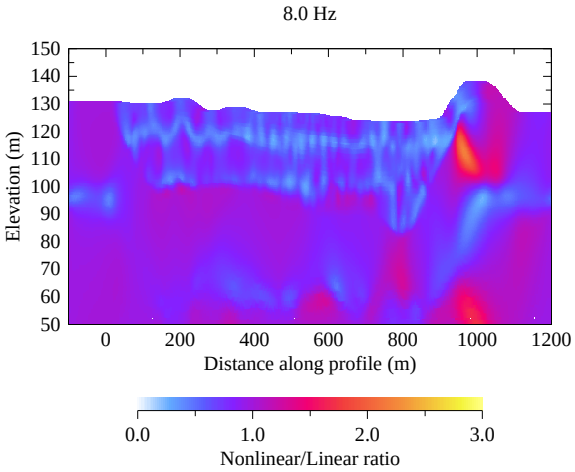

(e) Nonlinear/linear ratio (0.1g outcropping PGA)

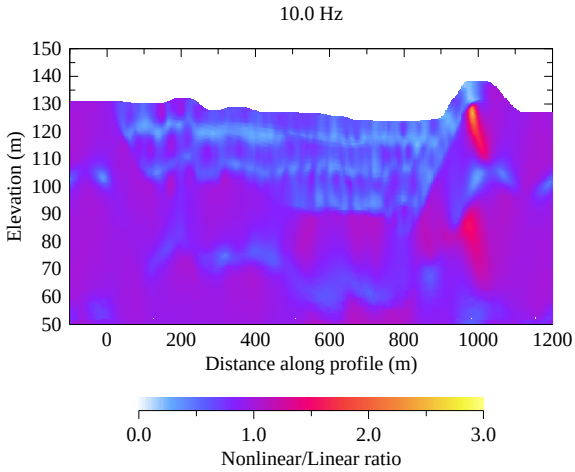

(f) Nonlinear/linear ratio (0.1g outcropping PGA)

Figure 6.9: Ratio of acceleration Fourier spectrum between nonlinear and linear rheology at 0.1g outcropping PGA

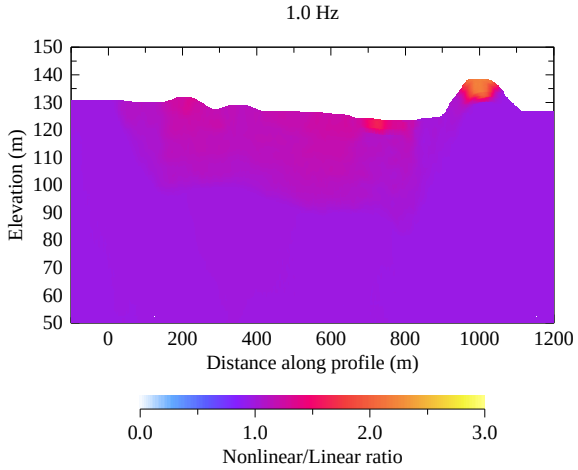

(a) Nonlinear/linear ratio (0.2g outcropping PGA)

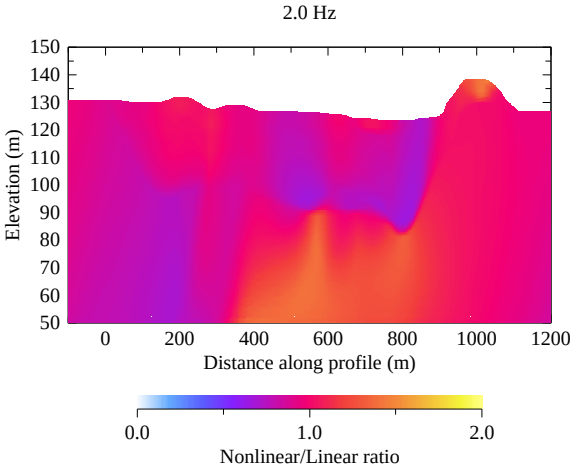

(b) Nonlinear/linear ratio (0.2g outcropping PGA)

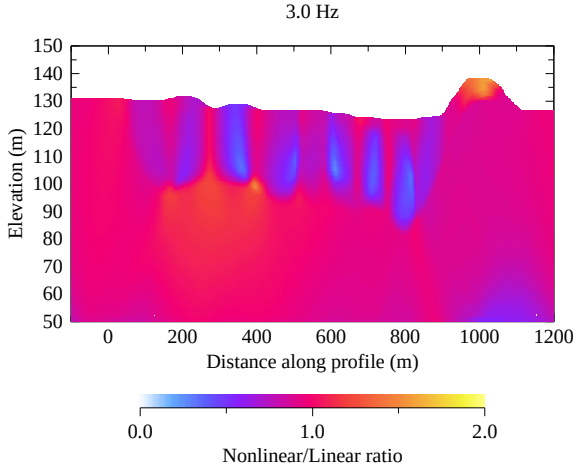

(c) Nonlinear/linear ratio (0.2g outcropping PGA)

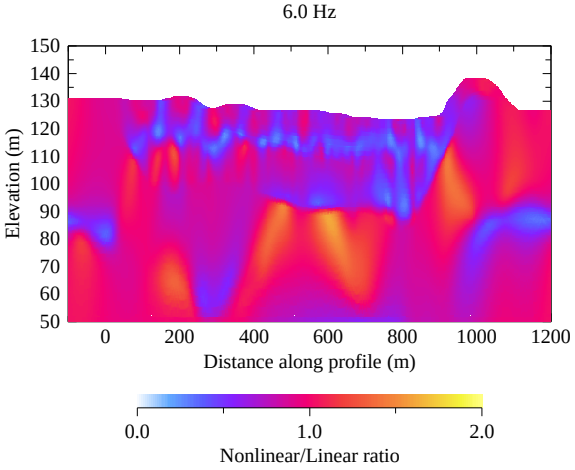

(d) Nonlinear/linear ratio (0.2g outcropping PGA)

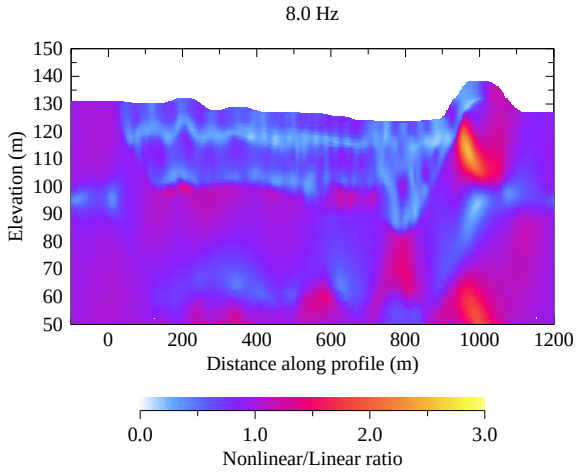

(e) Nonlinear/linear ratio (0.2g outcropping PGA)

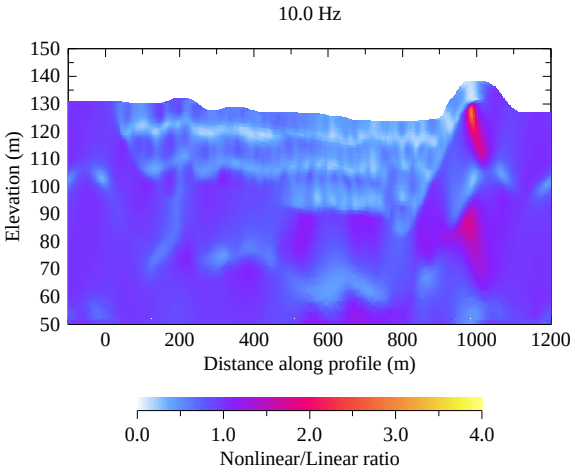

(f) Nonlinear/linear ratio (0.2g outcropping PGA)

Figure 6.10: Ratio of acceleration Fourier spectrum between nonlinear and linear rheology at $0.2g$ outcropping PGA

6.4 Linear and nonlinear dynamic soil-structure interaction

6.4.1 Definition of the problem

In order to investigate the effect of soil nonlinearity on dynamic soil-structure interaction, a 10-story building is considered as shown in Fig.6.11. The building is $16m$ wide and $30m$ high. The total mass of the structure is approximately $178t$. An elastic behavior is considered for structure materials. The fundamental frequency of the structure based on a rigid base is equal to the 2.91Hz. For the sake of simplicity, the foundation is rigid, massless, rectangular plate resting on the surface of the soil.

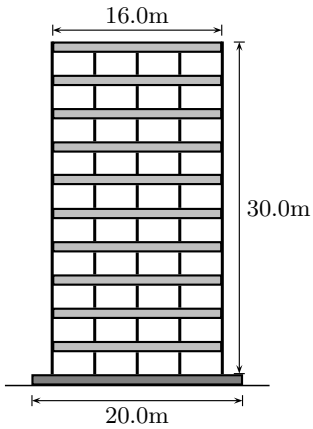

Figure 6.11: Geometric properties of 10-story studied building

Beam elements are used to model the columns and the beams of the selected reinforced concrete buildings. The solid elements are used for modeling the foundation.

The first frequency of the basin where the structure is placed, is around 2Hz. Therefore, the fundamental frequency of the structure (2.91Hz) is larger than the resonance frequency of the soil. Consequently, based on the previous chapter results, a significant soil-structure interaction should be expected.

The finite element model is presented in Fig.6.12. The time step is $2.10^{-4} sec$. The absorbing layers presented in Table 5.3 are used at the base of model to avoid the reflection of the waves to the basin.

A significant shift of the fundamental frequency of the soil-structure system was observed in the previous section during the parametric study on dynamic soil-structure interaction. One reason was probably the presence of the contact elements at the interface of the soil and the foundation. In order to investigate the effect of this issue, we did not use these elements in this chapter and the foundation is directly placed on the soil. Therefore, tension stresses may be produced during the structure oscillation.

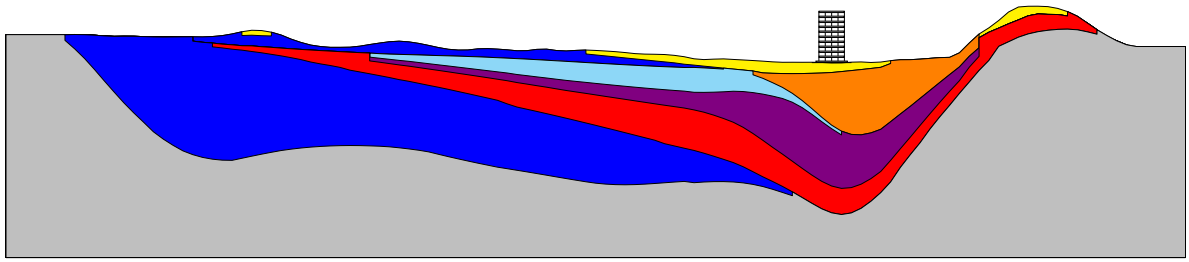

Figure 6.12: Finite element model of the Nice basin and the 10-story concrete building

The same Gabor wavelet presented in §6.2.2 is used. Two different levels of input motion

are considered. The first one introduces an outcropping PGA equal to 0.1g and the second one equal to 0.2g.

6.4.2 Soil response

Figure 6.13 illustrates the accelerations computed at the surface of the basin at different places. Linear soil behavior is assumed for the layers of the basin in this analysis. A 0.1g outcropping PGA is applied at the base of the Nice basin. This means that the actual input is half of the outcrop (removal of the free surface effect). We observed that the response of the basin is completely different depending on the location. In addition to the different soil properties of the basin layers, the topographic condition also influences the basin response.

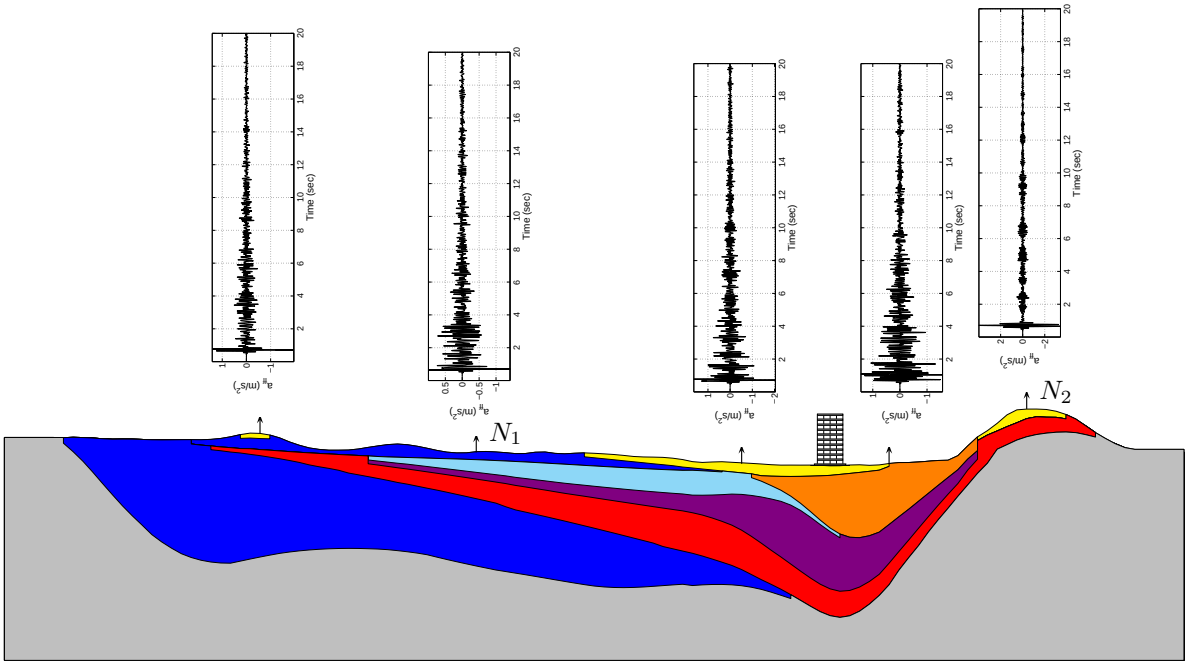

Figure 6.13: Various computed accelerations at the surface of Nice basin with linear soil behavior at 0.1g outcropping PGA

Two analyses with 0.1g and 0.2g outcropping PGA's are performed in order to investigate the effect of soil nonlinearity on the basin response. A complete time-frequency analysis is performed in §6.3. Consequently, we compare the results between linear and nonlinear analyses only in some points. For instance, the response of the basin at points N1 and N2 (shown in Fig.6.13) are presented in Fig.6.14. We observe that the amplitude of the waves due to the complex geometry and topographic effects decreases because of soil nonlinearity especially after the first two seconds of the propagation.

Figure 6.15 gives a closer view for the first two seconds of the propagation of the aforementioned accelerations. The soil nonlinearity effect is different for these two responses. Peak acceleration at point N1 at $0.2g$ outcropping PGA is larger than $0.1g$ for both linear and nonlinear soil behaviors. But at point N2, the peak acceleration at $0.1g$ for linear soil behavior is larger than both responses for nonlinear soil behavior. Waves propagate through different soil layers before reaching the point N1, consequently, due to the stiffness contrast between these layers, the waves are amplified. This feature competes with soil nonlinearity and neutralizes a large part of nonlinearity effect. At point N2 the wave propagation is different. There is only two soil layers for waves to reach this point, therefore lower amplification takes place than at point N1. In addition, these soil layers are close to the free surface and consist of the soft soils comparing to other layers, consequently, strong energy dissipation occurs and the effect of soil nonlinearity

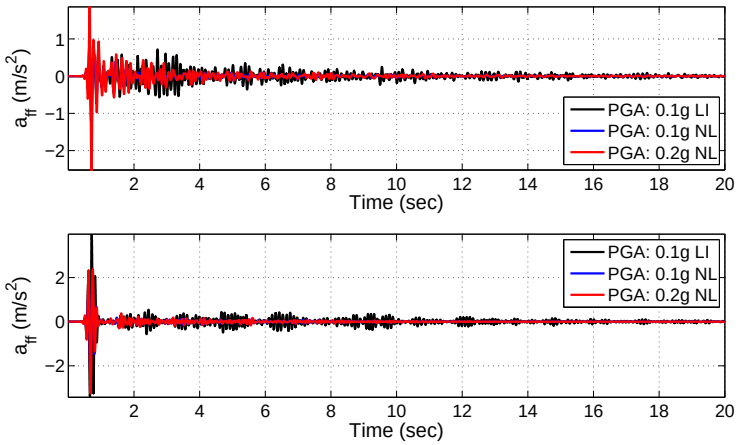

Figure 6.14: Comparison between the basin responses (acceleration) due to different soil behaviors and input motions at points N_1 (top) and N_2 (bottom)

is more than the amplification. Therefore, the peak acceleration for soil linear behavior at $0.1g$ outcropping PGA is larger than nonlinear cases, even with a 0.2g outcropping PGA.

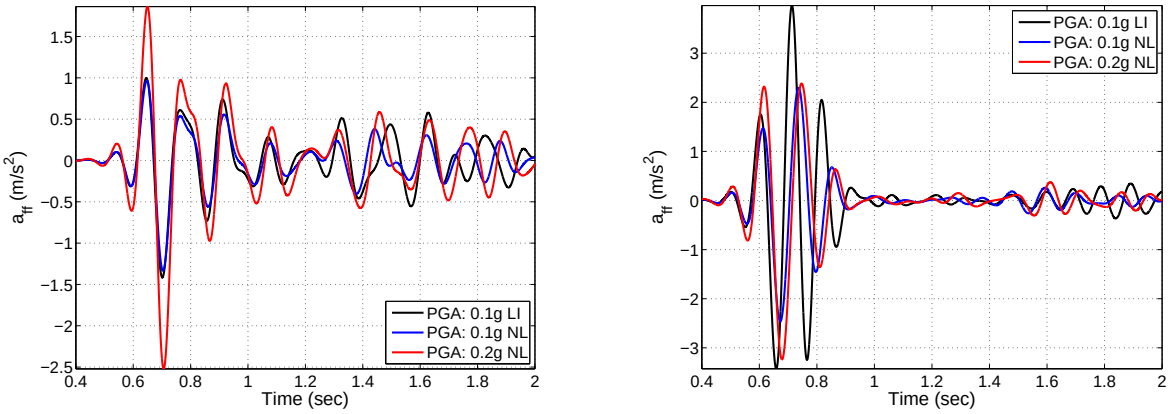

(a) Acceleration at point N_1

(b) Acceleration at point N_2

Figure 6.15: Comparison between the basin responses (first $2sec$ of acceleration) due to different soil behaviors and input motions at points N_1 and N_2

The aforementioned remarks can be completed regarding the displacements obtained at points N_1 and N_2. Figure 6.16 illustrates the comparison of the displacements between different soil behaviors at these two points. We observe that a significant residual displacement is obtained for $0.2g$ outcropping PGA at point N_2, that justifies the lower peak acceleration despite its greater input motion than for linear soil behavior.

6.4.3 Structural response

The effect of soil nonlinearity on DSSI is studied considering the structure presented in §6.4.1. Acceleration obtained at the top of the structure is compared between linear and nonlinear soil behaviors at $0.1g$ and $0.2g$ outcropping PGA's (Fig.6.17). Acceleration at the top of the structure fades out in the linear case due to the radiation damping. For nonlinear cases, the combination of the soil nonlinearity and radiation damping decreases the structural response.

Also, the first two seconds of the propagation is displayed in Fig.6.18. The effect of soil nonlinearity is distinguished on modification of the amplitude and apparent wave velocity that change completely the structural response from the beginning of the propagation.

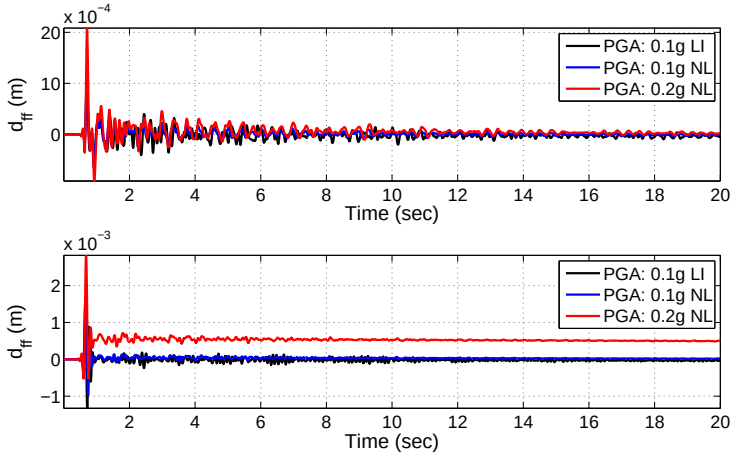

Figure 6.16: Comparison between the basin responses (displacement) due to different soil behaviors and input motions at the points N_1 (top) and N_2 (bottom)

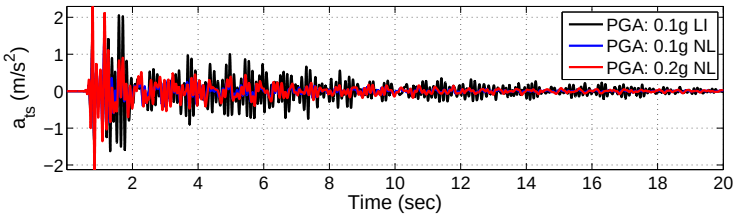

Figure 6.17: Acceleration at the top of the structure for different soil behaviors and input motions

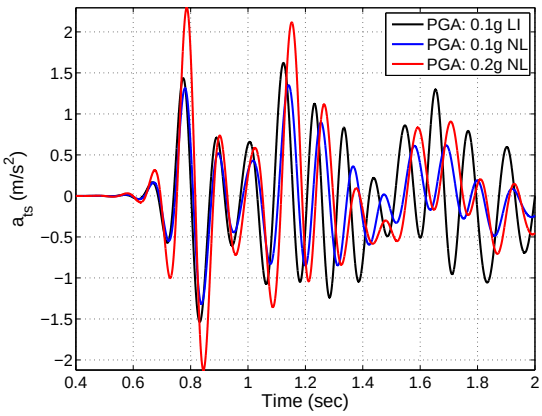

Figure 6.18: First two seconds of the acceleration at the top of the structure for different soil behaviors and input motions

Displacement at the top of the structure is presented in Fig.6.19. We observe that the residual displacement is not significant in the soil, however, the soil nonlinearity has its effects on displacement response of the structure, particularly on its amplitude. We should mention that due to the geometrical complexity and property variability of the basin the response of the structure depends also where it is constructed. The response spectrum at the surface of the basin could help to find approximately the structural response depending on its position. However, the response spectrum is significantly dependent on the frequency content of the input motion.

Since each surface point has a different response, the choice of free field to compute the fundamental frequency of the soil-structure system can change the results. Figure 6.20 illustrates

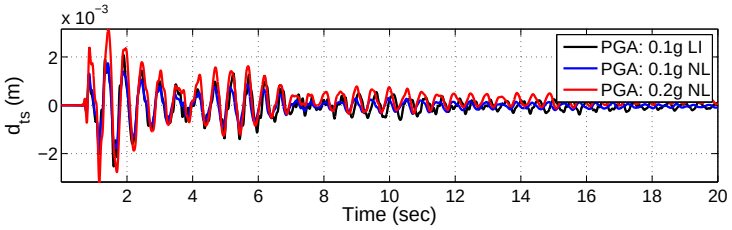

Figure 6.19: Displacement at the top of the structure for different soil behaviors and input motions

the transfer function between acceleration at the top of the structure and four different free surfaces. The four selected points are outcropping, point N_1, point N_2 (see Fig.6.13) and finally the base of the structure, below the left column of the structure. The fundamental frequency of the structure on a fixed base is equal to 2.91Hz. When it is based on the soft soil, its fundamental frequency shifts to the low frequencies. We observe that depending on the reference point, it changes from 2.07Hz to 1.86Hz for linear soil behavior and from 2.07Hz to 1.81Hz for nonlinear soil behavior.

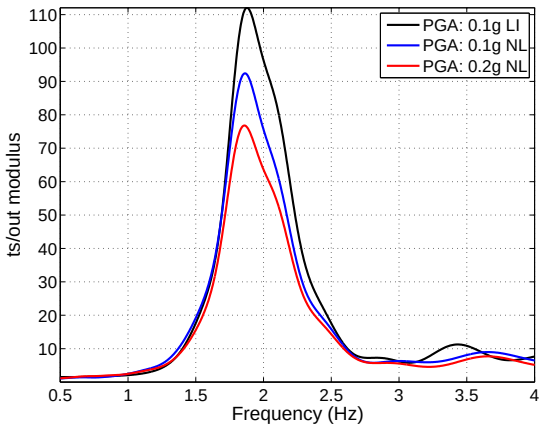

(a) TF of top of structure/outcropping

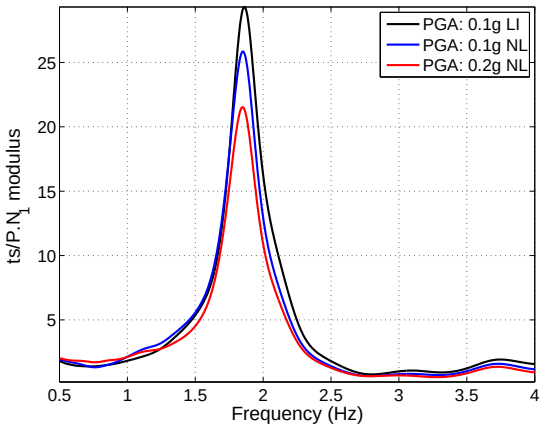

(b) TF of top of structure/point N_1

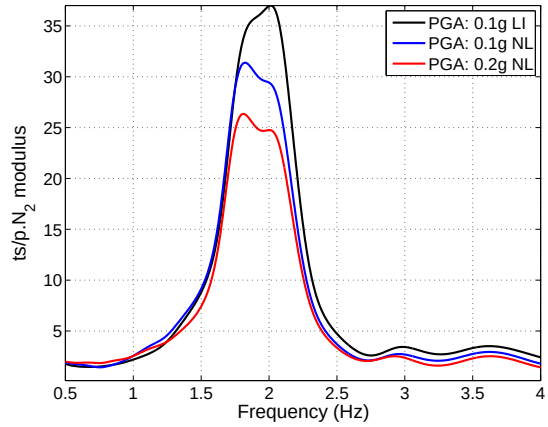

(c) TF of top of structure/point N_2

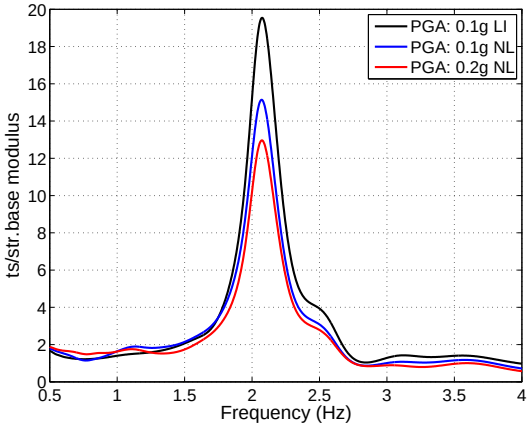

(d) TF of top of structure/structure base

Figure 6.20: Transfer function of acceleration between top of the structure and four different reference points situated at outcropping, point N_1, point N_2 and the below the left column of the structure

In the previous chapter, we mentioned that one of the reason of a significant difference between fundamental frequency of a fixed base structure and the soil-structure system could be

the presence of the interface elements below the foundation. In this chapter the structure is positioned directly on the soil. However, we observe that in this case the shift is also significant and varies from 29% to 38%. It seems that the effect of the contact elements on fundamental frequency of the soil-structure system is negligible. We observe in Fig.6.20c that there are two peaks in the computed transfer function. This may be due to the topographic effects.

There is no difference between the fundamental frequency of the soil-structure system considering linear and nonlinear soil behavior. This is in accordance with the results of the previous chapter. Nevertheless, due to the energy dissipation into the soil, the amplitude of the transfer function for the nonlinear soil behavior is lower than for the linear one. Again the fundamental frequency is not a good index (see previous chapter). However, the deamplification is clearly seen.

In the next section, the dissipated energy within the Nice basin is studied.

6.4.4 Dissipated energy into the soil

The cumulative dissipated energy up to end of propagation is computed in Nice basin. Equation 5.4 is used to calculate the energy dissipation. However, the dissipated energy presented in this section is due only to the shear components. In addition, the effect of the structure weight on stress confinement and consequently, on low-strain shear moduli is neglected. Also, due to the geometric complexity of the basin, the effect of confinement stress on low-strain shear moduli is not taken into account. Consequently, the elastic shear wave velocity and low-strain shear moduli are constant in each basin layer.

The cumulative dissipated energy into the basin for $0.1g$ and $0.2g$ outcropping PGA are shown in Fig.6.21 and Fig.6.22, respectively. The legends of these iso-values are shown in Fig.6.23. The impedance contrast between the layers amplifies the response. More energy dissipates in the soft layers. The basin geometry is complex and the layers are inclined, therefore, the normal stresses are produced in the basin. There is also the topographic effects and the oscillation of the structure that produce surface waves and radiation damping. Combination of all these aforementioned points adds complexity to the energy dissipation into the soil.

Since the horizontal direction of the basin is greater than its vertical one, different scales are used to display the results which deteriorates the images quality. We observe in Fig.6.21 and 6.22 that more energy is dissipated close to the surface in the softer layers such as layer 1 and 3 (See Fig.6.2 for the layers number).

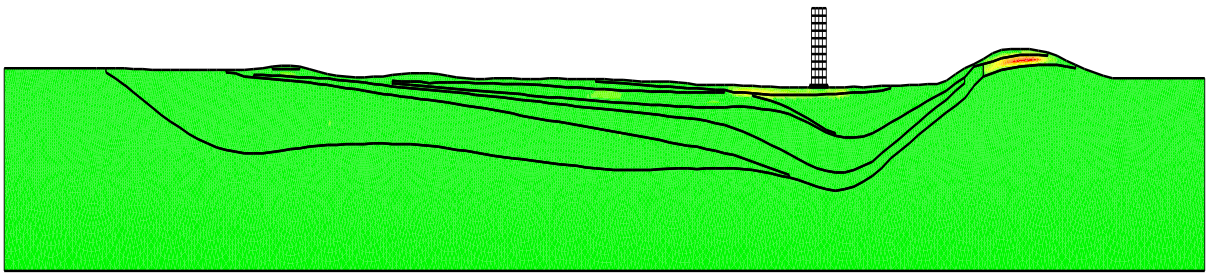

Figure 6.21: Cumulative dissipated energy into the basin due to the shear stress components for $0.1g$ outcropping PGA (different horizontal and vertical scales)

The same trend is obtained for dissipated energy at $0.1g$ and $0.2g$ outcropping PGA's in the basin. However, looking at the maximum dissipated energy in each case (Fig.6.23), the results are totally different. The maximum cumulative dissipated energy at $0.2g$ outcropping PGA is four times the $0.1g$. A closer view of Fig.6.22 around the structure is shown in Fig.6.24. The structure is positioned on one of the softest layer of the basin, where the dissipated energy is significant.

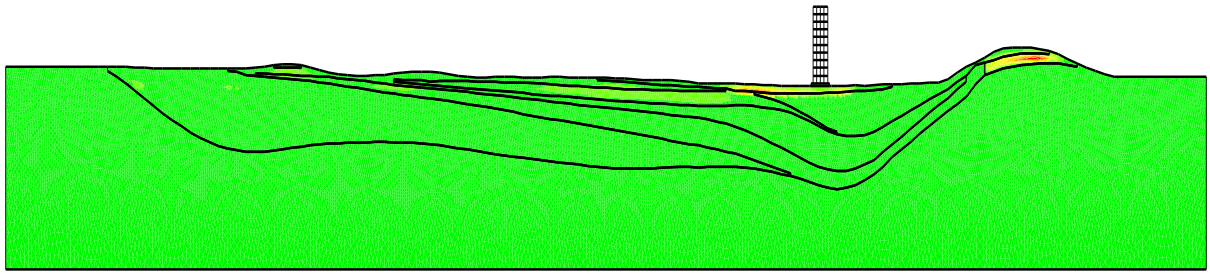

Figure 6.22: Cumulative dissipated energy into the basin due to the shear stress components for $0.2g$ outcropping PGA (different horizontal and vertical scales)

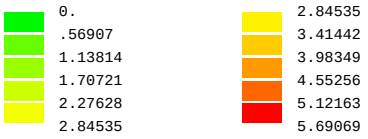

(a) Figure 6.21 legend (J/m^3)

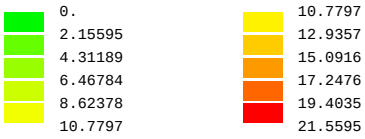

(b) Figure 6.22 legend (J/m^3)

Figure 6.23: Legend of the iso-values of the dissipated energy (J/m^3) in Nice basin, shown in Fig.6.21 and 6.22

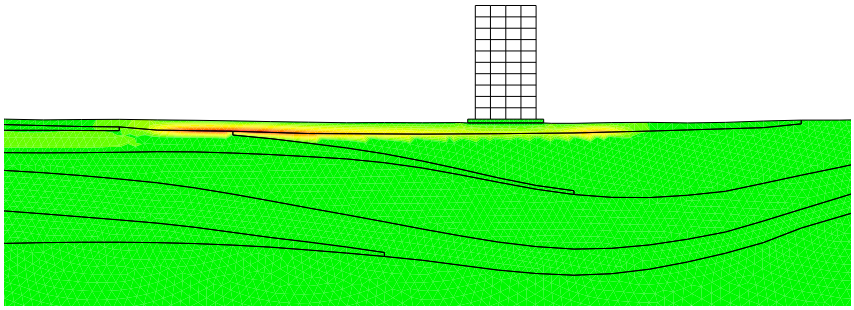

Figure 6.24: Cumulative dissipated energy into the basin due to the shear stress components for $0.2g$ outcropping PGA (different horizontal and vertical scales), close view around the superstructure

6.4.5 Maximum shear strain in the soil

The maximum shear strain reached during the propagation is computed in the soil for two different input motions. Figures 6.25 and 6.26 illustrates the results for $0.1g$ and $0.2g$ outcropping PGA's. The legend of these two figures is shown in Fig.6.27.

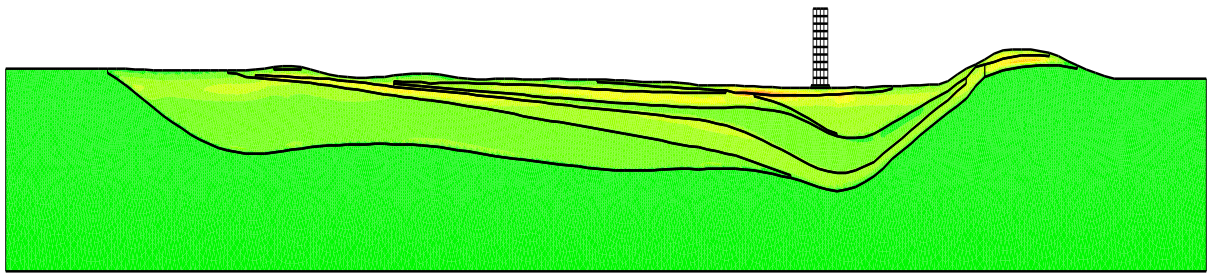

Figure 6.25: Maximum shear strain for $0.1g$ outcropping PGA in Nice basin

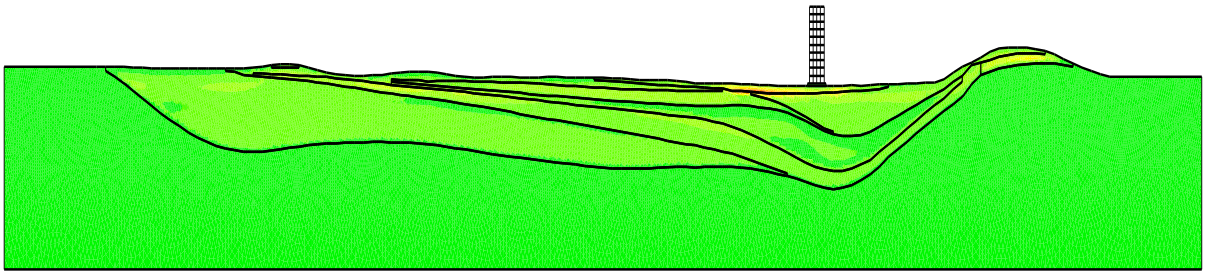

Figure 6.26: Maximum shear strain for $0.2g$ outcropping PGA in Nice basin

The maximum shear strain for two cases is reached at the base of the soil layer 1 (See Fig.6.2 for the layers number) not too far from the building. The maximum shear strain that occurs in this layer is equal to 0.02258% at $0.1g$ outcropping PGA and equal to 0.06713% at $0.2g$ outcropping PGA. Since the hyperbolic model is used for shear modulus reduction curve of the basin layers, easily we can find the reduction of shear modulus related to the shear strain. For example, at $0.1g$ outcropping PGA, for the maximum shear strain value of G/G_0 reduces to 0.73, and it decreases to 0.47 at $0.2g$ outcropping PGA. We observe that even for a moderate excitation, the reduction of shear moduli is very strong in some layers of the basin.

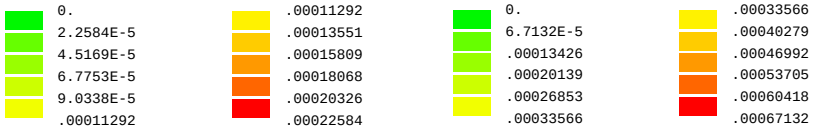

Figure 6.27: Legend of the iso-values of the maximum shear strain in Nice basin, shown in Fig.6.25 and 6.26

A closer view of the iso-values of the maximum shear strain are displayed in Fig.6.28 around the superstructure and the hill at $0.2g$ outcropping PGA.

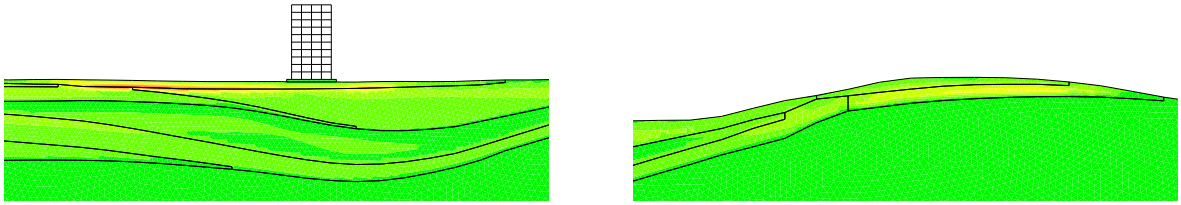

Figure 6.28: Closer view of the iso-values of the maximum shear strain around the superstructure and the hill at $0.2g$ outcropping PGA

6.5 Concluding remarks

The implemented soil constitutive model was used in this chapter to investigate site effects and dynamic soil-structure interaction for a real site with complex geometry. The basin of Nice was considered to reach this goal. This basin was analyzed considering linear and nonlinear soil behavior for basin layers for different input motions to investigate the effect of soil nonlinearity on site effect. In addition, a structure was positioned on the basin in order to study the dynamic soil-structure interaction and soil nonlinearity.

Complex wavefield due to the geometry of the basin was observed. For both nonlinear cases, the wavefield was rapidly attenuated after 1.5 - 2.0sec. We also observed the concentration of the kinetic energy in the basin, particularly for linear soil behavior.

Through a 2D transfer function of the basin response, the resonance frequencies of the basin were obtained at different positions considering linear and nonlinear soil behaviors. The maximum amplification in the basin reaches up to 6. Comparing the results of linear and nonlinear soil behaviors, the amplification of the high frequencies decreases significantly, particularly at $0.2g$ outcropping PGA.

The basin response was strongly dependent on the combination of soil nonlinearity, topographic effects and impedance contrast between the soil layers.

There was no difference between the fundamental frequency of the soil-structure system considering linear and nonlinear soil behavior. Nevertheless, due to the energy dissipation into the soil, the amplitude of the transfer function for the nonlinear soil behavior was lower than for the linear one. In a similar way, the fundamental frequency change is very small, thus making this an inadequate index to characterize nonlinear behavior.

General conclusions and perspectives

In the preceding chapters we have investigated various aspects of nonlinear dynamic soil-structure interaction. Even if this problem has been the subject of numerous investigations, no simple realistic solution exists for the introduction of nonlinear soil behavior. Indeed, numerous rheologies, complex soil geometry (such as basins), topographic effects and complex behavior of the foundation and the superstructure make the problem difficult to solve.

During this thesis we tried to study the problem from a numerical point of view. A simple soil rheology for soil was implemented in CESAR-LCPC code. The model only needs the shear modulus reduction curve to characterize the soil nonlinearity. This feature is very important since complex constitutive models generally involve numerous mechanical properties difficult to characterize experimentally.

A realistic description of the soil and structure is used during this work. In addition, the basin of Nice, which has a complex soil geometry and several buildings composed of beams and columns are studied here. To avoid parasite waves produced due to the artificial truncation of the boundary, a realistic absorbing boundary is presented and used. The stability conditions of the wave propagation problems is studied and it was shown that the linear and nonlinear behavior are very different when dealing with numerical dispersion. It is shown that the 10 points per wavelength rule, recommended in the literature for the elastic media is not sufficient for the nonlinear case. When the material is nonlinear, during the propagation of the shear waves, the shear modulus of the material reduces and therefore the shear velocity decreases. Consequently, the wavelength changes and the initial number of points per wavelength decreases. It was shown that comparing the energy dissipation in the media, it seems that the coarse meshes are more dissipative than fine meshes. The nonlinear constitutive model used in this work requires only the shear modulus reduction curve as nonlinear property. The manner in which this curve (number of springs) is discretized can influence the results. We showed that when the number of the springs decreases the nonlinearity in the media also decreases.

Depending on the soil properties, frequency content of the soil response could change significantly due to the soil nonlinearity. The peaks of the transfer function between free field and outcropping responses shift to lower frequencies and amplification happens at this frequency range. Amplification reduction for the high frequencies and even deamplication may happen for high level input motions. These changes influence the structural response. We observed that when the fundamental frequency of the structure on a fixed base is smaller than the natural frequency of the soil, the effect of soil-structure is not significant. However, the effect of structure weight and rocking of the superstructure could change the results. For structures with a fixed base, having a fundamental frequency more than the first natural frequency of soil, the soil-structure interaction is significant.

For the selected structures and soil profiles of this work, the performed numerical simulations showed that the shift of the fundamental frequency is not a good index to discriminate linear from nonlinear soil behavior. Because such shift is not dramatic as it is observed by equivalent-linear models (e.g. Pitilakis (2006), ...). However, the structural response amplitude may be

more discriminant.

The basin of Nice was used as an example of wave propagation on a heterogeneous nonlinear media and dynamic soil-structure interaction. Complex wavefield due to the geometry of the basin was observed. For nonlinear cases, the wavefield was rapidly attenuated after 1.5 - 2.0sec. We also observed the concentration of the kinetic energy in the basin. The basin response was strongly dependent on the combination of soil nonlinearity, topographic effects and impedance contrast between soil layers. There was no difference between the fundamental frequency of the soil-structure system considering linear and nonlinear soil behavior. Nevertheless, due to the energy dissipation into the soil, the amplitude of the transfer function for the nonlinear soil behavior was lower than for the linear one. Again, we observed that the fundamental frequency was not a good index to discriminate linear from nonlinear soil behavior.

We observe that one important effect of soil nonlinearity is the residual displacement than are produced during the wave propagation which can not be seen using the common springs instead of the real soil. In addition, it is not possible to model the soil nonlinearity using springs in presence of complex geometry such as basins and topography.

In this work we were limited to the borehole condition for applying the input motion. Consequently, an important subject of future work could be the implementation of the incident wavefield into CESAR-LCPC code. This development would help to use earthquake data. The necessary elements were added to CESAR-LCPC code to take into account the initial conditions of the soil-structure problem (lithostatic effects). Therefore, the effect of initial conditions of the problem could be another important subject to investigate.

Another issue is the effect of soil nonlinearity on the vertical component. Indeed, this is an important topic since this component has surface waves generated at the basin edges. Their interaction with the soil properties is something that still needs to be addressed. Variability of the ground motion and its effect on dynamic soil-structure interaction is also very important and should be taken into account.

The presence of pore pressure in the soil can significantly change the soil response. A dry soil hypothesis was used during this thesis, therefore, the effect of pore pressure should be added to the rheological model in order to have a realistic constitutive model. Also, the soil model used in this work is basically 3D model. Consequently, a 3D dynamic soil-structure could be the topic of future works that needs the implementation of necessary elements into the CESAR-LCPC code.

Appendix A

Contact elements

A.1 Introduction

In the field of geotechnical and civil engineering, modeling of contact phenomena is a very important issue. Indeed, many structures have surfaces of discontinuity that may play an important role in their mechanical behavior. For example, the interfaces between soil and structure, soil and pile, etc. can be cited. Specially, in the soil-structure interaction, a realistic interface is needed between soil and structure. The contact elements, previously implemented in TACT module (A computation module for the contact problem between solids) of CESAR-LCPC code, are implemented and adopted in MCCI module in spite of taking into account the discontinuity between the soil and structure.

A.2 Definition of the contact area and the contact elements

To model the contact between two solids S_1 and S_2, three distinct surfaces are defined (Fig.A.1) as follows (CESAR-LCPC, 2001):

S_c: Potential contact surface; The surface where the contact may be happened.

S: Effective contact surface; This is the current contact surface between two solids.

S_0: Initial contact surface;

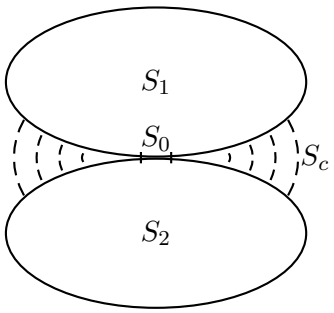

Figure A.1: Different contact 2D areas

The potential contact area is presented by an artificial material. Modeling of this artificial material is performed by means of the contact finite elements. These elements ensure, in the effective area of contact, the continuity of the normal and tangential displacements of the solids in contact. These elements will be called "active" if they belong to the effective area of contact, otherwise "inactive". The stiffness of an inactive element is identically zero.

Each modification in the effective area of contact is a change in the global stiffness matrix of the studied system. The principle of resolution is to make a gradual change so as to follow

the effective area of the contact. The determination of the successive levels of the loading is performed using the criterion of non-interpenetration of solids and the criteria of tensile strength. For each successive load levels, both equilibrium equations and all the criteria of the contact should be checked using an iterative process.

The potential surface of the contact is modeled here by means of the six nodes quadrilateral finite elements (Fig.A.2). These elements are quadratic in the tangent direction to the contact, and linear along the normal direction. They may well be connected to all quadratic elements existing in CESAR-LCPC.

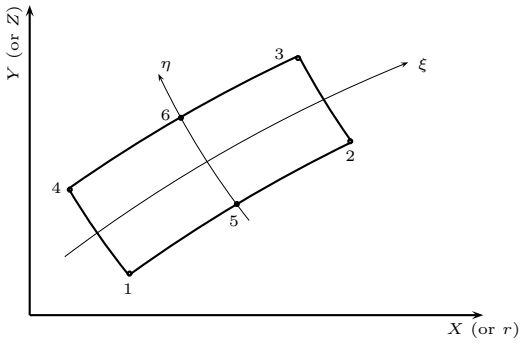

Figure A.2: Six nodes quadrilateral finite element

The relation between Cartesian coordinates of any points of the element and the nodes of the element are as follows,

$$\left\{ \begin{array}{c} x \\ y \end{array} \right\} = \sum_{K=1}^{N} H^K(\xi,\eta) \left\{ \begin{array}{c} x^K \\ y^K \end{array} \right\} \tag{A.1}$$

H^K is the shape function of the node K, where it is linear following the normal direction on contact, η, and quadratic following the tangential direction, ξ. N is the number of nodes. (x, y) are the global Cartesian coordinates of a point in the element. (ξ, η) are the local coordinates of the selected point, and finally, (x^K, y^K) are the Cartesian coordinates of the node K. In the same way, the displacement vector of any point is related to the displacement vector of the nodes. Therefore, the contact elements are isoparametric.

$$\left\{ \begin{array}{c} u \\ v \end{array} \right\} = \sum_{K=1}^{N} H^K(\xi,\eta) \left\{ \begin{array}{c} u^K \\ v^K \end{array} \right\} \tag{A.2}$$

When the solids are in contact, the thickness of the contact element is zero. This leads to a singular behavior of the element. To avoid this singularity, the zero thickness of the contact element is replaced with a very small value.

Fig.A.3 illustrates a plane contact element and its local numbering. The real geometry of the contact element is calculated from the position of nodes 1, 5 and 2, forming a curve selected as the reference curve. Using the coordinates of these three nodes and quadratic shape functions, we obtain the normal vector to this curve in each of these nodes. Then, we place at each of these three normal vectors, the nodes 2, 6 and 3 at a distance e for each corresponding node (Fig.A.4).

Therefore, the calculation is as follows; For example, $M(x, y)$, a point on the curve 1, 5 and 2 of the curvilinear coordinate ξ.

$$\left\{ \begin{array}{l} x(\xi) = g^1(\xi)x^1 + g^2(\xi)x^2 + g^5(\xi)x^5 \\ y(\xi) = g^1(\xi)y^1 + g^2(\xi)y^2 + g^5(\xi)y^5 \end{array} \right.$$

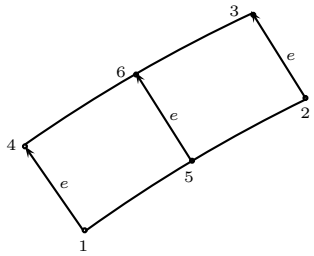

Figure A.3: Local node numbering of a plane contact element

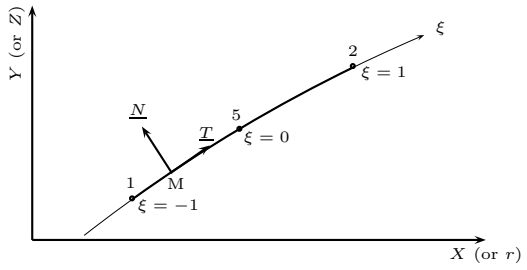

Figure A.4: Local coordinates of the reference curve

where,

$$\begin{aligned} g^1(\xi) &= \frac{\xi}{2}(1-\xi) \\ g^2(\xi) &= \frac{\xi}{2}(1+\xi) \\ g^5(\xi) &= (1-\xi)(1+\xi) \end{aligned} \tag{A.3}$$

If $(\underline{T}, \underline{N})$ is the local coordinate in M, the normal vector $\underline{N}$ can be expressed as,

$$\underline{N}(\xi) = \begin{cases} -y_{,\xi} = -\frac{1}{2}(-y^1 + y^2) - \xi(y^1 + y^2 - 2y^5) \\ \\ x_{,\xi} = \frac{1}{2}(-x^1 + x^2) - \xi(x^1 + x^2 - 2x^5) \end{cases} \tag{A.4}$$

Then, the coordinates of the nodes 3, 4 and 6 can be obtained as follow,

$$\left\{ \begin{array}{c} x^3 \\ y^3 \end{array} \right\} = \left\{ \begin{array}{c} x^2 \\ y^2 \end{array} \right\} + e.x.\frac{\underline{N}(\xi = +1)}{\parallel N(+1) \parallel} \tag{A.5}$$

$$\left\{ \begin{array}{c} x^4 \\ y^4 \end{array} \right\} = \left\{ \begin{array}{c} x^1 \\ y^1 \end{array} \right\} + e.x.\frac{\underline{N}(\xi = -1)}{\parallel N(-1) \parallel} \tag{A.6}$$

$$\left\{ \begin{array}{c} x^6 \\ y^6 \end{array} \right\} = \left\{ \begin{array}{c} x^5 \\ y^5 \end{array} \right\} + e.x.\frac{\underline{N}(\xi = 0)}{\parallel N(0) \parallel} \tag{A.7}$$

The value e is considered the product of a characteristic size of the mesh and a penalty coefficient, 10^{-n} :

$$e = L.10^{-n} \tag{A.8}$$

And for the plane problems :

$$L = \frac{1}{2}\left[(x_{max} - x_{min}) + (y_{max} - y_{min})\right]$$

where, x_{max}, x_{min}, ... present the extreme values of the coordinates of the contact nodes. The penalty coefficient has a sensitive influence on the stiffness matrix. The value 10^{-4} for the plane problems, seems to give a good behavior of the contact elements.

A.3 Stress-strain relation of the contact elements

For each contact element, a constitutive law that takes into account different contact types is associated. The general form of the stress-strain relation for contact elements is as follow,

$$\{\sigma\} = [E]\{\epsilon\} \tag{A.9}$$

where, for the plane problems,

$$\{\sigma\} = \left\{ \begin{array}{c} \sigma_{11} \\ \sigma_{22} \\ \sigma_{12} \end{array} \right\} \qquad \{\epsilon\} = \left\{ \begin{array}{c} \epsilon_{11} \\ \epsilon_{22} \\ \epsilon_{12} \end{array} \right\}$$

Different constitutive laws can be considered such as : perfect sliding, adhesion, Coulomb friction, etc. For each one of these laws, a behavior matrix, $[E]$, that ensure the continuity of the displacements is related. These matrices could only be expressed in the local coordinate of the contact element. For 2D problem, the local coordinates $(\underline{V}_1, \underline{V}_2)$, are as follows,

$$\underline{V}_1 \left\{ \begin{array}{c} x_{,\xi} \\ y_{,\xi} \end{array} \right\} \qquad\qquad \underline{V}_2 \left\{ \begin{array}{c} -y_{,\xi} \\ x_{,\xi} \end{array} \right\} \tag{A.10}$$

The local constitutive law of the contact element is shown as $[E^\ell]$. For each constitutive law, the matrix $[E^\ell]$ is obtained as follow,

- *Perfect sliding:*

  The contact finite elements should ensure the continuity of the normal displacements. Therefore, in the local coordinates and for the plane problems we have,

  $$[E^\ell] = \left[\begin{array}{ccc} 0 & 0 & 0 \\ 0 & E & 0 \\ 0 & 0 & 0 \end{array} \right]$$

  where the second direction is normal to the contact and E represents the Young modulus of the contact material.

- *Adhesion:*

  The contact finite elements should ensure the continuity of the normal and tangential displacements of the solids in contact. Therefore, in local coordinates we have,

  $$[E^\ell] = \left[\begin{array}{ccc} 0 & 0 & 0 \\ 0 & E & 0 \\ 0 & 0 & G \end{array} \right]$$

- *Coulomb friction:*

  Its constitutive matrix is the same as adhesion. This means, it should ensure the continuity of the normal and tangential displacements. The difference is at the relation of the normal stress - shear stress expressed by Coulomb friction laws. These relations will be presented at §A.6.2.3 as friction criterion.

The transfer of the local coordinates to the global ones can be obtained by means of the transform matrix $[R]$, as follows,

$$\{\sigma\} = [R]\{\sigma^\ell\} \quad \text{and} \quad \{\epsilon^\ell\} = [R]^T\{\epsilon\} \tag{A.11}$$

The stress-strain relation in the local coordinates is,

$$\{\sigma^\ell\} = [E^\ell]\{\epsilon^\ell\}$$

By means of equation A.11 we have,

$$\{\sigma\} = [R]\{\sigma^\ell\} = [R][E^\ell]\{\epsilon^\ell\} = [R][E^\ell][R]^T\{\epsilon\} \tag{A.12}$$

Matrix $[R]$ can be expressed be means of the components of the local coordinates vector represented in the global coordinates. For the plane problem,

$$\underline{V}_1 \left\{ \begin{array}{c} c_1 \\ c_2 \end{array} \right\} \qquad\qquad \underline{V}_2 \left\{ \begin{array}{c} d_1 \\ d_2 \end{array} \right\}$$

With these notation, the matrix $[R]$ is obtained as,

$$[R] = \left[\begin{array}{ccc} c_1^2 & d_1^2 & 2c_1d_1 \\ c_2^2 & d_2^2 & 2c_2d_2 \\ c_1c_2 & d_1d_2 & c_1d_2 + c_2d_1 \end{array} \right] \tag{A.13}$$

A.4 Stiffness matrix of the contact elements

The principal of the virtual work, kinematically admissible for all the displacement fields can be expressed as,

$$\delta W_{int} + \delta W_{ext} = 0 \tag{A.14}$$

where δW_{int} is the virtual work of the internal forces and δW_{ext}, the virtual work of the external forces. The virtual work of the internal forces for an element is :

$$\delta W_{int} = \int_{\Omega e} \sigma_{ij}\delta\epsilon_{ij} d\Omega$$

where $d\Omega$ represents the volume of the considered element. This expression is decomposed as a product of the matrices for only nodal displacement as unknowns. The virtual work of the internal forces can be represented in matrix form as,

$$\delta W_{int} = \int_{\Omega e} \langle\sigma\rangle\{\delta\epsilon\} d\Omega$$

The strain is a function of the nodal displacements. For the plane problem,

$$\{\epsilon\} = \left\{ \begin{array}{c} \epsilon_{xx} \\ \epsilon_{yy} \\ 2\epsilon_{xy} \end{array} \right\} = \left[\begin{array}{cccc} 1 & 0 & 0 & 0 \\ 0 & 0 & 0 & 1 \\ 0 & 1 & 1 & 0 \end{array} \right] \left\{ \begin{array}{c} U_{,x} \\ U_{,y} \\ V_{,x} \\ V_{,y} \end{array} \right\}$$

Supposing $\{\epsilon\} = [A]\{U_{,x}\}$. We have also,

$$\left\{ \begin{array}{c} \frac{\partial}{\partial x} \\ \\ \frac{\partial}{\partial y} \end{array} \right\} = [J^{-1}] \left\{ \begin{array}{c} \frac{\partial}{\partial \xi} \\ \\ \frac{\partial}{\partial \eta} \end{array} \right\}$$

where $[J]$ represents the Jacobian matrix and can be expressed as,

$$[J] = \begin{bmatrix} x_{,\xi} & y_{,\xi} \\ x_{,\eta} & y_{,\eta} \end{bmatrix}$$

Consequently, the strain can be rewritten as follows,

$$\{\epsilon\} = [A]\{U_{,x}\} = [A] \overbrace{\begin{bmatrix} J^{-1} & 0 \\ 0 & J^{-1} \end{bmatrix}}^{[T]} \begin{Bmatrix} U_{,\xi} \\ U_{,\eta} \\ V_{,\xi} \\ V_{,\eta} \end{Bmatrix}$$

And,

$$\{U_{,\xi}\} = \begin{Bmatrix} U_{,\xi} \\ U_{,\eta} \\ V_{,\xi} \\ V_{,\eta} \end{Bmatrix} = \begin{bmatrix} H^1_{,\xi} & 0 & H^2_{,\xi} & 0 & ... \\ H^1_{,\eta} & 0 & H^2_{,\eta} & 0 & ... \\ 0 & H^1_{,\xi} & 0 & H^2_{,\xi} & ... \\ 0 & H^1_{,\eta} & 0 & H^2_{,\eta} & ... \end{bmatrix} \begin{Bmatrix} U^1 \\ V^1 \\ U^2 \\ V^2 \\ . \\ . \\ U^6 \\ V^6 \end{Bmatrix}$$

This means $\{U_{,\xi}\} = [L]\{U^e\}$. As it was said before, the strain tensor components can be expressed by means of the nodal displacements,

$$\{\epsilon\} = \underbrace{[A][T][L]}_{[B]}\{U^e\} \tag{A.15}$$

Therefore, the stress-strain relation can be calculated.

$$\{\sigma\} = [E]\{\epsilon\} = [R][E^\ell][R]^T\{\epsilon\}$$

$$\langle\sigma\rangle = \langle\epsilon\rangle[E] = \langle U^e\rangle[B]^T[E] \tag{A.16}$$

And finally,

$$\begin{aligned} \delta W_{int} = -\int_{\Omega e} \langle\sigma\rangle\{\delta\epsilon\}\delta\Omega &= -\int_{\Omega e} \langle U^e\rangle[B]^T[E][B]\{\delta U^e\}\delta\Omega \\ &= -\langle U^e\rangle[K]^e\{\delta U^e\} \end{aligned}$$

where,

$$[K^e] = \int_{\Omega e} [B]^T[E][B]\delta\Omega \tag{A.17}$$

$[K^e]$ is the stiffness matrix of the element, $[B] = [A][T][L]$ and $[E] = [R][E^\ell][R]^T$. $[A]$ and $[E^\ell]$ are the constant matrices. $[L]$ is composed of the derivative of the shape functions on ξ and η. This matrix is linear through the normal direction to the contact. $[J]$, $[R]$ and $[T]$ can be considered constant matrix through the normal direction to the contact.

Finally, different methods such as Gauss and Newton-Cotes exist to calculate the numerical integration of the stiffness matrix of the elements.

A.4.1 Mechanical characteristics of the contact element

The constitutive matrix $[E]^{\ell}$, of the contact element consists of the parameters E and G representing Young and shear modulus. Since it consists of modeling an artificial material for the contact elements, these parameters do not have any physical interpretation. To numerically ensure the continuity of the displacement, the value of Young modulus of the contact is equal to the lower value of the Young modulus of the two solids in contact.

The Poisson coefficient has no influence on the behavior of the contact elements, consequently, its value is equal to zero.

A.5 Stress calculation in the contact elements

Since the problem is nonlinear, the stress tensor is calculated through an incremental way. For any point M, the incremental stress $\Delta\sigma$ is related to the incremental strain through the equation:

$$\{\Delta\sigma\} = [E]\{\Delta\epsilon\}$$

Or in local coordinates for point M,

$$\{\Delta\sigma^{\ell}\} = [E^{\ell}][R]^{T}\{\Delta\epsilon\}$$

By means of the notations previously defined, the stress increment can be expressed as incremental displacement.

$$\{\Delta\sigma^{\ell}\} = [E^{\ell}][R]^{T}[A][T][L]\{\Delta U\} \tag{A.18}$$

The stresses are calculated at the integration points of the stiffness matrix of the element.

A.6 Numerical resolution of the contact problem

A.6.1 Introduction

Two types of nonlinearity exist in our problem, geometrical nonlinearity and the behavior nonlinearity. The first is because of final contact surface that is not initially known. The second one comes from the possibility of the sliding with friction at the contact surface. The incremental method is used to solve these problems. The calculation of the loading increments is achieved using two different criteria, the non-interpretation criterion and the resistance to the traction criterion. For each loading increment, the nonlinear problem is solved either by Newton-Raphson or modified Newton-Raphson method. The surface S_c (Fig.A.1) is modeled by means of the contact finite elements. However, the contact elements belonging to S_c and not belonging to S, have a stiffness matrix equal to zero. These elements do not have any contribution at the global stiffness matrix and they are called inactive. All the elements belonging to the surface S are active.

An integration point of a contact element is inactive (or disconnected) if the contribution of this point at the stiffness matrix is zero. In another case, the integration point is active (or in contact). Also, an element can be partially in contact and partially disconnected.

A.6.2 Contact criteria

A.6.2.1 Non-interpenetration criterion

The non-interpenetration criterion is a geometric criterion to avoid the solids S_1 and S_1 to penetrate into each other (Fig.A.5). This physical limitation is numerically ensured in the effective contact surface by means of the stiffness matrix of the elements of this zone. For the

nodes of the solids S_1 or S_2 belonging to the inactive contact elements, a geometric test is necessary to validate the calculated displacements.

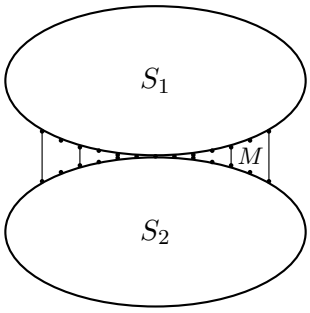

Figure A.5: State of the contact elements, M is a point of the contact element in disconnected state (or partially disconnected)

Considering (x, y) the coordinates of the point M, under the loading ΔP, the point M transfers to the point M^*,

$$\begin{cases} x^* & = x + \Delta u \\ y^* & = y + \Delta v \end{cases}$$

This modification changes the initial surface of the element dS around the point M , to a new surface dS^*,

$$\begin{cases} dS & = dx.dy \\ dS^* & = dx^*.dy^* \end{cases}$$

Consequently, we have,

$$dS^* = \begin{bmatrix} \frac{\partial x^*}{\partial x} & \frac{\partial x^*}{\partial y} \\ \\ \frac{\partial y^*}{\partial x} & \frac{\partial y^*}{\partial y} \end{bmatrix} dxdy$$

and,

$$dS^* = |F^*| \qquad \text{where} \qquad [F^*] = \begin{bmatrix} \frac{\partial x^*}{\partial x} & \frac{\partial x^*}{\partial y} \\ \\ \frac{\partial y^*}{\partial x} & \frac{\partial y^*}{\partial y} \end{bmatrix}$$

The contact between solids exists at the point M when $dS^* = 0$. In general, we can conclude that,

- $|F^*| < 0$: The solids are disconnected at M.
- $|F^*| = 0$: The solids are in contact at M.
- $|F^*| > 0$: The solids interpenetrate into each other at M.

A.6.2.2 Resistance to the traction criterion

- **Adhesion and unilateral contact**

The contact between an elastic solid and a rigid support is said unilateral when all the displacements through the external normal direction of the support are kinematically admissible. All the displacements in the opposite direction are forbidden. In this situation, the separation of the two solids in contact do not need any work. This hypothesis is not always acceptable. To express the adhesion between solids, a contact energy U_s is introduced in the computation of the potential energy.

$$U_s = -wA$$

where A, is the surface of the contact and w, represents the energy density of the adhesion of Dupré (CESAR-LCPC, 2001). This energy density is expressed as a function of the energy densities of the two surfaces in contact, γ_1, γ_2, and the energy density of the interfacial γ_{12} :

$$w = \gamma_1 + \gamma_2 - \gamma_{12}$$

This equation expresses that to separate two solids in contact at unity surface, the energies γ_1 and γ_2 should be provided while the energy γ_{12} is returned.

- **Resistance to traction criterion**

Considering M a point belonging to an active contact element, σ_n the normal stress at point M and R_T, the resistance to the traction of the contact element, the resistance to traction criterion is defined as follow,

$$\sigma_n < R_T$$

A.6.2.3 Friction criteria

The friction phenomena between the solids in contact is expressed by means of the Coulomb friction law. Considering M a point belonging to an active contact element, σ_n and τ, normal and tangential stresses at point M, c and ϕ the cohesion and friction angle, the natural characteristics of the contact element, the Coulomb friction law can be expressed as,

$$|\tau| < c - \sigma_n \tan\phi$$

A.6.3 Automatic loading increments

The goal of the automatic loading increments is to follow the evolution of the effective surface of the contact. This is obtained by means of the non-interpenetration and resistance to the traction criteria.

A.6.3.1 Non-interpenetration

If M a point of an inactive contact element, considering a loading increment $\{\Delta P\}$, we observe an interpenetration at point M. This means we have : $|F^*| < 0$. This solution is not physically admissible. Now, considering the loading increment is no more $\{\Delta P\}$ but $\alpha\{\Delta P\}$ with $0 < \alpha < 1$. Therefore, the initial point M, under loading $\alpha\{\Delta P\}$ transforms to another point M_α as,

$$\begin{cases} x_\alpha &= x + \alpha\Delta u \\ y_\alpha &= y + \alpha\Delta v \end{cases}$$

We have also $|F_{\alpha=0}| = 1 > 0$ and $|F_{\alpha=1}| = |F^*| < 0$. Therefore, there is at least one α_0 between 0 and 1 that $|F_{\alpha_0}| = 0$. This equation is second degree for α in case of 2D problems. For loading increment $\alpha_0\{\Delta P\}$, the displacement increment $\alpha_0\{\Delta U\}$ keeps the solids to be in contact at point M. The non-interpenetration criterion is checked also for all the inactive integration points of the contact elements. For any point that interpenetration is observed, the corresponding α_i is obtained. Finally, the minimum α_i, (or α_{min}), is taken into account to avoid all interpenetration of the solids. New integration points in contact are declared active. Their contributions on the stiffness matrix of the element is added to the global stiffness matrix.

A.6.3.2 Resistance to the traction

The disconnection takes place at one point of an active element when the normal stress reaches the resistance to the traction of the element. This criterion is expressed as $\sigma_n < R_T$. Considering $(\{U^0\}, \{\sigma^0\}, \{P^0\})$, an equilibrium state of the studied structure. If a new loading increment applied at this structure, a new state of the equilibrium is obtained as,

$$\begin{cases} \{U\} & = \{U^0\} & +\{\Delta U\} \\ \{\sigma\} & = \{\sigma^0\} & +\{\Delta\sigma\} \\ \{P\} & = \{P^0\} & +\{\Delta P\} \end{cases}$$

The resistance to the traction criterion should be checked for all the points of the effective contact region. For instance, the point M that does not satisfy this criterion; this means,

$$\sigma_n = \sigma_n^0 + \Delta\sigma_n \geq R_T$$

So, we calculate λ that satisfy : $\sigma_n^0 + \lambda\Delta\sigma_n = R_T$. Or,

$$\lambda = \frac{R_T - \sigma_n^0}{\Delta\sigma_n} \qquad \text{and} \qquad 0 < \lambda \leq 1$$

The loading increment $\lambda\{\Delta P\}$ can give exactly the beginning of the disconnection at point M. All the integration points of the elements of the active contact zone are checked in order to compute the λ_i, each time the criterion is not respected. Finally, $\lambda_{min} = min(\lambda_i)$ is obtained and ΔP is replaced by $\lambda_{min}\Delta P$. The new equilibrium state is calculated as,

$$\begin{cases} \{U\} & = \{U^0\} & +\lambda_{min}\{\Delta U\} \\ \{\sigma\} & = \{\sigma^0\} & +\lambda_{min}\{\Delta\sigma\} \\ \{P\} & = \{P^0\} & +\lambda_{min}\{\Delta P\} \end{cases}$$

The obtained loading increment is related to the first rupture in traction in the effective contact zone. Consequently, the corresponding integration points are declared inactive. The stress tensor at these points is canceled and their contributions at the global stiffness matrix is erased.

Appendix B

Soil nonlinearities and dynamic soil-structure interaction [1]

B.1 Introduction

The nonlinear stress-strain behavior of soils can be more accurately modeled by cyclic nonlinear laws that follow the actual stress-strain path during cyclic loading (Kramer, 1996). Such models are able to represent the shear strength of the soil. A variety of cyclic nonlinear models have been developed; all are characterized by a backbone curve and a series of rules that govern unloading-reloading behavior, stiffness degradation, and other effects. The stress-strain model used in this work was initially proposed by Iwan (1967) and used by Joyner and Chen to compute the nonlinear ground response to earthquakes (Joyner and Chen, 1975; Lenti, 2006). They presented a method based on the Iwan model that accounts for nonlinear, hysteretic soil behaviors and offers considerable flexibility for incorporating laboratory data on soil behavior (Joyner, 1975; Joyner et al., 1981).

This form of model has a rich history of application in the fields of material plasticity, structural dynamics and vibrations, control systems and magnetics. After Segalman and Starr (2008), Iwan models may be called Masing-Prandtl-Ishlinskii-Iwan (MPII) models. They showed that for any material or structural model expressible as a Masing model, there exists a unique parallel-series (displacement based) Iwan system that characterizes such model as a function of the displacement history. The MPII model is used and implemented in the framework of Finite Element method to investigate the effect of soil nonlinearity on dynamic soil-structure interaction.

B.2 Soil constitutive model

The soil model initially proposed by Iwan (1967) is used in this work. The model is composed of simple linear springs and Coulomb friction elements arranged as shown in Fig.3.7. The friction elements remain locked until the stress exceeds the yield stress Y_i. Generally, the yield stress of the first element Y_1 is set to be zero to simulate the elastic behavior of the soil. By appropriate specification of the spring constants G_i and the yield stresses Y_i we can model a very broad range of material behavior as dictated by laboratory experiments (Joyner, 1975). The number N of elements affects the calculation duration and the accuracy of the model.

[1] Extracted from :A. Gandomzadeh, M.P. Santisi d'Avila, J.F. Semblat, L. Lenti and F. Bonilla, Influence of soil nonlinearities on dynamic soil-structure interaction, *Fifth International Conference on Recent Advances in Geotechnical Earthquake engineering and Soil Dynamics, May 24-29, 2010, San Diego (USA)*
A. Gandomzadeh, M.P. Santisi d'Avila, J.F. Semblat, L. Lenti, and F. Bonilla. Soil nonlinearities and dynamic soil-structure interaction, *14th European Conference on Earthquake Engineering, Ohrid, Macedonia, Septembre 2010*

The Iwan model can be used to represent, to any target accuracy, the behavior of any material whose hysteresis loops satisfy the Masing criterion and do not depend on the number of cycles of loading (Joyner, 1975). It should be noted that the rheological model used here involves no viscous damping, and as a result the stress depends on the strain (and strain history) but not on the strain rate. Therefore, the energy dissipation per cycle does not depend upon the frequency.

B.3 Numerical model

The Finite Element code, CESAR-LCPC Humbert et al. (2005) is used to simulate the dynamic soil-structure interaction. The solution method of the DSSI problem is based on time and space discretization. The second order implicit Newmark scheme is used to integrate the equation of motion in time. The unconditional stability factors are considered in all the simulations. The Newton-Raphson algorithm is combined to Newmark scheme to solve this nonlinear dynamic problem. The MPII model is implemented in the framework of the Finite Element method, and nonlinear seismic wave propagation is investigated. In this work, a borehole condition is considered at the base of the soil model except when it is indicated. For the lateral boundaries a periodic condition is assumed. Consequently, the displacement, strain and stresses are equal on both lateral boundaries. The model is numerically verified by means of different programs (see §3.4 for more details).

B.4 Nonlinear dynamic soil-structure interaction

The effect of soil nonlinearity is now investigated by means of the MPII model implemented in the framework of the Finite Element method (CESAR-LCPC code).

B.4.1 Structural model

As the main objective of this paper is to study the effect of soil nonlinearities on the DSSI, the elastic material behavior is considered for the structures. The structures are modeled by 2D frames with one span and one floor. The columns are massless and the beams have a large stiffness. The flexibility of the foundations is not taken into account (rigid foundations). Seven structural models are studied, each having a different fundamental frequency (Table B.1).

Case Number	Beam mass t/m^3	Fund. frequency (Hz)
1	5	3.3937
2	8.5	2.6124
3	23.5	1.5764
4	24.5	1.544
5	25.5	1.5136
6	28	1.4446
7	50	1.0818

Table B.1: Fundamental frequency of the various structures

B.4.2 Soil model

The soil is composed of 5 different material properties (Fig.B.1a). The shear modulus reduction curve versus cyclic shear strain for different layers is shown in Fig.B.1b. The foundation and the soil are perfectly connected and the sliding and uplift of the foundation are not considered.

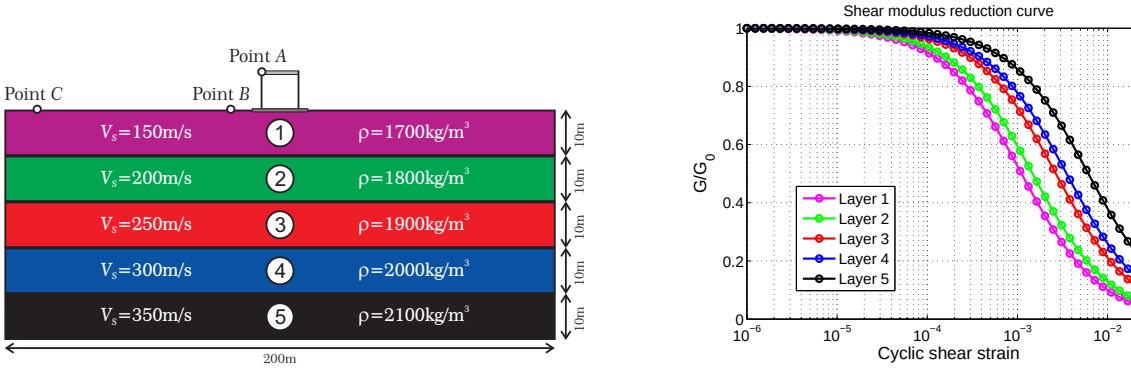

(a) Soil-structure model (b) Shear modulus reduction curves

Figure B.1: Soil-structure model and related shear modulus reduction curves in the various soil layers

B.4.3 Soil-structure interaction

To study the effect of soil nonlinearity, the soil-structure model is excited by a Ricker wavelet (order zero) with various amplitudes. The nonlinear response of the soil-structure system is compared to the linear one. Acceleration, velocity and displacement at the top of the structure are compared for different input levels (PGA equal to 0.1, 0.25 and 0.5g). Figure B.2 displays the results of the first 5 seconds of propagation for structure 6 (fundamental frequency equal to 1.4446 Hz). We observe that the amplitudes of the acceleration and velocity decrease, especially when the PGA is equal to $0.5g$. Furthermore, the soil nonlinearity yields a significant residual displacement. Because of soil nonlinearity part of the energy dissipates into the soil before reaching the structure and consequently the amplitude at the top of the structure is smaller compared to its linear counterpart. Indeed, the amplitudes for all nonlinear cases are less than linear ones with an input PGA equal to $0.1g$. The apparent wave velocity is also different for these four cases; we can observe that it decreases for increasing soil nonlinearity (see late arrival times).

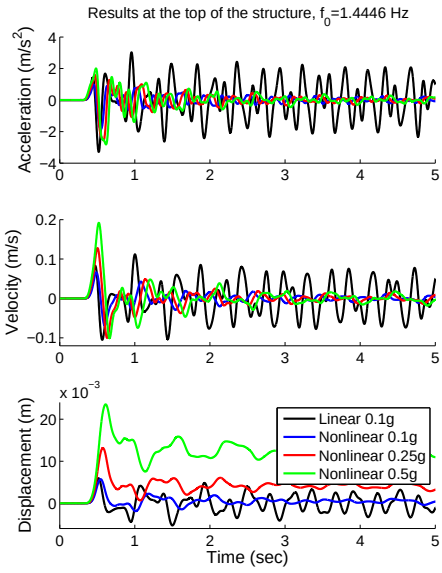

Figure B.2: Response (acceleration, velocity and displacement) of the structure 6 to Ricker excitation for different input motions

The Fourier transform of the displacement at the top of this structure for all the different

cases is shown in Fig.B.3b. The fundamental frequency of this frame on fixed base is 1.4446 Hz. The first natural frequency of the soil profile (linear behavior) is 1.465 Hz. Considering the soil-structure interaction with linear behavior of the soil, the fundamental frequency of the system shifts to a lower frequency equal to 1.358 Hz. This means that we have a 6% reduction. Considering the nonlinear behavior of the soil, the fundamental frequency of the system keeps decreasing and it changes from 1.343 Hz (PGA: 0.1g) to 1.328 Hz (PGA: 0.5g). This means that the fundamental frequency decreases again of 2.2% for the nonlinear soil with PGA of 0.5g in comparison with the linear one. We observed that the decrease of the soil-structure system fundamental frequency is different for the selected structures. The only difference between these structures is their mass and consequently their fundamental frequency. This means the mass plays an important role in DSSI. Also, the relative position of the first soil natural frequency and the fundamental frequency of the structures is important and affects nonlinear SSI, but more structures are needed to reveal a general trend. In addition, we can have the same fundamental frequency (on fixed base) with different geometries, stiffnesses and masses of the structures which make it even more complicated to reach this general trend.

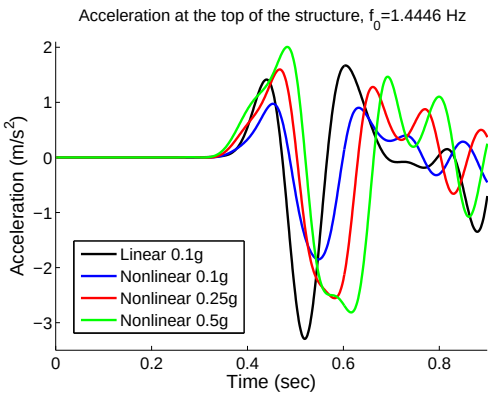

(a) acceleration at the top of structure

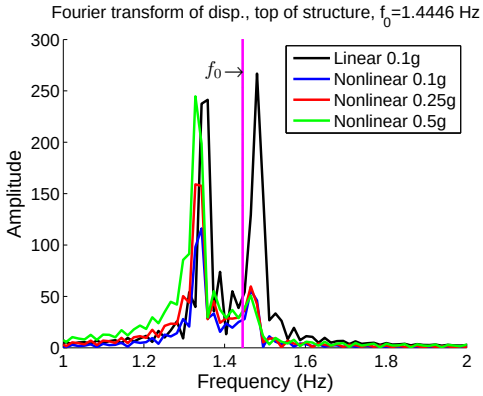

(b) Fourier transform of the displacement

Figure B.3: First second of acceleration at the top of structure and Fourier transform of the displacement of structure 6 for different input motions

B.4.4 Soil response

We now present some results in the soil volume in order to understand what causes the reduction of the structure response. The hysteresis cycles at different soil layers are shown in Fig.B.4 for the soil-structure model of structure 7 (fundamental frequency of 1.0808 Hz on fixed base).

As the dissipated energy is related to the area of the stress-strain cycles, we observe that the energy dissipation is more significant for the layer close to the surface of the soil (5m to the surface). In this case the maximum shear strain reaches 0.04% (PGA: 0.1g, Fig.B.4a). The soil behavior remains elastic in layers 1 and 2. The results are coherent with the shear modulus reduction curve of the soil profile shown in Fig.B.1. This shows the effect of the confining stress that changes the dynamic behavior of the soil. That is, for an increasing confining stress, increasing seismic excitation is needed for the soil to enter in its plastic regime. Figure B.4b displays the hysteresis cycles of the same soil- structure model for an input motion having a PGA of 0.5g. In this case the nonlinearity in layer 1 is visible. The shear strain in the soil layer 5 reaches up to 0.12%. For this strain level, the energy dissipation is larger than the for 0.1g case. For this reason, the accelerations are approximately equal at the top of the structure in spite of the large difference between the input motions (Fig.B.2).

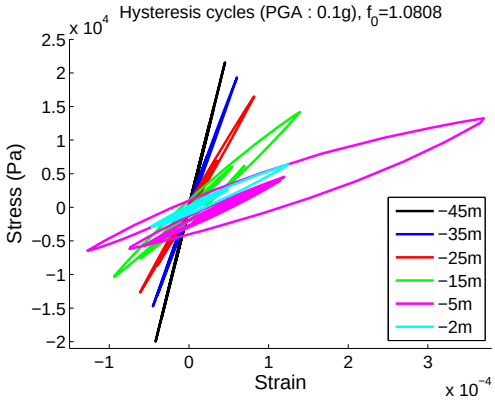

(a) Hysteresis cycles for $0.1g$ PGA

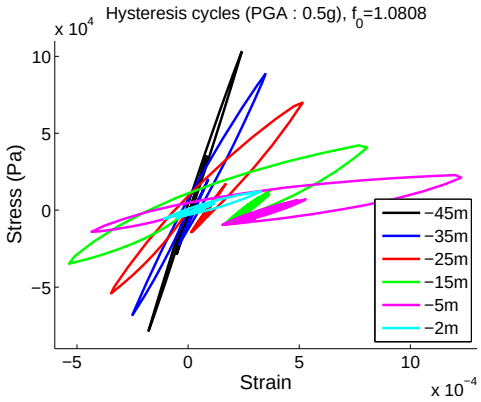

(b) Hysteresis cycles for $0.5g$ PGA

Figure B.4: Hysteresis cycles at different soil layers ($0.1g$ PGA), left, and, ($0.5g$ PGA), right for the structure 7

B.4.5 Structural response

For the seven structures in Fig.B.1, the normalized maximum acceleration at the top of the structure is shown versus structure normalized frequency (Fig.B.5a). The maximum acceleration at the top of the structure is normalized by the maximum acceleration of the input motion.

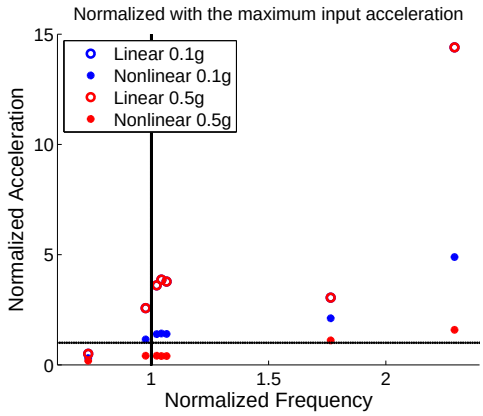

(a) Acceleration normalized by maximum input acceleration

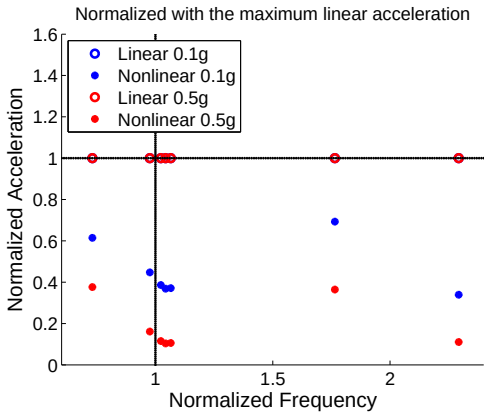

(b) Acceleration normalized by maximum linear acceleration

Figure B.5: Normalized acceleration vs. normalized frequency for different structures and various input motions

The fundamental frequency of the structures (fixed base) is normalized by the first natural frequency of the soil (1.465 Hz). Considering the soil nonlinear behavior, the input motion with a PGA of $0.5g$ leads to a lower amplification than the $0.1g$ one in all cases, because the nonlinearity in the soil layers is larger. For the higher normalized frequency (structure 1), the amplification in nonlinear cases is larger. It should be noticed that the mass of the structure is the only difference between these seven structures and higher normalized frequency means smaller mass of the structure.

For the structures with normalized frequency smaller than 1, considering nonlinear behavior of the soil, the acceleration at the top of the structure is less than the input motion. In Fig.B.5b, the same results are analyzed considering another definition of the normalized acceleration. The maximum acceleration is normalized by the maximum acceleration of the corresponding linear case. The acceleration strongly decreases for the normalized frequency close to 1. It should be noticed that these results are for the structural type that we considered and may be different for other types of structures. The same graphs are shown in Fig.B.6 for normalized displacement. In

Fig.B.6a, the maximum displacement at the top of the structure is normalized by the maximum displacement of the input motion. The normalized displacement in the linear case is larger than other cases for the normalized frequency close to 1, meaning that the structures have fundamental frequencies close to the soil natural frequency. This shows the resonance in the system.

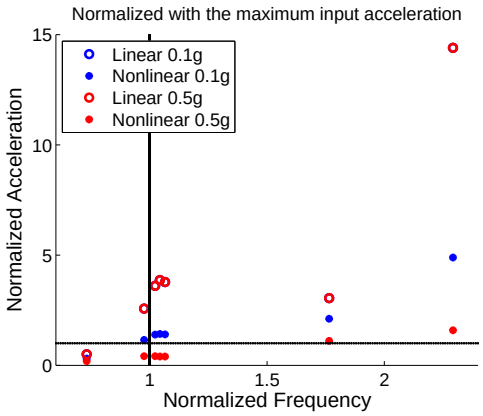

(a) Displacement normalized by maximum input displacement

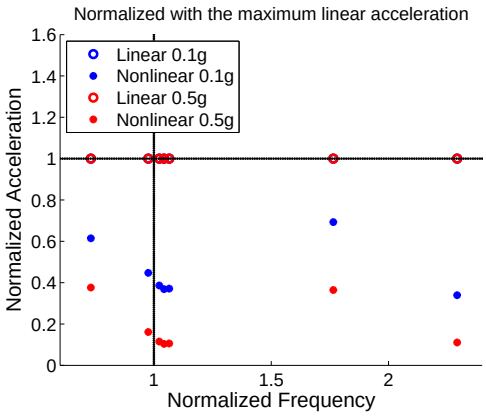

(b) Displacement normalized by maximum linear displacement

Figure B.6: Normalized displacement vs. normalized frequency for different structures and various input motions

Comparing the results in Fig.B.5a and Fig.B.6a, we notice that the maximum normalized acceleration for the $0.5g$ PGA input motion is less than for 0.1g, but the maximum normalized displacement for $0.5g$ PGA is larger than that of $0.1g$. We may conclude that the acceleration is more influenced by soil nonlinearity. In Fig.B.6b, the normalized displacement is obtained by normalizing the maximum displacement at the top of the structure by the corresponding linear maximum displacement. We observe that, for the normalized frequency close to 1, the nonlinearity is more significant and the maximum normalized displacement is less than for other structures except for the highest normalized frequency (structure 1). It means that the mass of the structure is also very important. Also, it seems that, for the structures with the normalized frequency below 1, the DSSI is less influenced by soil nonlinearity.

B.5 Elastic boundary condition

In this case, the structure 7 and the same soil profile is used, but the difference with the previous example is that the absorbing layers are added at the base of the model, so no reflected waves come from the basement. The simple numerical absorbing layer presented by Semblat et al. (2010, 2011) is used in this work. The horizontal acceleration and displacement are shown at three control points (A, B and C, Fig.B.1a) in Fig.B.7.

The analyses are performed for an input PGA of 0.5g considering the nonlinear behavior of the soil. The model is excited by Ricker wavelet (order zero) at the soil base. Because of the absorbing layers, the Ricker wavelet obviously works as an impact force and the structure (Point A) continues to oscillate with amplitude which decreases because of the geometric damping and nonlinearity of the soil. At point B there is a little oscillation due to the surface wave.

At point C, (Free field) there is no oscillation as the reflected waves are absorbed due to the soil nonlinearity. To have a better idea on what is happening in the soil, the transfer functions are displayed in Fig.B.8 and Fig.B.9.

The transfer function in Fig.B.8 is the ratio of the acceleration at the top of the structure to acceleration at the different points of the structural model. The zero level is placed at the surface of the soil and in this case, it is the control point C. Fig.B.8 compares the difference

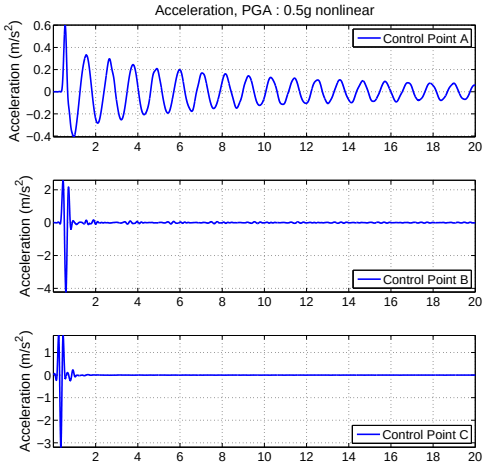

(a) Acceleration at three control points

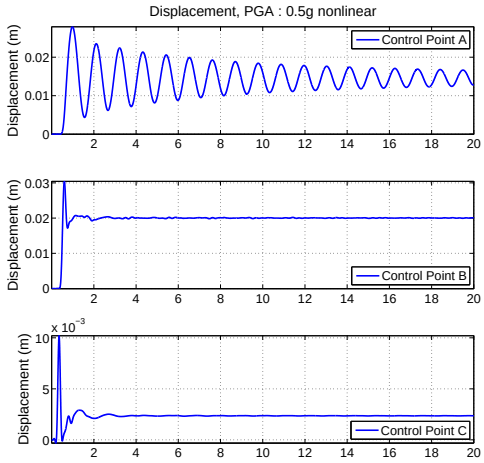

(b) Acceleration at three control points

Figure B.7: Horizontal acceleration and displacement for three control points A, B and C of structure 7 (PGA: 0.5g)

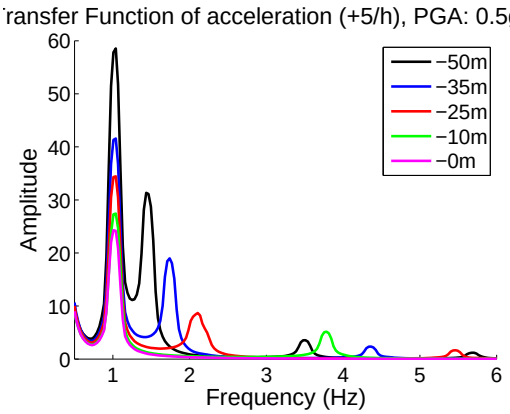

(a) TF with linear soil behavior

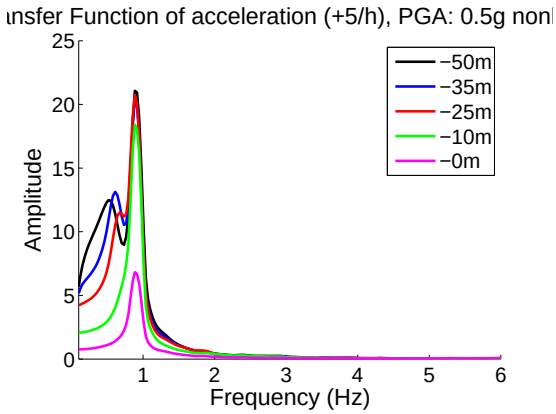

(b) TF with nonlinear soil behavior

Figure B.8: Transfer function (top of structure/different levels in soil) with linear and nonlinear behavior for 0.5g PGA

between the linear (Fig.B.8a) and nonlinear (Fig.B.8b) soil behavior. The first peak of the linear transfer function indicates the fundamental frequency of the soil-structure system and the other peaks concern the approximate natural frequencies of the soil layers. As we see in the nonlinear case (Fig.B.8b) the fundamental frequency of the soil-structure system decreases and the natural frequencies of the soil are filtered.

This nonlinear effect is more obvious in Fig.B.9, where the transfer function between the free field and different points in soil is compared between linear (left) and nonlinear (right) cases. The natural frequency of the soil is 1.465Hz (First peak of the black line). The nonlinear behavior of the soil tends to filter the high frequencies (Fig.B.9b) and the amplitudes are much lower than linear case. The fundamental frequency of this structure on rigid base is 1.0818 Hz (case 7, Fig.B.1), considering linear soil-structure interaction, the fundamental frequency decreases to 1.009 Hz, it means 6.7%, and finally for the nonlinear case with high strain level (Input PGA: 0.5g), it reaches 0.901 Hz, 10.7% less than for the linear case. As it mentioned above, the level of nonlinearity is so high that the natural frequencies of the soil are filtered. In both transfer functions, a high level of the amplitude attenuation is seen because of soil nonlinearity.

The dissipated energy in the soil is computed by means of equation 5.4. The dissipated

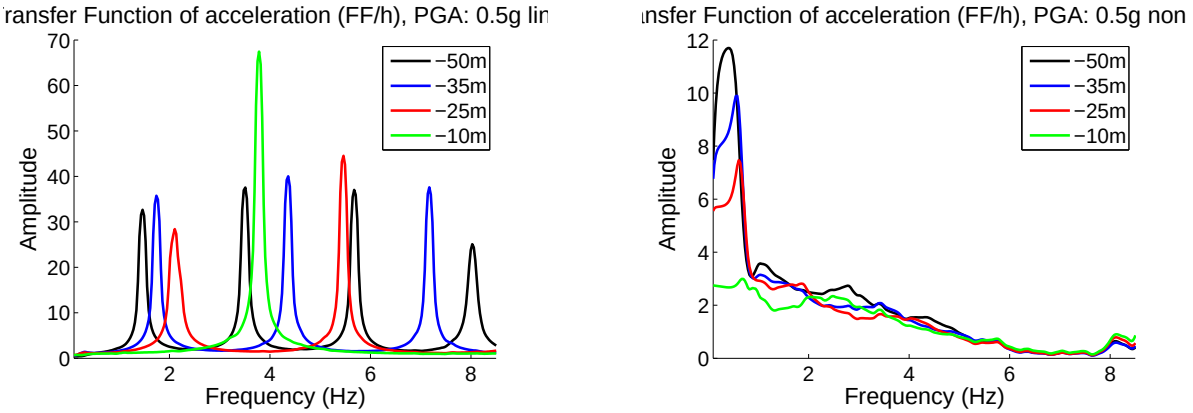

(a) TF with linear soil behavior

(b) TF with nonlinear soil behavior

Figure B.9: Transfer function (free field/different levels in soil) with linear and nonlinear behavior for $0.5g$ PGA

energy is obtained firstly due to all the components of the equation and secondly, due to the shear components. Then, the ratio between the second and first dissipated energies is obtained. The iso-values of the computed ratio is shown in Fig.B.10. This figure demonstrates the area which is influenced by the oscillation of the structure, because the difference between two dissipated energies is due to the normal components.

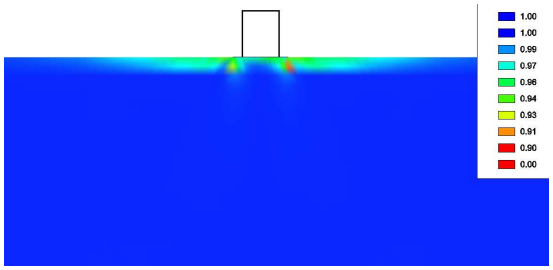

Figure B.10: Approximate influence zone of the structure obtained by means of the dissipated energy in the soil

B.6 Concluding remarks

The MPII model is implemented in the framework of the Finite Element method (CESAR-LCPC code), and nonlinear seismic wave propagation is investigated for the problem of dynamic soil-structure interaction. We observe that, because of soil nonlinearity, part of the input energy (depending on the strain level) dissipates into the soil before reaching the surface. Consequently, the structural response in terms of acceleration, velocity and displacement at its top decreases.

Considering soil nonlinearity, the fundamental frequency of the soil-structure system decreases compared to the structure based on a linear soil, but it is not significant. The total mass of the structure is a very important factor that influences the reduction of fundamental frequency of soil-structure interaction. Finally, the response of the structure is more influenced by the soil nonlinearity when the structure's fundamental frequency is close to the soil natural frequency. Conversely, when the structure's fundamental frequency is less than the natural frequency of the soil, the effect of soil nonlinearity is less.

Bibliography

Ainsworth, M. (2004). Dispersive and dissipative behaviour of high order discontinuous galerkin finite element methods. *Journal of Computational Physics*, 198:106–130.

Ainsworth, M., Monk, P., and Muniz, W. (2006). Dispersive and dissipative properties of discontinuous galerkin finite element methods for the second-order wave equation. *Journal of Scientific Computing*, 27(1-3):5–40.

Andria-Ntoanina, I. (2011). *Caractérisation dynamique de sables de référence en laboratoire - Application à la réponse sismique de massifs sableux en centrifugeuse*. PhD thesis, Université Paris-Est.

Aochi, H., Bonilla, L., Madariaga, R., and Pecker, A. (2008). Project ANR-DEBATE 2008-2011. Technical report.

Arias, A. (1970). A measure of earthquake intensity. In *Seismic design for nuclear power plants*, pages 438–483. R.J. Hansen. MIT Press. Cambridge, USA.

Ashrafi, S. A. and Smyth, A. W. (2007). Generalized masing approach to modeling hysteretic deteriorating behavior. *Journal of Engineering Mechanics*, 133(5):495–505.

Asik, M. Z. and Isbuga, V. (2007). Nonlinear response of a layered medium. *Journal of Vibration and Control*, 13(9-10):1313–1320.

Askes, H., Wang, B., and Bennett, T. (2008). Element size and time step selection procedures for the numerical analysis of elasticity with higher-order inertia. *Journal of Sound and Vibration*, 314:650–656.

Assimaki, D., Kausel, E., and Whittle, A. (2000). Model for dynamic shear modulus and damping for granular soils. *Journal of Geotechnical and Geoenvironmental Engineering*, 126:859–869.

Aubry, D. and Clouteau, D. (1992). A subdomain approach to dynamic soil-structure interaction. In *Recent Advances in Earthquake Engineering and Structural Dynamics*, pages 209–224. Ouest Edition/AFPS, Nantes, France.

Aubry, D. and Modaressi, A. (1992). Strain localization in multipotential elastoplasticity. *International Journal for Numerical Methods in Engineering*, 34(1):349–363.

Babuška, I., Ihlenburg, F., Strouboulis, T., and Gangaraj, S. K. (1997a). A posteriori error estimation for finite element solution of the Helmholtz equation - part II: estimation of the pollution error. *International Journal for Numerical Methods in Engineering*, 40:3883–3900.

Babuška, I., Strouboulis, T., and Copps, K. (1997b). hp optimization of finite element approximations: Analysis of the optimal mesh sequences in one dimension. *Computer methods in applied mechanics and engineerlng*, 150:89–108.

Bao, G., Wei, G. W., and Zhao, S. (2004). Numerical solution of the Helmholtz equation with high wavenumbers. *International Journal for Numerical Methods in Engineering*, 59:389–408.

Bardet, J. P., Ichii, K., and Lin, C. H. (2000). *EERA, A Computer Program for Equivalent-linear Earthquake site Response Analyses of Layered Soil Deposits*. University of Southern California.

Bardet, J. P. and Tobita, T. (2001). *NERA, A Computer Program for Nonlinear Earthquake site Response Analyses of Layered Soil Deposits*. University of Southern California.

Basu, U. and Chopra, A. (2003). Perfectly matched layers for time-harmonic elastodynamics of unbounded domains: theory and finite-element implementation. *Computer Methods in Applied Mechanics and Engineering*, 192:1337–1375.

Bayliss, A. and Turkel, E. (1980). Radiation boundary conditions for wave-like equations. *Communications on Pure and Applied Mathematics*, 33(6):707–725.

Belyaev, A. K. and Irschik, H. (1996). Non-linear waves in complex structures modelled by elastic-viscoplastic stochastic media. *International Journal of Non-Linear Mechanics*, 31(5):771–777.

Bérenger, J. (1994). A perfectly matched layer for the absorption of electromagnetics waves. *Journal of Computational Physics*, 114:185–200.

Beresnev, I. A. and Wen, K.-L. (1996). Nonlinear soil response, a reality? *Bulletin of the Seismological Society of America*, 86(6):1964–1978.

Beskos, D. (1997). Boundary elements methods in dynamic analysis: Part II (1986-1996). *Applied Mechanics Reviews (ASME)*, 50(3):149–197.

Betbeder-Matibet, J. (2003). *Génie parasismique: Prévention parasismique*. Hermes Science Publication, Paris.

Bielak, J., Loukakis, K., Hisada, Y., and Yoshimura, C. (2003). Domain reduction method for three-dimensional earthquake modeling in localized regions, part I: theory. *Bulletin of the Seismological Society of America*, 93(2):817–824.

Bode, C., Hirschauer, R., and Savidis, S. (2002). Soil-structure interaction in the time domain using halfspace green's functions. *Soil Dynamics and Earthquake Engineering*, 22(4):283–295.

Bonilla, L. F. (2000). *Computation of linear and nonlinear site response for near field ground motion*. PhD thesis, University of California, Santa Barbara.

Bonilla, L. F., Archuleta, R. J., and Lavallée, D. (2005). Hysteretic and dilatant behavior of cohesionless soils and their effects on nonlinear site response: Field data observations and modeling. *Bulletin of the Seismological Society of America*, 95(6):2373–2395.

Bonnet, M. (1999). *Boundary Integral Equation Methods for Solids and Fluids*. Wiley: Chichester, U.K.

Borja, R. I., Lint, C.-H., Samat, K. M., and Masada, G. M. (2000). Modelling non-linear ground response of non-liquefiable soils. *Earthquake Engineering and Structural Dynamics*, 29:63–83.

Boulanger, R. W. (2010). Sand plasticity model for nonlinear seismic deformation analyses. In *Fifth International Conference on Recent Advances in Geotechnical Earthquake Engineering and Soil Dynamics, San Diego, California*.

Bourbié, T., Coussy, O., and Zinzsner, B. (1987). *Acoustics of Porous Media*. Technip, Paris, France.

Buehler, M., Wienbroer, H., and Rebstock, D. (2006). A full seismic soil-foundation-structure interaction approach. In *First European Conference on Earthquake Engineering and Seismology, Geneva, Switzerland, 3-8 September*.

Cai, Y., Gould, P., and Desai, C. (2000). Nonlinear analysis of 3D seismic interaction of soil-pile-structure systems and application. *Engineering Structures*, 22:191–199.

Casciati, S. and Borja, R. (2004). Dynamic FE analysis of South Memnon Colossus including 3D soil-foundation-structure interaction. *Computers and Structures*, 82:1719–1736.

Caughey, T. (1960). Classical normal modes in damped linear systems. *Journal of Applied Mechanics*, 27:269–271.

CESAR-LCPC (2001). *Manuel théorique du module TACT*. Laboratoire Central des Ponts et Chaussées, Paris, 5ème edition.

Chadwick, E., Bettess, P., and Laghrouche, O. (1999). Diffraction of short waves modelled using new mapped wave envelope finite and infinite elements. *International Journal for Numerical Methods in Engineering*, 45:335–354.

Chaillat, S. (2008). *Fast multiple method for 3-D elastodynamic boundary integral equations. Application to seismic wave propagation*. PhD thesis, Ecole National des Ponts et Chaussées.

Chaillat, S., Bonnet, M., and Semblat, J. (2009). A new fast multi-domain BEM to model seismic wave propagation and amplification in 3D geological structures. *Geophysical Journal International*, 177:509–531.

Chaljub, E. (2006). Spectral element modeling of 3D wave propagation in the alpine valley of grenoble, france. In *3th International Symposium on the Effects of Surface Geology on Seismic Motion, Grenoble, France*.

Chaljub, E., Moczo, P., Tsuno, S., Bard, P., Kristek, J., Kaser, M., Stupazzini, M., and Kristekova, M. (2010). Quantitative comparison of four numerical predictions of 3D ground motion in the grenoble valley, france. *Bulletin of the Seismological Society of America*, 100(4):1427–1455.

Chatzigogos, C. (2007). *Comportement sismique des fondations superficielles: Vers la prise en compte d'un critère de performance dans la conception*. PhD thesis, Ecole Polytechnique, Palaiseau, France.

Chew, W. and Liu, Q. (1996). Perfectly matched layers for elastodynamics: a new absorbing boundary condition. *Journal of Computational Acoustics*, 4(4):341–359.

Chopra, A. (2001). *Dynamics of Structures, Theory and Applications to Earthquake Engineering*. Prentice Hall, New Jersey.

Clouteau, D. and Aubry, D. (2003). *Boundary Element Methods for soil-structure interaction*, chapter Computational soil-structure interaction, pages 61–126. Kluwer Academic Publishers.

Collino, F. and Tsogka, C. (2001). Application of the PML absorbing layer model to the linear elastodynamic problem in anisotropic heterogeneous media. *Geophysics*, 66(1):294–307.

Cotton, F., Scherbaum, F., Bommer, J. J., and Bungum, H. (2006). Criteria for selecting and adjusting ground-motion models for specific target regions: Application to central europe and rock sites. *Journal of Seismology*, 10:137–156.

Dangla, P. (1988). A plane strain soil-structure interaction model. *Earthquake Engineering and Structural Dynamics*, 16:1115–1128.

Dauksher, W. and Emery, A. F. (1999). An evaluation of the cost effectiveness of chebyshev spectral and p-finite element solutions to the scalar wave equation. *International Journal for Numerical Methods in Engineering*, 45:1099–1113.

Delépine, N., Bonnet, G., Lenti, L., and Semblat, J. (2009). Nonlinear viscoelastic wave propagation: an extension of nearly constant Q models. *Journal of Engineering Mechanics (ASCE)*, 135(11):1305–1314.

Delépine, N. and Semblat, J. (2006). Site effects in a deep alpine valley for various seismic sources. In *3th International Symposium on the Effects of Surface Geology on Seismic Motion, Grenoble, France*.

Deraemaeker, A., Babuska, I., and Bouillard, P. (1999). Dispersion and pollution of the FEM solution for the Helmholtz equation in one, two and three dimensions. *International Journal for Numerical Methodes in Engineering*, 46:471–499.

Duval, A. (1996). Détermination de la réponse d'un site aux séisme á l'aide du bruit de fond - evaluation expérimentale. Technical report, Rapport Etude et Recherche des Laboratoires des Ponts et Chaussées, n. GT62, 264p., LCPC, Paris, France.

Duval, A., Meneroud, J., Vidal, S., and Bard, P. (1998). Relation between curves obtained from microtremor and site effects observed after Caracas 1967 earthquake. In *11th European Conference on Earthquake Engineering, Paris, France*.

Elgamal, A., Yang, Z., Parra, E., and Ragheb, A. (2003). Modeling of cyclic mobility in saturated cohesionless soils. *International Journal of Plasticity*, 19:883–905.

Emmerich, H. and Korn, M. (1987). Incorporation of attenuation into time-domain computations of seismic wave fields. *Geophysics*, 52(9):1252–1264.

Engquist, B. and Majda, A. (1979). Radiation boundary conditions for acoustic and elastic wave. *Communications on Pure and Applied Mathematics*, 32(3):313–357.

Estorff, O. and Firuziaan, M. (2000). Coupled BEM/FEM approach for nonlinear soil/structure interaction. *Engineering Analysis with Boundary Elements*, 24:715–725.

Faccioli, E., Maggio, F., Paolucci, R., and Quarteroni, A. (1997). 2D and 3D elastic wave propagation by a pseudo-spectral domain decomposition method. *Journal of Seismology*, 1:237–251.

Faccioli, E., Maggio, F., Quarteroni, A., and Taghan, A. (1996). Spectral-domain decomposition methods for the solution of acoustic and elastic wave equations. *Geophysics*, 61:1160–1174.

Fäh, D., Suhadolc, P., Mueller, S., and Panza, G. (1994). A hybrid method for the estimation of ground motion in sedimentary basins: quantitative modeling for Mexico city. *Bulletin of Seismological Society of America*, 84(2):383–399.

Fahey, M. (1992). Shear modulus of cohesionless soil: variation with stress and strain level. *Canadian Geotechnical Journal*, 29(1):157–161.

Festa, G. and Nielsen, S. (2003). PML absorbing boundaries. *Bulletin of the Seismological Society of America*, 93(2):891–903.

Festa, G. and Vilotte, J. (2005). The Newmark scheme as velocity-stress time-staggering: an efficient PML implementation for spectral element simulations of elastodynamics. *Geophysical Journal International*, 161:789–812.

Festa, G., Vilotte, J., and Delavaud, E. (2005). Interaction between surface waves and absorbing boundaries for wave propagation in geological basins: 2D numerical simulations. *Geophysical Research Letters*, 32(20):L20306.1–L20306.4.

Field, E., Johnson, P., Beresnev, I., and Zeng, Y. (1997). Nonlinear ground-motion amplification by sediments during 1994 Northridge earthquake. *Nature*, 390:599–602.

Field, E. H., Kramer, S., Elgamal, A. W., Bray, J. D., Matasovic, N., Johnson, P. A., Cramer, C., Roblee, C., Wald, D. J., Bonilla, L. F., Dimitriu, P. P., and Anderson, J. G. (1998). Nonlinear site response: Where we're at (a report from a scec/peer seminar and workshop). *Seismological Research Letters*, 69(3):230–234.

Fujiwara, H. (1998). The fast multipole method for the integral equations of seismic scattering problems. *Geophysical Journal International*, 133:773–782.

Fung, Y. C. and Tong, P. (2001). *Classical and Computational Solid Mechanics*. World Sientific Publishing Co.

Gandomzadeh, A., Santisi d'Avila, M., Semblat, J., Lenti, L., and Bonilla, F. (May 2010). Influence of soil nonlinearities on dynamic soil-structure interaction. In *Fifth International Conference on Recent Advances in Geotechnical Earthquake Engineering and Soil Dynamics, San Diego, USA*.

Gaul, L. and Schanz, M. (1999). A comparative study of three boundary element approaches to calculate the transient response of viscoelastic solids with unbounded domains. *Computer Methods in Applied Mechanics and Engineering*, 179(1-2):111–123.

Gelis, C., Bonilla, F., Regnier, J., Bertrand, E., and Duval, A. (2008). On the use of Saenger's finite difference stencil to model 2D P-SV nonlinear basin response; Application to Nice, France. In *SEISMIC RISK 2008: Earthquake in northwest Europe, Liege, Belgium*.

GEMGEP (2005). Le risque sismique á Nice, apport méthodologique, résultats et perspectives opérationnelles. Technical report, CETE Méditerranée, Laboratoire de Nice, France.

Gerolymos, N. and Gazetas, G. (2006). Static and dynamic response of massive caisson foundations with soil and interface nonlinearities-validation and results. *Soil Dynamics and Earthquake Engineering*, 26:377–394.

Givoli, D. (1991). Non-reflecting boundary conditions. *Journal of Computational Physics*, 94:1–29.

Gouasmia, A. and Djeghaba, K. (2007). Non-linear seismic soil-structure interaction analysis of structures based on the superstructure method. *Asian Journal of Civil Engineering (Building and Housing)*, 8(2):183–201.

Guellec, P., Humbert, P., and Ricard, A. (1976). La méthode des éléments finis et le système ROSALIE. Technical Report 81, Bulletin de liaison des laboratoires des Ponts et Chaussées, Paris, France.

Gutta, S. K., Yamamuro, J. A., and Lade, P. V. (2003). Predictions of large three-dimensional stress reversals in sand. In *16th Engineering Mechanics Conference (ASCE), Seattle, USA*.

Halabian, A. and Naggar, M. H. E. (2002). Effet of non-linear soil-structure interaction on seismic response of tall slender structures. *Soil Dynamics and Earthquake Engineering*, 1(22):639–658.

Harari, I. (1997). Reducing spurious dispersion, anisotropy and reflection in finite element analysis of time-harmonic acoustics. *Computer methods in applied mechanics and engineering*, 140:39–58.

Harari, I. and Nogueira, C. L. (2002). Reducing dispersion of linear triangular elements for the Helmholtz equation. *Journal of Engineering Mechanics*, 128(3):351–358.

Harari, I. and Schohet, Z. (1998). On non-reflecting boundary conditions in unbounded elastic solids. *Computer Methods in Applied Mechanics and Engineering*, 163(1-4):123–139.

Hardin, B. O. and Drnevich, V. P. (1972a). Shear modulus and damping in soils: design equations and curves. *Journal of the Soil Mechanics and Foundations Division*, 98(7):667–692.

Hardin, B. O. and Drnevich, V. P. (1972b). Shear modulus and damping in soils: Measurement and parameter effects. *Journal of the Soil Mechanics and Foundations Division*, 98(6):603–624.

Hayashi, H., Honda, M., Yamada, T., and Tatsuoka, F. (1994). Modeling of nonlinear stress-strain relations of sands for dynamic response analysis. In *Earthquake Engineering, Tenth World conference, Balkema, Rotterdam.*

Hughes, T. (1987). *The Finite Element Method, Linear Static and Dynamic Finite Element Analysis.* Prentice-Hall: Englewood Cliffs, NJ, Mineola, New York.

Hughes, T., Reali, A., and Sangalli, G. (2008). Duality and unified analysis of discrete approximations in structural dynamics and wave propagation: Comparison of p-method finite elements with k-method nurbs. *Cmput. Methods Appl. Mech. Engrg.*, 197:4104–4124.

Hujeux, J. (1985). Une loi de comportement pour le chargement cyclique des sols. In *Génie Parasismique*, pages 287–302. Presse ENPC.

Humbert, P. (1989). Un code général de calculs par éléments finis. Technical Report 160, Bulletin de liaison des Laboratoires des Ponts et Chaussées, Paris, France.

Humbert, P. and Dubouchet, A. (2001). *CESAR-LCPC 3.3, manuel de formation.* Laboratoire Central des Ponts et Chaussées, 7 edition.

Humbert, P., Dubouchet, A., Fezans, G., and Remaud, D. (2005). CESAR-LCPC, un progiciel de calcul dédié au gnie civil. Technical Report 256-257, Bul. des Laboratoires des Ponts et Chausses, Paris, France.

Iai, S. (1991). A strain space multiple mechanism model for cyclic behavior of sand and its application. Technical report, Port and Harbor Research Institute, Japan.

Iai, S., Matsunaga, Y., and Kameoka, T. (1990). Parameter identification for a cyclic mobility model. Technical Report 29, Report of the port and harbour research institute.

Iai, S., Matsunaga, Y., and Kameoka, T. (1992). Strain space plasticity model for cyclic mobility. *Soils and Foundations*, 32(2):1–15.

Idriss, I., Seed, H., and Serff, N. (1974). Seismic response by variable damping finite elements. *Journal of the Geotechnical Engineering Division (ASCE)*, pages 1–13.

Idriss, I. M., Dobry, R., and Singh, R. D. (1978). Nonlinear behavior of soft clays during cyclic loading. *Journal of the Geotechnical Rngineering Division*, 104(GT12):1427–1447.

Ihlenburg, F. and Babuška, I. (1995a). Dispersion analysis and error estimation of galerkin finite element methods for the Helmholtz equation. *International Journal for Numerical Methods in Engineering*, 38:3745–3774.

Ihlenburg, F. and Babuška, I. (1995b). Finite element solution of the Helmholtz equation with high wave number part I: The h-version of the FEM. *Computers Math. Applic.*, 30(9):9–37.

Iwan, W. D. (1967). On a class of models for the yielding behavior of continuous and composite systems. *Journal of Applied Mechanics*, pages 612–617.

Iwan, W. D. and Cifuentes, A. O. (1986). A model for system identification of degrading structures. *Earthquake Engineering and Structural Dynamics*, 14:877–890.

Jeremic, B., Jie, G., Preisig, M., and Tafazzoli, N. (2009). Time domain simulation of soil-foundation-structure interaction in non-uniform soils. *Earthquake Engineering and Structural Dynamics*, 38:699–718.

J.M.Carcione, Cavallini, F., Mainardi, F., and Hanyga, A. (2002). Time-domain modeling of constant-Q seismic waves using fractional derivatives. *Pure and Applied Geophysics*, 159(7-8):1719–1736.

Joyner, W. B. (1975). A method for calculating nonlinear seismic response in two dimensions. *Bulletin of the Seismological Society of America*, 65(5):1337–1357.

Joyner, W. B. and Chen, A. T. F. (1975). Calculation of nonlinear ground response in earthquake. *Bulletin of the Seismological Society of America*, 65(5):1315–1336.

Joyner, W. B., Warrick, R. E., and Fumal, T. (1981). The effect of quaternary alluvium on strong ground motion in the coyote lake, california, earthquake of 1979. *Bulletin of Seismological Society of America*, 71(4):1333–1349.

Kausel, E. and Assimaki, D. (2002). Seismic simulation of inelastic soils via frequency-dependent moduli and damping. *Journal of Engineering Mechanics*, 128(1):34–47.

Kjartansson, E. (1979). Constant q wave propagation and attenuation. *Journal of Geophysical Research*, 48:4737–4748.

Koh, C., Ho, Y., and Balendra, T. (1995). A substructure approach to dynamic soil-structure interaction due to incident plane waves. *Journal of Sound and Vibration*, 180(5):686–796.

Komatitsch, D. and Martin, R. (2007). An unsplit convolutional perfectly matched layer improved at grazing incidence for the seismic wave equation. *Geophysics*, 72(5):155–167.

Komatitsch, D., Vilotte, J., Vai, R., Castillo-Covarrubias, J., and Sanchez-Sesma, F. (1999). The spectral element method for elastic wave equations-application to 2D and 3D seismic problems. *International Journal for Numerical Methods in Engineering*, 45:1139–1164.

Kondner, R. L. (1963). Hyperbolic stress-strain response : cohesive soils. *Journal of the Soil Mechanics and Foundation Division*, 89(SM 1):115–143.

Konno, K. and Ohmachi, T. (1998). Ground-motion characteristics estimated from spectral ratio between horizontal and vertical components of microtremor. *Bulletin of Seismological Society of America*, 88(1):228–241.

Kramer, S. (1996). *Geotechnical Earthquake Engineering*. Prentice Hall, New Jersey.

Kramer, S. L. (2006). Engineering and science needs for gsma sites: an invited opinion paper. In *International Workshop for Site Selection, Installation, and Operation of Geotechnical Strong-Motion Arrays, La Jolla, California, USA*.

Lebrun, B., Hatzfeld, D., and Bard, P. (2001). Site effects study in urban area: experimental results in grenoble. *Pure and Applied Geophysics*, 158:2543–2557.

Lee, J.-S., Choo, Y.-W., and Kim, D.-S. (2009). A modified parallel Iwan model for cyclic hardening behavior of sand. *Soil Dynamics and Earthquake Engineering*, 29:630–640.

Lenti, L. (2006). *Modellazione di effetti non lineari in terreni soggetti a carico ciclico e dinamico.* Dissertation, University of Bologna, Italy.

Li, S. and Liu, W. (2007). *Meshfree Particle Methods.* Springer: Berlin.

LoPresti, D. C. F., Lai, C. G., and Puci, I. (2006). Onda: Computer code for nonlinear seismic response analyses of soil deposits. *Journal of Geotechnical and Geoenvironmental Engineering, ASCE*, 132(2):223–236.

Lu, X., Li, P., Chen, B., and Chen, Y. (2005). Computer simulation of the dynamic layered soil-pile-structure interaction system. *Canadian Geotechnical Journal*, 42:742–751.

Lubarda, V., Sumarac, D., and Krajcinovic, D. (1993). Preisach model and hysteretic behaviour of ductile materials. *Eur. J. Mech., A/Solids*, 12(4):445–470.

Lussou, P. (2006). *Manuel d'utilisation de CESAR-LCPC, le module MCCI.* Laboratoire Central des Ponts et Chaussées, 2 edition.

Makdisi, F. I. and Wang, Z. L. (2004). Non linear analyses for site response. In *International Workshop on the Uncertainties in Nonlinear Soil Properties and their Impact on Modeling Dynamic Soil Response, March 18-19.*

Marcinkovich, C. and Olsen, K. (2003). On the implementation of perfectly matched layers in a three-dimensional fourth-order velocity-stress finite difference scheme. *Journal of Geophysical Research*, 108(B5):2276.

Mayama, T., Sasaki, K., and Ishikawa, H. (2007). A constitutive model of cyclic viscoplasticity considering changes in subsequent viscoplastic deformation due to the evolution of dislocation structures. *International Journal of Plasticity*, 23:915–930.

Meek, J. and Wolf, J. (1992). Cone models for homogeneous soil. *Journal of Geotechnical Engineering (ASCE)*, 118(5):667–685.

Mestat, P. (1993). Lois de comportement des géomatériaux et modélisation par la méthode des éléments finis - GT52. Technical report, Etudes et recherches des Laboratoires des Ponts et Chaussées, Paris, France.

Meza-Fajardo, K. and Papageorgiou, A. (2008). A nonconvolutional, split-field, perfectly matched layer for wave propagation in isotropic and anisotropic elastic media: stability analysis. *Bulletin of the Seismological Society of America*, 98(4):1811–1836.

Miller, J. D. and Quinn, D. D. (2009). A two-sided interface model for dissipation in structural systems with frictional joints. *Journal of Sound and Vibration*, 321(1-2):201 – 219.

Moczo, P. and Kristek, J. (2005). On the rheological models used for time-domain methods of seismic wave propagation. Research Letter 32, American Geophysical Union.

Moczo, P., Kristek, J., Vavrycuk, V., Archuleta, R., and Halada, L. (2002). 3D heterogeneous staggered-grid finite-difference modeling of seismic motion with volume harmonic and arithmetic averaging of elastic moduli and densities. *Bulletin of the Seismological Society of America*, 92(8):3042–3066.

Moczo, P. and Robertsson, J. (2007). The finite-difference time-domain method for modeling of seismic wave propagation. *Advance Geophysics*, 48:421–516.

Modaressi, H. and Benzenati, I. (1992). An absorbing boundary element for dynamic analysis of two-phase media. In *10th World Conference on Earthquake Engineering, Madrid*, pages 1157–1163.

Montáns, F.-J. (2000). Bounding surface plasticity model with extended masing behavior. *Computer Methods in Applied Mechanics and Engineering*, 182(1-2):135 – 162.

Munjiza, A., Owen, D., and Crook, A. (1998). An $M(M^{-1}K)^m$ proportional damping in explicit integration of dynamic structural systems. *International Journal for Numerical Methods in Engineering*, 41:1277–1296.

Muravskii, G. (2005). On description of hysteretic behaviour of materials. *International Journal of Solids and Structures*, 42(9-10):2625 – 2644.

Muravskii, G. (2009). Application of hysteresis functions in vibration problems. *Journal of Sound and Vibration*, 319(1-2):476 – 490.

Muravskii, G. and Frydman, S. (1998). Site response analysis using a non-linear hysteretic model. *Soil Dynamics and Earthquake Engineering*, 17:227–238.

Muravskii, G. B. (2001). Application of experimental results on cyclic deforming of soils to seismic response analysis. *Soil Dynamics and Earthquake Engineering*, 21:661–669.

Mylonakis, G. and Gazetas, G. (2000). Seismic soil-structure interaction: beneficial or detrimental? *Journal of Earthquake Engineering*, 4(3):277–301.

Ng, T. T. and Dobry, R. (1994). Numerical simulations of monotonic and cyclic loading of granular soil. *Journal of Geotechnical Engineering*, 120(2):388–403.

Osinov, V. (2003). Cyclic shearing and liquefaction of soil under irregular loading: an incremental model for the dynamic earthquake-induced deformation. *Soil Dynamics and Earthquake Engineering*, 23:535–548.

Papadimitriou, A. G. and Bouckovalas, G. D. (2002). Plasticity model for sand under small and large cyclic strains: a multiaxial formulation. *Soil Dynamics and Earthquake Engineering*, 22(3):191 – 204.

Papadimitriou, A. G., Bouckovalas, G. D., and Dafalias, Y. F. (2001). Plasticity model for sand under small and large cyclic strains. *Journal of Geotechnical and Geoenvironmental Engineering*, 127(11):973–983.

Park, J. and Kausel, E. (2004). Numerical dispersion in the thin-layer method. *Computers & Structures*, 82:607–625.

Pecker, A. (2008). *Dynamique des structures et des ouvrages*. École Nationale des Ponts et Chaussées, France.

Pitilakis, D. (2006). *Soil-structure interaction modeling using equivalent linear soil behavior in the sustructure method*. PhD thesis, Ecole Centrale de Paris.

Prevost, J. H. (1978). Plasticity theory for soil stress-strain behavior. *Journal of the Engineering Mechanics Division*, 104(5):1177–1194.

Prevost, J. H. (1985). A simple plasticity theory for frictional cohesionless soils. *Soil Dynamics and Earthquake Engineering*, 4(1):9–17.

Prevost, J. H. (1989). Dyna1d: A computer program for nonlinear seismic site response analysis - technical documentation. Technical report, Multidisciplinary Center for Earthquake Engineering Research, Report NCEER-89-0025.

Prevost, J. H. and Keane, C. M. (1990). Shear stress-strain curve generation from simple material parameters. *Journal of Geotechnical Engineering*, 116(8):1255–1263.

Prevost, J. H. and Popescu, R. (1996). Constitutive relations for soil materials. *Electronic Journal of Geotechnical Engineering*.

Puzrin, A., Frydman, S., and Talesnick, M. (1995). Normalized nondegrading behavior of soft clay under cyclic simple shear loading. *Journal of the Geotechnical Engineering Division*, 121(12):836–843.

Puzrin, A. and Shiran, A. (2000a). Effects of the constitutive relationship on seismic response of soils. Part I. constitutive modeling of cyclic behavior of soils. *Soil Dynamics and Earthquake Engineering*, 19:305–318.

Puzrin, A. and Shiran, A. (2000b). Effects of the constitutive relationship on seismic response of soils. Part II. the site amplification study. *Soil Dynamics and Earthquake Engineering*, 19:319–331.

Pyke, R. (2004). Evolution of soil models since the 1970s. In *International Workshop on the Uncertainties in Nonlinear Soil Properties and their Impact on Modeling Dynamic Soil Response, University of California, Berkeley*.

Pyke, R. M. (1979). Nonlinear soil models for irregular cyclic loadings. *Journal of the Geotechnical Engineering Division*, 105:715–726.

Ramsamooj, D. V. and Alwash, A. J. (1990). Model prediction of cyclic response of soils. *Journal of Geotechnical Engineering*, 116(7):1053–1072.

Rao, S. N. and Panda, A. (1999). Non-linear analysis of undrained cyclic strength of soft marine clay. *Ocean Engineering*, 26:241–253.

Rizos, D. and Wang, Z. (2002). Coupled BEM-FEM solutions for direct time domain soil-structure interaction analysis. *Engineering Analysis with Boundary Elements*, 26:877–888.

Saez, E. (2009). *Dynamic nonlinear soil-structure interaction*. PhD thesis, École Centrale Paris.

Sarmany, D., Botchev, M., and van der Vegt, J. (2007). Dispersion and dissipation error in high-order runge-kutta discontinuous galerkin discretisations of the maxwell equations. *J. Sci. Compu.*, 33:47–74.

Schnabel, P. B., Lysmer, J., and Seed, H. B. (1972). SHAKE: a computer program for earthquake response analysis of horizontally layered sites. Technical report, UCB/EERC-72/12, Earthquake Engineering Research Center, University of California, Berkeley, 92 pages.

Segalman, D. J. (2001). An initial overview of Iwan modeling for mechanical joints. Technical report, SANDIA.

Segalman, D. J. (2002). A four-parameter Iwan model for lap-type joints. Technical report, SANDIA.

Segalman, D. J. and Starr, M. J. (2004). Relationships among certain joint constitutive models. Technical report, SANDIA.

Segalman, D. J. and Starr, M. J. (2008). Inversion of Masing models via continuous Iwan systems. *International Journal of Non-Linear Mechanics*, 43:74–80.

Semblat, J. (1997). Rheological interpretation of rayleigh damping. *Journal of Sound and Vibration*, 206(5):741–744.

Semblat, J. and Brioist, J. (1998). Wave propagation in non-homogenesouly damped medium: numerical vs experimental approach. In *11th European Conference on Earthquake Engineering*.

Semblat, J. and Brioist, J. (2000). Efficiency of higher order finite elements for the analysis of seismic wave propagation. *Journal of Sound and Vibration*, 231(2):460–467.

Semblat, J., Dangla, P., Kham, M., and Duval, A. (2002). Seismic site effects for shallow and deep alluvial basins: in-depth motion and focusing effect. *Soil Dynamics and Earthquake Engineering*, 22:849–854.

Semblat, J. and Pecker, A. (2009). *Waves and Vibrations in Soils: Earthquakes, Traffic, Shocks, Construction works*. IUSS Press: Pavia, Italy.

Semblat, J.-F., Duval, A.-M., and Dangla, P. (2000). Numerical analysis of seismic wave amplification in nice (france) and comparisons with experiments. *Soil Dynamics and Earthquake Engineering*, 19:347–362.

Semblat, J.-F., Gandomzadeh, A., and Lenti, L. (2010). A simple numerical absorbing layer method in elastodynamics. *Comptes Rendus Mcanique*, 338(1):24 – 32.

Semblat, J.-F., Lenti, L., and Gandomzadeh, A. (2011). A simple and efficient multi-directional absorbing layer method to simulate elastic wave propagation in unbounded domains. *International Journal for Numerical Methods in Engineering*, 85(12):1543 – 1563.

Sercombe, J. (1997). *Modélisation du comportement du béton en dynamqiue rapide, application au calcul des conteneurs à haute intégrite*. PhD thesis, Ecole Nationale des Ponts et Chaussées.

Shiryayev, O., Page, S., Pettit, C., and Slater, J. (2007). Parameter estimation and investigation of a bolted joint model. *Journal of Sound and Vibration*, 307(3-5):680 – 697.

Singh, S., Mena, E., and Castro, R. (1988). Some aspects of source characteristics of the 19 september 1985 Michoacan earthquake and ground motion amplification in the near Mexico City from strong motion data. *Bulletin of the Seismological Society of America*, 78(2):451–477.

S.M.Day and Minster, J. (1984). Numerical simulation of wavefields using a padé approximant method. *Geophysical Journal of the Royal Astronomical Society*, 78:105–118.

Song, Y., Hartwigsen, C. J., McFarland, D. M., Vakakis, A. F., and Bergman, L. A. (2004). Simulation of dynamics of beam structures with bolted joints using adjusted Iwan beam elements. *Journal of Sound and Vibration*, 273(1-2):249 – 276.

Steffens, L. M. and Dez, P. (2009). A simple strategy to assess the error in the numerical wave number of the finite element solution of the Helmholtz equation. *Comput. Methods Appl. Mech. Engrg.*, 198:1389–1400.

Steidl, J., Tumarkin, A. G., and Archuleta, R. (1996). What is a reference site? *Bulletin of the Seismological Society of America*, 86(6):1733–1748.

Stewart, J., Fenves, G., and Seed, R. (1999). Seismic soil-structure interaction in buildings i: Analytical methods. *Journal of Geotechnical and Geoenvironmental Engineering*, 125(1):26–37.

Taylor, P. W. and Larkin, T. J. (1978). Seismic site response of nonlinear soil media. *Journal of the Geotechbnical Engineering Division*, 104(GT3):369–383.

Thompson, L. L. and Pinsky, P. M. (1995). A galerkin least squares finite element method for the two-dimensional Helmholtz equation. *International Journal for Numerical Methods in Engineering*, 38:371–397.

Towhata, I. and Ishihara, K. (1985). Modelling soil behavior under principl stress axes rotation. In *Fifth International Conference on Numerical Methods in Geomechanics, Nagoya, 1-5 April 1985*.

Ueng, T.-S. and Chen, J.-C. (1992). Computational procedures for determining parameters in Ramberg-Osgood elastoplastic model based on modulus and damping versus strain. Technical report, Office of Scientific and Technical Information (OSTI), USA.

Veletsos, A. and Meek, J. (1974). Dynamic behavior of building-foundation systems. *Earthquake Engineering and Structural Dynamics*, 3:121–138.

Virieux, J. (1986). P-SV wave propagation in heterogeneous media: velocity-stress finite-difference method. *Geophysics*, 51:889–901.

Vucetic, M. (1990). Normalized behavior of clay under irregular cyclic loading. *Canadian Geotechnical Journal*, 27:29–46.

Vucetic, M. and Dobry, R. (1991). Effect of soil plasticity on cyclic responcse. *Journal of Geotechnical Engineering, ASCE*, 117(1):89–107.

Wang, Z.-L., Dafalias, Y. F., and Shen, C.-K. (1990). Bounding surface hypoplasticity model for sand. *Journal of Engineering Mechanics*, 116(5):983–1001.

Wolf, J. (1985). *Dynamic Soil-Structure Interaction*. Prentice Hall, Englewood Cliffs, New Jersey.

Zhou, J. and Zhou, Y. (2007). A new simple method of implicit time integration for dynamic problems of engineering structures. *Acta Mech Sin*, 23:91–99.

Zienkiewicz, O. and Taylor, R. (2000). *The Finite Element Method, Volume 1: The Basis*. Butterworth-Heinemann.